Technische Universität München
TUM School of Natural Sciences

Deciphering the Active Role of Carboxylate-type MOFs in Alkaline OER: From Pristine Structures to Functional Intermediates

Xiaoxin Ma

Vollständiger Abdruck der von der TUM School of Natural Sciences der Technischen Universität München zur Erlangung einer

Doktorin der Naturwissenschaften (Dr. rer. nat.)

genehmigten Dissertation.

Vorsitz:	Prof. Dr. Torben Gädt
Prüfende der Dissertation:	1. Prof. Dr. Roland A. Fischer
	2. Prof. Dr. Aliaksandr S. Bandarenka
	3. Prof. Dr. Hong-Cai Zhou

Die Dissertation wurde am 19.09.2024 bei der Technischen Universität München eingereicht und durch die TUM School of Natural Sciences am 21.10.2024 angenommen.

Acknowledgment

Every journey has its beginning and end, and my doctoral journey will now reach its conclusion. Reflecting on the past years, I would like to express my heartfelt gratitude to many individuals whose support and help have been invaluable in completing this dissertation.

Firstly, I would like to thank my PhD supervisor, **Prof. Roland A. Fischer**, for giving me the opportunity to work in his group at TUM. He provided me the freedom to explore my interests and encouraged discussions and debates about unbridled ideas. I am grateful for his generosity and support, as well as for sharing his extensive knowledge of chemistry, which has always greatly inspired me.

I am also profoundly thankful to my co-supervisor, **Prof. Dr. Aliaksandr S. Bandarenka**, for allowing me to work in his ECS group within the physics department. His insightful advice and discussions have been instrumental throughout my PhD study, and I am honored to have been part of the ECS group.

My sincere appreciation goes to my subgroup leader, **Dr. Julien Warner**, for his continuous encouragement and support over the years. I would also like to thank the e-conversion subgroup members: **Dr. Kathrin Kollmannsberger**, **Sarah Dummert**, **Johanna Haimerl**, **Vanessa Ramm**, **Simon Deger**, **Nadine Schmaus**, **Shufan Wu**, **Dr. Philip Stanley**, and **Yishuo Chen**. Working with you all has been a pleasure.

I am deeply grateful to the China Scholarship Council (CSC) for financially supporting my studies and life abroad.

I extend my gratitude to **Prof. Yang Shao-Horn** and **Prof. Ifan E.L. Stephens** for their valuable suggestions, which significantly benefited my research. Special thanks to my collaborators: **Daniel J, Zheng**; **Mikaela Görlin** (Massachusetts Institute of Technology), **Caiwu Lang** (Imperial College London), **Qing Ai** and **Guanhui Gao** (Rice University), **Maider Zarrabeitia** (Helmholtz Institute Ulm), **Max Koch** (Chemistry, TUM), **Rachit Khare** (Chemistry, TUM), **János Mink** (Institute of Materials and Environmental Chemistry, Hungary), and **Kristina Liu** (Chemistry,

TUM). Your support in measurements and discussions has been invaluable.

I am also grateful to **Martin Schellerer** and **Dana Weiß** for their assistance with numerous bureaucratic and formal matters. Dana Weiß's encouragement and kindness have been particularly helpful. Thanks to Dr. **Christian Gemel**, Dr. **Eliza Gemel**, **Rodica Dumitrescu**, Dr. **Mian Zahid Hussain**, and Dr. **Christian Jandl** for their support in my project.

I would like to thank all members of AMC for the enjoyable times and working atmosphere. Special thanks to colleagues in AMC: Dr. **Anna Lisa Semrau**, Dr. **Lena Staiger**, Dr. **Karina Hemmer**, Dr. **Stefan Burger**, Dr. **Sebastian Weishäupl**, Dr. **Pengchen Liu**, Dr. **Jan Berger**, **Margit Aust**, **Lena Schröck**, and **Lang Lv**. It has been a pleasure working with you all. Also, my gratitude goes to my ECS members: Dr. **Batyr Garlyyev**, Dr. **Sebastian Watzele**, Dr. **Song Xue**, Dr. **Xing Ding**, Dr. **Regina Kluge**, Dr. **Xaver Lamprecht**, Dr. **Elena Gubanova**, **Kun-Ting Song**, **Peter Schneider**, **Göktug Yesilbas**, **Rainer Götz**, **Raphael Streng**, **Christian Schott**, and **Siegfried Schreier**. It has been a joy to be part of the ECS family.

Thanks to the SURMOF Lab members: Dr. **Wei-Jin Li**, Dr. **Soumya Mukherjee**, Dr. **Ladawan Pukdeejorhor**, Dr. **Zhenyu Zhou**, Dr. **Shujin Hou**, **Shufan Wu**, **Liangzhen Liu**, **Da Lie**, and **RuiRui Zhang**. Special thanks to Dr. **Zhiying Fan** and Dr. **Shengyang Guan** for our engaging discussions.

Last but certainly not least, I deeply appreciate my family and friends for their unconditional love, patience, and support. Your understanding and encouragement have been a constant source of strength and hope throughout this journey. And the final thank is to myself.

Xiaoxin Ma

July 2024

I think, therefore I am

ego cogito, ergo sum

René Descartes

Zusammenfassung

Metallorganische Gerüstverbindungen (MOFs) stellen einen bedeutenden Fortschritt in der Koordinationschemie dar. Sie bieten eine große Vielseitigkeit durch die Auswahl von Metallen und Liganden sowie die Möglichkeit, chemische Koordinationsbindungen zu manipulieren und Porengrößen und -strukturen anzupassen. Diese einzigartigen Eigenschaften haben MOFs zu vielversprechenden Kandidaten für verschiedene Anwendungen gemacht, insbesondere im Bereich der Elektrokatalyse für energiebezogene Prozesse wie die Wasserspaltung. Im letzten Jahrzehnt wurden MOFs ausführlich auf ihr Potenzial bei Sauerstoffentwicklungsreaktionen (OER) untersucht. Es bleibt jedoch eine Debatte darüber, ob unberührte MOFs als direkte Katalysatoren oder lediglich als Vorläufer fungieren, wobei abgeleitete Zwischenprodukte zur beobachteten OER-Aktivität beitragen.

Ziel dieser Dissertation ist es, die Rolle unberührter Ni(Fe)-MOFs in alkalischen OER-Anwendungen aufzuklären. Die Forschung ist in drei Hauptziele unterteilt: (1) Bestimmung, ob ursprüngliche MOFs als Katalysatoren oder Vorläufer wirken, (2) Untersuchung der Auswirkungen der ursprünglichen MOF-Struktur auf die OER-Aktivität und (3) Gewinnung von Erkenntnissen aus dem MOF-Transformationsprozess, um die Entwicklung effizienterer Katalysatoren zu unterstützen.

In Kapitel 3 wurde die Stabilität ursprünglicher MOFs in alkalischen Elektrolyten untersucht. Dabei wurde festgestellt, dass diese MOFs im alkalischen OER-Prozess eher als Vorläufer denn als Katalysatoren dienen. Eine Reihe von Ni-MOFs mit unterschiedlichen Carboxylat-Linkerlängen wurde synthetisiert und analysiert. Dies zeigte, dass die ursprüngliche MOF-Struktur das elektrokatalytische Verhalten erheblich beeinflusst. Zeitabhängige PXRD- und Raman-Spektroskopie wurden eingesetzt, um den Abbau und die Rekonstruktion von MOFs unter alkalischen Bedingungen zu untersuchen. Dabei wurde die Rolle der Linker-Wahl bei der

Umwandlung in unterschiedliche Nickelhydroxidphasen hervorgehoben.

In Kapitel 4 wurde der Einfluss der Stabilität der MOF-Struktur auf die OER-Aktivitäten mithilfe von In-situ- und Ex-situ-Charakterisierungstechniken weiter untersucht. Durch die Einführung eines zusätzlichen Linkers in den Elektrolyten wurde die Alkalistabilität der MOFs verbessert und der Rekonstruktionsprozess besser kontrolliert. Dieser Ansatz verzögerte den Übergang von ungeordneten zu geordneten Metallhydroxidphasen, was zu einer verbesserten OER-Leistung führte.

Die hier erzielten Ergebnisse liefern wertvolle Einblicke in das Verhalten und die Transformationsmechanismen von MOFs in alkalischen Lösungen. Obwohl einige Phänomene noch getestet und Annahmen bewiesen werden müssen, glauben wir, dass unsere Arbeit ein Beispiel in diesem Bereich liefern, zu einem tieferen Verständnis der OER-Mechanismen beitragen und neue Wege im Bereich der Katalyse eröffnen könnte.

Abstract

Metal-organic frameworks (MOFs) represent a significant advancement in coordination chemistry, offering extensive versatility through the selection of metals and ligands, as well as the ability to manipulate chemical coordination bonds and tune pore sizes and structures. These unique properties have made MOFs promising candidates in various applications, particularly in the field of electrocatalysis for energy-related processes such as water splitting. Over the past decade, MOFs have been extensively studied for their potential in oxygen evolution reactions (OER). However, there remains a debate about whether pristine MOFs function as direct catalysts or merely as precursors, with derived intermediates contributing to the observed OER activity.

This dissertation aims to elucidate the role of pristine Ni(Fe) MOFs in alkaline OER applications. The research is divided into three main objectives: (1) determining whether pristine MOFs act as catalysts or precursors, (2) exploring the impact of the original MOF structure on OER activity, and (3) gaining insights from the MOF transformation process to inform the design of more efficient catalysts.

In Chapter 3, the stability of pristine MOFs in alkaline electrolytes was investigated, revealing that these MOFs serve as precursors rather than catalysts in the alkaline OER process. A series of Ni-MOFs with varying carboxylate linker lengths were synthesized and analyzed, demonstrating that the original MOF structure significantly influences the electrocatalytic behavior. Time-dependent PXRD and Raman spectroscopy were employed to study the degradation and reconstruction of MOFs in alkaline conditions, highlighting the role of linker choice in the transformation into distinct nickel hydroxide phases.

Chapter 4 further examined the influence of MOF structure stability on OER activities using in-situ and ex-situ characterization techniques. By introducing an additional linker in the electrolyte, the alkali stability of the MOFs was enhanced, and the reconstruction process was better controlled. This approach delayed the transition

from disordered to ordered metal hydroxide phases, resulting in improved OER performance.

The results obtained herein provide valuable insights into the behavior and transformation mechanisms of MOFs in alkaline solutions. Although some phenomena remain to be tested and assumptions to be proven, we believe our work could provide an example in this area, contribute to a deeper understanding of OER mechanisms, and open new avenues in the field of catalysis.

Table of Contents

List of Abbreviations

A	Surface Area of Electrode
AEM	Adsorbate Evolution Mechanism
AFM	Atomic Force Microscopy
aq	Aqueous Solution
BC	Benzene Acid
BDC	Terephthalic Acid
BET	Brunauer–Emmett–Teller
BPDC	Biphenyl-4,4'-Dicarboxylate
BPTC	Biphenyl-3,4′,5-Tricarboxylic Acid
BTC	1,3,5-Benzenetricarboxylic Acid
Ca	Adsorption Capacitance
CE	Counter Electrode
CIFs	Crystallographic Information Files
CSD	Cambridge Structural Database
CV	Cyclic Voltammetry
D	Derivatives
DCM	Double Cystal Monochromator
DFT	Density Functional Theory
EDS	Energy Dispersive Spectroscopy
EEC	Equivalent Electric Circuit
EIS	Electrochemical Impedance Spectroscopy
Et_3N	Trimethylamine
EXAFS	Extended X-ray Absorption Fine Structure
ex-CL	Extra Carboxylate linker
f	Force Constant
F	Faraday Constant
FTIR	Fourier Transform Infrared Spectroscopy
GCE/GC	Glassy Carbon Electrodes
GIXRD	Grazing Incidence X-ray Diffraction
HAADF-STEM	High-Angle Annular Dark-Field Scanning

	TEM
H_{ads}	Adsorbed Hydrogen Atoms
HER	Hydrogen Evolution Reaction
HKUST	Hong Kong University of Science and Technology
HPLC	High-Performance Liquid Chromatography
HRTEM	high-resolution transmission electron microscope
HSAB	Hard Soft Acid Base
ICP-OES	Inductively Coupled Plasma Atomic Emission Spectroscopy
IEA	International Energy Agency
iR	Ohmic Drop
ImZ	Imaginary Part of the Impedance
ITO	Indium Tin Oxide
j	Current Density
L	Linker
LbL	Layer-by-Layer
LOM	Lattice Oxygen Oxidation Mechanism
m	Mass
M	Metal
M-H	Metal-Hydrogen Bond
MIL	Matérial Institut Lavoisier
MO	Metal-Oxygen group
MOFs	Metal-Organic Frameworks
MOH	Metal and Hydroxyl group
MOOH	Metal and Oxyhydroxyl group
N	Nitrogen
n	Number of Moles
NDC	2,6-Naphthalic acid
NMR	Nuclear Magnetic Resonance
OCP	Open Circuit Potential
OER	Oxygen Evolution Reaction

ORR	Oxygen Reduction Reaction
P	Phosphorous
PEM	Proton Exchange Membrane
p-KOH	Purified KOH
Q	Charge
RDE	Rotating Disk Electrode
RE	Reference Electrode
RHE	Reversible Hydrogen Electrode
rpm	Revolutions Per Minute
Ra	Adsorption Resistance
Rct	Charge Transfer Resistance
Rs	Electrolyte Resistance
S	Sulfur
s	Solid
SBUs	Secondary Building Units
SEM	Scanning Electron Microscope
SURMOFs	Surface-Mounted Metal-Organic Frameworks
t	Time
TEM	Transmission Electron Microscope
TOF	Turnover Frequency
TPDC	p-Terphenyl-4,4"-Dicarboxylate
UIO	Universitet i Oslo
UV	Ultraviolet Spectroscopy
WE	Working Electrode
W_{S1}	Warburg Short Element
XANES	X-ray Absorption Near-Edge Structure
XAS	X-ray Absorption Spectroscopy
XPS	X-ray Photoelectron Spectroscopy
Zdl	Double Layer Impedance
ZIF	Zeolitic Imidazolate Framework
ΔE_0	Energy-Shift
ΔG_{H^*}	Free Enthalpy of H Adsorption
ΔG_{HO^*}	The Gibbs Free Energy of Adsorbed Hydroxyl

	Intermediate
ΔG_O	The Gibbs Free Energy of an Oxygen intermediate
ΔG_O-ΔG_{HO*}	The Disparity between ΔG_O and ΔG_{HO*}
ΔG_1	The Gibbs Energy of 1st reaction steps in the Adsorbate Evolution Mechanism
ΔG_2	The Gibbs Energy of 2nd reaction steps in the Adsorbate Evolution Mechanism
ΔG_3	The Gibbs Energy of 3rd reaction steps in the Adsorbate Evolution Mechanism
ΔG_4	the Gibbs Energy of 4th reaction steps in the Adsorbate Evolution Mechanism
1	Ni-BDC-MOF
2	Ni-NDC-MOF
2D	Two Dimensions
3	Ni-BPDC-MOF
3D	Three Dimensions
4	Ni-TPDC-MOF

1. Introduction

1.1 The Importance of Green Hydrogen Production

The contemporary global energy landscape stands at a crossroads, where the imperative of transitioning toward sustainable energy sources is increasingly evident. In 2023, our society's energy consumption reached 183,230 TWh, with fossil fuels contributing approximately 76.5% of the total energy supply, as shown in **Figure 1.1**.[1-4] This increasing energy demand is facing substantial challenges, as public fossil fuel reserves are nearing depletion and are expected to be exhausted within a few hundred years.[5] Fossil fuels, including crude oil, coal, and natural gas, are generally considered by geologists to be the result of ancient plants undergoing compression and heating over extensive geological epochs. Consequently, there is an urgent need to advance technologies for generating renewable energy resources to address the various issues arising from the energy crisis and the unequal distribution of mineral resources across different regions.

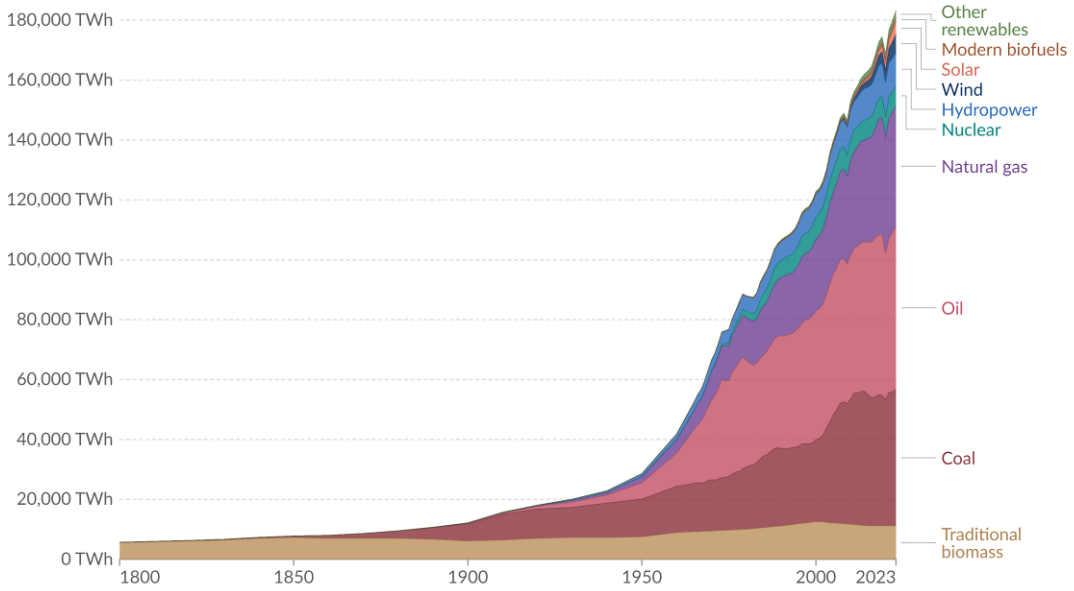

Figure 1.1 Global primary energy consumption by source 2023, reprinted under the permission by website of Our World in Data from ref[1], with license CC BY.

Along with renewable energy sources such as solar, wind, hydropower, and nuclear

energy, green hydrogen produced from water is emerging as a significant topic of interest due to its high energy density and the abundant availability of water resources.[6, 7] According to the International Energy Agency, global hydrogen consumption reached 95 million tons in 2022, representing a nearly 3% increase from 2021.[8] This consumption is projected to rise to 150 million tons by 2030, driven by the substantial demand in the refining, chemical, and steel industries, as well as the growing requirements for electricity and heating as shown in **Figure 1.2**.

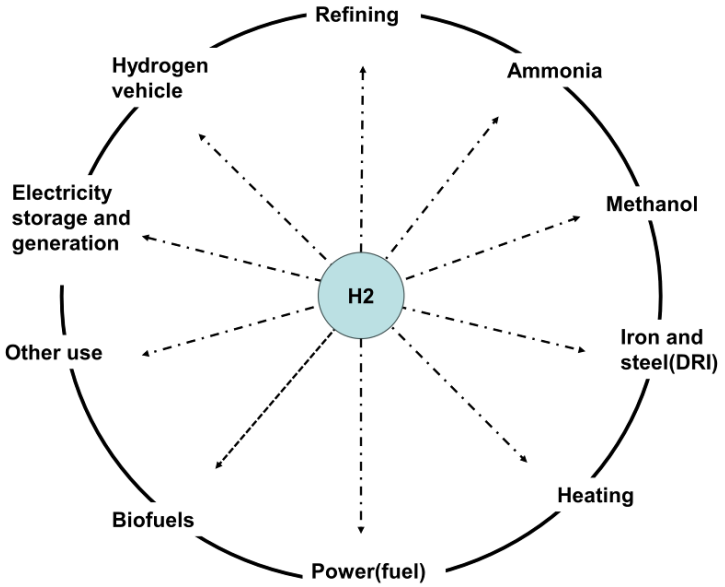

Figure 1.2 Schematic of the application area of hydrogen.

However, despite advancements in green energy technologies and robust support from governments worldwide, the majority of hydrogen production still relies on fossil fuels, with natural gas accounting for 62% and coal for 21% in 2022.[8] This continued reliance on fossil fuels for hydrogen production fails to reduce CO_2 emissions effectively.[9] CO_2 emissions are a significant role in the development of green energy as well. Following the UN Climate Change Conference in Paris 2015, it has become widely recognized that reducing CO_2 emissions is necessary to mitigate environmental degradation. This is particularly important in addressing climate change and the growing occurrence of extreme weather events such as floods, droughts, heat waves, and hurricanes gradually. Thus, green hydrogen production, which does not emit CO_2, is expected to gradually replace the traditional method of

hydrogen production in the future.

1.2 General Aspect of Water Splitting

Green hydrogen is primarily produced through photo/electrochemical methods of water splitting. Since photocatalytic water splitting has a lower conversion efficiency, water electrolysis, also known as electrocatalytic water splitting, has experienced more fast progress and practical implementation. This technology has a history of almost two centuries, starting from its first discovery in 1789 by Paets van Troostwijk and Deiman through the use of static electricity generated by friction.[10] The electrochemical approach efficiently surpasses the energy barrier of water splitting, which has a ΔG value of 237.1 kJ/mol, by utilizing a voltage of 1.23V at 25°C and 1 bar. Alternatively, the direct thermolysis of water requires considerably greater temperatures above 4000 K. [6]

Subsequently, there was rapid progress in industrial water electrolysis, especially after the establishment of a large-scale water electrolysis facility in 1939 and the introduction of Nafion-based proton exchange membrane (PEM) water electrolysis in 1966.[11, 12] However, hydrogen production through this method remains relatively low, accounting for less than 1% of total hydrogen production in 2022, primarily due to the high cost of electrocatalysts. Despite this, with the increasing focus on clean hydrogen to reduce reliance on fossil fuels and mitigate environmental impact, the International Energy Agency (IEA) predicts that the market share of hydrogen production via electrocatalytic water splitting will rise to approximately 22% by 2050.[8]

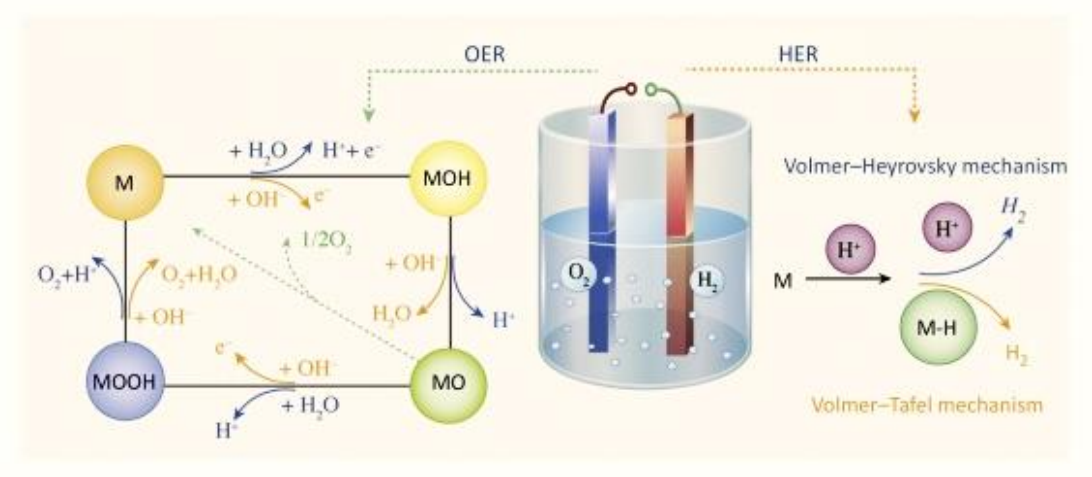

Figure 1.3 Illustration of oxygen evolution reaction (OER) and the hydrogen evolution reaction (HER) in Electrochemical Water Splitting, M is a catalytically active metal center. reprinted under the permission from ref[13], Copyright © 2019 Published by Elsevier Inc.

Water splitting consists of two half-reactions: the oxygen evolution reaction (OER) at the anode and the hydrogen evolution reaction (HER) at the cathode as shown in **Figure 1.3**. Electrolysis can be classified into two types based on the pH of the electrolyte: acidic/neutral electrolysis and alkaline electrolysis. The general chemical equations for water electrolysis are shown in **Scheme 1.4** (acidic electrolyte) and **Scheme 1.5** (alkaline electrolyte).[14]

In an acidic electrolyte in **Scheme 1.4** , water acts as the reagent at the anode, where it undergoes electrochemical oxidation, producing molecular oxygen, electrons, and protons. The protons travel through the electrolyte, while the electrons move through the electrical circuit to the cathode, where they combine to form H_2.

In an alkaline electrolyte in **Scheme 1.5**, hydroxyl ions serve as the reactant at the anode, resulting in the production of water molecules, molecular oxygen, and electrons. At the cathode, water molecules undergo reduction, forming molecular hydrogen and hydroxyl ions in conjunction with the electrons. The hydroxyl ions then migrate across the electrolyte towards the anode.

Scheme 1.4: Water electrolysis in acidic and neutral electrolyte

Overall	$2H_2O \rightarrow O_2 + 2\ H_2$
Anode (OER)	$2H_2O \rightarrow O_2 + 4\ H^+ + 4\ e^-$
Cathode (HER)	$4H^+ + 4\ e^- \rightarrow 2\ H_2$

Scheme 1.5: Water electrolysis in alkaline electrolyte

Overall	$2H_2O \rightarrow O_2 + 2\ H_2$
Anode (OER)	$4OH^- \rightarrow O_2 + 2\ H_2O + 4\ e^-$
Cathode (HER)	$4H_2O + 4\ e^- \rightarrow 2\ H_2 + 4\ OH^-$

1.3 Alkaline water splitting

Despite acidic water electrolysis's positive features, like high current densities, high voltage efficiency, and high gas purity, its low durability and restricted selection of noble electrocatalysts hinder its large-scale growth. As a result of its more effective long-term stability and the wide range of non-precious catalyst options, water electrolysis in alkaline media has been used in large-scale industrial applications for more than a century, despite the initial discovery of splitting water into hydrogen and oxygen gases in an acidic electrolyte.[15]

1.3.1 Hydrogen Evolution Reaction in Alkaline Water Splitting

Under alkaline water electrolysis, the hydrogen evolution reaction is comparatively more straightforward than the oxygen evolution reaction. The HER involves a two-electron process with a single reaction intermediate involving metal-hydrogen (M-H) bonding.[16] The HER begins with the Volmer step, where an electron (e^-) transfers to the electrode and the water molecule on the catalyst surface, producing adsorbed hydrogen atoms (H_{ads}). This is followed by either an electrochemical route (Heyrovsky step) or a chemical route (Tafel step) to generate hydrogen. In the Heyrovsky step, the adsorbed hydrogen combines with a water molecule and an electron to produce hydrogen. In the Tafel step, two adsorbed hydrogen atoms

combine to form a hydrogen molecule.[17]

Due to the simple adsorption-desorption behavior and the single reaction intermediate (M-H) process, the suitability of an HER catalyst can be roughly predicted using the Sabatier principle.[18, 19] According to this principle, the catalyst should have a binding energy for M-H that is neither too strong nor too weak, allowing reactants to adsorb easily and products to desorb readily from the metal surface, thus preventing blockage of active sites.

If the Sabatier principle were the sole rate-determining factor of a specific reaction, it would be possible to plot the reaction rate against the adsorption-free energy of the intermediate as shown in the **Figure 1.6a**.[20, 21] In such a plot, the free enthalpy of hydrogen adsorption should ideally be zero. Based on this principle, a volcano curve model was first proposed independently by Gerischer and Parsons in the 1950s to visualize the activities of metals toward electrochemical H_2 evolution.[22, 23] Trasatti later constructed this model using experimental data obtained from polycrystalline metal surfaces and measured hydrogen heats of adsorption.[24] Trasatti and other researchers identified platinum-based compounds as the most active monometallic HER catalysts, occupying a position near the top of the volcano curve.

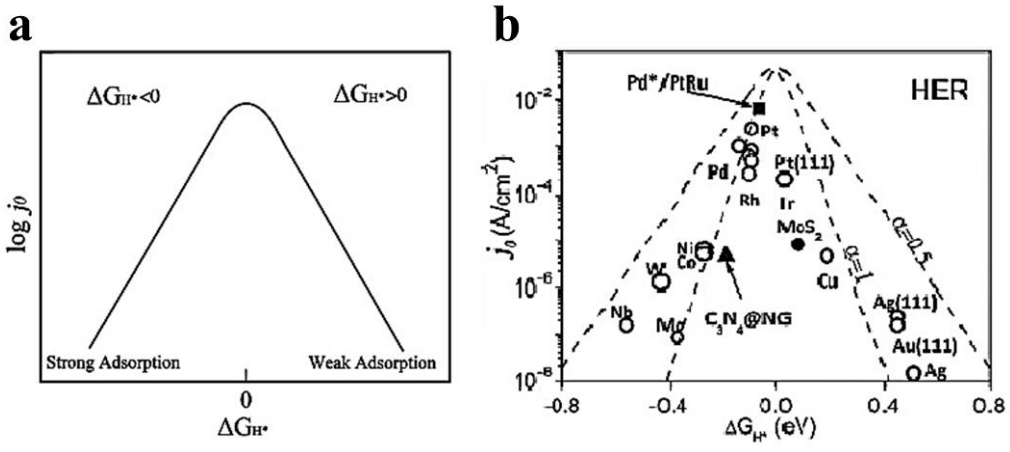

Figure 1.6 a) Relationship between exchange current density j0 and free enthalpy of H adsorption ΔG_{H^*}. b) The 'volcano plot' describing the HER activity trends for the surface of different materials as a function of as a function of the ΔG_{H^*}. Reproduced under the permission from ref[20], © 2015 WILEY-VCH Verlag GmbH & Co. KGaA,

Weinheim.

Today, with the availability of immense computational power, accurate electronic structures of catalysts can be explored using density functional theory (DFT).[25, 26] This advancement has led to developing more sophisticated descriptors of material properties in **Figure 1.6b**, such as the formation potential of OH adsorbates. Consequently, the predictive power in catalyst design has significantly improved, enabling the discovery and optimization of new and efficient HER catalysts.

1.3.2 Oxygen Evolution Reaction in Alkaline Water Splitting

The hydrogen evolution reaction involves only two electron-transfer steps, whereas the oxygen evolution reaction requires significantly higher energy to overcome the kinetic barrier associated with the four electron-proton coupled steps.[27] Numerous research groups have proposed mechanisms for OER at the anode under both acidic and alkaline conditions. Despite some disparities, these proposed mechanisms share similarities, particularly in the intermediates involved, such as MOH and MO.[28] The primary differences often revolve around the specific reaction steps that lead to the formation of oxygen.

1.3.2.1 Oxygen Evolution Reaction Mechanism

In OER, the bonding interactions (M–O) within the intermediates (MOH, MO, and MOOH) are crucial for the overall electrocatalytic efficiency. As a heterogeneous reaction, the strength and nature of these interactions significantly impact the reaction kinetics and mechanisms. It is widely accepted that OER can proceed through two distinct mechanisms: the adsorbate evolution mechanism (AEM) and the lattice oxygen oxidation mechanism (LOM), also known as the lattice oxygen-mediated mechanism. These mechanisms are depicted in **Figure 1.7**.[29]

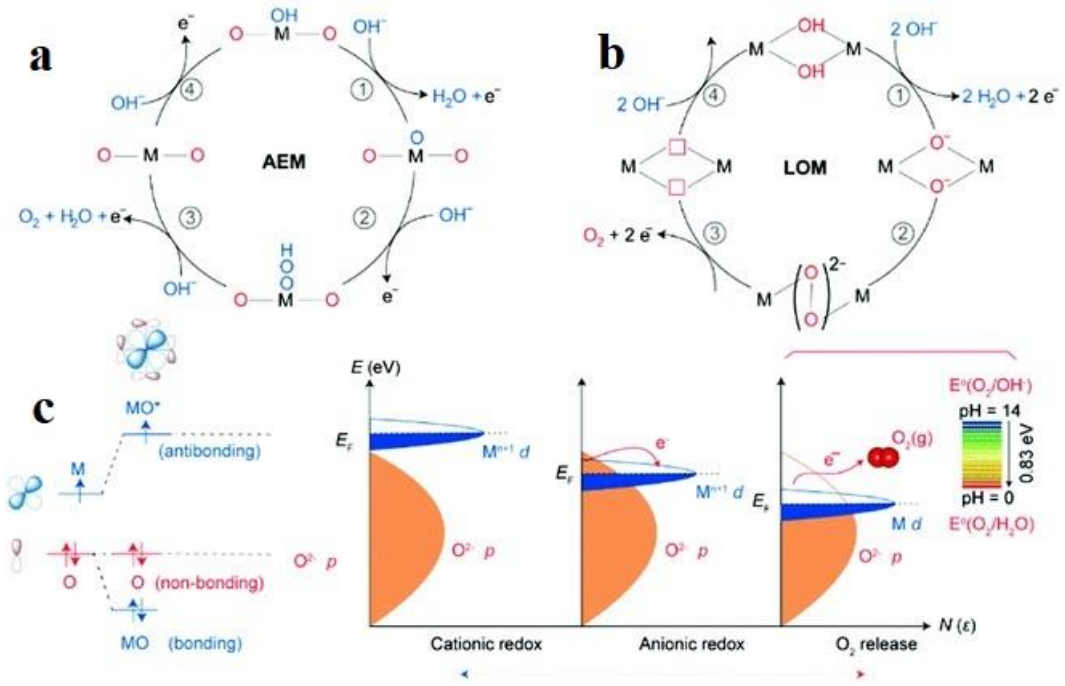

Figure 1.7 Schematic illustration of the OER mechanisms about (a) AEM and and (b) LOM. (c) Schematic band structure of perovskite oxides to demonstrate the different redox processes as the energy of M d band decreases with respect to the O 2p band. Reprinted from ref[29], with permission from the Royal Society of Chemistry.

The adsorbate evolution mechanism (AEM) is widely acknowledged in the field of OER, where OH species usually adsorb onto the catalyst surface, undergoing successive proton and electron transfers. The equations of the AEM in the alkaline are written in the following **Equation 1.8**.

Equation 1.8 OER step of the AEM in the alkaline electrolytes

$M + OH^- \rightarrow M\text{-}OH + e^- (\Delta G_1)$	1-1
$M\text{-}OH + OH^- \rightarrow M\text{-}O + H_2O + e^- (\Delta G_2)$	1-2
$2M\text{-}O \rightarrow O_2 + 2M^+ + 2e^-$ or $M\text{-}O + OH^- \rightarrow M\text{-}OOH + e^- (\Delta G_3)$	1-3
$M\text{-}OOH + OH^- \rightarrow M + O_2 + H_2O + e^- (\Delta G_4)$	1-4

At each stage, a proton is introduced into the electrolyte and ultimately combines with the transferred electron at the cathode. Initially, hydroxyl (OH) molecules adsorb onto the surface at an oxygen vacancy site. The adsorbed OH then

deprotonates to form an oxygen (O*) intermediate. In the subsequent step, an O-O bond is formed, where O* reacts with another OH molecule, producing the hydroperoxo (HOO*) intermediate. In the final stage, molecular oxygen (O_2) is generated through the deprotonation of HOO* and the restoration of the active site.[30]

As an alternative to AEM, the lattice oxygen mechanism (LOM) has been proposed for OER, particularly when dynamic structural changes are observed on the catalyst's surface.[31] The LOM process involves lattice oxygen derived from the catalyst's structure. This mechanism has been found to have a lower reaction barrier and typically occurs when the catalyst's covalency increases.[29] As the ability of metal cations to bind with oxygen weakens, it becomes easier to facilitate O–O bonding through the reversible formation of oxygen vacancies.[32-34]

When the metal d band is located above the oxygen p band, the metal center of the oxides serves as the adsorption site and redox center in **Figure 1.7c**, enabling water oxidation to follow the AEM. Conversely, when the energy of the occupied metal d band is lower than that of the oxygen p band, electrons from the p band transfer to the d band, creating ligand holes. This promotes the formation of oxygenated species $(O_2)_n$ through structural rearrangement to attain a stable state. Consequently, the OER mechanism can switch from AEM to LOM when the metal–oxygen covalency increases.[35, 36]

1.3.2.2 Oxygen Evolution Reaction Catalysts

The OER is governed by multifaceted factors, making the prediction of effective catalysts particularly challenging. This complexity arises because the reaction is influenced by a combination of properties rather than a singular factor. Significant research efforts have been directed towards identifying highly effective OER catalysts and understanding the active sites responsible for this reaction.[12] Among the investigated properties, factors such as the bond energy between the metal and hydroxyl group (M-OH),[37, 38] the number of d-electrons,[39, 40] electron occupancy in the eg orbital,[41] and the adsorption energy differences (ΔG_O - ΔG_{OH}) have been

prominent in influencing activity.[42]

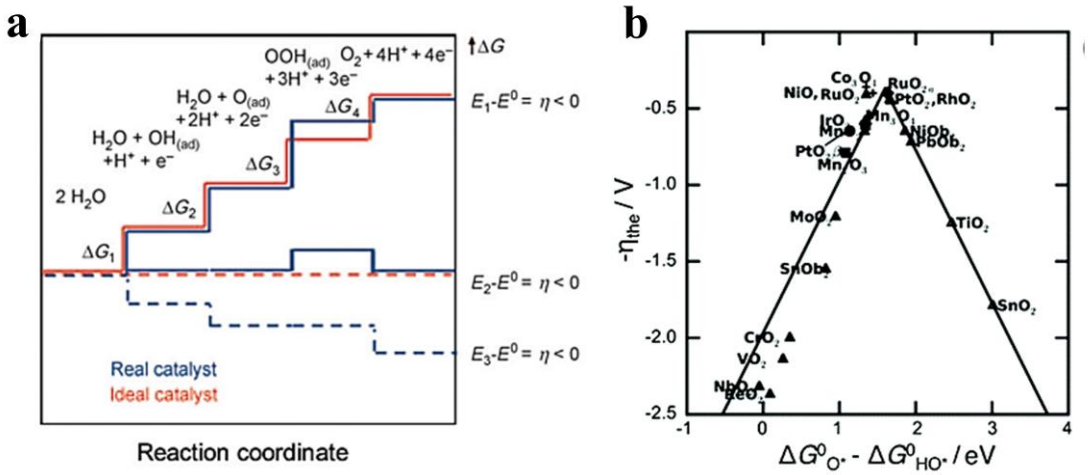

Figure 1.9 a) Plot of Gibbs free energy of reactive species and intermediates of the OER versus the reaction coordinate. Reproduced under the permission from ref[43], Copyright © 2010 WILEY-VCH Verlag GmbH & Co. KGaA, Weinheim b) Activity trends towards oxygen evolution, for rutile, anatase and oxides**.** Reproduced under the permission from ref[42], Copyright © 2011 WILEY-VCH Verlag GmbH & Co. KGaA, Weinheim

1) M-OH Bond Energy: Historically, the simplest predictive method involved using the M-OH bond energy to estimate the activity of the OER.[38, 44] In 1955, Rüetschi and Delahay first proposed that the energy of the M-OH bond could significantly impact OER activity.[37] They noted a roughly linear relationship where increasing bond energy corresponded to decreasing overpotential. Subsequent studies, including those by Hu and colleagues, reinforced this correlation by demonstrating that stronger M-OH bond strengths in binary or ternary metal hydr(oxy)oxides (e.g., $NiFeO_x$, $CoFeO_x$, and $NiCoFeO_x$) were indicative of improved OER properties.[45] However, this approach is notably limited and applicable primarily to specific materials. Furthermore, accurate determination of bond energies and enthalpies remains a formidable challenge due to the presence of numerous confounding variables.

2) Electron Occupancy: The occupation of the eg orbital emerged later as a predictor of OER activity.[28, 46, 47] Comprehensive studies conducted by Shao-Horn and her team

on perovskites revealed that 3d electron occupancy in the eg orbital could effectively indicate catalytic activity, particularly in ABO_3-type perovskite oxide materials.[41] This method has been extended to assess OER performance in spinel oxides, where the eg orbital occupancy by 3d electrons at the octahedral site can be manipulated through variations in oxidation and spin states.[48-50]

3) Adsorption Energy and OER Activity**:** Advancements in density functional theory simulations have highlighted the primary role of adsorption energies of intermediates (OH, O, and OOH) on the surface in dictating OER activity, showing in **Figure 1.9**. In many catalysts, neither the Gibbs energy from 1st reaction steps (ΔG_1) nor from the 4th reaction steps (ΔG_4) consistently serves as the decisive step in evaluating potential. The disparity between ΔG_O and ΔG_{HO*} (ΔG_O-ΔG_{HO*}) has been identified as a universal predictor for OER activity, particularly when the catalyst exhibits moderate oxygen binding strength.[42, 51] This parameter also elucidates the characteristic volcano-shaped interaction observed in catalytic materials,[52] providing a theoretical framework for the strategic development of effective catalysts as depicted in the accompanying **Figure 1.9b**. Due to meticulous analysis of the multistep reaction process, this descriptor has been widely accepted as a reliable indicator of OER activity.

RuO_2 and IrO_2 are currently recognized as the most effective catalysts for the oxygen evolution reaction, primarily due to their predicted catalytic activity as in the **Figure 1.9**. However, the scarcity and high cost of these precious metals further complicate their widespread industrial application.

Historically, the exploration of metal oxide catalysts, incorporating various transition metals, has been a focal point for enhancing OER efficiency.[28, 53, 54] Metal oxides such as perovskite-type catalysts[55, 56] and spinel-type oxides[57] have shown significant promise. These materials are not only more abundant and cost-effective but also exhibit superior stability in alkaline environments and moderate conductivities, making them viable alternatives for electrocatalytic applications in OER.

In addition to metal oxides, metal (oxy)hydroxides have also been effectively used for OER electrocatalysis.[58, 59] Among the various metal (oxy)hydroxides utilized for OER, $Ni(OH)_2$ stands out, particularly in its two polymorphic forms, α-phase and β-phase. The transformation of these phases during electrochemical operations, often referred to as the Bode Scheme.[60] α-$Ni(OH)_2$ was transformed into β-$Ni(OH)_2$ by aging, while β-NiOOH might be turned into γ-NiOOH by overcharging.[61] In the beginning, β-NiOOH has long been regarded as the active phase for the OER.[62, 63] Recent studies have highlighted the γ-NiOOH phase as particularly effective for OER.[64, 65] Experimental data have demonstrated that α-$Ni(OH)_2$ exhibits superior OER activity compared to β-$Ni(OH)_2$.[66-68] Additionally, the integration of iron into $Ni(OH)_2$, forming NiFe-based materials, has significantly enhanced its performance, establishing these compounds as highly effective OER electrocatalysts within transition metal systems.[69-71]

In recent advancements within the field of electrocatalysis, Metal-Organic Frameworks (MOFs) have garnered attention as promising candidates for OER applications.[72, 73] Characterized by their intricate lattice structures, MOFs offer high porosity and extensive surface areas, which are advantageous for catalytic processes. Furthermore, their excellent thermal stability, low density, and the ability to tailor their chemical and physical properties enhance their suitability for OER.[74-76] These distinctive attributes position MOFs as potential transformative agents in the development of efficient, durable, and economically viable OER catalysts, as will be elaborated in the following **section 1.4.**

1.4 Metal-organic frameworks

Metal-organic frameworks represent a class of innovative materials crafted based on coordination chemistry. These structures are assembled from organic ligands and metal nodes—or metal clusters known as secondary building units (SBUs)—to create a periodic crystalline framework.[77-79] This intricate arrangement allows MOFs to exhibit unique properties and functionalities, making them highly versatile for

various applications.

1.4.1 Historical Development of Metal-Organic Frameworks

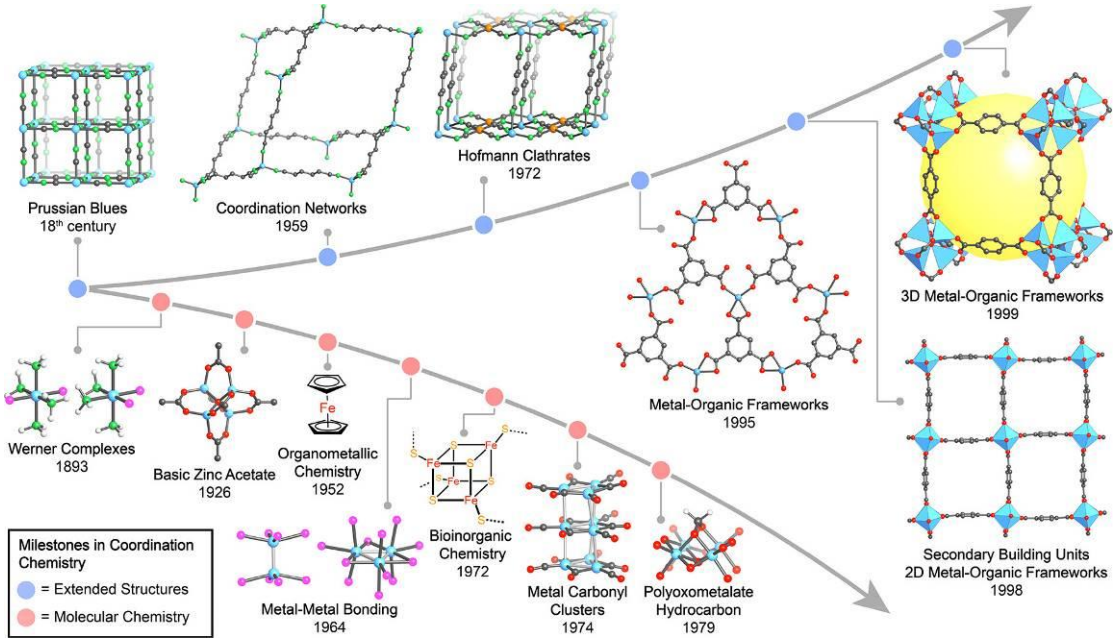

Figure 1.10 Chronology of advances in coordination chemistry from the discovery of Werner to the development of metal–organic frameworks. Reprinted under the permission from ref[80], Copyright © 2018 American Chemical Society.

The foundational concept of MOFs can be traced back to the pioneering work of Alfred Werner in 1893 as shown in **Figure 1.10**.[80, 81] Werner's introduction of a structural model for $[Co(NH_3)_6]Cl_3$ marked a seminal moment in the advent of modern coordination chemistry.[82, 83] His insights into the oxidation states and coordination numbers of molecular complexes significantly advanced the understanding of coordinative bonding within molecular complexes and larger extended structures. In 1926, advancements continued with the elucidation of basic zinc acetate structures, highlighting the application of coordination bonds extending from neutral donor ligands to charged ligands such as organic carboxylates.[84, 85] These discoveries facilitated the formation of polynuclear clusters, a crucial step in the evolution of MOFs. The exploration of coordination chemistry further expanded in subsequent decades with significant contributions such as Albert Cotton's work on metal-metal bond compounds in 1964[86, 87] and the study of polyoxomolybdate-

hydrocarbon interactions exemplified by the $CH_2Mn_4O_{15}H^{3-}$ anion in 1979.[80, 88]

In parallel, the geometric combination structure is also advancing, building upon Werner's finding. In 1897, Karl A. Hofmann first described compounds such as $Ni(CN)_2(NH_3)(C_6H_6)$, where benzene (C_6H_6) served as a guest molecule.[89] Yet, the precise structure of these networks remained elusive for nearly six decades due to the limitations in structural characterization techniques of the time. It was not until 1952 that Powell and his colleagues, through pioneering X-ray crystallographic analysis, unveiled a 2D square grid by Ni^{2+} ions linked with cyanide.[90] This compound, known as Hofmann clathrate, is considered a forerunner to contemporary MOFs.[91]

Progress continued into 1959 when Saito et al. synthesized a coordination polymer network utilizing single-metal nodes of Cu^+ connected by neutral organic donor linkers such as adiponitrile ($NC(CH_2)_4CN$).[92] This structure emerged from the crystallization processes of bis(alkyl nitrile)copper(I). Through the late 1980s and 1990s, extensive experimental efforts were made to investigate how variations in metal ions and neutral donor linkers influenced the formation of coordination networks.[91] These studies revealed that such compounds typically adopted a limited number of structural types, constrained by the coordination geometries permissible with single-metal nodes.

The journey of metal-organic frameworks has been marked by significant milestones and rapid advancements since the early 1990s. In 1990, Makoto Fujita utilized ethylenediamine-capped Pd^{2+} units to synthesize a square-shaped polynuclear macrocyclic complex with the composition $[(en)Pd(BIPY)(NO_3)_8]$ (en = ethylenediamine, BIPY = 4,4 -bipyridine).[93] In 1994, when the capped Pd^{2+} units were substituted with uncapped Cd^{2+} ions, an extended 2D square grid structure was formed.[94] In 1995, two extensive coordination networks associated with $M(BIPY)_2$ were documented, both of which play a crucial role in advancing the study of MOFs. The phrase “metal-organic framework” was initially introduced in one of these publications, where Omar M. Yaghi and his coworkers described the solvothermal

synthesis of $[Cu(BIPY)_{1.5}](NO_3)$.[95] In the same year, Michael J. Zaworotko and his colleague reported the discovery of another coordination network called formula $Zn(BIPY)_2SiF_6$.[96] This network consists of a square grid of octahedral Zn^{2+} ions that are connected by BIPY. Subsequently, the investigation into the various structures of MOF materials has rapidly progressed.[97]

To date, over 100,000 MOFs have been synthesized, with their crystallographic information files (CIFs) cataloged in the Cambridge Structural Database (CSD).[77] MOFs are celebrated for their structural variety, ultra-high porosities, surface areas as expansive as 10,000 m^2/g, thermal stability up to 500°C, low densities, and tunable chemical and physical properties.[98] These features make MOFs exceptionally suitable for a wide range of applications, including gas storage and separation,[99-101] catalysis,[102, 103] biomedicine,[104] chemical sensing,[105, 106] electrical conductivity,[107, 108] and light harvesting.[109] Notably, stable and easily prepared series such as HKUST-1,[110] UIO,[111] MIL,[112, 113] and ZIF[114, 115] have broadened the practical applications of MOFs, making them some of the most compelling materials of our century.

1.4.2 Metal–Organic Frameworks-based Catalysts for Electrochemical Oxygen Evolution

The diversity of MOFs has exerted a profound influence on the field of electrocatalysis. These materials are distinguished by their variable morphologies, particle sizes, and the ability to incorporate bimetallic or trimetallic combinations, all of which contribute to their versatility as electrocatalysts. As a result, MOFs are increasingly being investigated as electrocatalysts, particularly in OER applications, and the rough development is shown in the **Figure 1.11**.

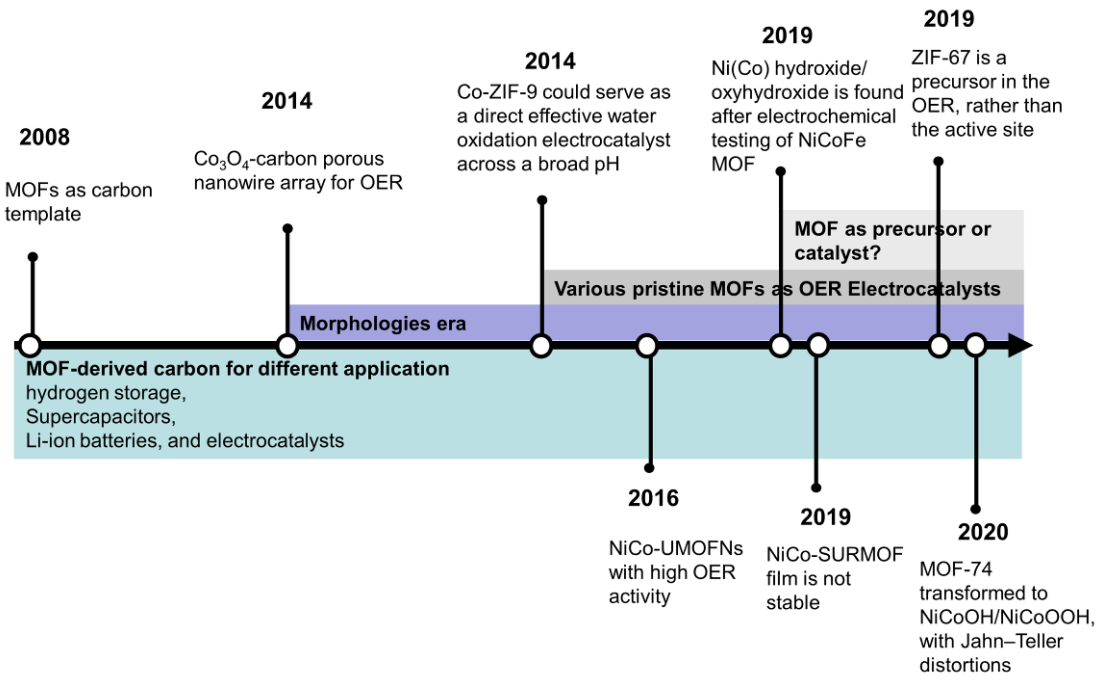

Figure 1.11 Chronology of advances in MOFs as OER catalysts.

1.4.2.1 MOFs as Catalyst Templates

Arising the attention of the electrochemical water splitting, the boosting development of MOFs has attracted more interest to their use in water oxidation.[72, 73, 116]

In 2008, Xu and colleagues pioneered the use of MOF-5 with furfuryl alcohol in the pores as a template for preparing nanoporous carbon.[117] This material was carbonized under an argon atmosphere at 1000 °C for eight hours, resulting in a carbon with a high specific surface area of 2872 m^2/g (BET) and enhanced electrochemical properties. This breakthrough spurred the use of MOF-derived carbons in applications ranging from hydrogen storage and supercapacitors to Li-ion batteries and electrocatalysts. In 2014, Qiao's group designed a hybrid Co_3O_4-carbon porous nanowire array for OER, achieving a lower operational voltage of 1.52 V compared to 1.54 V for IrO_2/C at a current density of 10.0 mA cm^{-2}.[118] This marked the first use of MOFs as carbon templates to enhance OER catalysts' conductivity and charge transfer capabilities.

The subsequent period saw rapid developments in the design and application of MOF-derived carbon materials in OER, especially after discovering the inherited

diverse and complex shapes. Diverse morphologies, such as cubic,[119, 120] polyhedral,[121] spherical,[122] 3D flower-like,[123] hollow,[124] and core-shell structures,[125] were reported. Notably, the ZIF family of MOFs has been extensively utilized due to its simple synthesis and easily tunable morphologies.[126]

Beyond serving as conductive carbon templates, MOF-derived materials can be modified through controlled pyrolysis, annealing, and calcination processes under specific atmospheric conditions and temperatures.[127] The doping of additional elements like N, P, and S into MOF-derived materials has been explored to enhance the activity of OER catalysts.[72, 128] As a representative example, Lou and coworkers present a beautiful application using this strategy to develop double-shelled Co_3O_4/Co-Fe oxide nano boxes starting from ZIF-67 nanocubes. These nanoboxes served as an efficient electrocatalyst for OER, requiring a low overpotential of approximately 297 mV to achieve a current density of 10 mA cm^{-2}.[129]

1.4.2.2 Pristine MOFs as OER Electrocatalysts

With more attention to alkaline electrolytes, pristine MOFs have also been tried as direct electrocatalysts without pre-treatment. For instance, Wang et al. demonstrated in 2014 that Co-ZIF-9 could serve as a direct effective water oxidation electrocatalyst across a broad pH range of 2.3 to 13.4.[130] Following this, Tang et al. in 2016 reported the development of an ultrathin NiCo bimetallic MOF (NiCo-UMOFNs) exhibiting exceptional OER activity, requiring only a 250 mV overpotential to achieve a current density of 10 mA cm^{-2}, surpassing the performance of commercial RuO_2.[131] This groundbreaking activity encouraged researchers' enthusiasm for using pristine MOFs as OER catalysts, particularly those based on carboxylate linkers.

Researchers have continuously explored MOFs with various carboxylate linkers, such as NDC (2,6-Naphthalic acid),[132] BTC (1,3,5-Benzenetricarboxylic acid),[133] and BPTC(biphenyl-3,4′,5-tricarboxylic acid),[134] in 2D/3D topologies and multi-metallic nodes, including CoFe-,[135] NiCu-,[136] FeNi-,[137] NiCo-,[138] and NiCoFe[139]-based systems. For example, Zhao et al. developed an in-situ method to grow ultrathin

nanosheet arrays of Ni(Fe)-NDC-MOFs directly on Ni-foam, which exhibited superior OER performance with an overpotential of just 240 mV at 10 mA cm^{-2}.[132] Moreover, the intrinsic tunability of MOFs has led to the development of several innovative modification strategies to enhance their electrocatalytic performance. Yan et al. created a lattice-strained NiFe-MOF using a mixed linker approach with benzene acid (BC) and terephthalic acid (BDC), improving the MOF's OER activity.[140] Concurrently, the Li group introduced carboxy ferrocene into CoBDC by missing-linker method to modify the electronic structure and enhance catalytic efficiency.[141] Additionally, Liu et al. applied ultraviolet irradiation to adjust the plane (200) spacing in a NiFe-NDC MOF, employing a lattice strain technique that underscores the potential of pristine MOFs as highly effective electrocatalysts for OER applications.[142]

1.4.3 Development Advancements in Understanding Pristine MOFs as OER Electrocatalysts

As the investigation of pure MOFs as alkali-OER catalysts continues to increase, motivated by their impressive performance, the knowledge of their principle is advancing. Traditionally, researchers have compared the electrochemical performance of these materials before and after catalytic tests or during long-term electrocatalysis (using techniques such as chronopotentiometry or chronoamperometry), typically associating electrochemical stability with minimal or no observable differences in performance.[143] Initially, it was widely believed that the metal nodes within MOFs acted as the primary active sites, a perspective supported by unchanged morphologies and XRD patterns during OER processes (including the authors in part above).

However, in 2019, Zhang's group discovered that their trimetallic NiCoFe MOF was not stable after cyclic voltammetry (CV) testing, as evidenced by the disappearance of the MOFs' XRD peaks and their replacement by peaks corresponding to Ni(Co) hydroxide/oxyhydroxide.[144] This finding suggested that these metal hydroxides and

oxyhydroxides might evolve from the pristine MOF structure, potentially acting as active intermediates. In the same year, Li from our group used the Layer-by-Layer (LbL) technique to fabricate a NiCo-SURMOF film, demonstrating a faster transformation with more detailed surface information.[145] Controlling the film thickness using the LbL method achieved faster electrolyte diffusion. Remarkably, the thickness of NiCo-SURMOFs, initially around 780 nm, was reduced to approximately 350 nm after brief exposure to an alkaline electrolyte (0.1 M potassium hydroxide), with AFM measurements confirming this reduction. Moreover, the GIXRD peaks of the SURMOFs disappeared and were replaced by $Ni(OH)_2$ and $Co(OH)_2$ phases, further indicating the instability of the initial MOF structure under alkaline conditions.

With increasing instances of metal hydroxide or oxyhydroxide formation in alkali electrolytes, more researchers have begun to recognize the structural instability of MOFs, as most MOFs are sensitive to water exposure, either to liquid water or humidity.[146, 147] Meanwhile, the relatively weaker coordination bonds between metal nodes and organic linkers in MOFs, compared to the ionic bonds in inorganic solids, also raise concerns about their structural stability in electrochemical settings. Kim et al. later conducted a detailed study using in-situ UV and Raman spectroscopy, demonstrating that ZIF-67 undergoes a two-step evolution: initially transforming to α-$Co(OH)_2$ and β-$Co(OH)_2$ with ligand substitution at low potential rage and eventually converting to a CoOOH structure upon high cycling potential.[148] TEM analysis after amperometric testing revealed rapid morphological and structural changes on the surface, producing primarily α-$Co(OH)_2$ and a polycrystalline structure of α/β-$Co(OH)_2$ as well as CoOOH, then more $Co(OH)_2$/CoOOH can be found inside the bulk via diffusion. This evolving body of research, including a report by Najafpour, challenges the initial belief in the direct catalytic role of MOFs. Using a variety of spectroscopic and imaging techniques (XPS, Raman, FTIR, UV−vis, NMR, EMs, and XAS), Najafpour demonstrated that the NiCo MOF initially

reported by the Tang group in 2016 served not as the true catalyst but merely as a precatalyst, decomposing during OER to form well-known OER-active Co/Ni hydroxides.[149] These studies collectively suggest that it is not the metal node but rather the generated intermediates that play a role in the electrocatalytic activities of MOFs.

Furthermore, in a 2020 study, Tang's group advanced their understanding of the role of MOF-74 derivatives as electrocatalysts for the oxygen evolution reaction (OER) in 0.1 M KOH.[137] Utilizing in-situ X-ray Absorption Spectroscopy (XAS), they delineated two key structural transformation steps that occur during OER. Initially, the MOF structure transitions to NiCoOH, followed by a further transformation to NiCoOOH, which features Jahn–Teller distortions. These findings underscored that the active sites for OER catalysis are not the original MOF structures but rather these dynamically transformed intermediates, specifically the NiCoOOH phase.

1.4.4 The Challenging Exploration of the Mechanism during the Pristine MOF as OER Electrocatalysts

The journey to unravel the operational mechanisms of pristine MOFs in alkaline-OER applications has been fraught with uncertainties and complexities. MOFs, with their intricate systems, present a challenging yet intriguing subject for studying their effectiveness in OER. The diversity in morphologies, powder sizes, and topologies of MOFs offers numerous advantages. However, these same attributes complicate the identification of the real factors influencing their catalytic performance, as critical information can often be obscured by interfering factors.

Impact of Morphology and Particle Size MOFs are celebrated for their diverse morphologies, which vary widely in terms of physical size, flatness, and sphericity. The structural range of MOFs, which includes spheres, cubes, cuboctahedra, octahedra, rods, filaments, sheets, and intricate hierarchical structures such as flower-like forms, has been extensively documented in the scientific literature,[150] as shown in the **Figure 1.12**. These variations in morphology significantly impact the surface

area and, consequently, the diffusion processes crucial for catalytic reactions.

In the realm of catalysis, the size of the MOF particles is particularly critical. For instance, Batyr and Kathrin from our group have employed computational screening theories to predict optimal Pt nanoparticle sizes—specifically near 1, 2, and 3 nm—for efficient Oxygen Reduction Reaction (ORR).[151] Utilizing a MOF template approach, they synthesized Pt nanoparticles, achieving an optimal size of approximately 1.1 nm. These nanoparticles demonstrated a more sensitive surface structure and superior catalytic activity, particularly in proton-exchange-membrane fuel cells.

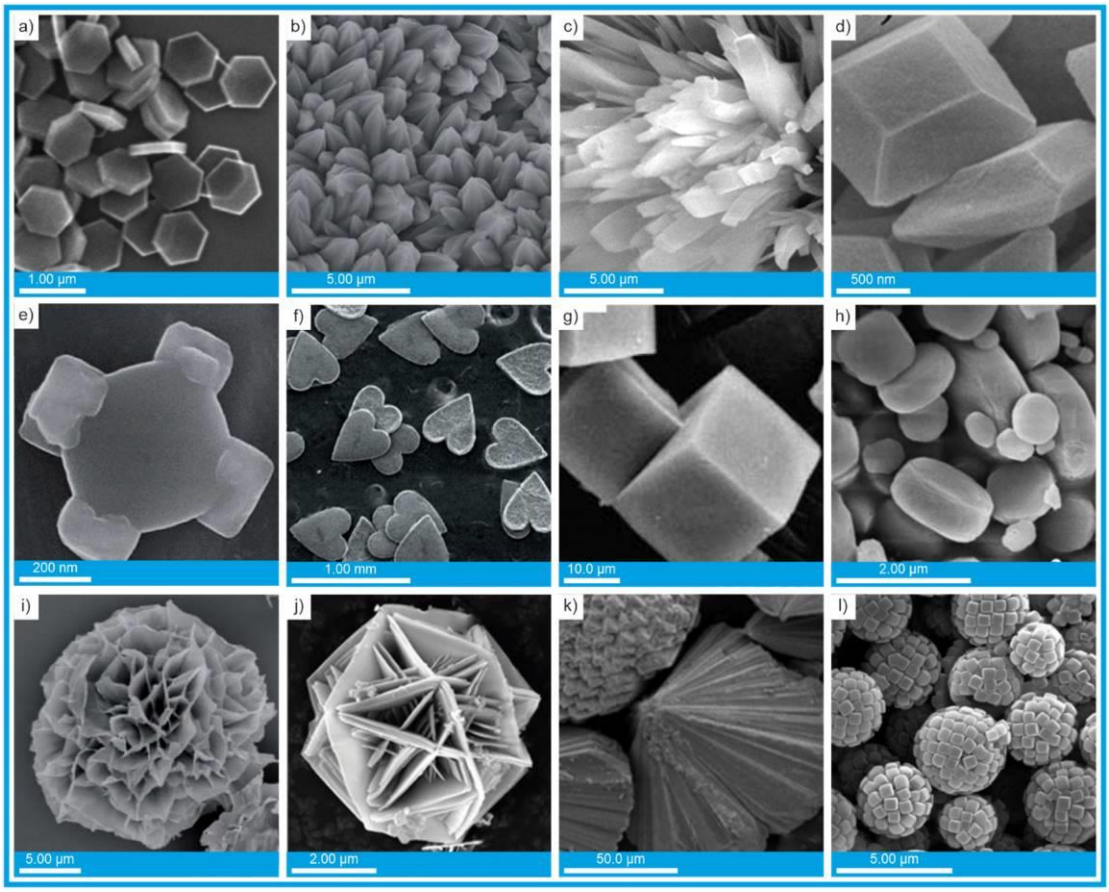

Figure 1.12 Examples of MOF's morphologies. Reprinted under the permission from ref[150], Copyright © 2023 The Authors. Published by Elsevier B.V. with license CC BY.

Further emphasizing the importance of particle size, the Chorkendorff group successfully prepared size-selected NiFe particles via magnetron sputtering for use in

Oxygen Evolution Reaction.[152] Their findings revealed that the smallest NiFe particles, measuring 3.9 and 5.4 nm, exhibited significantly higher mass activity compared to larger particles. These examples underscore the need for more attention over morphologies, especially the power size, to understand the underlying mechanisms of MOFs in OER applications correctly.

The Impact of Iron Impurities on Ni-based MOFs in OER Catalysis In the realm of alkaline OER catalysis, transition metals such as Ni, Co, and Fe are commonly employed as metal nodes to construct metal-organic frameworks. While the specific impact of iron impurities within Ni-based MOFs has not yet been extensively documented, the significant influence of Fe impurities from electrolytes on $Ni(OH)_2$ is well-established. Boettcher and his colleagues devised a straightforward method to purify KOH electrolytes, effectively removing Fe impurities.[64] Their research further demonstrated a notable enhancement in the OER performance of $Ni(OH)_2$/NiOOH thin films when Fe impurities were present, challenging the previously held belief that β-NiOOH is inherently more active than γ-NiOOH. This finding suggests that Fe impurities absorbed into the electrode are responsible for the increased catalytic activity observed in aged $Ni(OH)_2$/NiOOH.[153-155]

Additionally, Bell and his team employed in-situ Raman spectroscopy to investigate the effects of Fe impurities on electrodeposited $Ni(OH)_2$.[67] They discovered that Fe impurities influence aging, transitioning from α-$Ni(OH)_2$ to β-$Ni(OH)_2$. In conditions devoid of Fe, the deposited $Ni(OH)_2$ predominantly exhibits characteristics of β-$Ni(OH)_2$ after the aging process. However, when aged in unpurified KOH, the films show less phase transformation. The Fe impurity can be incorporated with the Ni-(oxy)hydroxide catalyst to enhance the OER activity.

Over the years, various hypotheses regarding the nature of the catalytically active sites on the brucite layers of these materials have evolved.[157, 158] Initially, theories focused on individual Fe or Ni active sites. More recently, attention has shifted towards the mechanistic role of oxygen ligands in the edge-connected M-O octahedra

within the 2D brucite layers as shown in **Figure 1.13**.[156] A novel model has emerged, highlighting the primary catalytic role of specific oxygen bridges between adjacent Ni and Fe sites.[159] Given these insights, the presence of Fe impurities in Ni-based MOFs and their influence on OER catalysis warrants careful consideration to avoid complicating the understanding of these systems. This attention to detail is crucial for advancing the mechanism.

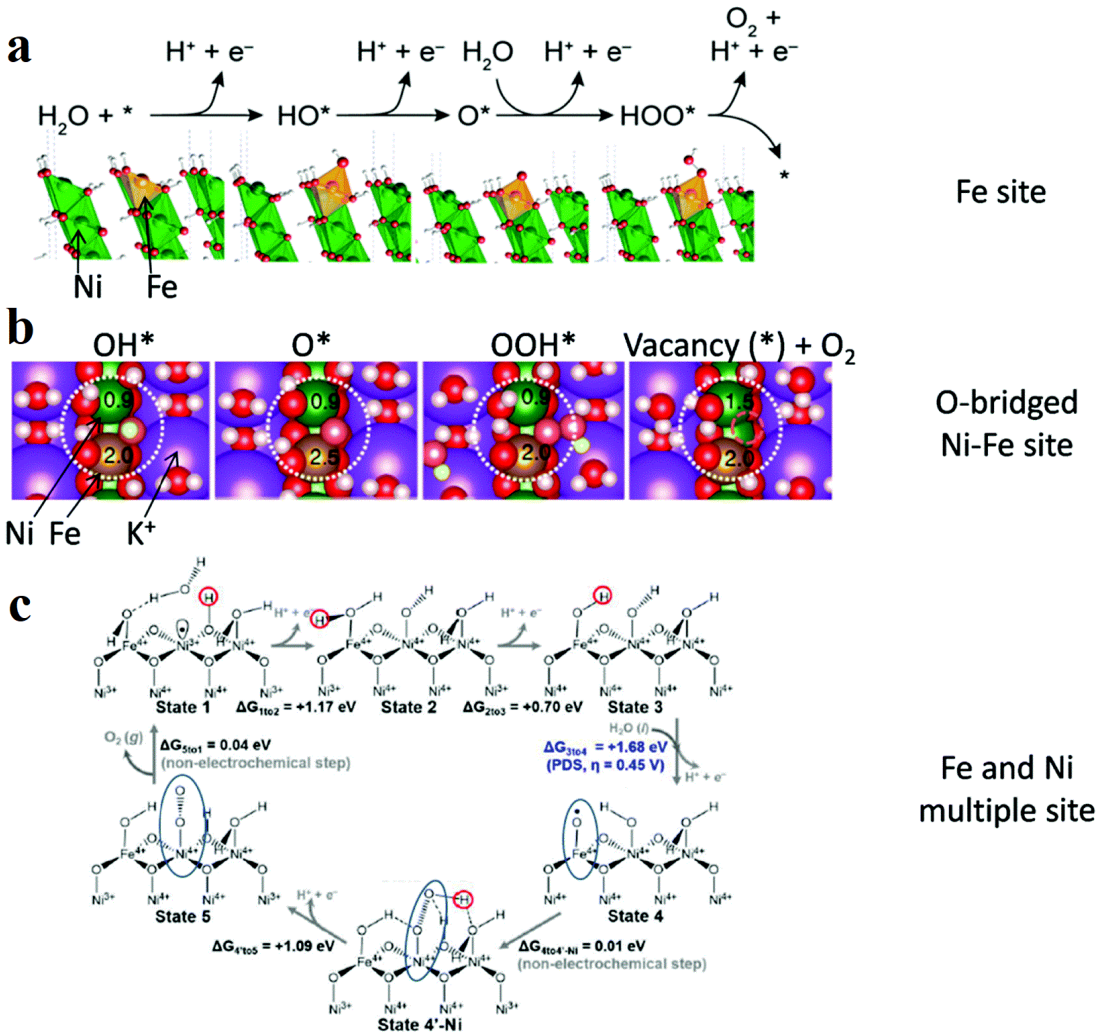

Figure 1.13 Discussions on the Active Site of NiFe (Oxy)hydroxide. Reprinted from ref[156], with permission from the Royal Society of Chemistry.

The Impact of Substrate Selection on OER Catalysis Substrate choice is pivotal in optimizing the oxygen evolution reaction (OER) under alkaline conditions, as evidenced by diverse outcomes observed with different materials. Common substrates in OER research include glass carbon, carbon paper or cloth, nickel foam

(Ni foam), copper foam (Cu foam), indium tin oxide (ITO), nickel mesh (Ni mesh), and stainless-steel mesh.

Wang's comparative analysis of commercial substrates reveals distinct variations in catalytic activity across these materials.[160] Glassy carbon electrodes (GCE) and ITO substrates showed negligible changes in activity within a potential cycling range of 1.23 to 1.8 V vs. RHE. In contrast, three-dimensional (3D) metal substrates demonstrated more pronounced OER activity. For instance, Cu foam and Ni mesh required higher overpotentials of 464 mV and 491 mV at a current density of 10 mA/cm^2, respectively. Meanwhile, Ni foam and stainless steel mesh required overpotentials of 337 mV and 277 mV, respectively, showcasing superior performance compared to RuO_2 on GCE.

One significant challenge with 3D metal substrates is the potential non-homogeneity of the coating and the difficulty in accurately determining the real surface area. The choice of substrate is critical not only for enhancing catalytic performance but also for ensuring the integrity of mechanistic studies. Therefore, non-metal substrates like glass carbon are often more suitable for investigating the intrinsic effects of MOFs in OER catalysis, as they minimize the introduction of additional variables that could obscure the underlying mechanisms.

The Impact of Stability of MOFs on OER Catalysis While chemical stability does not necessarily equate to electrochemical stability, it remains a crucial factor in the study of active sites for catalysis. The stability of MOFs is influenced by an array of factors, including thermodynamic and kinetic considerations, as well as other environmental conditions during operation.[161]

Thermodynamic stability primarily pertains to the strength of metal-ligand coordination bonds, which can be theoretically predicted using Pearson's Hard Soft Acid Base (HSAB) theory. According to HSAB principles, high-valent metal ions (hard acids) with high charge density tend to form strong coordination bonds with oxygen donor ligands (hard bases). This results in MOFs that typically exhibit robust

chemical stability due to the strength of their coordination bonds.[162] Examples of such hard acids include high-valent transition metals, which, when paired with hard bases, yield MOFs with desirable stability properties.[163]

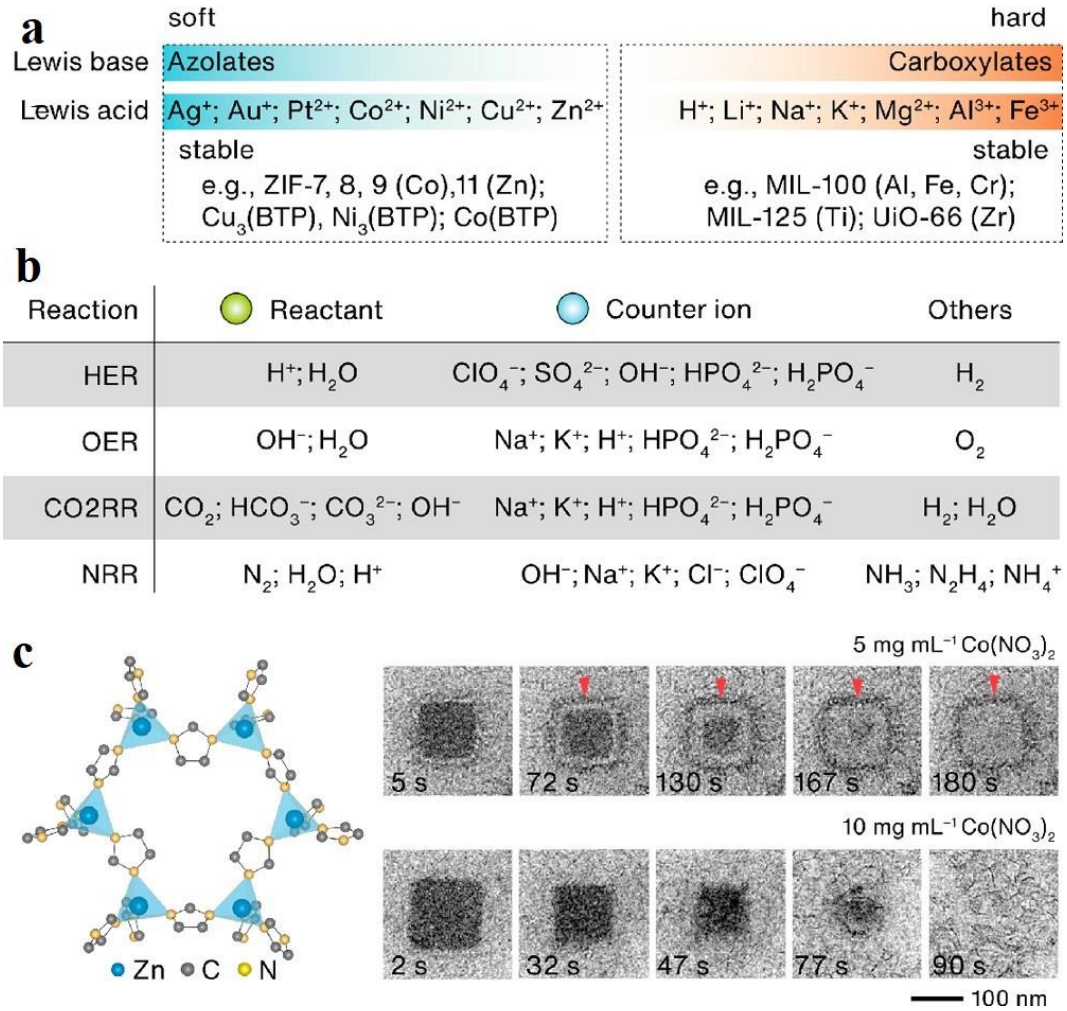

Figure 1.14 Scheme of the stability factors of MOFs in OER a) Hard and soft acid–base theory for stable MOF design. b) Chemical environments in aqueous electrolytes of some common electrocatalytic reactions. c) Left: structure of ZIF-8. Right: time series of images showing the structural evolution of a ZIF-8 nanocube in 5 (top) and 10 mg mL^{-1} (bottom) $Co(NO_3)_2$ solution. Reprinted from ref[143], Copyright © 2021, American Chemical Society.

Conversely, low-valent metal ions like Zn^{2+}, Co^{2+}, Ni^{2+}, Fe^{2+}, and Ag^{+} are categorized as soft acids. These ions can form highly stable MOFs when coordinated with appropriate nitrogen-containing linkers (soft bases) as shown in **Figure 1.14**.[143, 162,

[163] This adaptability in choosing the right metal and ligand types allows for the tailoring of MOFs to enhance both their chemical and electrochemical stability.

Thus, when comparing the behavior of different MOFs in alkaline-OER settings, selecting MOF types based on their predicted stability and suitability for the specific catalytic environment should also be a priority. This targeted approach helps better understand their performance dynamics and ensures the reliability of the comparable mechanisms found in OER studies.

1.5 Reference

1) Energy Institute - Statistical Review of World Energy (**2024**); Smil (2017) – with major processing by Our World in Data. *Our World in Data* *https://ourworldindata.org/energy-production-consumption*.

2) Hannah Ritchie, P. R. a. M. R., Energy Production and Consumption Published online at OurWorldInData.org. Retrieved from: 'https://ourworldindata.org/energy-production-consumption' [Online Resource]. **2020**.

3) Energy Institute -Statistical Review of World Energy (**2024**).

4) Energy Transitions: Global and National Perspectives, 2nd edition, Appendix A, Vaclav Smil (**2017**).

5) Energy Institute - Statistical Review of World Energy (2024) – with major processing by Our World in Data. *https://ourworldindata.org/grapher/years-of-fossil-fuel-reserves-left*.

6) Zuttel, A.; Remhof, A.; Borgschulte, A.; Friedrichs, O., Hydrogen: the future energy carrier. *Philosophical Transactions of the Royal Society A* **2010,** *368*, 3329-42.

7) Seh, Z. W., Kibsgaard, J.,Dickens, C. F.,Chorkendorff, I.,Norskov, J. K.,Jaramillo, T. F., Combining theory and experiment in electrocatalysis: Insights into materials design. *Science* **2017,** *355*.

8) Global Hydrogen Review 2023 *IEA (2023), Global Hydrogen Review 2023, IEA, Paris https://www.iea.org/reports/global-hydrogen-review-2023, Licence: CC BY 4.0* **2023**.

9) Anwar, S.; Li, X., Production of hydrogen from fossil fuel: A review. *Frontiers in Energy* **2023,** *17*, 585-610.

10) Levie, R. d., The electrolysis of water. *Journal of Electroanalytical Chemistry* **1999,** *476* 92–93.

11) Smolinka, T., Water Electrolysis. *Encyclopedia of Electrochemical Power Sources* **2009**, 394-413.

12) Yu, Z. Y.; Duan, Y.; Feng, X. Y.; Yu, X.; Gao, M. R.; Yu, S. H., Clean and Affordable Hydrogen Fuel from Alkaline Water Splitting: Past, Recent Progress, and Future Prospects. *Advanced Materials* **2021,** *33*, e2007100.

13) Yang, W.; Wang, Z.; Zhang, W.; Guo, S., Electronic-Structure Tuning of Water-Splitting Nanocatalysts. *Trends in Chemistry* **2019,** *1*, 259-271.

14) Suen, N. T.; Hung, S. F.; Quan, Q.; Zhang, N.; Xu, Y. J.; Chen, H. M., Electrocatalysis for the oxygen evolution reaction: recent development and future perspectives. *Chemical Society Reviews* **2017,** *46*, 337-365.

15) Tuysuz, H., Alkaline Water Electrolysis for Green Hydrogen Production. *Accounts of Chemical Research* **2024,** *57*, 558-67.

16) Morales-Guio, C. G.; Stern, L. A.; Hu, X., Nanostructured hydrotreating catalysts for electrochemical hydrogen evolution. *Chemical Society Reviews* **2014,** *43*, 6555-69.

17) Wang, J.; Gao, Y.; Kong, H.; Kim, J.; Choi, S.; Ciucci, F.; Hao, Y.; Yang, S.; Shao, Z.; Lim, J., Non-precious-metal catalysts for alkaline water electrolysis: operando characterizations, theoretical calculations, and recent advances. *Chemical Society Reviews* **2020,** *49*, 9154-9196.

18) Sabatier, P., Hydrogénations et déshydrogénations par catalyse. *Berichte der deutschen chemischen Gesellschaft* **2006,** *44*, 1984-2001.

19) I. Chorkendotff, J. W. N., Concepts of Modern Catalysis and Kinetics. *John Wiley & Sons* **2017.**

20) Zheng, Y.; Jiao, Y.; Jaroniec, M.; Qiao, S. Z., Advancing the electrochemistry of the hydrogen-evolution reaction through combining experiment and theory. *Angewandte Chemie International Edition* **2015,** *54*, 52-65.

21) Zheng, Y.; Jiao, Y.; Zhu, Y.; Li, L. H.; Han, Y.; Chen, Y.; Du, A.; Jaroniec, M.; Qiao, S. Z., Hydrogen evolution by a metal-free electrocatalyst. *Nature Communications* **2014,** *5*, 3783.

22) Parso, R., The rate of electrolytic hydrogen evolution and the heat of adsorption of hydrogen,. *Transactions of the Faraday Society* **1958,** *54*, 1053-1063.

23) Gerischer, H., Mechanismus der elektrolytischen wasserstoffabscheidung und adsorptionsenergie von atomarem wasserstoff *Bulletin des Sociétés Chimiques Belges* **1958** *67* 506-527.

24) Trasatti, S., Work function, electronegativity, and electrochemical behaviour of metals: III. Electrolytic hydrogen evolution in acid solutions. *Journal of Electroanalytical Chemistry and Interfacial Electrochemistry* **1972,** *39* 163-181.

25) J. K. Nørskov, T. B., A. Logadottir, J. R. Kitchin, J. G. Chen, S. Pandelov, and U. Stimming, Trends in the Exchange Current for Hydrogen Evolution. *Journal of the Electrochemical Society* **2005,** *152*, J23-J26.

26) Greeley, J.; Jaramillo, T. F.; Bonde, J.; Chorkendorff, I. B.; Norskov, J. K., Computational high-throughput screening of electrocatalytic materials for hydrogen evolution. *Nature Materials* **2006,** *5*, 909-13.

27) Jiao, Y.; Zheng, Y.; Jaroniec, M.; Qiao, S. Z., Design of electrocatalysts for oxygen- and hydrogen-involving energy conversion reactions. *Chemical Society Reviews* **2015,** *44*, 2060-86.

28) Hong, W. T.; Risch, M.; Stoerzinger, K. A.; Grimaud, A.; Suntivich, J.; Shao-Horn, Y., Toward the rational design of non-precious transition metal oxides for oxygen electrocatalysis. *Energy & Environmental Science* **2015,** *8*, 1404-1427.

29) Song, J.; Wei, C.; Huang, Z. F.; Liu, C.; Zeng, L.; Wang, X.; Xu, Z. J., A review on fundamentals for designing oxygen evolution electrocatalysts. *Chemical Society Reviews* **2020,** *49*, 2196-2214.

30) Rossmeisl, J.; Logadottir, A.; Nørskov, J. K., Electrolysis of water on (oxidized) metal surfaces. *Chemical Physics* **2005,** *319*, 178-184.

31) May, K. J.; Carlton, C. E.; Stoerzinger, K. A.; Risch, M.; Suntivich, J.; Lee, Y.-L.; Grimaud, A.; Shao-Horn, Y., Influence of Oxygen Evolution during Water Oxidation on the Surface of Perovskite Oxide Catalysts. *The Journal of Physical Chemistry Letters* **2012,** *3*, 3264-3270.

32) Exner, K. S., Why the breaking of the OOH versus OH scaling relation might cause decreased electrocatalytic activity. *Chem Catalysis* **2021,** *1*, 258-271.

33) Chen, F.-Y.; Wu, Z.-Y.; Adler, Z.; Wang, H., Stability challenges of electrocatalytic oxygen evolution reaction: From mechanistic understanding to reactor design. *Joule* **2021,** *5*, 1704-1731.

34) Grimaud, A.; Diaz-Morales, O.; Han, B.; Hong, W. T.; Lee, Y. L.; Giordano, L.; Stoerzinger, K. A.; Koper, M. T. M.; Shao-Horn, Y., Activating lattice oxygen

redox reactions in metal oxides to catalyse oxygen evolution. *Nature Chemistry* **2017,** *9*, 457-465.

35) Grimaud, A.; Hong, W. T.; Shao-Horn, Y.; Tarascon, J. M., Anionic redox processes for electrochemical devices. *Nature Materials* **2016,** *15*, 121-6.

36) Hwang, J.; Rao, R. R.; Giordano, L.; Katayama, Y.; Yu, Y.; Shao-Horn, Y., Perovskites in catalysis and electrocatalysis. *Science* **2017,** *358*, 751–756

37) Rüetschi, P.; Delahay, P., Influence of Electrode Material on Oxygen Overvoltage: A Theoretical Analysis. *The Journal of Chemical Physics* **1955,** *23*, 556-560.

38) Trasatti, S., Electrocatalysis by oxides — Attempt at a unifying approach. *Journal of Electroanalytical Chemistry and Interfacial Electrochemistry* **1980,** *111*, 125-131.

39) Zeradjanin, A. R.; Masa, J.; Spanos, I.; Schlögl, R., Activity and Stability of Oxides During Oxygen Evolution Reaction-From Mechanistic Controversies Toward Relevant Electrocatalytic Descriptors. *Frontiers in Energy Research* **2021,** *8*.

40) Tseung, P. R. a. A. C. C., The Role of the Lower Metal Oxide/Higher Metal Oxide Couple in Oxygen Evolution Reactions. *Journal of The Electrochemical Society 131* 803.

41) Suntivich, J.; May, K. J.; Gasteiger, H. A.; Goodenough, J. B.; Shao-Horn, Y., A perovskite oxide optimized for oxygen evolution catalysis from molecular orbital principles. *Science* **2011,** *334*, 1383-5.

42) Man, I. C.; Su, H. Y.; Calle-Vallejo, F.; Hansen, H. A.; Martínez, J. I.; Inoglu, N. G.; Kitchin, J.; Jaramillo, T. F.; Nørskov, J. K.; Rossmeisl, J., Universality in Oxygen Evolution Electrocatalysis on Oxide Surfaces. *ChemCatChem* **2011,** *3*, 1159-1165.

43) Dau, H.; Limberg, C.; Reier, T.; Risch, M.; Roggan, S.; Strasser, P., The Mechanism of Water Oxidation: From Electrolysis via Homogeneous to Biological Catalysis. *ChemCatChem* **2010,** *2*, 724-761.

44) Trasatti, S., Electrocatalysis in the anodic evolution of oxygen and chlorine. *Electrochimica Acta* **1984,** *29*, 1503-1512.

45) Morales-Guio, C. G.; Liardet, L.; Hu, X., Oxidatively Electrodeposited Thin-Film Transition Metal (Oxy)hydroxides as Oxygen Evolution Catalysts. *Journal of the American Chemical Society* **2016,** *138*, 8946-57.

46) Yu, M.; Li, G.; Fu, C.; Liu, E.; Manna, K.; Budiyanto, E.; Yang, Q.; Felser, C.; Tuysuz, H., Tunable e(g) Orbital Occupancy in Heusler Compounds for Oxygen Evolution Reaction*. *Angewandte Chemie International Edition* **2021,** *60*, 5800-5805.

47) Lee, J. G.; Hwang, J.; Hwang, H. J.; Jeon, O. S.; Jang, J.; Kwon, O.; Lee, Y.; Han, B.; Shul, Y. G., A New Family of Perovskite Catalysts for Oxygen-Evolution Reaction in Alkaline Media: BaNiO3 and BaNi(0.83)O(2.5). *Journal of the American Chemical Society* **2016,** *138*, 3541-7.

48) Tong, Y.; Guo, Y.; Chen, P.; Liu, H.; Zhang, M.; Zhang, L.; Yan, W.; Chu, W.; Wu, C.; Xie, Y., Spin-State Regulation of Perovskite Cobaltite to Realize Enhanced Oxygen Evolution Activity. *Chem* **2017,** *3*, 812-821.

49) Duan, Y.; Sun, S.; Xi, S.; Ren, X.; Zhou, Y.; Zhang, G.; Yang, H.; Du, Y.; Xu, Z. J., Tailoring the Co 3d-O 2p Covalency in LaCoO3 by Fe Substitution To Promote Oxygen Evolution Reaction. *Chemistry of Materials* **2017,** *29*, 10534-10541.

50) Cai, P.; Huang, J.; Chen, J.; Wen, Z., Oxygen-Containing Amorphous Cobalt Sulfide Porous Nanocubes as High-Activity Electrocatalysts for the Oxygen Evolution Reaction in an Alkaline/Neutral Medium. *Angewandte Chemie International Edition* **2017,** *56*, 4858-4861.

51) J. K. Nørskov, J. R., A. Logadottir, and L. Lindqvist, Origin of the Overpotential for Oxygen Reduction at a Fuel-Cell Cathode. *The Journal of Physical Chemistry B* **2004,** *108*, 17886-17892.

52) Rossmeisl, J.; Qu, Z. W.; Zhu, H.; Kroes, G. J.; Nørskov, J. K., Electrolysis of water on oxide surfaces. *Journal of Electroanalytical Chemistry* **2007,** *607*, 83-89.

53) Hu, C.; Zhang, L.; Gong, J., Recent progress made in the mechanism comprehension and design of electrocatalysts for alkaline water splitting. *Energy & Environmental Science* **2019,** *12*, 2620-2645.

54) Subbaraman, R.; Tripkovic, D.; Chang, K. C.; Strmcnik, D.; Paulikas, A. P.; Hirunsit, P.; Chan, M.; Greeley, J.; Stamenkovic, V.; Markovic, N. M., Trends in activity for the water electrolyser reactions on 3d M(Ni,Co,Fe,Mn) hydr(oxy)oxide catalysts. *Nature Materials* **2012,** *11*, 550-7.

55) Wang, K.; Han, C.; Shao, Z.; Qiu, J.; Wang, S.; Liu, S., Perovskite Oxide Catalysts for Advanced Oxidation Reactions. *Advanced Functional Materials* **2021,** *31*.

56) Zhang, M.; Jeerh, G.; Zou, P.; Lan, R.; Wang, M.; Wang, H.; Tao, S., Recent development of perovskite oxide-based electrocatalysts and their applications in low to intermediate temperature electrochemical devices. *Materials Today* **2021,** *49*, 351-377.

57) Baek, J.; Hossain, M. D.; Mukherjee, P.; Lee, J.; Winther, K. T.; Leem, J.; Jiang, Y.; Chueh, W. C.; Bajdich, M.; Zheng, X., Synergistic effects of mixing and strain in high entropy spinel oxides for oxygen evolution reaction. *Nature Communications* **2023,** *14*, 5936.

58) Hunter, B. M.; Gray, H. B.; Muller, A. M., Earth-Abundant Heterogeneous Water Oxidation Catalysts. *Chemical Reviews* **2016,** *116*, 14120-14136.

59) Yu, J.; Wang, Q.; O'Hare, D.; Sun, L., Preparation of two dimensional layered double hydroxide nanosheets and their applications. *Chemical Society Reviews* **2017,** *46*, 5950-5974.

60) Bode, H.; Dehmelt, K.; Witte, J., Zur kenntnis der nickelhydroxidelektrode—I.Über das nickel (II)-hydroxidhydrat. *Electrochimica Acta* **1966. ,** *11*. , 1079-1087.

61) Oliva, P.; Leonardi, J.; Laurent, J. F.; Delmas, C.; Braconnier, J. J.; Figlarz, M.; Fievet, F.; Guibert, A. d., Review of the structure and the electrochemistry of nickel hydroxides and oxy-hydroxides. *Journal of Power Sources* **1982,** *8* 229 - 255.

62) Yeo, B. S.; Bell, A. T., In Situ Raman Study of Nickel Oxide and Gold-Supported Nickel Oxide Catalysts for the Electrochemical Evolution of Oxygen. *The Journal of Physical Chemistry C* **2012,** *116*, 8394-8400.

63) Louie, M. W.; Bell, A. T., An investigation of thin-film Ni-Fe oxide catalysts for the electrochemical evolution of oxygen. *Journal of the American Chemical Society* **2013,** *135*, 12329-37.

64) Trotochaud, L.; Young, S. L.; Ranney, J. K.; Boettcher, S. W., Nickel–Iron Oxyhydroxide Oxygen-Evolution Electrocatalysts: The Role of Intentional and Incidental Iron Incorporation. *Journal of the American Chemical Society* **2014,** *136*, 6744-6753.

65) Görlin, M.; Chernev, P.; Ferreira de Araújo, J.; Reier, T.; Dresp, S.; Paul, B.; Krähnert, R.; Dau, H.; Strasser, P., Oxygen Evolution Reaction Dynamics, Faradaic Charge Efficiency, and the Active Metal Redox States of Ni–Fe Oxide Water Splitting Electrocatalysts. *Journal of the American Chemical Society* **2016,** *138*, 5603-5614.

66) Steimecke, M.; Seiffarth, G.; Schneemann, C.; Oehler, F.; Förster, S.; Bron, M., Higher-Valent Nickel Oxides with Improved Oxygen Evolution Activity and Stability

in Alkaline Media Prepared by High-Temperature Treatment of Ni(OH)2. *ACS Catalysis* **2020,** *10*, 3595-3603.

67) Klaus, S.; Cai, Y.; Louie, M. W.; Trotochaud, L.; Bell, A. T., Effects of Fe Electrolyte Impurities on Ni(OH)2/NiOOH Structure and Oxygen Evolution Activity. *The Journal of Physical Chemistry C* **2015,** *119*, 7243-7254.

68) Tao, S.; Wen, Q.; Jaegermann, W.; Kaiser, B., Formation of Highly Active NiO(OH) Thin Films from Electrochemically Deposited Ni(OH)2 by a Simple Thermal Treatment at a Moderate Temperature: A Combined Electrochemical and Surface Science Investigation. *ACS Catalysis* **2022,** *12*, 1508-1519.

69) Dionigi, F., Strasser, Peter, NiFe-Based (Oxy)hydroxide Catalysts for Oxygen Evolution Reaction in Non-Acidic Electrolytes. *Advanced Energy Materials* **2016,** *6*, 1600621.

70) Dionigi, F.; Zeng, Z.; Sinev, I.; Merzdorf, T.; Deshpande, S.; Lopez, M. B.; Kunze, S.; Zegkinoglou, I.; Sarodnik, H.; Fan, D.; Bergmann, A.; Drnec, J.; Araujo, J. F.; Gliech, M.; Teschner, D.; Zhu, J.; Li, W. X.; Greeley, J.; Cuenya, B. R.; Strasser, P., In-situ structure and catalytic mechanism of NiFe and CoFe layered double hydroxides during oxygen evolution. *Nature Communications* **2020,** *11*, 2522.

71) Xu, Q.; Jiang, H.; Duan, X.; Jiang, Z.; Hu, Y.; Boettcher, S. W.; Zhang, W.; Guo, S.; Li, C., Fluorination-enabled Reconstruction of NiFe Electrocatalysts for Efficient Water Oxidation. *Nano Letters* **2021,** *21*, 492-499.

72) Wang, H.-F.; Chen, L.; Pang, H.; Kaskel, S.; Xu, Q., MOF-derived electrocatalysts for oxygen reduction, oxygen evolution and hydrogen evolution reactions. *Chemical Society Reviews* **2020,** *49*, 1414-1448.

73) Du, J.; Li, F.; Sun, L., Metal-organic frameworks and their derivatives as electrocatalysts for the oxygen evolution reaction. *Chemical Society Reviews* **2021,** *50*, 2663-2695.

74) Kirchon, A.; Feng, L.; Drake, H. F.; Joseph, E. A.; Zhou, H.-C., From fundamentals to applications: a toolbox for robust and multifunctional MOF materials. *Chemical Society Reviews* **2018,** *47*, 8611-8638.

75) Troyano, J.; Legrand, A.; Furukawa, S., Mechanoresponsive Porosity in Metal-Organic Frameworks. *Trends in Chemistry* **2021,** *3*, 254-265.

76) Arrozi, U. S. F.; Bon, V.; Kutzscher, C.; Senkovska, I.; Kaskel, S., Towards highly active and stable nickel-based metal-organic frameworks as ethylene oligomerization catalysts. *Dalton Transactions* **2019,** *48*, 3415-3421.

77) Zhang, X.; Wasson, M. C.; Shayan, M.; Berdichevsky, E. K.; Ricardo-Noordberg, J.; Singh, Z.; Papazyan, E. K.; Castro, A. J.; Marino, P.; Ajoyan, Z.; Chen, Z.; Islamoglu, T.; Howarth, A. J.; Liu, Y.; Majewski, M. B.; Katz, M. J.; Mondloch, J. E.; Farha, O. K., A historical perspective on porphyrin-based metal-organic frameworks and their applications. *Coordination Chemistry Reviews* **2021,** *429*.

78) Schoedel, A.; Li, M.; Li, D.; O'Keeffe, M.; Yaghi, O. M., Structures of Metal–Organic Frameworks with Rod Secondary Building Units. *Chemical Reviews* **2016,** *116*, 12466-12535.

79) Markus J. Kalmutzki, N. H., Omar M. Yaghi, Secondary building units as the turning point in the development of the reticular chemistry of MOFs. *Science Advances* **20180,** *4* eaat918.

80) Diercks, C. S.; Kalmutzki, M. J.; Diercks, N. J.; Yaghi, O. M., Conceptual Advances from Werner Complexes to Metal-Organic Frameworks. *ACS Central Science* **2018,** *4*, 1457-1464.

81) Werner, A., Beitrag zur Konstitution anorganischer Verbindungen. *Zeitschrift für anorganische Chemie* **2004,** *3*, 267-330.

82) GADE, L. H., Alfred Werners Koordinationstheorie. *Chemie in unserer Zeit* **2002**.

83) Bowman-James, K., Alfred Werner revisited: the coordination chemistry of anions. *Acc Chem Res* **2005,** *38*, 671-8.

84) Wyart, J., Structure of basic acetate of zinc determined by x-ray analysis. *Bull. Soc. Fr. Mineral* **1926,** *49*, 148.

85) Ohshima, T., evelopment of Tetranuclear Zinc Cluster-Catalyzed Environmentally Friendly Reactions and Mechanistic Studies. *Chemical & Pharmaceutical Bulletin* **2016,** *64*, 6.

86) Hargittai, I., The quadruple bond – 60 years – a tribute to F. Albert Cotton and other pioneers. *Structural Chemistry* **2024,** *35*, 1031-1034.

87) Cotton, F. A.; Curtis, N. F.; Harris, C. B.; Johnson, B. F. G.; Lippard, S. J.; Mague, J. T.; Robinson, W. R.; Wood, J. S., Mononuclear and Polynuclear Chemistry of Rhenium (III): Its Pronounced Homophilicity. *Science* **1964,** *145*, 1305-1307.

88) Day, V. F., M.; Klemperer, W.; Liu, R. , Polyoxomolyb date-hydrocarbon interactions. Synthesis and structure of the CH2Mo4O15H3-anion and related methylenedioxymolybdates. *Journal of the American Chemical Society* **1979,** *101*, 491−492.

89) Hofmann, K. A. K., F., Verbindungen von Kohlenwasserstoffen mit Metallsalzen. *Zeitschrift für anorganische Chemie* **1897,** *15*, 204-207.

90) Rayner, J. H., Powell, H.M., Structure of molecular compounds. Part 9. Crystal structure of the compound of benzene with an ammonia–nickel cyanide complex, Journal of the Chemical Society (Resumed). **1952,** *67*, 319–328.

91) Yaghi, A. S. a. O. M., Porosity in Metal–Organic Compounds. *in Macrocyclic and Supramolecular Chemistry, John Wiley & Sons, Ltd., Weinheim, Germany* **2016** *Chapter 9*, 200-219.

92) Yukio Kinoshita, I. M., Yoshihiko Saito, The crystal structure of bis(succinonitrilo)copper(I) nitrate. . *Bulletin of the Chemical Society of Japan* **1959,** *32*, 741−747.

93) Fujita, M., Yazaki,J., Ogura,K., Preparation of a Macrocyclic Polynuclear Complex, [(en)Pd(4,4,-bpy)]4(N03)8,[1] Which Recognizes an Organic Molecule in Aqueous Media. *Journal of the American Chemical Society* **1990,** *112*, 5645-5647. .

94) Makoto Fujita, Y. J. K., Satoru Washizu, and Katsuyuki Ogura·, Preparation, Clathration Ability, and Catalysis of a Two-Dimensional Square Network Material Composed of Cadmium(II) and 4,4'-Bipyridine. *Journal of the American Chemical Society* **1994,** *116* 1151-1152.

95) O. M. Yaghi , H. L., Hydrothermal Synthesis of a Metal-Organic Framework Containing Large Rectangular Channels. *Journal of the American Chemical Society* **1995,** *117*, 10401-10402.

96) Subramanian, S.; Zaworotko, M. J., Porous Solids by Design: [Zn(4,4′-bpy)2(SiF6)]n·xDMF, a Single Framework Octahedral Coordination Polymer with Large Square Channels. *Angewandte Chemie International Edition* **2003,** *34*, 2127-2129.

97) Kirlikovali, K. O.; Hanna, S. L.; Son, F. A.; Farha, O. K., Back to the Basics: Developing Advanced Metal-Organic Frameworks Using Fundamental Chemistry Concepts. *ACS Nanoscience Au* **2023,** *3*, 37-45.

98) Furukawa, H.; Cordova, K. E.; O'Keeffe, M.; Yaghi, O. M., The chemistry and applications of metal-organic frameworks. *Science* **2013,** *341*, 1230444.

99) Zhao, X.; Xiao, B.; Fletcher, A. J.; Thomas, K. M.; Bradshaw, D.; Rosseinsky, M. J., Hysteretic adsorption and desorption of hydrogen by nanoporous metal-organic frameworks. *Science* **2004,** *306*, 1012-5.

100) Shengqian Ma, D. S., Jason M. Simmons, Christopher D. Collier, Daqiang Yuan, and Hong-Cai Zhou, Metal-Organic Framework from an Anthracene Derivative Containing Nanoscopic Cages Exhibiting High Methane Uptake. *Journal of the American Chemical Society* **2008,** *130,*, 1012–1016.

101) Li, J. R.; Kuppler, R. J.; Zhou, H. C., Selective gas adsorption and separation in metal-organic frameworks. *Chemical Society Reviews* **2009,** *38*, 1477-504.

102) Lee, J.; Farha, O. K.; Roberts, J.; Scheidt, K. A.; Nguyen, S. T.; Hupp, J. T., Metal-organic framework materials as catalysts. *Chemical Society Reviews* **2009,** *38*, 1450-9.

103) Liu, J.; Chen, L.; Cui, H.; Zhang, J.; Zhang, L.; Su, C. Y., Applications of metal-organic frameworks in heterogeneous supramolecular catalysis. *Chemical Society Reviews* **2014,** *43*, 6011-61.

104) Wu, M. X.; Yang, Y. W., Metal-Organic Framework (MOF)-Based Drug/Cargo Delivery and Cancer Therapy. *Advanced Materials* **2017,** *29*.

105) Hu, Z.; Deibert, B. J.; Li, J., Luminescent metal-organic frameworks for chemical sensing and explosive detection. *Chemical Society Reviews* **2014,** *43*, 5815-40.

106) Lustig, W. P.; Mukherjee, S.; Rudd, N. D.; Desai, A. V.; Li, J.; Ghosh, S. K., Metal-organic frameworks: functional luminescent and photonic materials for sensing applications. *Chemical Society Reviews* **2017,** *46*, 3242-3285.

107) Sheberla, D.; Bachman, J. C.; Elias, J. S.; Sun, C. J.; Shao-Horn, Y.; Dinca, M., Conductive MOF electrodes for stable supercapacitors with high areal capacitance. *Nature Materials* **2017,** *16*, 220-224.

108) Sun, L.; Campbell, M. G.; Dinca, M., Electrically Conductive Porous Metal-Organic Frameworks. *Angewandte Chemie International Edition* **2016,** *55*, 3566-79.

109) Wang, J.-L.; Wang, C.; Lin, W., Metal–Organic Frameworks for Light Harvesting and Photocatalysis. *ACS Catalysis* **2012,** *2*, 2630-2640.

110) Stephen S.-Y. Chui, S. M.-F. L., Jonathan P. H. Charmant, A. Guy Orpen, Ian D. Williams1, A Chemically Functionalizable Nanoporous Material [Cu3(TMA)2(H2O)3]n. *Science* **1999,** *283*, 1148-1150.

111) Jasmina Hafizovic Cavka, S. J., Unni Olsbye, Nathalie Guillou, Carlo Lamberti, Silvia Bordiga, and Karl Petter Lillerud, A New Zirconium Inorganic Building Brick Forming Metal Organic Frameworks with Exceptional Stability. *Journal of the American Chemical Society* **2008,** *130*, 13850–13851.

112) Gérard Férey, C. M., -Draznieks, Christian Serre, Franck Millange, Crystallized Frameworks with Giant Pores: Are There Limits to the Possible? *Accounts of Chemical Research* **2005,** *38*, 217–225.

113) Hupp, J. T.; Poeppelmeier, K. R., Chemistry. Better living through nanopore chemistry. *Science* **2005,** *309*, 2008-9.

114) Huang, X. C.; Lin, Y. Y.; Zhang, J. P.; Chen, X. M., Ligand-directed strategy for zeolite-type metal-organic frameworks: zinc(II) imidazolates with unusual zeolitic topologies. *Angewandte Chemie International Edition* **2006,** *45*, 1557-9.

115) Kyo Sung Park, Z. N., Adrien P. Coˆ te´ , Jae Yong Choi, Rudan Huang, Fernando J. Uribe-Romo, Hee K. Chae, Michael O'Keeffe, and Omar M. Yaghi, xceptional chemical and thermal stability of zeolitic imidazolate frameworks.

Proceedings of the National Academy of Sciences of the United States of America **2006,** *103* 10186-10191.

116) Li, S.; Gao, Y.; Li, N.; Ge, L.; Bu, X.; Feng, P., Transition metal-based bimetallic MOFs and MOF-derived catalysts for electrochemical oxygen evolution reaction. *Energy & Environmental Science* **2021,** *14*, 1897-1927.

117) Bo Liu, H. S., Tomoki Akita, and Qiang Xu, Metal-Organic Framework as a Template for Porous Carbon Synthesis. *Journal of the American Chemical Society* **2008,** *130*, 5390–5391.

118) Ma, T. Y.; Dai, S.; Jaroniec, M.; Qiao, S. Z., Metal–Organic Framework Derived Hybrid Co3O4-Carbon Porous Nanowire Arrays as Reversible Oxygen Evolution Electrodes. *Journal of the American Chemical Society* **2014,** *136*, 13925-13931.

119) Zou, Y.; Liu, C.; Zhang, C.; Yuan, L.; Li, J.; Bao, T.; Wei, G.; Zou, J.; Yu, C., Epitaxial growth of metal-organic framework nanosheets into single-crystalline orthogonal arrays. *Nature Communications* **2023,** *14*, 5780.

120) Liu, H.; Guan, J.; Yang, S.; Yu, Y.; Shao, R.; Zhang, Z.; Dou, M.; Wang, F.; Xu, Q., Metal-Organic-Framework-Derived Co(2) P Nanoparticle/Multi-Doped Porous Carbon as a Trifunctional Electrocatalyst. *Advanced Materials* **2020,** *32*, 2003649.

121) Aijaz, A.; Masa, J.; Rosler, C.; Xia, W.; Weide, P.; Botz, A. J.; Fischer, R. A.; Schuhmann, W.; Muhler, M., Co@Co3O4 Encapsulated in Carbon Nanotube-Grafted Nitrogen-Doped Carbon Polyhedra as an Advanced Bifunctional Oxygen Electrode. *Angewandte Chemie International Edition* **2016,** *55*, 4087-91.

122) Yang, M.; Zhu, W.; Zhao, R.; Wang, H.; Ye, T.-N.; Liu, Y.; Yan, D., MOF-derived hollow spherical Co2P@C composite with micro-nanostructure for highly

efficient oxygen evolution reaction in alkaline solution. *Journal of Solid State Chemistry* **2020,** *288*.

123) Li, G.; Zhang, X.; Zhang, H.; Liao, C.; Jiang, G., Bottom-up MOF-intermediated synthesis of 3D hierarchical flower-like cobalt-based homobimetallic phophide composed of ultrathin nanosheets for highly efficient oxygen evolution reaction. *Applied Catalysis B: Environmental* **2019,** *249*, 147-154.

124) Yu, X. Y.; Yu, L.; Wu, H. B.; Lou, X. W., Formation of nickel sulfide nanoframes from metal-organic frameworks with enhanced pseudocapacitive and electrocatalytic properties. *Angewandte Chemie International Edition* **2015,** *54*, 5331-5.

125) Ding, D.; Shen, K.; Chen, X.; Chen, H.; Chen, J.; Fan, T.; Wu, R.; Li, Y., Multi-Level Architecture Optimization of MOF-Templated Co-Based Nanoparticles Embedded in Hollow N-Doped Carbon Polyhedra for Efficient OER and ORR. *ACS Catalysis* **2018,** *8*, 7879-7888.

126) Wen, H.; Zhang, S.; Yu, T.; Yi, Z.; Guo, R., ZIF-67-based catalysts for oxygen evolution reaction. *Nanoscale* **2021,** *13*, 12058-12087.

127) Cao, X.; Tan, C.; Sindoro, M.; Zhang, H., Hybrid micro-/nano-structures derived from metal–organic frameworks: preparation and applications in energy storage and conversion. *Chemical Society Reviews* **2017,** *46*, 2660-2677.

128) Xia, W.; Mahmood, A.; Zou, R.; Xu, Q., Metal–organic frameworks and their derived nanostructures for electrochemical energy storage and conversion. *Energy & Environmental Science* **2015,** *8*, 1837-1866.

129) Wang, X.; Yu, L.; Guan, B. Y.; Song, S.; Lou, X. W. D., Metal-Organic Framework Hybrid-Assisted Formation of Co(3) O(4) /Co-Fe Oxide Double-Shelled Nanoboxes for Enhanced Oxygen Evolution. *Advanced Materials* **2018,** *30*, 1801211.

130) Wang, S.; Hou, Y.; Lin, S.; Wang, X., Water oxidation electrocatalysis by a zeolitic imidazolate framework. *Nanoscale* **2014,** *6*, 9930-4.

131) Zhao, S.; Wang, Y.; Dong, J.; He, C.-T.; Yin, H.; An, P.; Zhao, K.; Zhang, X.; Gao, C.; Zhang, L.; Lv, J.; Wang, J.; Zhang, J.; Khattak, A. M.; Khan, N. A.; Wei, Z.; Zhang, J.; Liu, S.; Zhao, H.; Tang, Z., Ultrathin metal–organic framework nanosheets for electrocatalytic oxygen evolution. *Nature Energy* **2016,** *1*.

132) Duan, J.; Chen, S.; Zhao, C., Ultrathin metal-organic framework array for efficient electrocatalytic water splitting. *Nature Communications* **2017,** *8*.

133) Thangavel, P.; Ha, M.; Kumaraguru, S.; Meena, A.; Singh, A. N.; Harzandi, A. M.; Kim, K. S., Graphene-nanoplatelets-supported NiFe-MOF: high-efficiency and ultra-stable oxygen electrodes for sustained alkaline anion exchange membrane water electrolysis. *Energy & Environmental Science* **2020**.

134) Wang, X. L.; Dong, L. Z.; Qiao, M.; Tang, Y. J.; Liu, J.; Li, Y.; Li, S. L.; Su, J. X.; Lan, Y. Q., Exploring the Performance Improvement of the Oxygen Evolution Reaction in a Stable Bimetal-Organic Framework System. *Angewandte Chemie International Edition* **2018,** *57*, 9660-9664.

135) Xue, Z.; Li, Y.; Zhang, Y.; Geng, W.; Jia, B.; Tang, J.; Bao, S.; Wang, H.-P.; Fan, Y.; Wei, Z.-w.; Zhang, Z.; Ke, Z.; Li, G.; Su, C.-Y., Modulating Electronic Structure of Metal-Organic Framework for Efficient Electrocatalytic Oxygen Evolution. *Advanced Energy Materials* **2018,** *8*, 1801564.

136) Suresh, P.; Natarajan, A.; Rajaram, A., Multi-Active Sites Loaded NiCu-MOF@MWCNTs as a Bifunctional Electrocatalyst for Electrochemical Water Splitting Reaction. *Langmuir* **2024,** *40*, 9509-9519.

137) Zhao, S.; Tan, C.; He, C.-T.; An, P.; Xie, F.; Jiang, S.; Zhu, Y.; Wu, K.-H.; Zhang, B.; Li, H.; Zhang, J.; Chen, Y.; Liu, S.; Dong, J.; Tang, Z., Structural

transformation of highly active metal–organic framework electrocatalysts during the oxygen evolution reaction. *Nature Energy* **2020,** *5*, 881-890.

138) Wu, Y. P.; Tian, J. W.; Liu, S.; Li, B.; Zhao, J.; Ma, L. F.; Li, D. S.; Lan, Y. Q.; Bu, X., Bi-Microporous Metal-Organic Frameworks with Cubane [M(4) (OH)(4)] (M=Ni, Co) Clusters and Pore-Space Partition for Electrocatalytic Methanol Oxidation Reaction. *Angew Chem Int Ed Engl* **2019,** *58*, 12185-12189.

139) Abdelhafiz, A.; Mohammed, M. H.; Abed, J.; Lee, D. C.; Chen, M.; Helal, A. S.; Ren, Z.; Alamgir, F.; Sargent, E.; Kohl, P. A.; Elsaidi, S. K.; Li, J., Tri-Metallic Catalyst for Oxygen Evolution Reaction Enables Continuous Operation of Anion Exchange Membrane Electrolyzer at 1A cm−2 for Hundreds of Hours. *Advanced Energy Materials* **2024,** *14*.

140) Ji, Q.; Kong, Y.; Wang, C.; Tan, H.; Duan, H.; Hu, W.; Li, G.; Lu, Y.; Li, N.; Wang, Y.; Tian, J.; Qi, Z.; Sun, Z.; Hu, F.; Yan, W., Lattice Strain Induced by Linker Scission in Metal–Organic Framework Nanosheets for Oxygen Evolution Reaction. *ACS Catalysis* **2020,** *10*, 5691-5697.

141) Xue, Z.; Liu, K.; Liu, Q.; Li, Y.; Li, M.; Su, C.-Y.; Ogiwara, N.; Kobayashi, H.; Kitagawa, H.; Liu, M.; Li, G., Missing-linker metal-organic frameworks for oxygen evolution reaction. *Nature Communications* **2019,** *10*.

142) Cheng, W.; Zhao, X.; Su, H.; Tang, F.; Che, W.; Zhang, H.; Liu, Q., Lattice-strained metal–organic-framework arrays for bifunctional oxygen electrocatalysis. *Nature Energy* **2019,** *4*, 115-122.

143) Zheng, W.; Lee, L. Y. S., Metal–Organic Frameworks for Electrocatalysis: Catalyst or Precatalyst? *ACS Energy Letters* **2021,** *6*, 2838-2843.

144) Qian, Q.; Li, Y.; Liu, Y.; Yu, L.; Zhang, G., Ambient Fast Synthesis and Active Sites Deciphering of Hierarchical Foam-Like Trimetal–Organic Framework

Nanostructures as a Platform for Highly Efficient Oxygen Evolution Electrocatalysis. *Advanced Materials* **2019,** *31*, 1901139.

145) Li, W.; Watzele, S.; El-Sayed, H. A.; Liang, Y.; Kieslich, G.; Bandarenka, A. S.; Rodewald, K.; Rieger, B.; Fischer, R. A., Unprecedented High Oxygen Evolution Activity of Electrocatalysts Derived from Surface-Mounted Metal–Organic Frameworks. *Journal of the American Chemical Society* **2019,** *141*, 5926-5933.

146) Canivet, J.; Fateeva, A.; Guo, Y.; Coasne, B.; Farrusseng, D., Water adsorption in MOFs: fundamentals and applications. *Chemical Society Reviews* **2014,** *43*, 5594-617.

147) Liu, X.; Wang, X.; Kapteijn, F., Water and Metal-Organic Frameworks: From Interaction toward Utilization. *Chemical Reviews* **2020,** *120*, 8303-8377.

148) Zheng, W.; Liu, M.; Lee, L. Y. S., Electrochemical Instability of Metal–Organic Frameworks: In Situ Spectroelectrochemical Investigation of the Real Active Sites. *ACS Catalysis* **2019,** *10*, 81-92.

149) Mousazade, Y.; Mohammadi, M. R.; Chernev, P.; Bagheri, R.; Song, Z.; Dau, H.; Najafpour, M. M., Revisiting Metal-Organic Frameworks for Oxygen Evolution: A Case Study. *Inorganic Chemistry* **2020,** *59*, 15335-15342.

150) Luczak, J.; Kroczewska, M.; Baluk, M.; Sowik, J.; Mazierski, P.; Zaleska-Medynska, A., Morphology control through the synthesis of metal-organic frameworks. *Advances in Colloid and Interface Science* **2023,** *314*, 102864.

151) Garlyyev, B.; Kratzl, K.; Rück, M.; Michalička, J.; Fichtner, J.; Macak, J. M.; Kratky, T.; Günther, S.; Cokoja, M.; Bandarenka, A. S.; Gagliardi, A.; Fischer, R. A., Optimizing the Size of Platinum Nanoparticles for Enhanced Mass Activity in the Electrochemical Oxygen Reduction Reaction. *Angewandte Chemie International Edition* **2019,** *58*, 9596-9600.

152) Roy, C.; Sebok, B.; Scott, S. B.; Fiordaliso, E. M.; Sørensen, J. E.; Bodin, A.; Trimarco, D. B.; Damsgaard, C. D.; Vesborg, P. C. K.; Hansen, O.; Stephens, I. E. L.; Kibsgaard, J.; Chorkendorff, I., Impact of nanoparticle size and lattice oxygen on water oxidation on NiFeOxHy. *Nature Catalysis* **2018,** *1*, 820-829.

153) Deng, J.; Nellist, M. R.; Stevens, M. B.; Dette, C.; Wang, Y.; Boettcher, S. W., Morphology Dynamics of Single-Layered Ni(OH)(2)/NiOOH Nanosheets and Subsequent Fe Incorporation Studied by in Situ Electrochemical Atomic Force Microscopy. *Nano Letters* **2017,** *17*, 6922-6926.

154) Stevens, M. B.; Trang, C. D. M.; Enman, L. J.; Deng, J.; Boettcher, S. W., Reactive Fe-Sites in Ni/Fe (Oxy)hydroxide Are Responsible for Exceptional Oxygen Electrocatalysis Activity. *Journal of the American Chemical Society* **2017,** *139*, 11361-11364.

155) Kuai, C.; Xi, C.; Hu, A.; Zhang, Y.; Xu, Z.; Nordlund, D.; Sun, C. J.; Cadigan, C. A.; Richards, R. M.; Li, L.; Dong, C. K.; Du, X. W.; Lin, F., Revealing the Dynamics and Roles of Iron Incorporation in Nickel Hydroxide Water Oxidation Catalysts. *Journal of the American Chemical Society* **2021,** *143*, 18519-18526.

156) Chatenet, M.; Pollet, B. G.; Dekel, D. R.; Dionigi, F.; Deseure, J.; Millet, P.; Braatz, R. D.; Bazant, M. Z.; Eikerling, M.; Staffell, I.; Balcombe, P.; Shao-Horn, Y.; Schafer, H., Water electrolysis: from textbook knowledge to the latest scientific strategies and industrial developments. *Chemical Society Reviews* **2022,** *51*, 4583-4762.

157) Görlin, M.; Ferreira de Araújo, J.; Schmies, H.; Bernsmeier, D.; Dresp, S.; Gliech, M.; Jusys, Z.; Chernev, P.; Kraehnert, R.; Dau, H.; Strasser, P., Tracking Catalyst Redox States and Reaction Dynamics in Ni–Fe Oxyhydroxide Oxygen Evolution Reaction Electrocatalysts: The Role of Catalyst Support and Electrolyte pH. *Journal of the American Chemical Society* **2017,** *139*, 2070-2082.

158) Friebel, D.; Louie, M. W.; Bajdich, M.; Sanwald, K. E.; Cai, Y.; Wise, A. M.; Cheng, M.-J.; Sokaras, D.; Weng, T.-C.; Alonso-Mori, R.; Davis, R. C.; Bargar, J. R.; Nørskov, J. K.; Nilsson, A.; Bell, A. T., Identification of Highly Active Fe Sites in (Ni,Fe)OOH for Electrocatalytic Water Splitting. *Journal of the American Chemical Society* **2015,** *137*, 1305-1313.

159) Ferreira de Araujo, J.; Dionigi, F.; Merzdorf, T.; Oh, H. S.; Strasser, P., Evidence of Mars-Van-Krevelen Mechanism in the Electrochemical Oxygen Evolution on Ni-Based Catalysts. *Angewandte Chemie International Edition* **2021,** *60*, 14981-14988.

160) Hu, X.; Tian, X.; Lin, Y. W.; Wang, Z., Nickel foam and stainless steel mesh as electrocatalysts for hydrogen evolution reaction, oxygen evolution reaction and overall water splitting in alkaline media. *RSC Advances* **2019,** *9*, 31563-31571.

161) Ding, M.; Cai, X.; Jiang, H.-L., Improving MOF stability: approaches and applications. *Chemical Science* **2019,** *10*, 10209-10230.

162) Yuan, S.; Feng, L.; Wang, K.; Pang, J.; Bosch, M.; Lollar, C.; Sun, Y.; Qin, J.; Yang, X.; Zhang, P.; Wang, Q.; Zou, L.; Zhang, Y.; Zhang, L.; Fang, Y.; Li, J.; Zhou, H.-C., Stable Metal-Organic Frameworks: Design, Synthesis, and Applications. *Advanced Materials* **2018,** *30*, 1704303.

163) Howarth, A. J.; Liu, Y.; Li, P.; Li, Z.; Wang, T. C.; Hupp, J. T.; Farha, O. K., Chemical, thermal and mechanical stabilities of metal–organic frameworks. *Nature Reviews Materials* **2016,** *1*.

2. Motivation

Metal-Organic Frameworks (MOFs) represent a significant breakthrough derived from advancements in coordination chemistry. The versatility in choosing metals and ligands, along with the ability to manipulate chemical coordination bonds and tune pore size and structure, has opened up extensive possibilities for MOFs' applications. In the context of increasing focus on energy issues, MOFs have emerged as promising catalysts in new energy sectors, such as water splitting. Over the past decade, MOFs have been extensively studied for their potential in oxygen evolution reactions (OER). Numerous studies have demonstrated that MOFs, either as carbon templates or direct catalysts, exhibit impressive OER activity, thereby enhancing their application prospects.

When pristine MOFs are employed as direct OER catalysts, the metal nodes within the MOF structure are often considered the active sites, playing a crucial role in alkaline OER applications. This assertion is supported by evidence from X-ray diffraction (XRD) and electrochemical stability tests. However, there remains contention regarding the thermal stability of MOFs under harsh conditions, as reported in the literature. This ongoing debate about the precise role of pristine MOFs in alkaline OER applications underscores the need for further investigation.

Therefore, the primary objective of this dissertation is to elucidate the role of pristine MOFs in alkaline OER applications. The investigative focus of this thesis can be categorized into the following key questions:

1) Catalysts or Precursors?

The first objective is to determine the true role of pristine MOFs. Are they functioning as catalysts, as suggested by most published reports, with the metal nodes acting as active sites responsible for OER activity? Alternatively, are MOFs merely precursors, with derived intermediates being the actual contributors to OER activity?

2) Impact of MOFs' Original Structure on OER Activity

If MOFs act as precursors, it is essential to explore the conversion process and

examine the relationship between the original structure of MOFs and the resulting intermediates that contribute to OER activity.

3) Insights from MOFs' Transformation Process for Catalyst Design

The last question is whether the understanding the transformation process of MOFs can provide valuable insights into the design and development of more efficient catalysts.

Chapter 3

3. Structure-Activity Relationships in Ni-Carboxyl-Type Metal-Organic Frameworks' Conversion for Oxygen Evolution Reaction

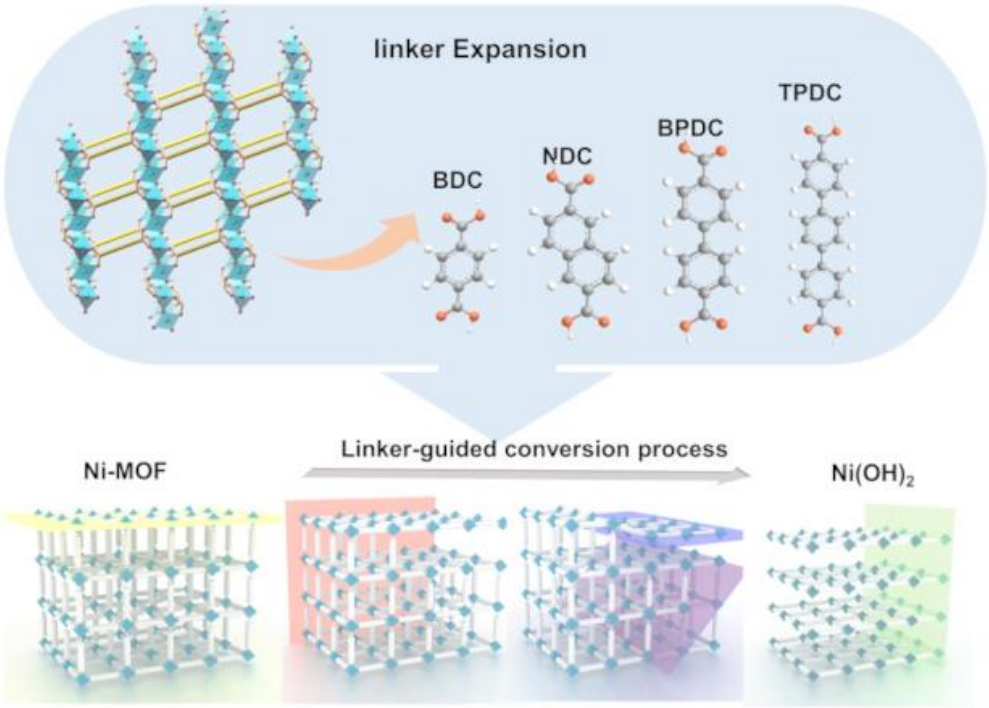

This is chapter is based on a manuscript of the same title from X. Ma, D. Zheng , S Hou, S. Mukherjee, R. Khare, G. Gao, Q. Ai, B. Garlyyev, W. Li, M. Koch, J. Mink, Y. Shao-Horn, J. Warnan, A. Bandarenka, R. Fischer (2023). Structure–Activity Relationships in Ni-Carboxylate-Type Metal–Organic Frameworks' Metamorphosis for the Oxygen Evolution Reaction. *ACS catalysis*, **13**(11), 7587-7596, reprinted with permission from Copyright © 2023, American Chemical Society.

The project was designed by X. Ma, J. Warnan, A. Bandarenka and R. Fischer. The synthesis experiments and most of the characterizations and electrochemical test were performed by X. Ma. The ICP-OES was performed by M. Koch, The HRETM was performed by G. Gao, Q. Ai,, The XAFS was performed R. Khare. The final manuscript was written by X. Ma and discussed and edited by all co-authors.

Abstract

Metal-organic frameworks (MOFs) are haven been reported to catalyze the oxygen evolution reaction (OER). Despite the established links between the pristine MOFs and their derived metal hydroxide electrocatalysts, several limitations still preclude understanding of the critical factors determining the OER performance. Of prime importance appears the choice of MOFs and how its compositions relate to the catalyst stability and in turn to the reconstruction mechanisms into the active species under OER conditions. An isoreticular series of Ni-MOFs [Ni2(OH)2L] was chosen to elucidate the effects of the carboxylate linker length expansion and modulation of the linker-linker p-p interactions. (L = 1,4-benzodicarboxylate, 2,6-napthalenedicarboxylate, biphenyl-4,4'-dicarboxylate and p-terphenyl-4,4''-dicarboxylate). Degradation and reconstruction of MOFs were systematically investigated. The linker controls the transformation of Ni-MOF into distinct nickel hydroxide phases, and the conversion from α-$Ni(OH)_2$ to β-$Ni(OH)_2$, thus correlating the Ni-MOFs composition with the OER activity of the Ni-MOF-derived metastable nickel hydroxide phase mixture.

3.1 Introduction

Metal-organic frameworks (MOFs) are regarded as promising electrocatalysts due to their modular compositions of redox-active building blocks, earth-abundant metal ions and organic linkers.[1-5] Reaping benefits from well-regulated morphologies, fine-tune properties and superior active site accessibility, bespoke MOFs are primed to push forward the state-of-the-art oxygen evolution reaction (OER) materials.[6-8] In parallel, research into MOF as OER electrocatalysts directly in alkaline media has recently gained prominence due to their remarkable performance.[9-13] However, controversy over electroactive MOFs behaving as a catalyst itself or as a precursor to yield the active catalyst nevertheless exists. On the one hand, MOFs show stable features with reported well preserved MOF structure after OER in some cases.[14] On the other hand, using *in situ* spectroelectrochemistry, *e.g.*, Zheng *et al.* have reported that ZIF-67, built of Co^{2+} ions and 2-methyl imidazole ligands, is unstable in aqueous alkaline medium and generate $Co(OH)_2$ as intrinsic to OER catalytic activity, instead of the Co^{2+} nodes of the intact ZIF-67.[15] Tang and co-workers have employed operando X-ray absorption spectroscopy (XAS) to show the deconstruction of NiCo/NiFe-MOF-74 and its subsequent reconstruction in metal oxy/hydroxide materials during the OER.[16]

Although these reports recognized the role of MOFs to derive metal hydroxides to enable OER electrocatalysis, the impact of the structure of the pristine MOFs on the formation and the nature of the intermediates and derived metal hydroxide electrocatalysts remain indeterminate.[15, 16] The diversity of structures of MOFs and their individual behavior under realistic electrochemical conditions in aqueous electrolyte media over time leads to a huge parameter space to be explored. Particularly, distinguishing derived metal hydroxides from their precursor MOFs and understanding the transformation mechanisms are still unclear. The synergistic impact of intrinsic parameters (*e.g.*, MOF composition and medium) and external

stimuli (*e.g.*, applied potential) on the MOF metamorphosis and/or deconstruction and catalyst assembly merits further detailed studies.

Unveiling the role of MOF precursors towards electrocatalyst-design in alkaline medium, herein, we systematically examine a family of four isoreticular Ni-MOFs of formula $[Ni_2(OH)_2L]$ (**Figure 3.1a**), each featuring the same Ni(II) coordination environments with differences in the length of the dicarboxylate linkers L. This systematic study presents an unambiguous case of degradation, as all Ni-MOFs demonstrated instability in alkaline electrolytes and under OER conditions. They quantitatively transform into α/β-$Ni(OH)_2$ phases over time. Interestingly, we discovered a correlation between the choice of the linker, the aging process and the Ni-MOF derived nickel-hydroxide catalyst performance over time which is related to the ratio of α-$Ni(OH)_2$ to β-$Ni(OH)_2$.

3.2 Results and Discussion

3.2.1 Ni-MOF Synthesis and Characterization

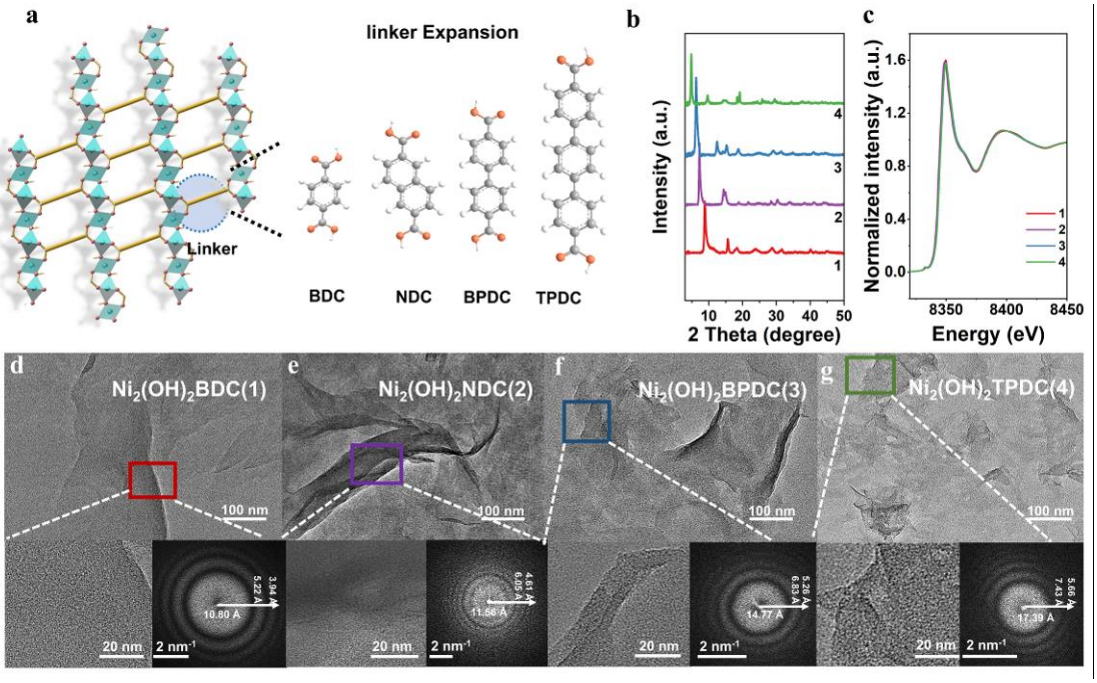

Figure 3.1. Structural characterization data of Ni-MOFs with general formula $[Ni_2(OH)_2L]$ (**1**, L = BDC; **2**, L = NDC; **3**, L = BPDC; **4**, L = TPDC). (a) Crystal

structure illustration where the length of the dicarboxylate linker directly contributes to the compositional modularity and variance of stability. (b) X-ray powder diffractograms. (c) Ni K-edge XANES data of Ni-MOFs. TEM images and FFT diffraction patterns for d) **1**, BDC; e) **2**, NDC; f) **3**, BPDC; and g) **4**, TPDC.

We synthesized a series of isoreticular Ni-based MOFs (**1**-**4**) of a general formula $[Ni_2(OH)_2L]$ (**Figure 3.1a**) with dicarboxylate arene linkers L of increasing length (L: **1**, 1,4-benzodicarboxylate, BDC; **2**, 2,6-napthalenedicarboxylate NDC; **3**, biphenyl-4,4'-dicarboxylate, BPDC; **4**, *p*-terphenyl-4,4"-dicarboxylate, TPDC).[17] Within the series, the node-to-node layer distance increases with the linker length variation from 6.7 to 15.0 Å for BDC to TPDC, respectively (**Figure 3.1a**).

The powder X-ray diffraction (PXRD) patterns of the MOFs (**1**-**4**) and the corresponding high-resolution transmission electron microscopy (HRTEM) images (displaying hexagonal configuration for each Ni(II)) were found to be in good agreement with respective literature data (**Figures 3.1b** and **A3.1**-**A3.2**).[17-20] Ni K-edge X-ray absorption spectroscopy (XAS) confirmed the expected, similar coordination environment of the Ni centers of **1**-**4** (**Figures 3.1c** and **A3.3-A3.4, Table A3.1**). Spectral traces in **Figure 3.1c** correspond to the electron transition from Ni 1s to the unoccupied 4p orbitals. For example, the spectral profile of **1** is close to the Ni^{2+} oxide reference or to the Ni^{2+}(aq) reference (**Figure A3.3a**), which reveals an average local Ni valence state of +2. The similar intensities of edge peaks in XANES and Ni K-edge $k^2\chi$ data of EXAFS oscillations indicate an identical structure in all the MOFs (**Figures 3.1c, A3.3b-c**, **Table A3.1**). As the linker length increases the interlayer distances, crystal orientation across the parallel Ni-oxo layers shifts towards lower 2θ values. Accordingly, the metal-ligand-metal lattice spacings were determined using Bragg´s Law (**1**, 10.0(1); **2**, 12.2(1); **3**, 14.2(2); **4**, 18.2(1) Å; **Table A3.2**). These values were in good agreement with the Fast Fourier transform (FFT) diffraction patterns of the TEM images (**Figure 3.1d**). Across the series **1**-**4**, crystallite morphologies observed by TEM and scanning electron microscopy (SEM)

images (**Figure 3.1d, Figure A3.5**) consistently revealed a 2D nanosheet type undulating morphology.

3.2.2 Ni-MOF Electrochemical OER Performance

Next, we tested electrochemical properties across the series **1**-**4**. As-synthesized Ni-MOFs (0.05 mg) were deposited on glassy carbon (GC) as working electrodes following a standard drop-casting technique. GC was chosen to limit uncertainty in specific surface area determination, a handicap often-encountered with the use of nickel foam or carbon paper as the substrate. At this point it is important to note that trace Fe further complicates the system since it greatly affects nickel-based OER activity of Ni-MOFs, and the active sites for Ni-Fe hybrids are not clearly defined until now.[21-24] Herein, we refrain from intentional integration of other metals such as Fe for enhancing the OER performance and keep the OER conditions Fe-free in high purity alkaline medium. Here, Fe-free, high purity 1 M KOH solution was used as an electrolyte to emulate Trotochaud's high purity conditions.[25]

Typically, samples were conditioned before OER testing by cyclic voltammetry (CV) from 1.16 to 1.64 V *vs.* RHE electrode with IR correction (Hg/HgO, 1 M NaOH, 0.140 V *vs.*NHE, was used as the experimental reference electrode and potentials were corrected for RHE) until stable CV curves were obtained, usually after 30 or 100 cycles with 20 mV/s, which corresponds to ~12-40 min of conditioning time (**Figures 3.2, A3.6-A3.8**). All MOFs demonstrated similar behavior, as the initial scans reveal negligible to only minor oxidative (anodic) peaks around ~ 1.47 V *vs*. RHE and a reductive (cathodic) wave at ~1.32 V *vs.* RHE. These features are ascribed to the pre-OER Ni^{2+}/Ni^{3+} redox transition of Ni centers.[26] For the BDC-MOF (**1**), alongside a dramatic increase in peak intensity with cycling, the pre-OER anodic peak potential is shifted from 1.49 to 1.50 to 1.56 V *vs*. RHE in the 1^{st}, 30^{th} and 100^{th} CV cycle, respectively (**Figures 3.2a, A3.6a** and **A3.8a**). A similar trend was observed for NDC-MOF (**2**) with its anodic peak observed at 1.46 V *vs*. RHE after 30 cycles (**Figures 3.2b** and **A3.8b**). The slower peak growth of **2** compared to

the case of **1** potentially suggests a higher activation energy barrier in case of the NDC linker present in **2**. Further cycling to 100 cycles revealed two anodic peaks at ~ 1.44 and ~ 1.5 V *vs*. RHE (**Figure A3.6b**). Activation of BPDC-MOF (**3**) resulted in a single, more anodic peak at ~1.44 and ~1.45 V *vs*. RHE after 30 and 100 cycles, respectively (**Figures 3.2c**, **A3.6c** and **A3.8c**). For TPDC-MOF (**4**) (**Figures 3.2d** and **A3.7-A3.8**), only subtle changes were observed during the first 30 cycles in the potential dynamic curves, as a new oxidation peak grew at 1.41 V *vs.* RHE, alongside the original at 1.48 V *vs.* RHE. Only the former continued growing in intensity until ~100th cycle (**Figure 3.2d**).

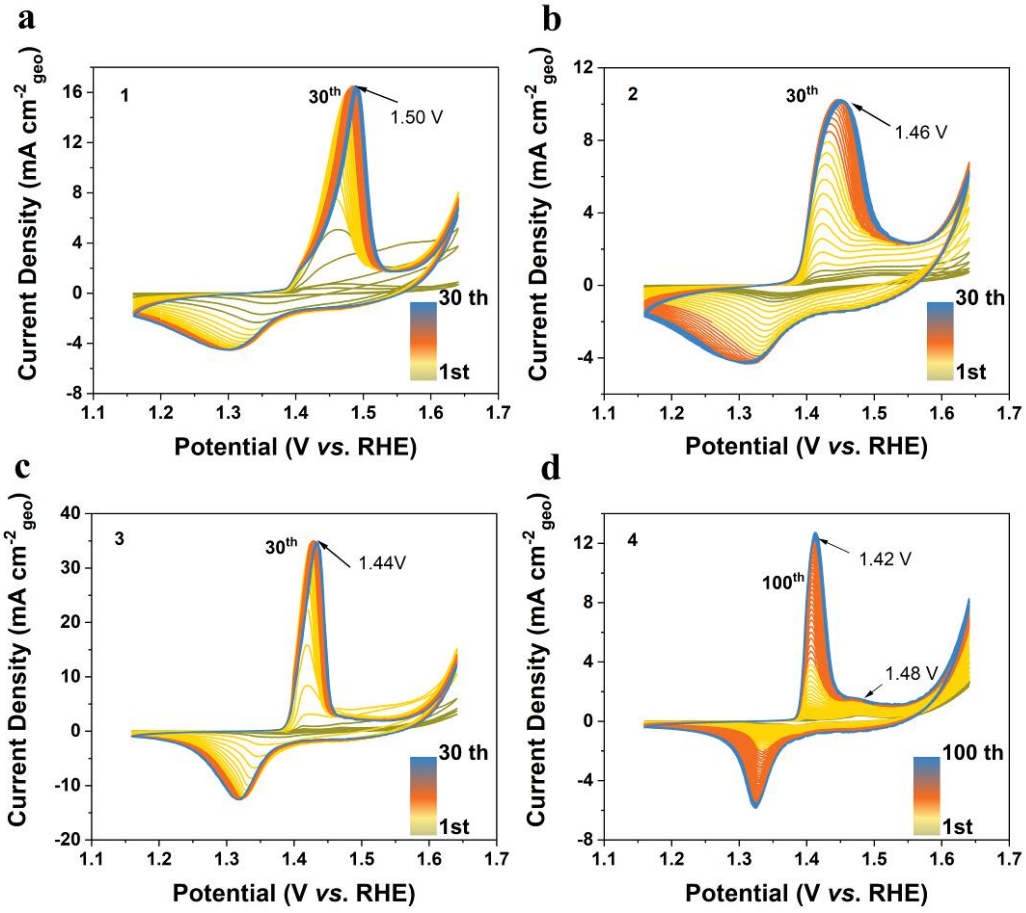

Figure 3.2. Conditioning of the MOF (**1-4**) coated glassy carbon (GC) electrodes. Continuous cyclic voltammograms (scan rate of 20 mV s^{-1} in Fe-free 1 M KOH). (a) **1**, BDC, 30 cycles; (b) **2**, NDC, 30 cycles; (c) **3**, BPDC, 30 cycles; (d) **4**, TPDC, 100 cycles; Each GC electrode contains about 255 $\mu g_{MOF} \cdot cm^{-2}_{geo}$.

Overall, the voltammetry data revealed the similar strong oxidation waves among all samples, which could be ascribed to the progressive exposure of electroactive Ni sites as the carboxylate linkers were leached and dissolve in the media while the vacant coordination sites at the Ni were saturated by hydroxide ions.[26] The main anodic pre-OER peak is shifted towards more cathodic (negative) potentials, *i.e.*, from 1.50 to 1.41 V *vs.* RHE after 30 cycles, as the ligand length increases within the series, where further cycling resulted in small anodic shift. These observations indicate that the reorganization of Ni-MOFs at their interface to the electrolyte can be MOF-structure dependent, continuous, long-term dynamic, stimulus-dependent and the phenomena are likely highly intricate.

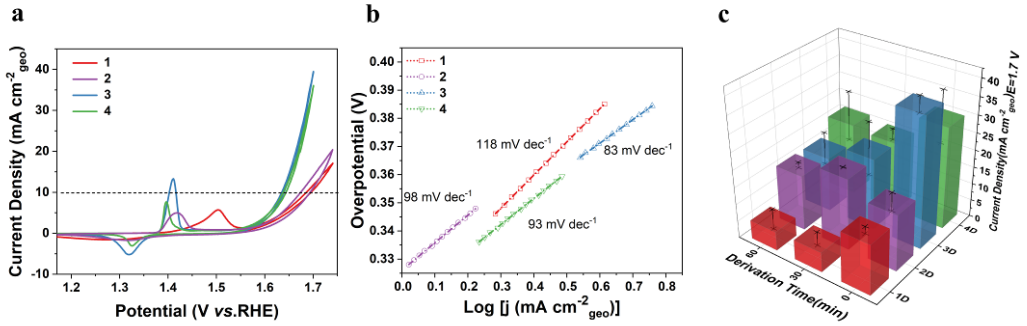

Figure 3.3. Electrochemical evaluation. The MOF (**1**-**4**) color code refers to the various linkers: **1**, *red* (BDC); **2**, *violet* (NDC); **3**, *blue*, (BPDC); **4**, *green* (TPDC). (a) Cyclic voltammograms of the MOF coated electrodes at a scan rate of 5 mV s^{-1} in 1 M KOH after CV pre-treatment: **1**-**3**, 30 cycles and **4**, 100 cycles (until which the anodic peaks do not longer increase). The dotted horizontal line is a guide to the eye showing a current density of 10 mA cm^{-2}_{geo}. (b) Tafel plots obtained from the data presented in a). (c) Current densities of derived MOFs (**1**D-**4**D) taken at E = 1.7 V *vs.* RHE. The derivation was done by immersing the MOF (**1**-**4**) coated electrodes to 1 M KOH for 0, 30, and 60 min derivation time without applying potential followed by CV-cycling similar to a).

After obtaining stable activation CVs (**Figures A3.9 and A3.10**), the performance of the conditioned MOFs coated electrodes were investigated towards the OER upon

recording CV plots under a scan speed of 5 mV s^{-1} (**Figure 3.3a**). For all MOFs **1**-**4**, the OER onset potential was found consistent at $E \approx 1.58$ V *vs.* RHE (experimental potential uncertainty ± 10 mV). The typical benchmarking current density of 10 mA cm^{-2}_{geo}, required an applied overpotential in the range of 420-450 mV (**1**, 446 ± 9; **2**, 432 ± 10; **3**, 415 ± 2; and **4**, 419 ± 10 mV. **Figure 3.3a and Figure A3.11**). The Raman spectra of MOFs **1**-**4** after the CV cycling are given in **Figure A3.12** and the absence of absorption bands of the linkers data indicate the complete transformation of all four MOFs to $Ni(OH)_2$/NiOOH after the activation process. Corresponding Tafel slope values are 83, 93, 98 and 118 mV dec^{-1}, respectively, underscoring the distinctly slower OER kinetics for the electrodes made of the BDC-MOF (**1**) (**Figure 3.3b**). Inductively coupled plasma atomic emission spectroscopy (ICP-OES) measurements of the MOFs coated electrodes (**Figure A3.13**) and integration of the oxidation peak in OER afforded the number of moles of Ni deposited at the GC electrode or reacted during CV process for each system and enabled the conservative estimation of the corresponding turnover frequency (TOF) per Ni center (**Figure A3.14).** Both TOF values followed a similar trend as previously observed for the Tafel slope, with the pristine MOFs' increased linker lengths resulting in higher TOF values. Furthermore, OER after a prolonged activation (100 cycles) was examined for all MOFs **1**-**4** resulting in somewhat higher overpotentials, but keeping the phenomenon of linker dependent slight variations (**Figure A3.15)**.

As we observed that the choice of the MOF linker could affect the OER activity over time, and knowing that linkers may be leached out in alkaline electrolyte environment, we investigated the impact of a KOH pre-treatment of the MOF samples before starting the OER experiments. The electrodes coated with the pristine MOFs **1**-**4** were soaked in the KOH electrolyte for periods of t_D = 30, 60, 480, and 1200 minutes ("derivation time") and *without* applying a potential. The resulting series of samples are denoted as **1**D-**4**D. Subsequently, the CV multi-scan

conditioning step was performed and then the OER testing was done similar to the series of initial series of OER experiments described above, which refer to t_D = 0 minutes, of course. All "derived" samples **1**D-**4**D displayed a decrease in OER activities with prolonged t_D with some variations within 60 min reaching a similar level after 1200 min, except for **1**D (**Figure 3.3c, A3.16-A3.17**). Sample **1**D, referring to the BDC-MOF, presented a significantly faster and stronger decay in terms of current densities at 1.7 V as compared with the three others. (**Figure 3.3c, A3.16-A3.17**). At t_D = 0 min we observe strong variation of the OER current densities with the choice of linkers for all four samples. Nevertheless, the current densities of **2**D, **3**D and **4**D converge around a moderate level of 8.5 ± 1.6 to 10.3 ± 1.4 mA·cm^{-2} at t_D = 1200 min (20 h) of KOH pre-treatment, which is still a distinctly higher value than 3.7 ±1 mA·cm^{-2} found for the BDC-MOF derived sample **1**D. The same trend is observed for the variation of the overpotential η of **1**D-**4**D with a clear differentiation of **1**D with η = 618 ± 5 mV from the others at t_D = 1200 min, such as **2**D, 493 ± 3; **3**D, 475 ± 5; **4**D, 468 ± 11 mV (**Figure A3.17**). Concomitantly, the series of measurements of the current densities of **1**D-**4**D at 1.7 V *vs.* RHE and calculated TOF results revealed that shorter KOH pre-treatment provide higher OER activities albeit still lower than the ones obtained without any prior exposure to KOH solution (**Figure 3.3c and A3.18**).

3.2.3 MOF Conversion Investigations

Powder X-ray Diffraction Studies. Following the discussion on MOF stability under OER conditions presented in the introduction, we investigated the hypothesis of MOF conversion into metal hydroxide materials, *e.g.* $Ni(OH)_2$, NiOOH, building upon the Bode scheme of redox transition in Ni hydroxide layered materials (**Figure A3.19**).[27] In a first series of experiments, microcrystalline powder samples of the pristine MOFs **1-4** were dispersed in 1M KOH (in the absence of potential) to replicate the basic media of the electrochemical experiments presented above and to ensure easy monitoring by standard PXRD instrumentation. PXRD patterns of the

collected materials (after centrifugation, washing and drying) were recorded after a defined derivation time t_D to monitor the time-dependent changes and the samples are again denoted as **1**D-**4**D (**Figure 3.4**). Upon immersing the MOF powders in 1 M KOH solution (pH = 14.0), all samples display a clear loss in crystallinity, as the intensity of the MOF characteristic peaks weaken, broaden and eventually disappear and new broad peaks appear between 30-40°. These latter diffraction peaks are assigned to nickel hydroxide phases and indicate the conversion the MOFs **1**-**4**.[28] While the reflection peak at 5-10° (**Figures 3.4a-c**), associated with the MOF's plane B (001) (**Figure 3.4e**) vanishes after 15 min for **1**D, it requires 60 and 30 min for **2**D and **3**D respectively, until its complete disappearance (**Figure 3.4a-c** and **Figure A3.20a)**. By contrast, samples **4**D samples retain the diffraction peaks of TPDC-MOF **4** even after 8 h (**Figure 3.4d**). This clearly indicates a much stronger tolerance and stability of **4** to basic electrolytes that is related to the more extended linker which presumably provide additional stabilization by enhanced π-π stacking.[20] Importantly, the characteristic MOF peaks coexist with the emerging peaks of α/β-$Ni(OH)_2$ in the PXRD patterns of all samples **2**D-**4**D, except for the BDC-MOF derived **1**D which transformation is very fast (at 33° plane C, (101) for α-$Ni(OH)_2$, (100) for β-$Ni(OH)_2$; and at 38° plane D (015) for α-$Ni(OH)_2$, (101) for β-$Ni(OH)_2$). These peaks between 30-40° sharpen and become more pronounced over time for all samples indicating the reorganization from a disordered α-$Ni(OH)_2$ to more ordered β-$Ni(OH)_2$ phase, as reflections for the planes C (100) and D (101) for β-$Ni(OH)_2$ intensify (**Figure 3.4)**.[28,29] Concomitantly, a broad peak ascribed to the plane E (001) of β-$Ni(OH)_2$ develops at ~ 20º albeit in a slow fashion. This suggests fast reorganization of the Ni-node layers of the MOFs (plane A) during their structural reconstruction to the related layers of edge sharing nickel hydroxide octahedra of the $Ni(OH)_2$ phases (plane C) (**Figure 3.4e)**. The conversion process of the MOFs to β-$Ni(OH)_2$ was found to be distinctly MOF-structure (linker) dependent as clear β-$Ni(OH)_2$ reflections can be observed after 30 min for the sample **1**D, referring to the

BDC-MOF, while 480 min (8 h) are required for the TPDC-MOF based sample **4**D**.** This time-dependent evolution of the mixed phase $[Ni_2(OH)_2L]/Ni(OH)_2$ nature of the materials **1**D-**4**D in alkaline media highlights that the linkers leach out gradually and indicate a stability trend of MOFs **1**-**4** as a function of the linkers: BDC < BPDC < NDC < TPDC. It also implies characteristic differences in the kinetics of alteration and transformation of the MOFs **1**-**4** at intermediate derivation times (t_D) as a function of the linker. If t_D is long enough (20 h and 48 h, **Figure A3.21**) all samples will show more or less broadened diffraction peaks assigned to α/β-$Ni(OH)_2$ phases. Additionally, we selected the most unstable MOF **1** to study the degradation and reconstruction as a function of the pH from neutral to alkaline conditions (using standard buffer solutions and diluted KOH). The MOF **1** remained relatively stable from pH 7.0 up to pH = 9.2 for 15-60 minutes, without indication of $Ni(OH)_2$ phase formation. Reconstruction of **1** was slower at pH = 11.0 and as well at pH = 13.1 as compared to pH = 14.0 (**Figure A3.22-A3.24)**. After immersing the MOFs in 0.1 M KOH (pH = 13.1) for 60 minutes, characteristic MOF peaks could still be observed. However, even at mild alkaline conditions at pH = 9.2, MOF **1** is clearly not stable. In the RAMAN spectra (see next section), a shoulder, characteristic for the ν(OH) absorption of β-$Ni(OH)_2$, is emerging after t_D = 60 min (**Figure A3.24**). From these data, we deduce that the MOF coatings of the actual electrodes would undergo a quite similar change during the electrochemical experiments over time, and most significantly at the solid-liquid interface to the electrolyte. Even at mild alkaline conditions, reconstruction of the MOF's interface to the electrolyte will take place during the OER experiment.

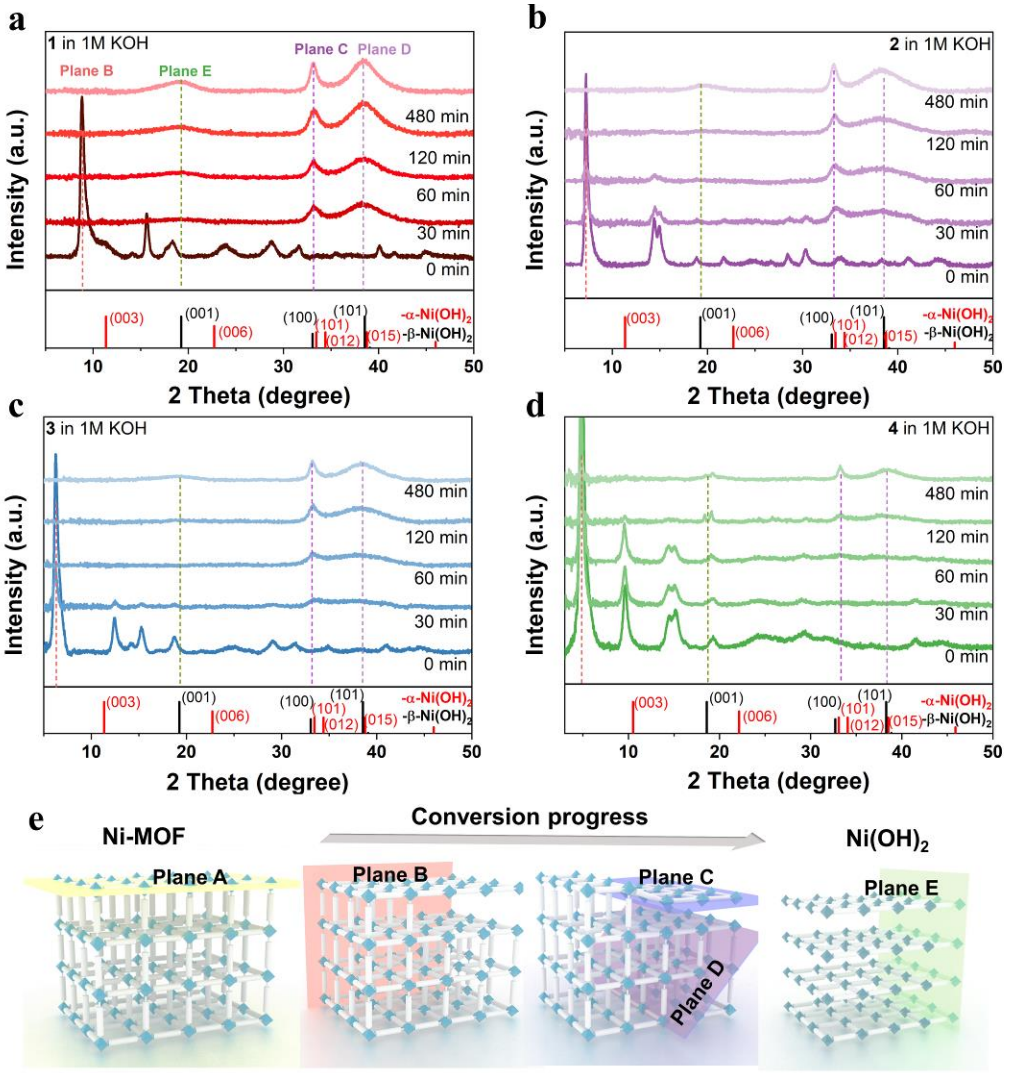

Figure 3.4. Monitoring structural transformation during MOF derivation in alkaline electrolyte solution as function of the linkers: (a) **1**D, BDC; (b) **2**D, NDC; (c) **3**D, BPDC; (d) **4**D, TPDC. Time-dependent powder X-ray diffractograms were taken after subjecting crystalline bulk samples of MOFs **1**-**4** to 1 M KOH without potential (derivation time: 30 min to 480 min).(e) Possible scheme of conversion process from the MOFs to β-$Ni(OH)_2$, Plane A, metal hydroxide layer in MOFs; Plane B, (001) node-to-node spacing in MOFs; Plane C, brucite-like metal layer, (101) for α-$Ni(OH)_2$, (100) for□β-$Ni(OH)_2$; Plane D (015) for α-$Ni(OH)_2$, (101) for β-$Ni(OH)_2$; Plane E, node-to-node spacing (001) of β-$Ni(OH)_2$.

Raman Spectroscopic Studies. Aiming for a better characterization of the transformation process, discrimination and quantification of the evolving $Ni(OH)_2$

phases of **1**D-**4**D during exposure to 1M KOH, Raman spectroscopic analysis was performed **(Figure 3.5, A3.25-A3.30)**. Pt modified quartz substrates were coated with the Ni-MOFs **1-4** in a similar fashion as done for the electrochemical characterizations of GC electrodes. At this point, we like to comment on the sharp, well separated band at ~3610 cm^{-1} found for in all pristine Ni-MOFs **1-4** (**Figure 3.5a-d**, t_D = 0 min) that, to the best of our knowledge was not previously discussed in the literature. The absence of this band in the Raman spectra of pure linkers (**Figure A3.31**) suggests its origin lies in the characteristic Ni-OH connectivity of the $[Ni_2(OH)_2L]$ structure, in line with typical ν(OH) stretching wavenumbers (3000−3800 cm^{-1}).[30-31] We synthesized the reference complex $[Ni(H_2O)_4NDC]$ to compare with NDC-MOF (**2**, $[Ni_2(OH)_2NDC]$) revealing ν(OH) at 3614 cm^{-1}. Compound $[Ni(H_2O)_4NDC]$ showed no band at ~3610 cm^{-1}, reinforcing the band attribution to a hydroxyl bridge ν(OH) present in $[Ni_2(OH)_2L]$ rather than belonging to Ni-H_2O scaffolds (**Figure A3.32)**.[32-34] The crystalline reference sample of BDC-MOF (**1**) featuring OH-groups solely coordinated at Ni(II) centers in a μ^3–OH mode reveals this band at 3613 cm^{-1}. Finally, the deuterium labelled sample $[Ni_2(OD)_2BDC]$ features a singular band at 2664.4 cm^{-1}, matching very well with the vibrational isotope shift expectation (**Figure A3.33)**. Thus, we firmly attribute the band at 3613 cm^{-1} to a stretching vibration of a characteristic μ^3–OH group bridging the Ni centers in all pristine MOFs **1-4**.[19]

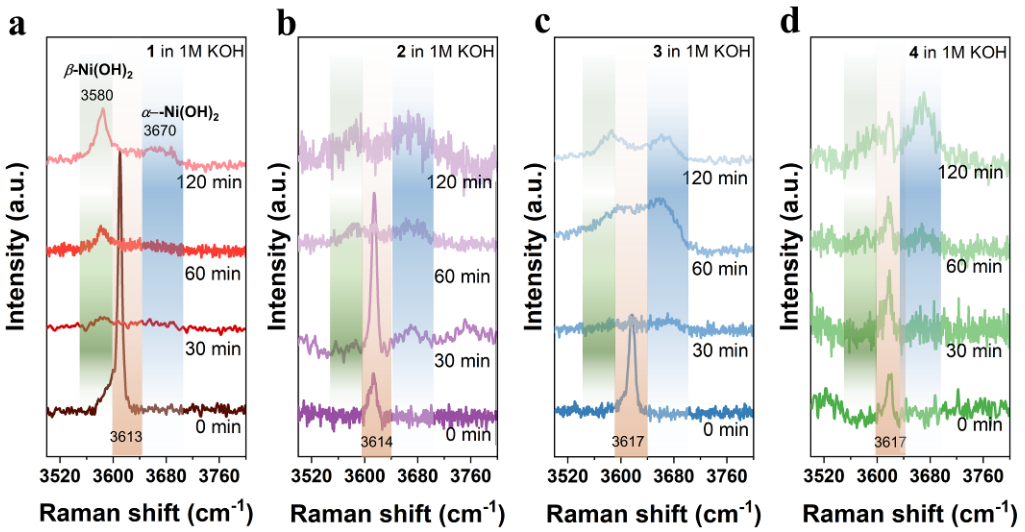

Figure 3.5. Raman spectroscopic monitoring of MOF derivation with different times t_D in Ar saturated 1 M KOH without potential. (a) **1**D, BDC; (b) **2**D, NDC; (c) **3**D, BPDC; (d) **4**D, TPDC. Green shadow refers to A_{1g} O-H stretch in β-Ni(OH)$_2$, the blue shadow refers to the respective O-H stretch in α-Ni(OH)$_2$; orange shadow refers to original μ^3–OH bond in MOFs' structure.

The first series of derivation experiments (1M KOH; t_D = 0, 30, 60, 120 min) were conducted without applying any potential, thus the conditions are identical to the derivation of the MOF powder samples monitored by PXRD as described above (**Figure 3.5**). Most MOF characteristic absorption bands originate from the phenyl rings and carboxylate groups of the linkers.[35,36] Overall, the intensities of these signals decreased with increasing t_D, a likely outcome of linker cleavage from Ni sites and leaching (**Figure A3.29**). The appearance of new broad peaks centered at 311(E_g) and 450 cm^{-1}(A_{1g}) characteristic for the Ni(OH)$_2$ phase also supported this reasoning (**Figure A3.25-A3.28**).[28,37] The MOF **1-4** characteristic μ^3–OH bridge signals at *ca.* 3610 cm^{-1}, discussed above, were found to be gradually replaced by a broad and noisy peak feature between 3550-3700 cm^{-1} for all MOF-derived samples **1**D-**4**D (**Figures 3.5**). Upon increasing t_D, this feature evolved into an intense sharp band at 3580 cm^{-1} and a small broad band at ~3670 cm^{-1}. The former has been reported as a characteristic A_{1g} O-H stretch for β-Ni(OH)$_2$, whereas the latter is

characteristic for related O-H stretch of disordered α-Ni(OH)$_2$.[28,29,37] Profound differences can be observed among the series' samples (**Figures 3.5** and **A3.34**). Clear signals of ordered β-Ni(OH)$_2$ can be noted for BDC-MOF derived **1**D after 30 min of KOH exposure, yielding a β-Ni(OH)$_2$:α-Ni(OH)$_2$ ratio of 1.2 obtained by peak integration and assuming the same oscillator strengths (**Figures 3.5a** and **A3.34a**). For BPDC-MOF derived **3**D, the α-Ni(OH)$_2$ Raman band at 3660 cm^{-1} appears first, within 30 minutes, with a β-Ni(OH)$_2$:α-Ni(OH)$_2$ ratio of 0.8 (**Figures 3.5c** and **A3.34c**). NDC-MOF derived **2**D and TPDC-MOF derived **4**D undergo slow conversion and most interestingly resulting in the exclusive appearance of α-Ni(OH)$_2$ peak after 30 min (**Figures A3.34b** and **A3.34d**) and a delayed emergence of the β-Ni(OH)$_2$ peaks. These observations suggest a linker kinetic influence on the formation of α-Ni(OH)$_2$ *vs*. β-Ni(OH)$_2$ phases. NDC and TPDC linkers appear to induce preference of α-Ni(OH)$_2$ over β-Ni(OH)$_2$ formation. For example for TPDC-MOF derived **4**D, at t_D = 120 min, the phase ratio was β-Ni(OH)$_2$:α-Ni(OH)$_2$ = 0.52. Correspondingly, for example, TEM imaging demonstrate higher ordering (crystallinity) of Ni(OH)$_2$ phases of **1**D *vs.* **3**D after a 30 min 1M KOH treatment (**Figures A3.35-A3.36**). Combining with the time-dependent changes in the XRD pattern discussed above, this trend within the series of linkers is also in agreement with stability trend.

Next, we investigated the joint impact of substrate polarization in 1M KOH electrolyte through exposing the samples to an anodic pre-OER potential of 1.17 or 1.37 V *vs*. RHE (*i.e.* 0.2 V or 0.4 V *vs.* Hg/HgO) for t_D = 30, 60 and 120 min (**Figures A3.24**). The effects were comparable for all MOFs. Increasing anodic potentials accelerated the conversion process as reflected in increased prominence of the characteristic β-Ni(OH)$_2$ peak at 3580 cm^{-1}.[37,38] All these observations are in line with the gradual leaching of linkers from MOFs towards formation of Ni(OH)$_2$ phases during an aging process induced by alkaline electrolyte and substrate polarization, resulting in a rearrangement of the associated bond lengths and angles

of the derived $Ni(OH)_2$ phases towards more ordered β-$Ni(OH)_2$ structures as deduced from the PXRD studies discussed above. In summary, the MOF stability and resiliency trends were confirmed by the Raman studies. The data show that an increased MOF structural stability under alkaline (electro-) conditions correlates with the preferred formation of the α-$Ni(OH)_2$ and the delayed formation of the β-$Ni(OH)_2$ phases. The Ni-MOF bulk materials' aging process can be delayed or may be inhibited if suitable linkers are found.

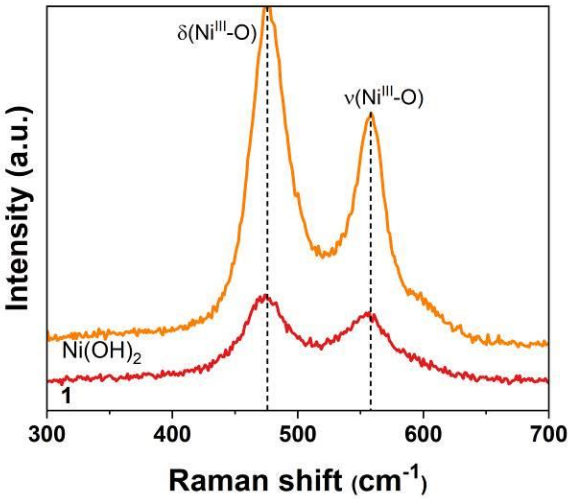

Figure 3.6. Raman spectras' characteristic section of Ni-O vibrations for the α/β-$Ni(OH)_2$ type material derived from BDC-MOF (**1**, $[Ni_2(OH)_2BDC]$; red trace) after 30 CV-cycling in 1M KOH compared with a β-$Ni(OH)_2$ reference material (orange trace) treated in the same way (see also **Figures A3.37-A3.39**).

Recently, most density functional theory (DFT) studies ignored the intrinsic instability of carboxylate-linker based MOFs and the derived process, and adopted a model based on the unchanged MOF structure in which the adsorbed OH^- coming from the electrolyte are additionally binding to Ni-sites and are the active sites to explain the better OER activity of the MOF as compared to the $Ni(OH)_2$ reference. However our results suggest that even in cases of comparably stable and slow conversion of MOFs at least the interface of the MOF-derived electrocatalyst coating to the electrolyte most likely will be a metal hydroxide, specifically a $Ni(OH)_2$ phase

mixture as we described above. Monitoring the Raman shifts of Ni^{III}-O in ^{18}O-labelled and ^{16}O-labelled alkaline electrolytes during CV, Hu *et al*. suggested that the lattice oxygen atoms are the active sites for Fe-free $Ni(OH)_2$ (**Figure A3.40**) whereas the surface adsorbed hydroxyls of the Fe-doped Ni-oxohydroxides are the active sites, with however unchanged Raman features of the Ni^{III}-O.[39] We compared the Raman spectra for $[Ni_2(OH)_2BDC]$ (**1**) and the Raman spectra of a reference sample □-$Ni(OH)_2$ after CV-testing in 1M KOH (**Figure 3.6, A3.41-A3.42**). After CV-cycling, all the MOF peaks for all samples disappeared with the occurrence of the two new Ni^{III}-O vibration modes at ~480 and ~560 cm^{-1} that are characteristic for the catalytically active NiOOH material.[39,40]

Furthermore, the Raman analysis of the other samples derived from MOF **2-4** indicate that the conditioning process (electrochemical activation) results in the full transformation of Ni-MOFs to $Ni(OH)_2$/NiOOH (**Figure A3.12**). However, the data of **Figure 3.3** reveal that the initial MOF structure, specifically the choice of the linker, still has a discernible impact on the OER activity. The chronopotentiometry tests (**Figure A3.43**) corroborate the result that the choice of linkers and their coordination with the Ni centers in the MOF has a lasting impact even after the complete MOF 'metamorphosis' to $Ni(OH)_2$/NiOOH. We suggest to name this phenomenon a 'linker memory effect' on the OER. Our results, as illustrated in **Figures 3.3** and **A3.16- A3.18**, indicate that the 'linker memory effect' becomes weaker over time, revealing that the choice of linker could delay the reconstruction process of Ni-MOF, but cannot prevent it and nevertheless impacts the abundance of ordered vs. disordered $Ni(OH)_2$/NiOOH phase (correlated with α/β-$Ni(OH)_2$ ratio as discussed above).

3.3 Conclusion

Catalyst or precursor? What role does MOF's structure play? Built upon an unambiguous case of MOF instability and using a prototypical, isoreticular Ni-MOFs family of carboxylate linker-length variation, we investigated their conversion into

active α/β-$Ni(OH)_2$ phases, NiOOH species respectively, under the alkali treatment and typical OER electrochemical conditions. Time-resolved PXRD data reveal different steps of the Ni-MOF metamorphosis. The corresponding Raman spectra establish that different Ni hydroxide phases are obtained after varying KOH treatment durations and the choice of linkers can decelerate Ni-MOF intermediates' aging and transformation into the α/β-$Ni(OH)_2$ phase mixture. The Ni-MOFs gradually transform to hydroxides by the cleavage of the Ni carboxylate coordination bond and the substitution by incoming hydroxide. The (100) and (101) oriented crystal planes were identified to undergo structural reconstruction first. Electrochemical testing demonstrated the MOFs' pristine structures could affect OER performance of the samples and even keeping disparity after long-term alkali-treatment and polarization, attributed to transformation kinetics from disordered α-$Ni(OH)_2$ to ordered β-$Ni(OH)_2$ under OER conditions. Our data highlight the coexistence of pristine Ni-MOF with intermediates and derivatives on the way towards the linker-free $Ni(OH)_2$ phase mixture. It is thus rather difficult to predominantly attribute OER performances to the pristine Ni-MOF structure without very specific definition of conditions (e.g. pH, applied potential, time) and deconvolution of the contribution of coexisting phases and the bulk from the surface (interface). Different from the idealized, pristine Ni-MOFs, the surface of the actual derived α/β-$Ni(OH)_2$ is likely non-uniform, and different distributions of active sites may cause the observed differences in the OER activities over derivation time and as well depending on the sample conditioning. The substitution of linkers by hydroxide and the structural reorganization may introduce possible strain (and disorder), which affects the overall activity of the derived material. This explains why the series of $[Ni_2(OH_2)L_2]$ (**1**-**4**) with different linkers yield different OER activities. Essentially, the formation of the actual catalytically relevant species is a kinetic phenomenon which depends heavily on the MOF-structure. From our data we conclude, that it is essentially the β:α-ratio of the $Ni(OH)_2$ material derived from the Ni-MOFs during

the activation and under OER conditions which is responsible for the differences we observe. It is thus an indirect effect of the linkers and not a direct, coordinating effect to the Ni sites. The OER characteristics tun out to be correlated with the different kinetics of the Ni-MOF reconstruction to the β/α-$Ni(OH)_2$ phases over time, caused by the different linkers and the conditions (i.e. alkaline electrolyte with or without potential and time). Interestingly, the nature of the β/α-$Ni(OH)_2$ phase mixture derived from Ni-MOFs differ in systematic fashion and the differences in the β:α ratio correlate with the choice of the linker. The slower the conversion the higher abundance of the α-$Ni(OH)_2$ phase and the better the OER performance.

The selection of a linker is a crucial determinant of the structure and the stability of MOFs, and thereby can impact the MOF reconstruction process under OER conditions. The entanglement of thermodynamic and kinetic factors influences MOFs stabilities. Generally, the more basic the linker (pK_a) and the higher the charge of the metal ion, the more stable the MOF will be. Other factors, including topology (connectivity of linkers and metal ion nodes), porosity (diffusion of reactants, electrolyte), hydrophilicity/hydrophobicity, linker π-π stacking (contributions to the lattice energy besides metal-linker bond energy), steric/coordinative shielding of metal-linker bond (kinetic stabilization), and MOF particle morphologies also affect stability.[41] For a given metal ion, the selection of linkers can alter MOF topologies and other factors leading to a diverse range of systems. Our data indicate that a more stable MOF which would not allow leaching of linkers and predominantly features coordinatively saturated metal ion sites is likely to be electrocatalytically less active as compared to a MOF-derived metaloxo/hydroxo phase. Essentially, MOF activation means loss of linkers, at least at the MOF/electrolyte interface. Our data and discussion may contribute to the controversy about carboxylate-linker based MOFs behaving as electrocatalysts and/or as precursors towards the catalytic species and may advance the understanding of MOF compositions' influence on electrocatalysts

and may stimulate ideas to obtain advanced water oxidation electrocatalysts inspired by the materials chemistry of MOFs.[42,43]

3.4 Appendix

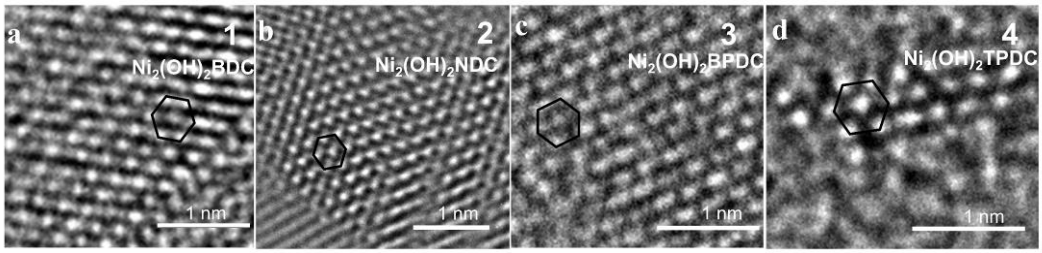

Figure A3.1. HRTEM images for MOF 1-4 of general formula [$Ni_2(OH)_2L$] (**1**, L = BDC; **2**, L = NDC; **3**, L = BPDC; **4**, L = TPDC). (a) BDC-MOF (**1**), (b) NDC-MOF (**2**), (c) BPDC-MOF (**3**), (d) TPDC-MOF (**4**).

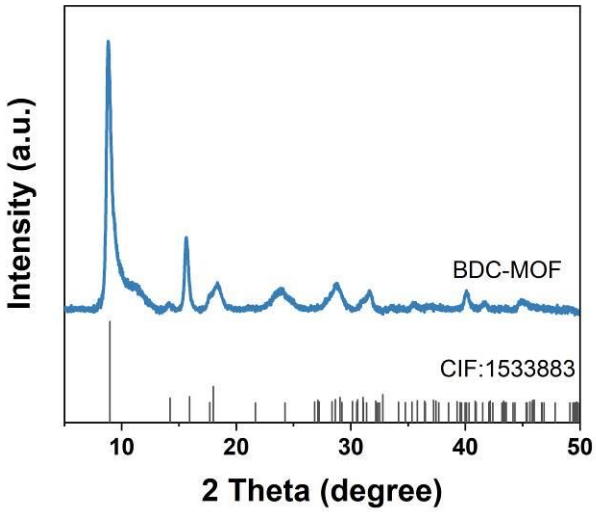

Figure A3.2. XRD pattern of MOF **1**(BDC-MOF) and CIF: 1533883.[19]

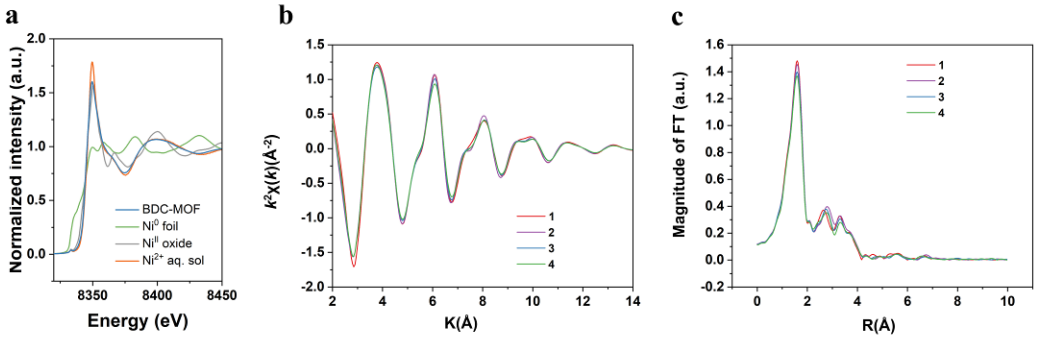

Figure A3.3. (a) Ni K-edge XAFS data of all four Ni-MOF samples **1-4** (a) Ni K-edge XANES data of Ni-BDC-MOF and reference samples, (b) and (c) Fourier transformed EXAFS spectra of the Ni-MOFs **1-4**. The similar intensity of edge peaks

in XANES and Ni K-edge $k^2\chi$ data of EXAFS oscillations indicate an identical nature of coordination environment and structure in all the MOFs

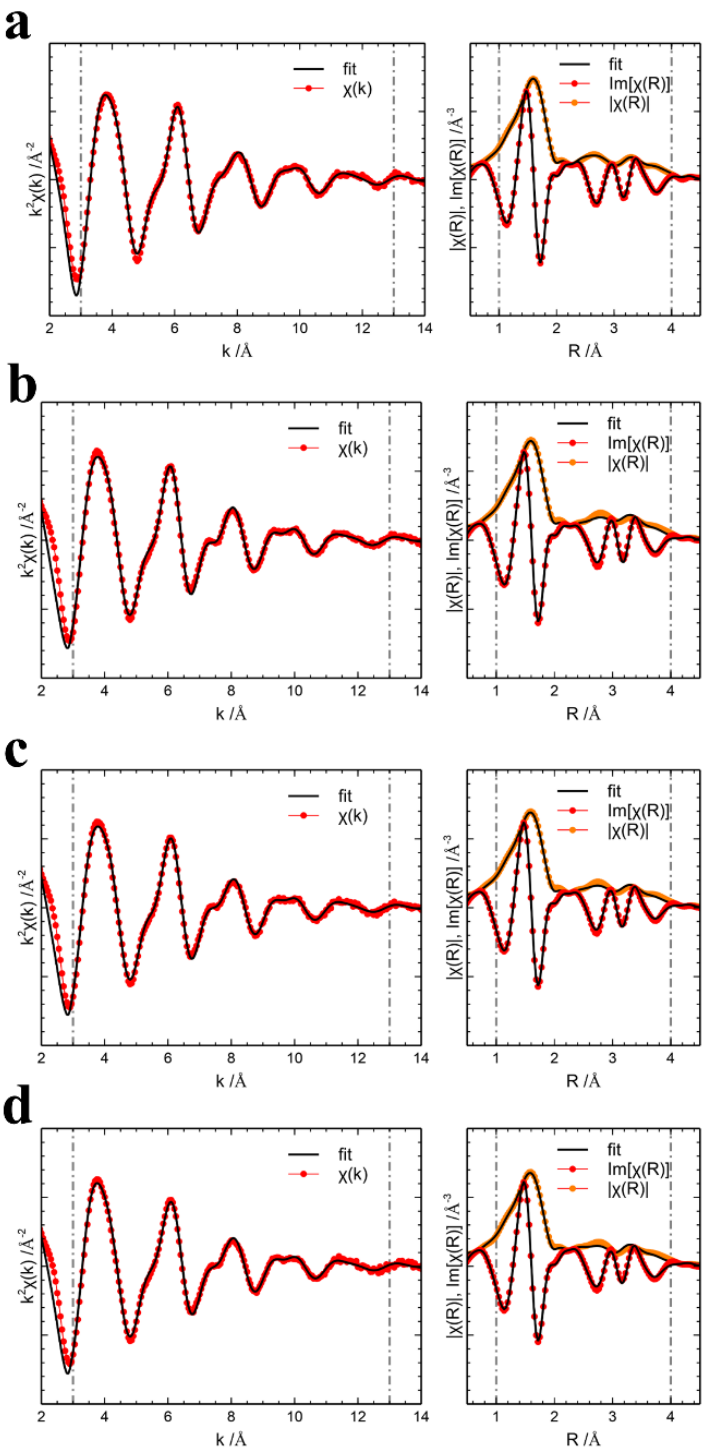

Figure A3.4 Ni K-edge XAFS data and Fourier transformed EXAFS spectra of (a) **1**, (b) **2**, (c) **3**, (d) **4**. The fitting parameters were shown in supplemental Table A3.1.

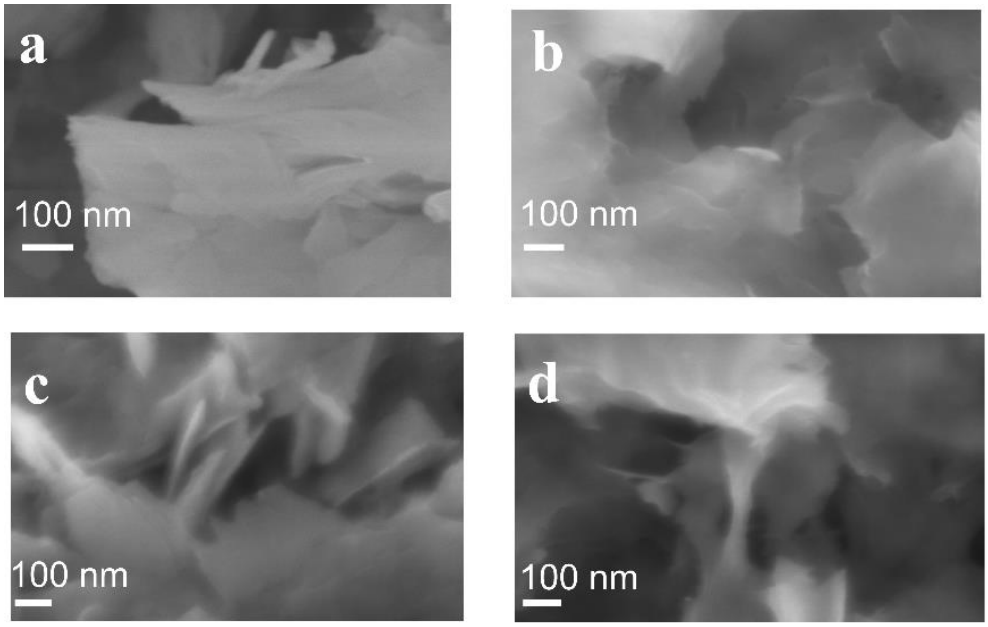

Figure A3.5. FESEM images of (a) BDC-MOF (**1**), (b) NDC-MOF (**2**), (c) BPDC-MOF (**3**), (d) TPDC-MOF (**4**), showing comparable morphology between all Ni-MOFs. Such similar thin film morphology, less prone to bulk effect, will further enable the correlation of the electrochemical performance and the MOF structures.

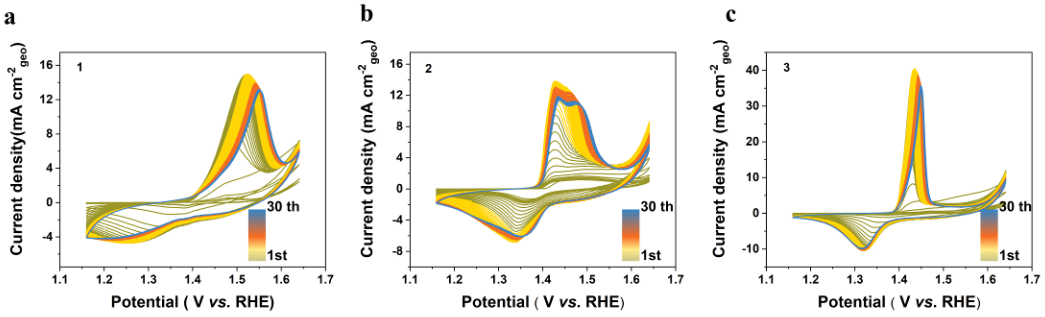

Figure A3.6. Continuous cyclic voltammograms study of the pre-catalytic conditioning process (a) **1**, (b) **2**, (c) **3** for 100 cycles at a scan rate of 20 mV s^{-1} in 1 M KOH. Prolonged experiments of Figures 3.2a, 3.2b and 3.2c, respectively.

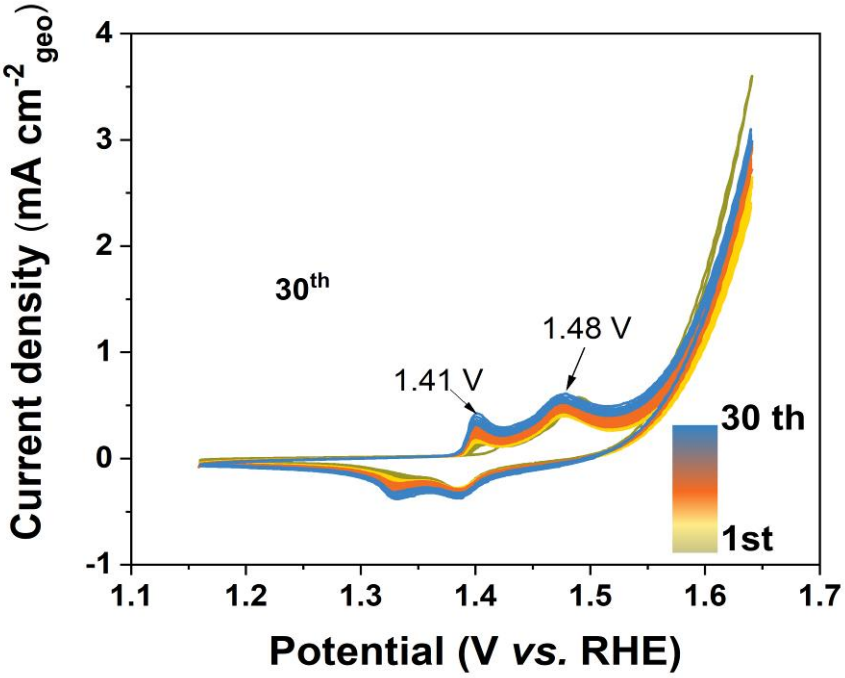

Figure A3.7. Continuous cyclic voltammograms study of the pre-catalytic conditioning process of TPDC-MOF (**4**) about 30 cycles at a scan rate of 20 mV s^{-1} in 1 M KOH, showing the slow growth of a new oxidation wave at 1.41 V *vs.* RHE, alongside the original at 1.48 V vs. RHE.

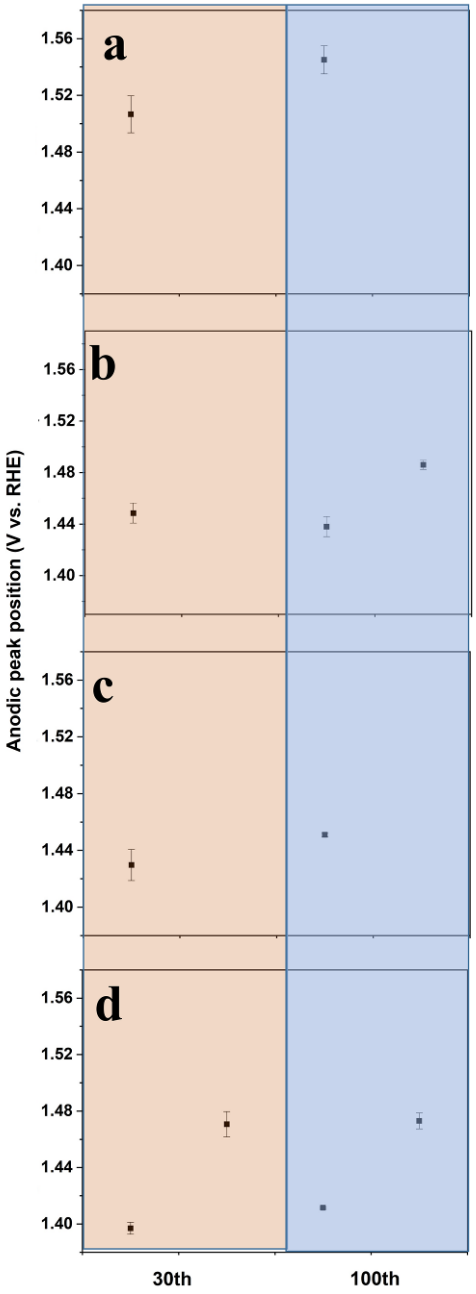

Figure A3.8. Anodic peak potentials after continuous cyclic voltammograms for MOF **1**-**4** (a) **1**, (b) **2**, (c) **3** and (d) **4** at 30th and 100th cycle with a scan rate of 20 mV s^{-1} in 1 M KOH. Values and error bars were showed minimal discrepancies in the peak position values. Differences are observed across the four MOFs as the main anodic peak is shifted towards more negative potentials after 30 cycles, as the ligand length increase within the series. Further cycling resulted in slightly anodically shifted waves or replaced by processes occurring at higher potentials.

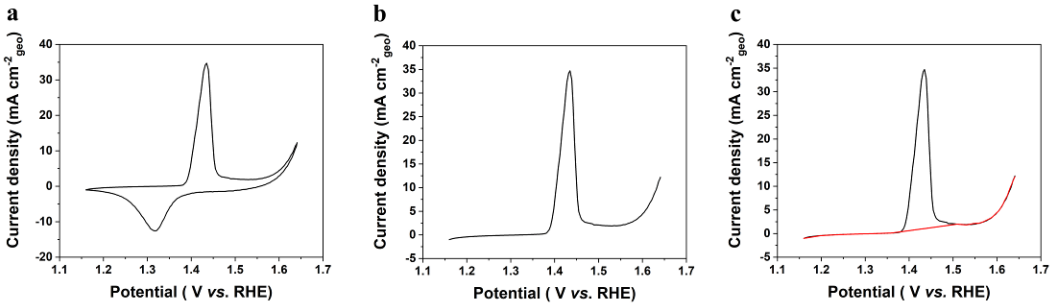

Figure A3.9. Example of CV fitting. (a) CV plot of the 30th cycle for the **3**, BPDC-MOF, (b, c) Anodic region of CV plot with background baseline.

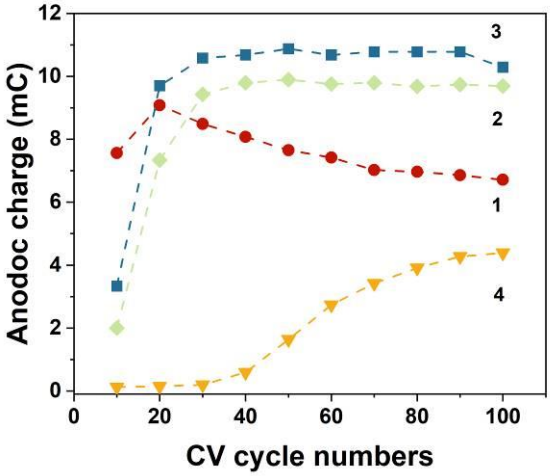

Figure A3.10. Charge of anodic charge (Q_{anodic} peak) for Ni-MOFs **1-4** with cycle number in precatalytic process according to CV data at a scan rate of 20 mV s^{-1} in 1 M KOH. Q_{anodic} peak= Area anodic peak /Cycling speed.

To facilitate interpretation, CV plots (using **3** of **Figure 3.2c** as an example) for the anodic peaks were deconvoluted to integrate the peak charge changes after cycling (detailed integration steps shown in (**Figure A3.9**). The anodic charges (Q) reach maximum and get stabilized after 20 to 30 cycles at ~ 8.49, ~ 9.42 and ~ 10.58 mC for **1**, **2** and **3**, respectively (**Figure A3.10 and Figure A3.6**), whereas Q stabilizes only after 90 cycles for TPDC-MOF (**4**) with 4.27 mC. This alludes to relatively slower conversions in **4** (**Figure 3.2d)**.

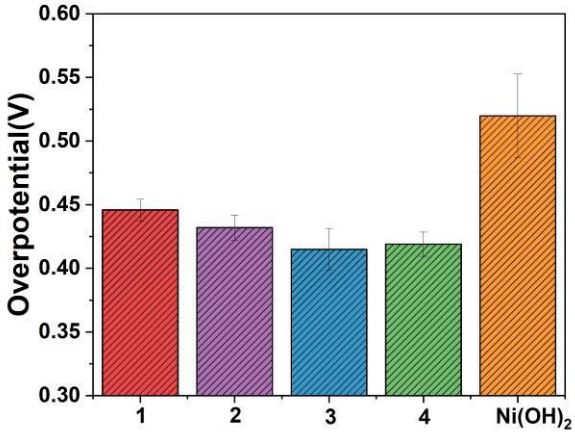

Figure A3.11. OER activities of electrocatalyst samples derived from MOF 1-4 color code refers to the various linkers: **1**, *red* (BDC); **2**, *violet* (NDC); **3**, *blue*, (BPDC); **4**, *green* (TPDC). Overpotential required for a current density of 10 mA cm^{-2} after CV precatalytic conditioning about 30 cycles for **1**-**3** 100 cycles for 4, and β-$Ni(OH)_2$.

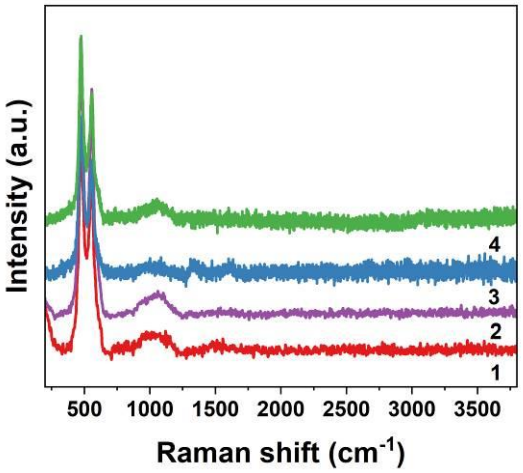

Figure A3.12. Raman spectra of MOF **1-4** after sample conditioning process (activation) by cyclic voltammetry (CV) from 1.16 to 1.64 V vs. RHE electrode for 30 cycles for MOF **1-3** (BDC, BPDC, NDC, -MOF), and 100 CV cycles for MOF **4** (TPDC-MOF).

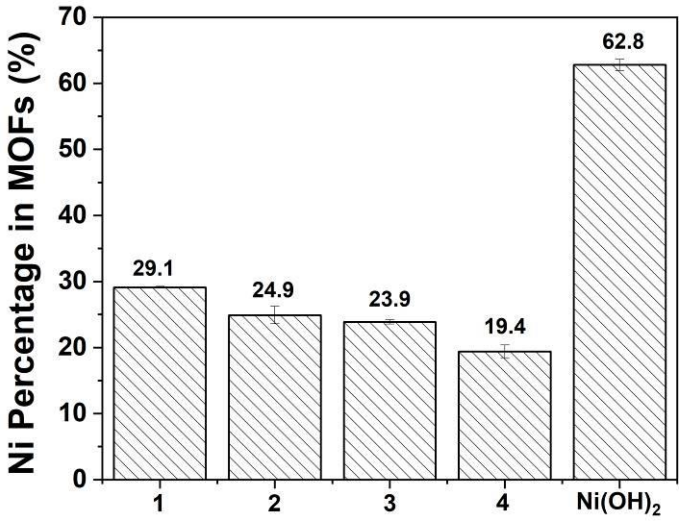

Figure A3.13. Experimental Ni ratio (weight %) in pristine Ni-MOFs **1-4** (BDC, NDC, BPDC, TPDC) and $Ni(OH)_2$ derived from ICP-OES data. Assuming the formula $[Ni_2(OH)_2L]$, the calculated mol% of Ni are: 24.5% (**1**) 20.2% (**2**) 18.6% (**3**) 15.0% (**4**) and 63.3% for $Ni(OH)_2$.

To decrease sluggish diffusion in large bulk samples and concentrate on the initial structure effect, the synthesized approach here may cause more incoordination Ni atoms with tiny miss-linker defects than the large bulk hydrothermal condition. Accordingly, the Ni ratio here is higher than theoretical calculation.

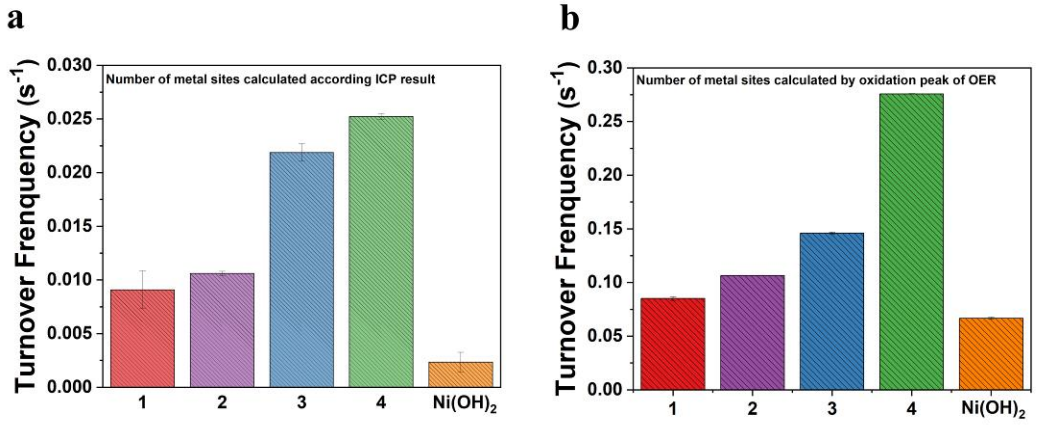

Figure A3.14. TOFs of MOFs (**1-4**) derived electrocatalyst samples. Colour code refers to the linkers. **(a)** TOFs calculated using the Ni sites numbers according to the ICP-OES results of pristine Ni-MOFs (**Figure A3.13**). **(b)** TOFs calculated the Ni sites numbers according to the oxidation peak area analysis of OER. TOFs obtained from the OER peak analysis are one order of magnitude higher than TOFs obtained

from the overall Ni content. Only the surface exposed Ni-sites may contribute to the TOF and the Ni sites in the bulk may not.

The TOFs were determined using the formula:

TOF = (j × A)/(4F × n), where j × A(surface area of GC electrode) denotes the current at an overpotential of 400 mV and n represents the number of moles of Ni deposited at the GC electrode.

Taking the BDC-MOF (**1**) according to the ICP-OES results as an example, the surface area of GC electrode (A) is 0.196 cm^{-2}, the current density (j) at an overpotential of 400 mV, then the current (j × A) =0.868 mA.

For preparation of the active materials on GC electrode, there are 5×10^{-2} mg MOFs on the electrode, and about 0.0146 mg Ni elements (n=2.479×10^{-4} mmol) on the substrate according to ICP-OES data in **Figure A3.13**. Faraday constant F =96485.3321 s A / mol. As the result of TOF_{Ni} for BDC-MOF (**1**): TOF ≈ 0.0091 s^{-1}.

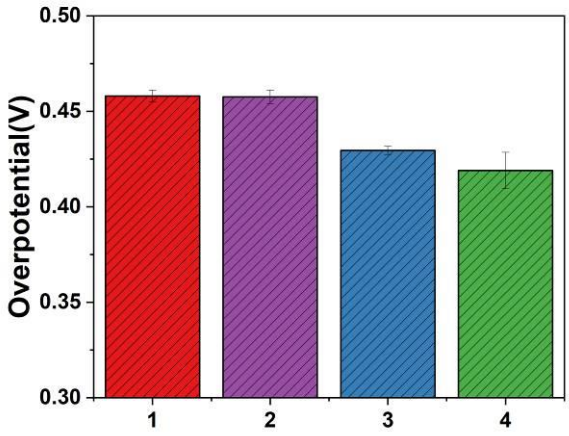

Figure A3.15. OER overpotential of MOF **1-4** after 100 cycles of activation process.

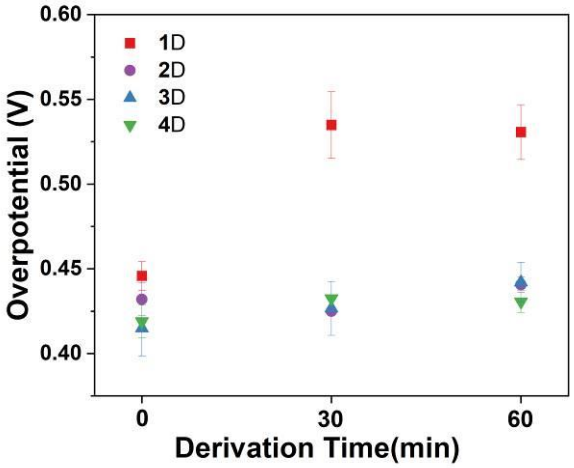

Figure A3.16. Overpotential of the MOF (**1**-**4**) derived electrocatalyst samples (**1**D-**4**D) on GC electrode after immersing in 1M KOH electrolyte with for 0 min, 30min, 60min without applying potential before CV-cycling.

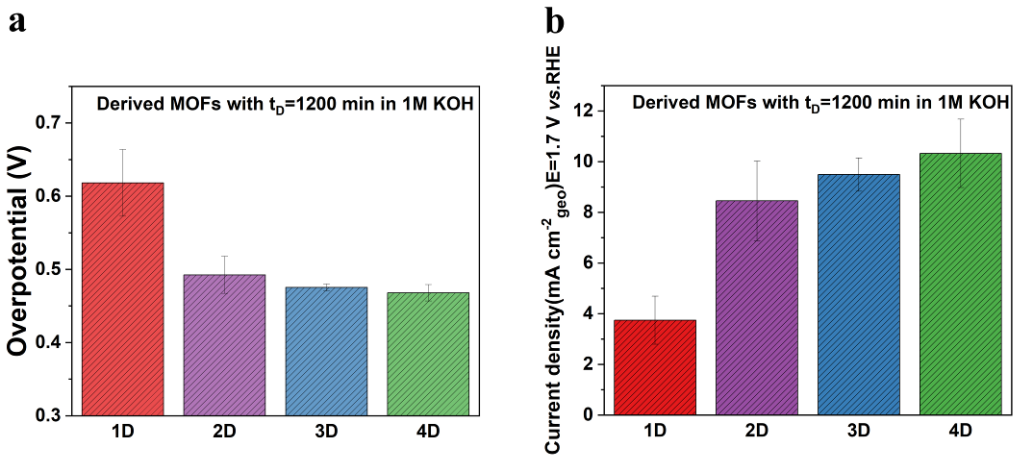

Figure A3.17. (a) Overpotential of MOF-derived electrocatalyst samples (**1**D-**4**D) on GC electrode after immersing in 1M KOH electrolyte for 1200 min before CV-cycling. (c) Current densities of derived MOFs (**1**D-**4**D) upon immersing Ni-MOFs in 1 M KOH for 1200 min taken at E = 1.7 V *vs.* RHE.

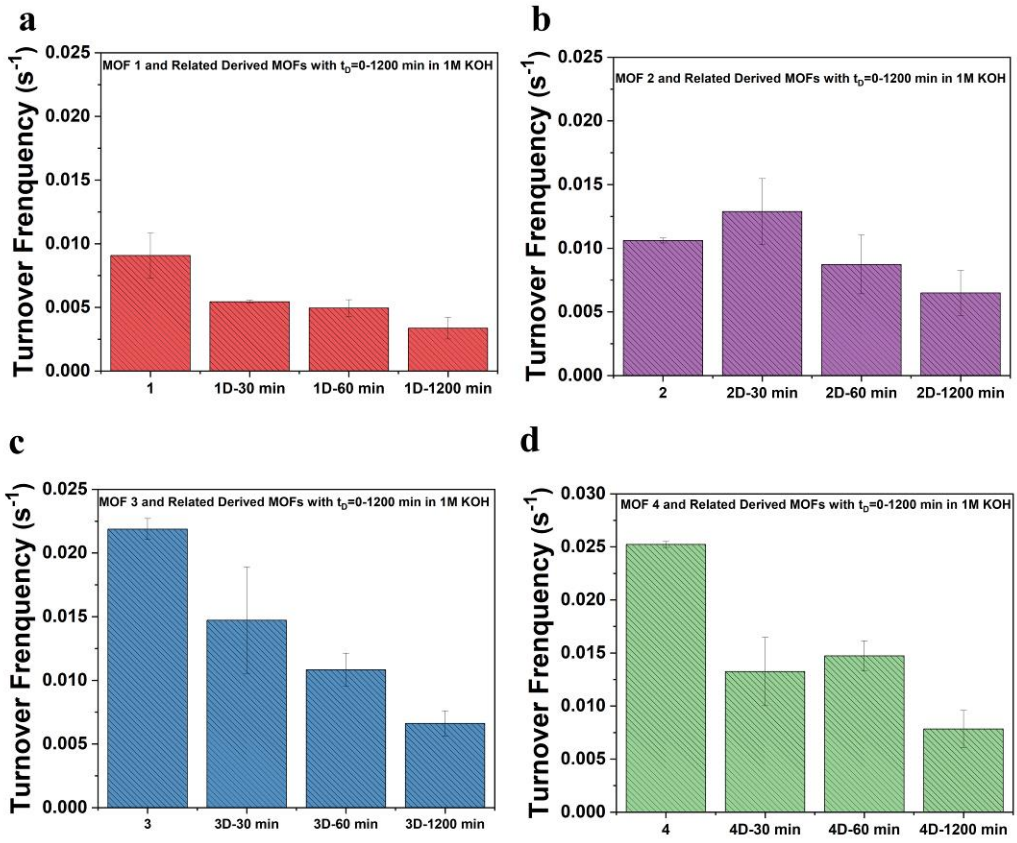

Figure A3.18. TOFs of the MOF-derived electrocatalyst samples (**1**D-**4**D) on GC electrode after immersing in 1M KOH electrolyte for 0-1200 min before CV-cycling, calculated the Ni sites numbers according to the ICP-OES results of Ni-MOFs with the same method as **Figure A3.13**.

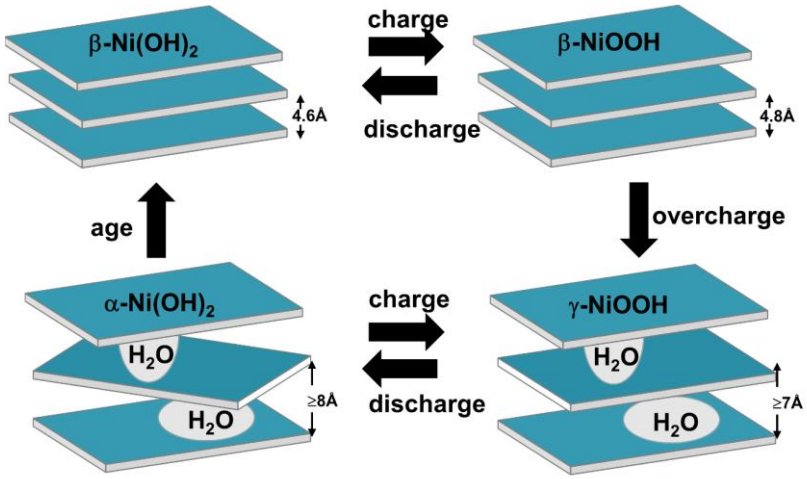

Figure A3.19. Bode scheme for the transformation of $Ni(OH)_2$/NiOOH with different phase.[27] The α-Ni(OH)2 phase is reported as a disordered phase, whereas the

more ordered β-$Ni(OH)_2$ phase is described. Bode scheme describes the transformations among the phases during OER process, in which the Ni oxidation state changes from $Ni(OH)_2$ to NiOOH or from NiOOH to $Ni(OH)_2$.

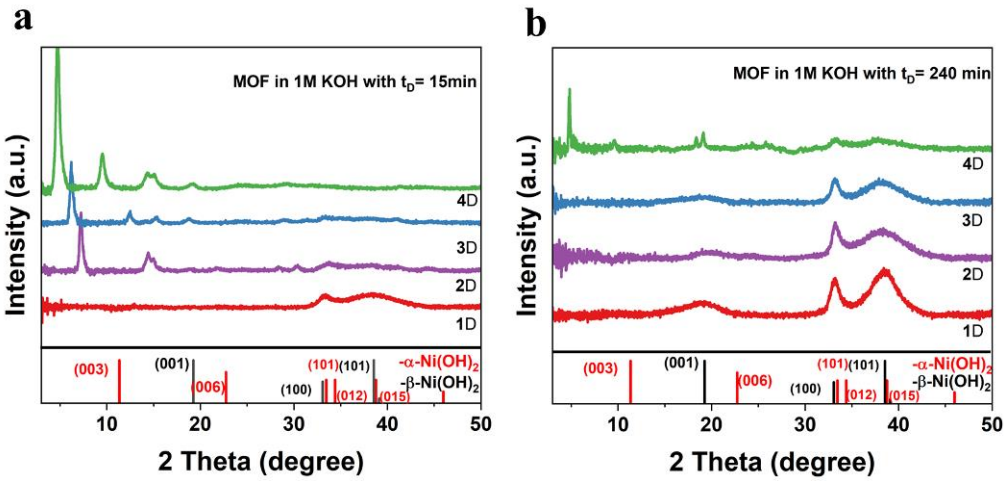

Figure A3.20. Monitoring structural transformation during MOF derivation in alkaline electrolyte solution as function of the linkers: (a) 15 min; (b)240 min. Time-dependent powder X-ray diffractograms were taken after subjecting micro-crystalline bulk samples of MOFs **1-4** to 1 M KOH without potential (derivation time:15 and 240 min).

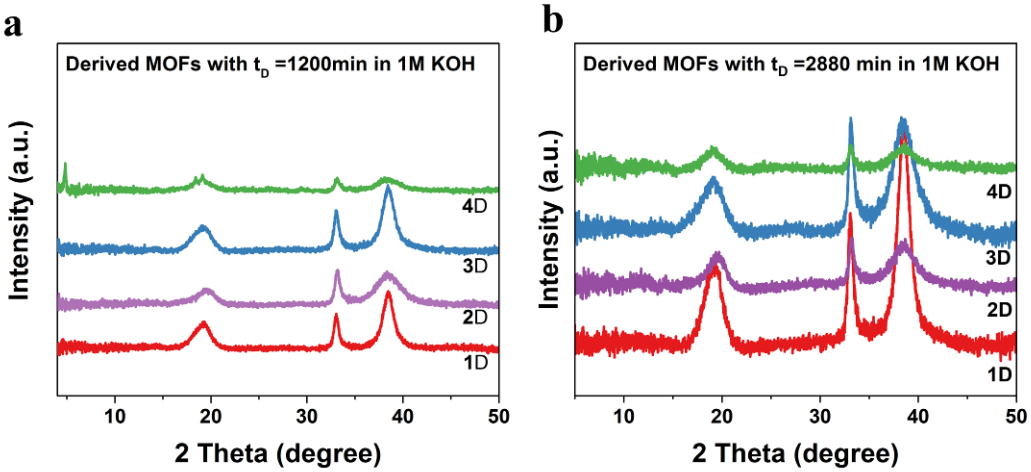

Figure A3.21. X-ray diffractograms for MOF 1D-4D after immersing in 1M KOH for (a) 20h. (b) 48h

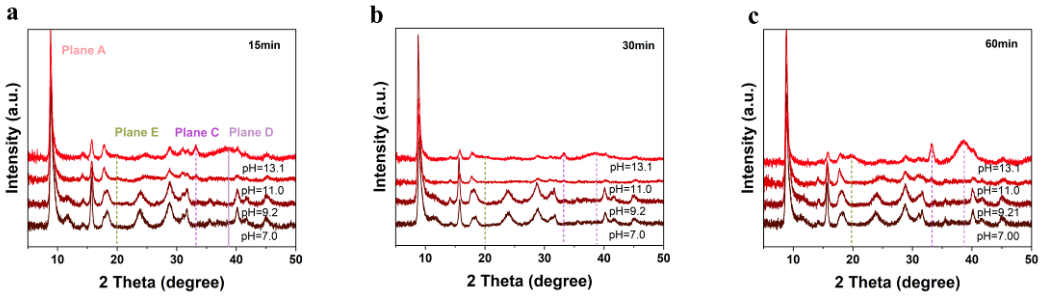

Figure A3.22. Monitoring structural transformation of MOF **1** (BDC-MOF) in electrolyte solutions of pH = 7.0-13.1 without applied potential: Powder X-ray diffractograms taken at (a) 15 min; (b) 30 min and (c) 60 min derivation time (t_D). Standard buffer (Mettler Toledo) pH: 7.0, 9.2, and 11.0; the pH 13.1 was obtained by diluting 1M KOH (purified, pH =14.0) to 0.1 M and measured by a pH meter.

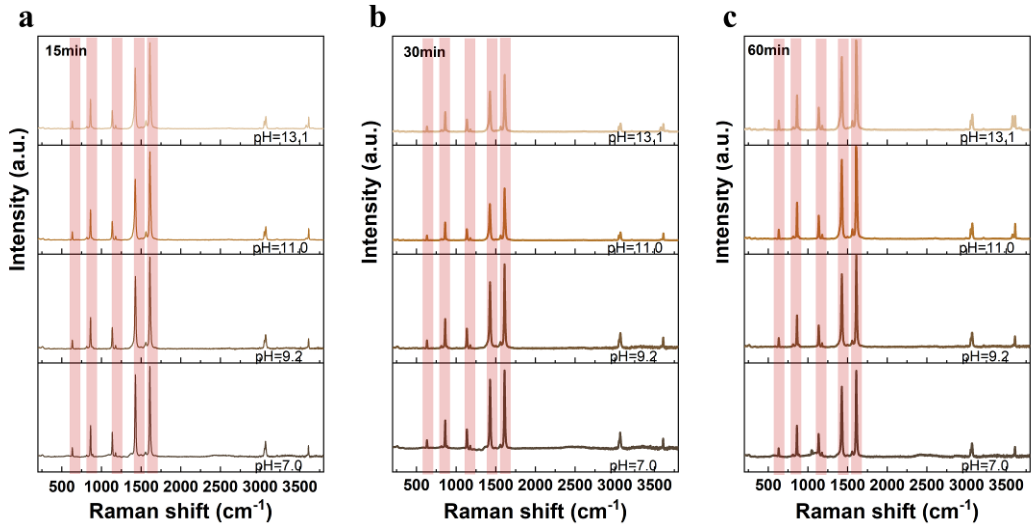

Figure A3.23. pH effect for structural transformation of MOF **1** (BDC-MOF) in electrolyte solutions of pH = 7.0-13.1 without applied potential: Raman spectra taken (a) 15 min; (b)30 min and (c) 60 min derivation time (t_D). Standard buffer (Mettler Toledo) pH: 7.0, 9.2, and 11.0. The pH 13.1 electrolyte was obtained from diluting 1M KOH (purified, pH =14.0) to 0.1 M and measured by a pH meter. Red area: peaks of BDC-MOF.

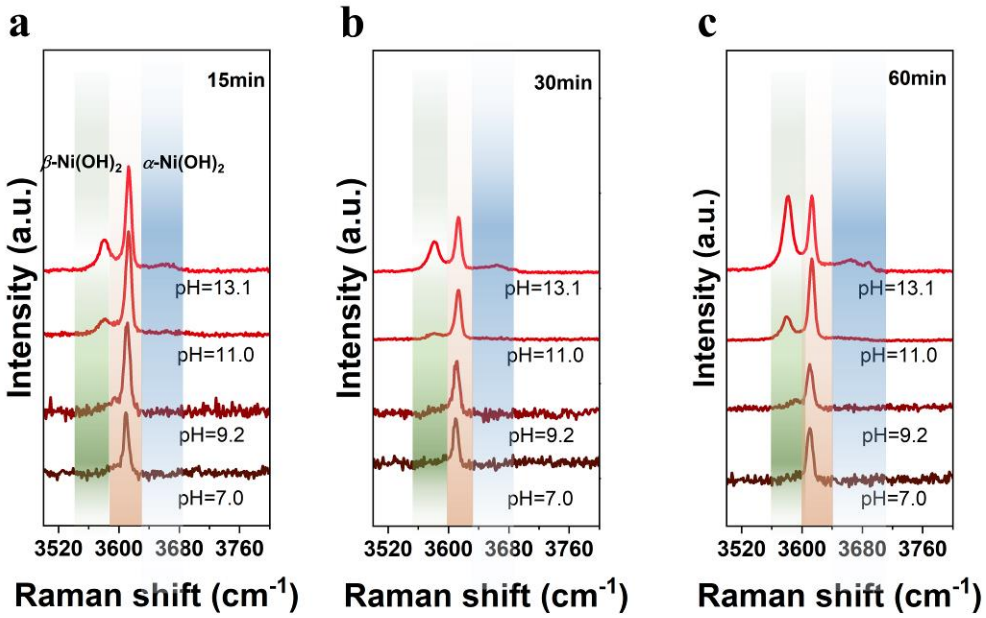

Figure A3.24. pH effect for structural transformation of MOF **1** (BDC-MOF) in electrolyte solutions of pH = 7.0-13.1 without applied potential: Raman spectra taken (a) 15 min; (b)30 min and (c) 60 min derivation time (t_D). Here, we display the characteristic section of the μ^3-(OH). Green shadow refers to A_{1g} O-H stretch in β–$Ni(OH)_2$, the blue shadow refers to the respective O-H stretch in α-$Ni(OH)_2$; orange shadow refers to the original μ^3–OH bond in MOFs' structure. More detailed explanation for μ^3-(OH) peak can be found in the **Figure A3.31 -A3.33**. Even at pH = 9.2, MOF **1** is not stable. A shoulder characteristic for β-$Ni(OH)_2$ is emerging after t_D = 60 min.

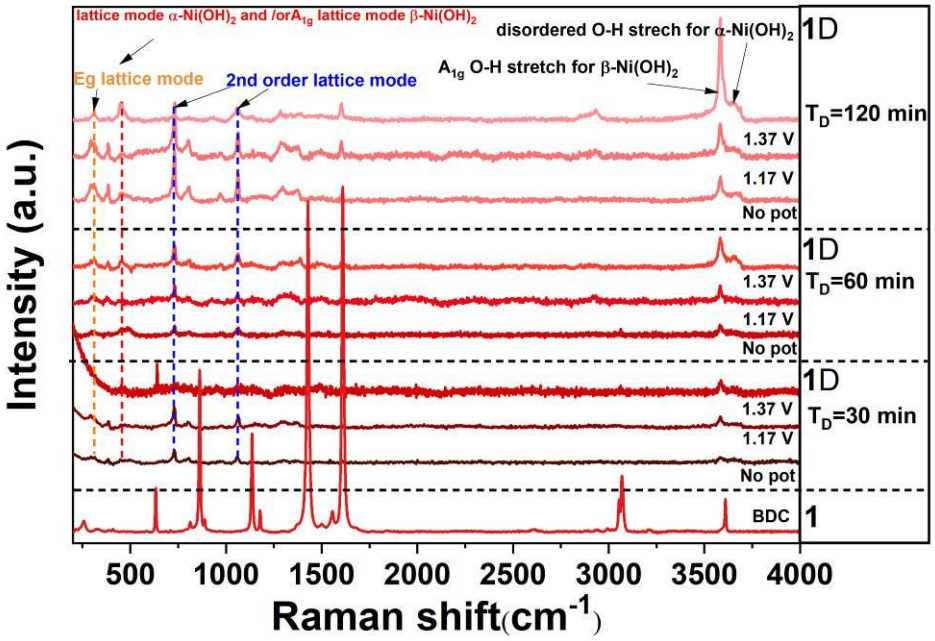

Figure A3.25. Raman spectra of **1**, the BDC-MOF, and the derived MOF 1D coated on Pt modified quartz under various potentials and immersion times from 30-120 min in 1 M KOH electrolyte. Potentials are refenced against RHE.

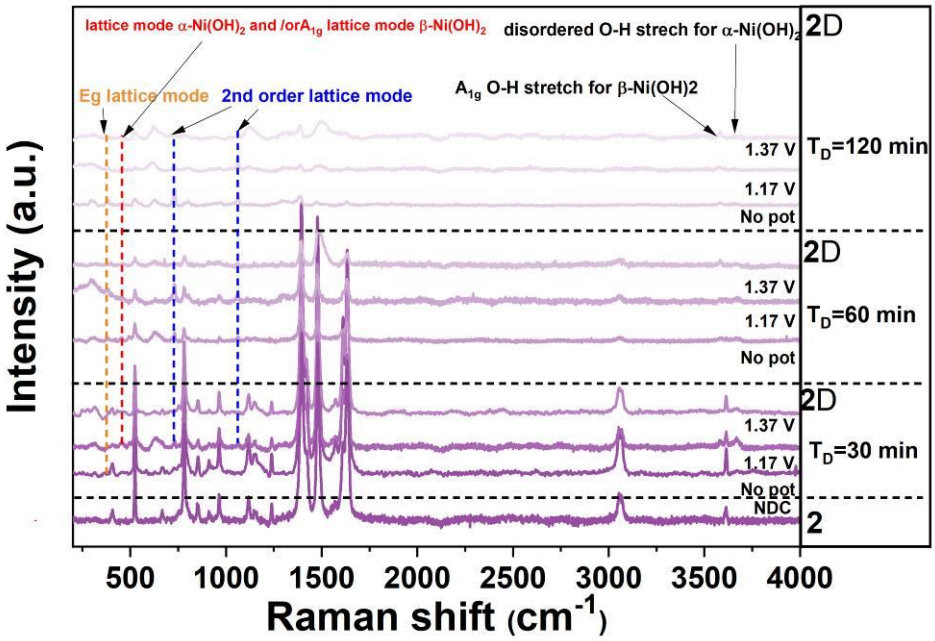

Figure A3.26. Raman spectra of **2**, the NDC-MOF, and the derived MOF **2**D coated on Pt modified quartz under various potentials and immersion times from 30-120 min in 1 M KOH electrolyte. Potentials are refenced against RHE.

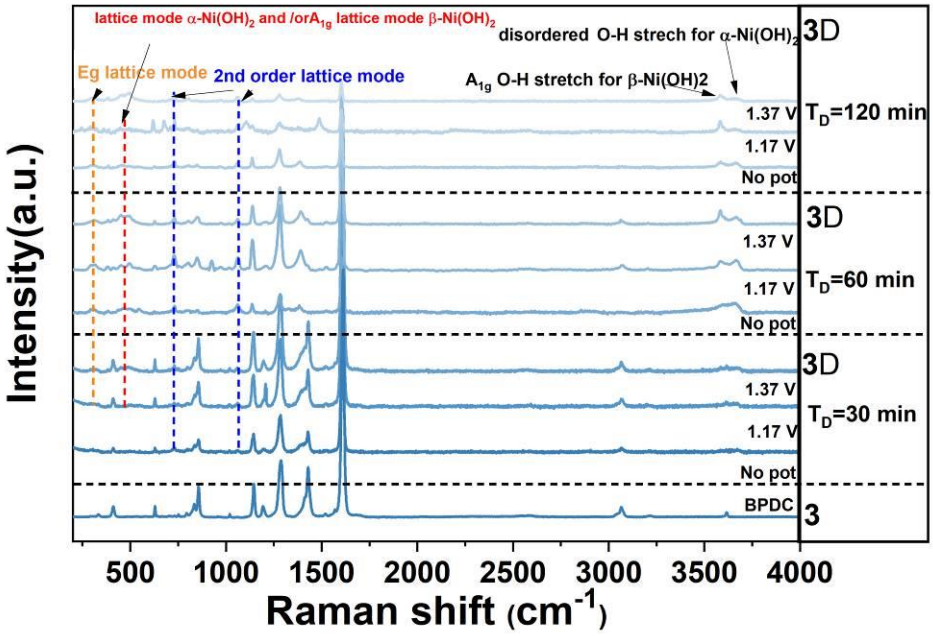

Figure A3.27. Raman spectra of **3**, the BPDC-MOF, and the derived MOF **3**D coated on Pt modified quartz under various potentials and immersion times from 30-120 min in 1 M KOH electrolyte. Potentials are refenced against RHE.

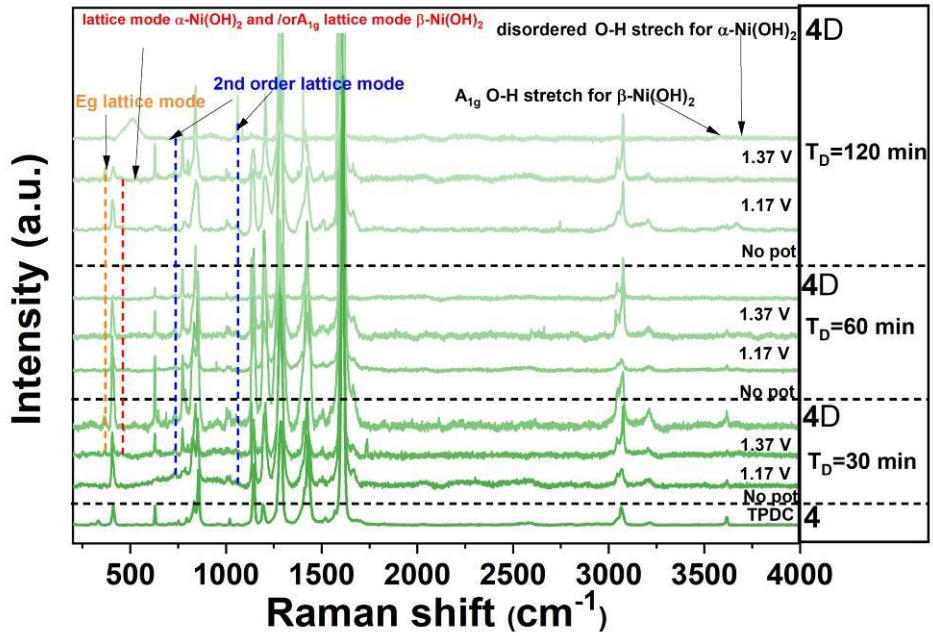

Figure A3.28. Raman spectra of **4**, the TPDC-MOF, and the derived MOF **4**D coated on Pt modified quartz under various potentials and immersion times from 30-120 min in 1 M KOH electrolyte. Potentials are refenced against RHE

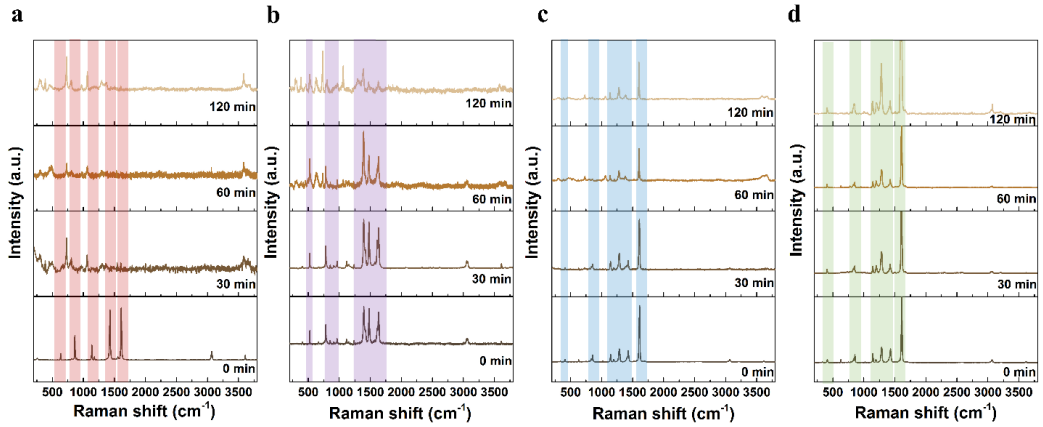

.

Figure A3.29. Raman spectra of Ni-MOFs, (a) **1** (BDC), (b) **2** (NDC), (c) **3** (BPDC), (d) **4** (TPDC) under different immersion times in 1 M KOH without applied potential. The linker peaks (coloured area) in the MOFs deceased with increasing the immersing time in alkaline-solution.

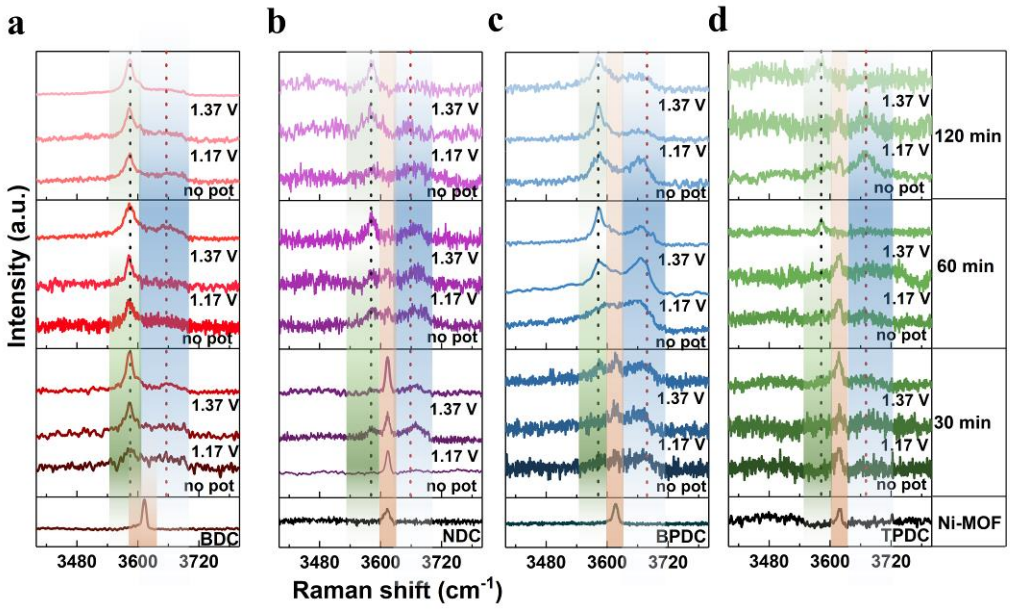

Figure A3.30. Raman spectra of Ni-MOFs, (a) **1** (BDC), (b) **2** (NDC), (c) **3** (BPDC), (d) **4** (TPDC), under different immersion times in 1 M KOH without applied potential. Orange area: MOF peaks; green area: β-$Ni(OH)_2$ peaks; blue area: α-$Ni(OH)_2$ peaks.

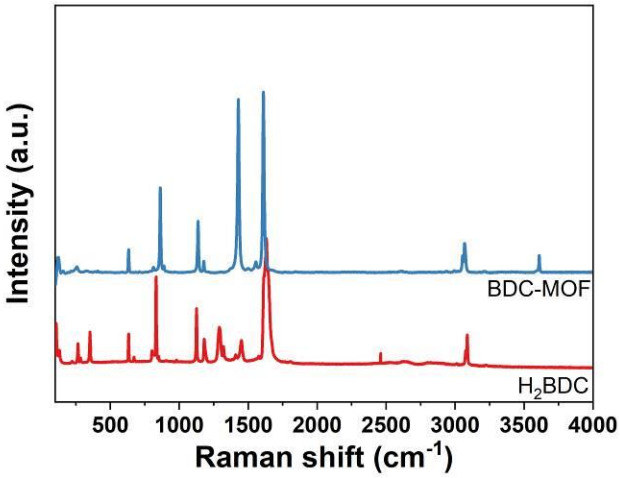

Figure A3.31. Raman spectra of BDC-MOFs (**1**) and H_2BDC. The band around 3610 cm^{-1} is assigned to the characteristic Ni-OH connectivity of the Ni-MOFs by the absence of this band cm^{-1} in the pure linkers' Raman spectra. Also, note the respective confirmations shown by **Figure A3.32 a**nd **Figure A3.33.**

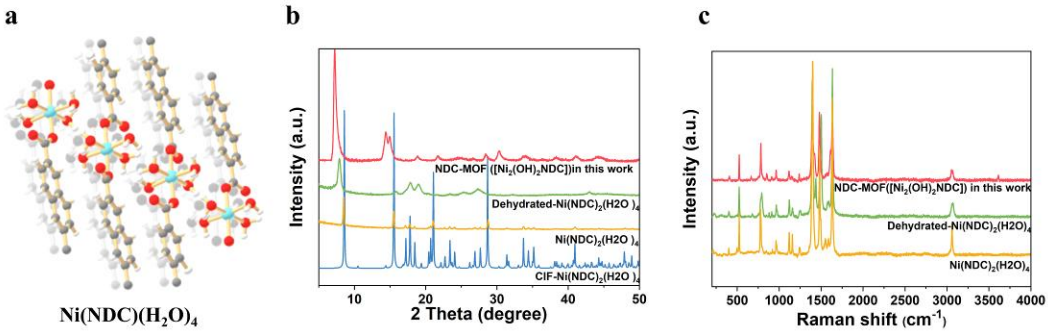

Figure A3.32. Structural characterization of $[Ni(NDC)(H_2O)_4]$. (a) X-ray diffractograms of reference $[Ni(NDC)(H_2O)_4]$ and NDC-MOF (**2**) in this work with the structure $[Ni_2(OH)_2(NDC)]$. (b) Raman spectra of $[Ni(NDC)(H_2O)_4]$ and NDC-MOF (**2**).

Further examining this peak's origin in **Figure 3.5** and **Figure A3.31**, we compared the spectral features of NDC-MOF (**2**) with those for the previously reported complex, $[Ni(NDC)(H_2O)_4]$ (**Figure A3.32a**). In $[Ni(NDC)(H_2O)_4]$, Ni(II) flanked by four coordinated water molecules and without any hydroxyl bridge could be clearly distinguished from our NDC-MOF (**2**).[32] After dehydration, it shows an obvious

lattice strain compared the original [Ni(NDC)(H_2O)$_4$] due to negative shift in XRD pattern (**Figure A3.32b**). The absence of this band at ~3610 cm^{-1} is reinforcing the band attribution observed for **2** to a hydroxyl bridge ν(OH) rather than belonging to Ni-H_2O scaffolds.

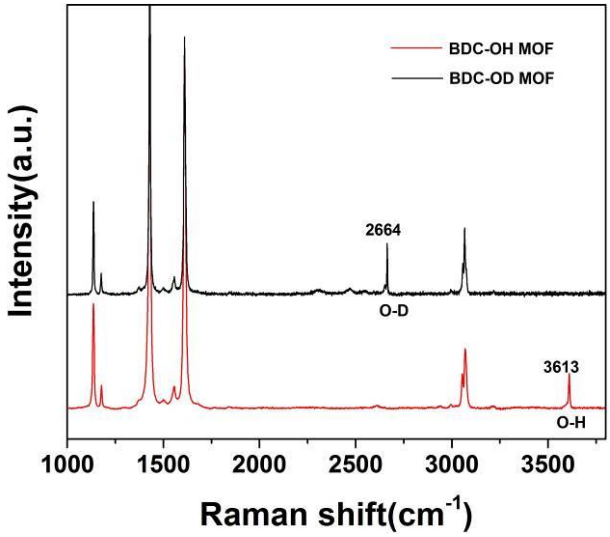

Figure A3.33. Raman spectra of MOF BDC-OH (**1$_{OH}$**, $Ni_2(OH)_2BDC$] and deuterium labelled sample named as BDC-OD (**1$_{OD}$**, [$Ni_2(OD)_2BDC$]. In a comparison of the Raman spectra of the deuterium-labeled sample **1$_{OD}$** with our standard sample **1$_{OH}$** as shown in **Figure A3.33**, the new unique band at 2664 cm^{-1} was seen for **1$_{OD}$**, while the peak at 3613 cm^{-1} **1$_{OH}$** disappeared. This phenomenon of isotope shift on the respective vibration confirms that the band at 3613 cm^{-1}, is safely assigned to Ni-OH of the pristine MOF structure, as we expected. [$\nu_{OD}/\nu_{OH} = (\mu OH/\mu OD)^{1/2}$ with $\mu = M_1M_2/(M_1+M_2)$; $M_1 = M_H$, M_D; $M_2 = M_O$; calculated ν_{OD}/ν_{OH} = 0.73; observed, ν_{OD}/ν_{OH} = 2664/3613 = 0.74; see also **Figure A3.39**.

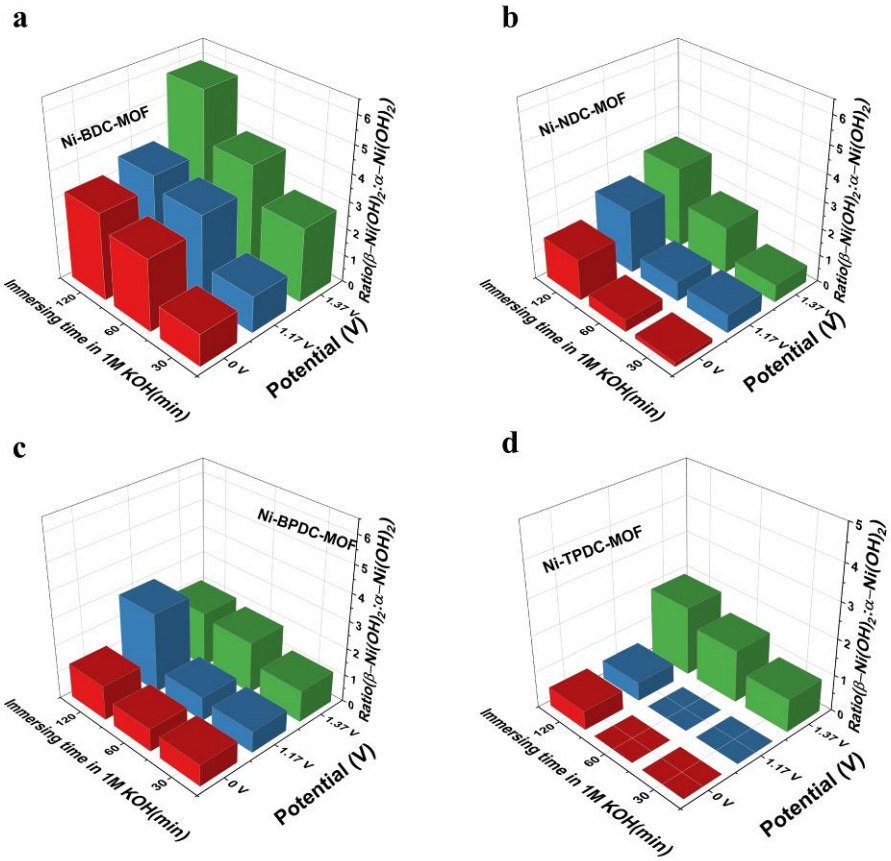

Figure A3.34. Molar ratio of β-$Ni(OH)_2$: α-$Ni(OH)_2$ (obtained from Raman data) of samples derived from Ni-MOFs, (a) **1** (BDC), (b) **2** (NDC), (c) **3** (BPDC), (d) **4** (TPDC), at different applied potentials and immersing time in 1 M KOH. "0V" refers to samples without applied potential. Potentials are referenced against RHE. The tendency of variation of the ratio β-$Ni(OH)_2$: α-$Ni(OH)_2$ supports that an increased MOF structural stability under alkaline (electro-)conditions, as induced by the linkers and their different lengths and π-π stacking features, can control to the transition from α-$Ni(OH)_2$ to β-$Ni(OH)_2$ phase and influences the overall aging process.

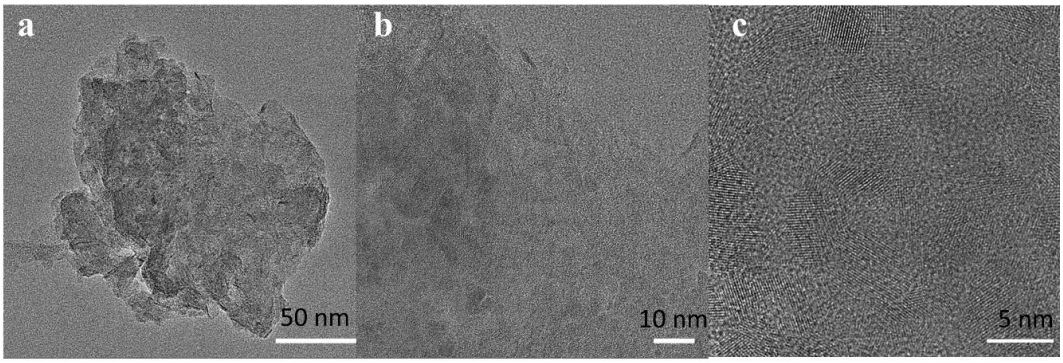

Figure A3.35. TEM images of BDC-MOF (**1**) after immersing in 1M KOH for 30 min.

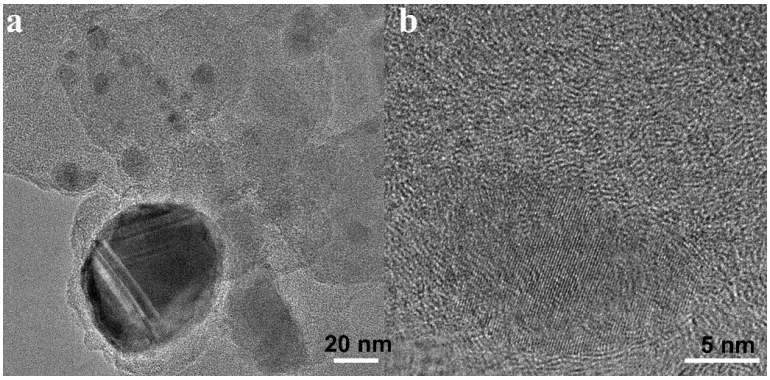

Figure A3.36. TEM images of BPDC-MOF (**3**) after immersing in 1 M KOH for 30 min.

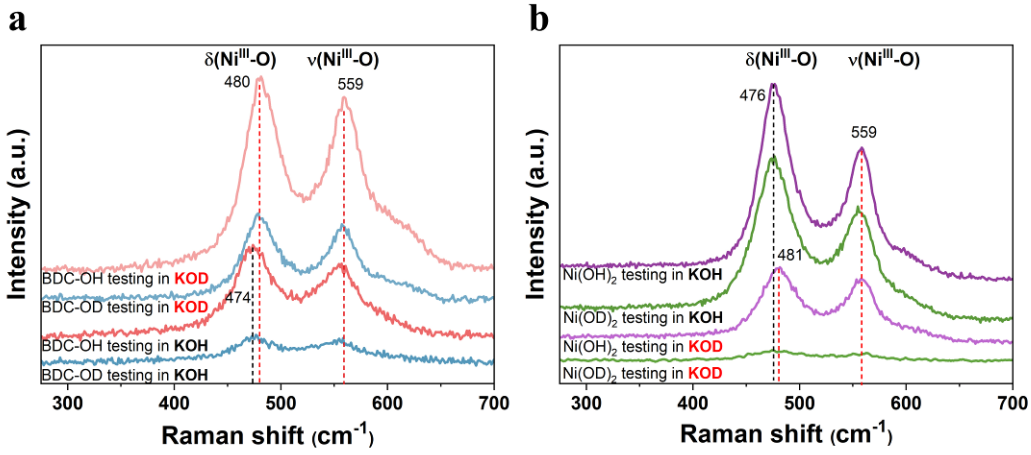

Figure A3.37. Comparing the Ni-MOF derived $Ni(OH)_2$ catalyst with a β-$Ni(OH)_2$ catalyst reference sample combined with H/D labelling experiments to monitor the

disappearance of the OH/OD characteristic feature. (a) The Raman spectra of MOFs BDC-OH (**1$_{OH}$**, [$Ni_2(OH)_2BDC$]) and BDC-OD (**1$_{OD}$**. [$Ni_2(OD)_2BDC$]) after 30 CV-cycling under 1.16 to 1.64 V *vs.* RHE in 1M KOH (H_2O) or KOD (D_2O). The red traces refer to **1$_{OH}$** tested in KOH or KOD and the blue traces refer to **1$_{OD}$** tested in KOH or KOD. (b) Raman spectra of the independently prepared reference samples β-$Ni(OH)_2$ and β-$Ni(OD)_2$ after 30 CV-cycling in 1M KOH (H_2O) or KOD (D_2O). The purple traces refer to $Ni(OH)_2$ tested in KOH or KOD and the green traces refer to $Ni(OD)_2$ tested in KOH or KOD. Note: The red dashed line refers to the $\delta(Ni^{III}\text{-}O)$ peak position at 480/481 cm^{-1} when the testing was done in KOD(D_2O) and the black dashed line refers to the $\delta(Ni^{III}\text{-}O)$ peak position at 474/476 cm^{-1} when the testing was done in KOH(H_2O).

The BDC-OH and BDC-OD samples yield the identical peak location for the $\delta(Ni^{III}\text{-}O)$ at 474 cm^{-1} and $\nu(Ni^{III}\text{-}O)$ at 559 cm^{-1} after testing in 1M KOH electrolyte. The same is observed in the KOD electrolyte, but a slight and reproducible shift of $\delta(Ni^{III}\text{-}O)$ to 480 cm^{-1} was found for both MOFs, BDC-OH (**1$_{OH}$**) and BDC-OD (**1$_{OD}$**) testing in the KOD electrolyte (**Figure A3.37a**). As a reference, samples of $Ni(OH)_2$ and $Ni(OD)_2$ were also compared by testing in 1M KOH and KOD electrolytes separately (**Figures A3.37b**). It shows $\delta(Ni^{III}\text{-}O)$ at 476 cm^{-1} and ν (Ni^{III}-O) 559 cm^{-1} for both samples after the OER process in KOH electrolyte, whereas δ (Ni^{III}-O) moved to 481 cm^{-1} for both samples after OER-tests in KOD electrolyte. Normal coordinate analysis calculations based on model Ni_3OH and Ni_3OD fragments in $Ni(OH/D)_2$ structure yield a tiny isotope shift on the Ni-O vibrations of about H/D at 1.033 quite matching with the absolute value of the observed shift, which however intuitively points into the wrong direction H/D labeling (larger frequencies for the OD treated samples). However, a strong hydrogen bond, such as Ni-O…..H, can downshift the Ni-O stretching, which effect may be larger as compared to weaker hydrogen bonds, such as Ni-O…..D. This could be the reason why we observe a slight positive shift (anomalous H/D isotope effect) for the samples treated in KOD.

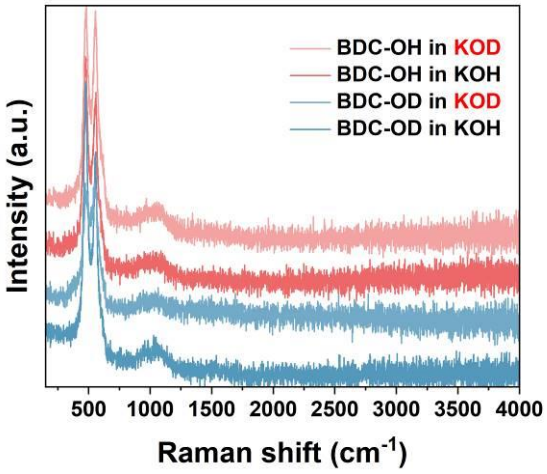

Figure A3.38. Raman spectra of BDC-OH MOF (**1OH**, $[Ni_2(OH)_2BDC]$) and deuterium labelled sample named as BDC-OD (**1OD**, $[Ni_2(OD)_2BDC]$ after 30 CV-cycling in 1M KOH (H_2O) or KOD (D_2O). The samples were coated on the 0.5cm*0.5cm Au substrates with the scan rate is 20 mV/s during cycling.

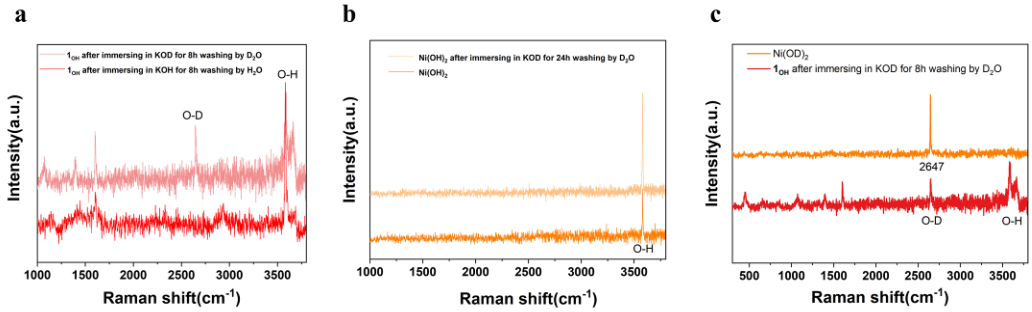

Figure A3.39. Raman spectra of a) the BDC-OH (**1OH**, $[Ni_2(OH)_2BDC]$) after immersing in KOD/KOH for 8h, and b) $Ni(OH)_2$ after immersing in KOD for 24h compared with pristine $Ni(OH)_2$, and c) $Ni(OD)_2$ (all experiments without applied potential).

After treating $\mathbf{1}_{OH}$ in 1M KOD/D_2O for 8h, a relatively intense peak at 2647 cm^{-1} was detected, which is associated to the ν(O-D) based on calculation and comparison with $Ni(OD)_2$ and $\mathbf{1}_{OD}$. Interestingly, there were still prominent ν(O-H) peaks attributed to α/β-$Ni(OH)_2$ at ~3580 cm^{-1} and ~3660 cm^{-1} with considerably lower intensity compared to the ν(O-H) of $\mathbf{1}_{OH}$ immersed in 1M KOH/H_2O as reference (**Figure A3.39a**). Pure β-$Ni(OH)_2$ reference samples only showed the ν(O-H) peak at 3580

cm^{-1} after 24 hours in 1 M KOD at ambient temperature (**Figure A3.39b**), suggesting that the exchange of OH/OD at the μ3-OH site in the $Ni(OH)_2$-type structure is sluggish under the condition in this experiment (RT, without potential). These H/D isotope labeling results suggest that the original OH-moiety introduced by the pristine [$Ni_2(OH)_2BDC$]) (**1**$_{OH}$) are not rapidly substituted by hydroxide in parallel to BDC leaching out and reconstruction of the material into the α/β-Ni(OH)2 phase.

For the isotope labelling experiment, the O-H is a diatomic molecule in this case, there is a frequency of vibrations of a diatomic molecule according to Hook's law and Newton's law[44]:

$$\nu = \frac{1}{2\pi}\sqrt{f\left(\frac{1}{m_1}+\frac{1}{m_2}\right)} \qquad \textbf{A3.39-1}$$

Where, v is the frequency of vibrations, f is the is the force constant, m1 is the mass of oxygen atom (O), m2 is the mass of hydrogen atom (H).

The Wavenumber unit ṽ:

$$\bar{\nu} = \frac{1}{2\pi c}\sqrt{f\left(\frac{1}{m_1}+\frac{1}{m_2}\right)} \qquad \textbf{A3.39-2}$$

Where the c is the light speed.

To better analysis,

$$\frac{u_H}{u_D} = \frac{m_3 m_2 (m_1 + m_2)}{m_1 m_2 (m_3 + m_2)} \qquad \textbf{A3.39-3}$$

$$u = \frac{1}{m_1} + \frac{1}{m_2} = \frac{m_1 + m_2}{m_1 m_2} \qquad \textbf{A3.39-4}$$

When the hydrogen atom (H) is replaced by its isotope deuterium (D), the different atom mass will change the u value, leading to the alter the wavenumber ṽ (Raman

shift), when the force constant f is not changed.

The m3 is the mass of deuterium D atom. The $\mu_H/\mu_D \approx 1.889$. Therefore, the $\tilde{\nu}(OH)/\tilde{\nu}(OD) = \sqrt{1.889} \approx 1.37$. According the theory of isotope effects in vibrational spectroscopy, the Ni-OD band is around 2613.1 to 2671.5 cm^{-1}, which is very close to the experimental Raman peak in **Figure A3.39**.

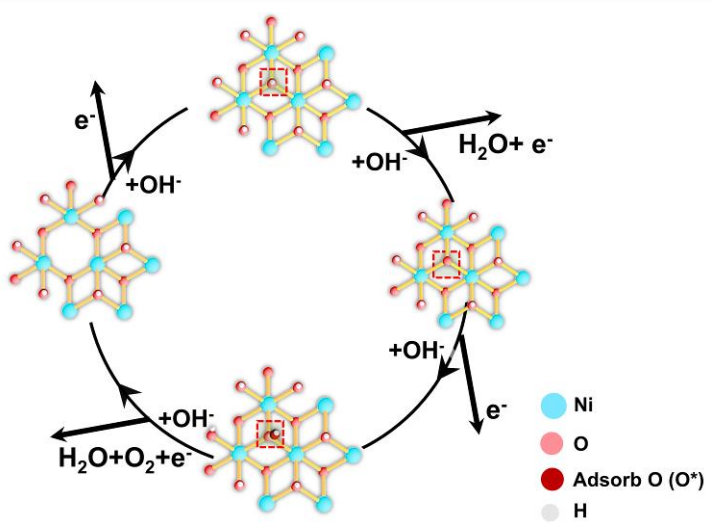

Figure A3.40. The OER mechanism for the $Ni(OH)_2$ material. The bridging Ni_3O/OH moiety is the active site.

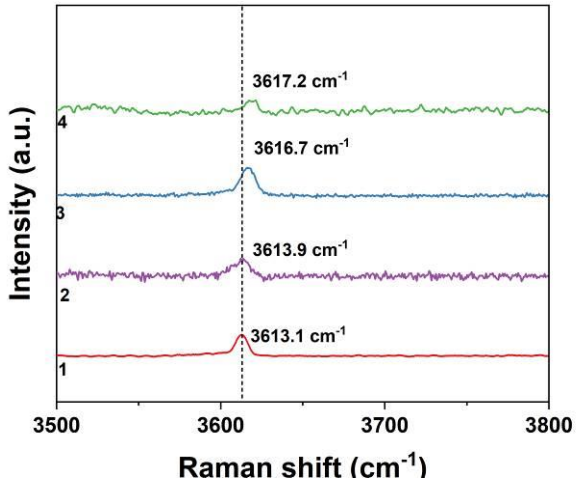

Figure A3.41. Raman spectra of MOFs **1-4** at the section of the v(OH) characteristic for the μ^3–OH bridge bond. The Raman peak position related to μ^3–OH stretch was also found to slightly vary between the four MOFs: **1** (BDC, 3613cm^{-1}) < **2** (NDC, 3614 cm^{-1}) < **3** (BPDC, 3617 cm^{-1}) ≤ **4** (TPDC, 3617 cm^{-1}). Lower O-H frequency is

in line with decreasing the O-H bond and increasing Ni-O distance, according to Duffy[45] and Brindley,[46] as the repulsion between Ni and oxygen atoms changed. Based on this theory, TPDC-MOF (**4**) display a lowest Ni-$O_{Hydroxyl}$ distance and strongest Ni-$O_{Hydroxyl}$ energy. The same trend applies to the O-H stretching in α/β-$Ni(OH)_2$ phases, which O-H bonds in disordered α-$Ni(OH)_2$ feature the higher Raman frequency and thus should show stronger Ni-$O_{Hydroxyl}$ energy.These considerations may suggest a physical reason for the observed correlation between the choice of linkers and the OER performance of the Ni-MOF derived α/β-$Ni(OH)_2$ phase mixture.

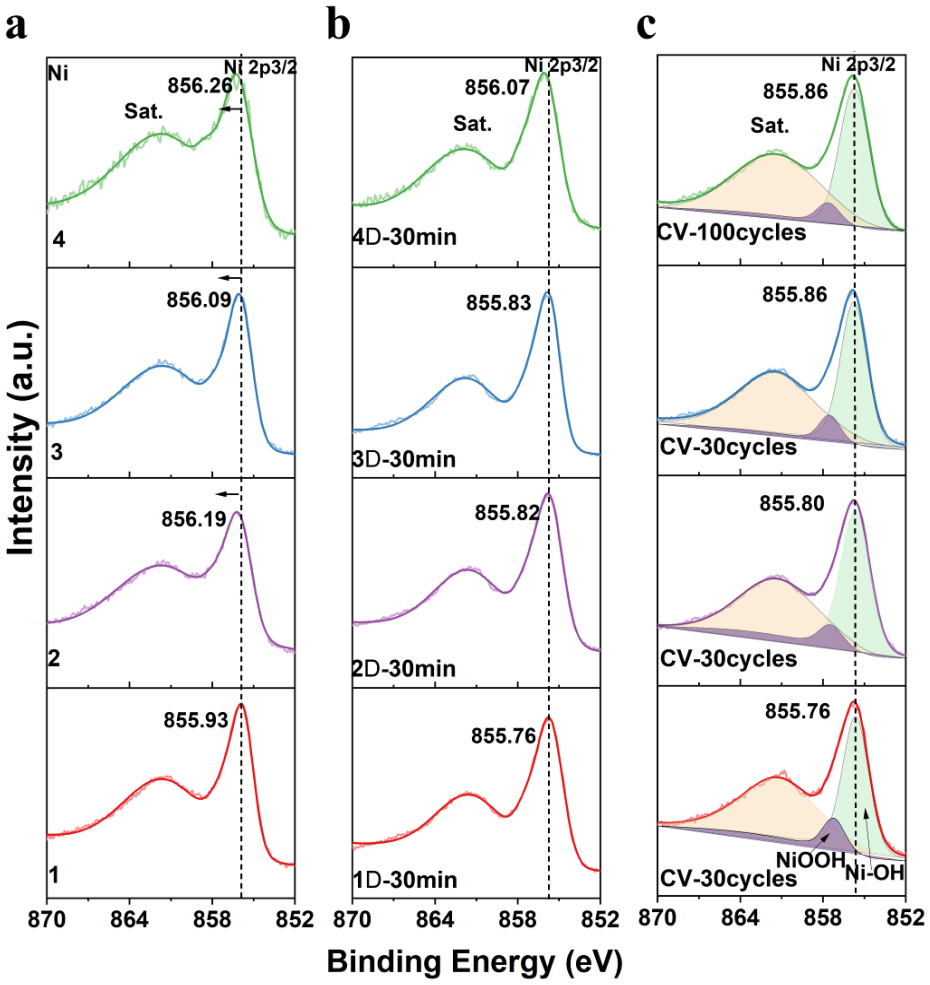

Figure A3.42. Ni 2p3/2 XPS data for (a) MOF **1**-**4**, (b) **1**D-**4**D in KOH for 30min and (c) the MOF after 30 CV-cycling.

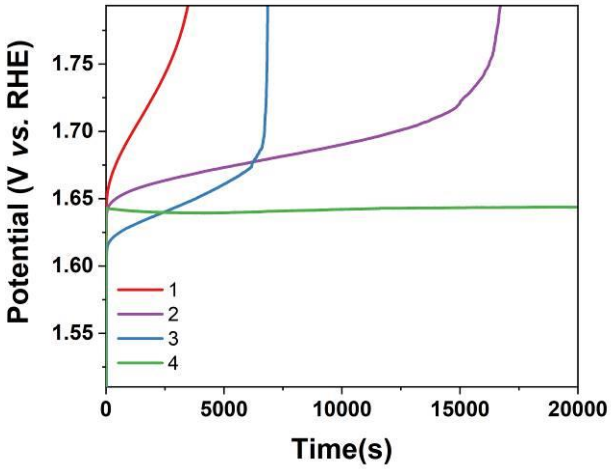

Figure A3.43. Chronopotentiometry tests for MOF **1**-**4** after sample conditioning of 30 cycles for MOF **1**-**3** (BDC, BPDC, NDC, -MOF), 100 cycles for MOF **4** (TPDC-MOF) under constant current 1.0(±0.2) mA (current density: 5 mA cm^{-2}). The instability of electrocatalyst samples derived from MOF **1**-**3** is clearly seen and indicate the more pronounced and continuously ongoing structural reorganisation as a function of time as compared to the electrocatalyst sample derived from MOF **4**.

Table A3.1 Fitting parameters of Ni K-edge EXAFS curves for Ni-BDC-MOF (**1**), Ni-NDC-MOF(**2**), Ni-BPDC-MOF(**3**) and Ni-TPDC-MOF(**4**).

	Path	**CN**	**R /Å**	**σ^2 × 1000 /Å^2**
Ni-BDC-MOF **(1)**	Ni-O Ni-C Ni-Ni Ni-O	6.9 ± 0.5 3.2 ± 1.3 6.2 ± 2.1 11.2 ± 3.8	2.05 ± 0.005 3.04 ± 0.030 3.51 ± 0.010 4.43 ± 0.035	7.5 ± 0.6 9.6* 14.5 ± 2.9 16.3*
Ni-NDC-MOF **(2)**	Ni-O Ni-C Ni-Ni Ni-O	7.1 ± 0.5 4.5 ± 2.8 6.8 ± 2.0 10.8 ± 4.0	2.05 ± 0.005 3.11 ± 0.056 3.52 ± 0.009 4.41 ± 0.038	7.8 ± 0.7 19.8* 13.8 ± 2.4 16.9*

Ni-BPDC-MOF **(3)**	Ni-O Ni-C Ni-Ni Ni-O	6.9 ± 0.5 4.0 ± 2.4 6.5 ± 2.4 11.0 ± 4.6	2.05 ± 0.006 3.09 ± 0.053 3.51 ± 0.011 4.41 ± 0.045	8.1 ± 0.8 16.6* 14.4 ± 3.1 18.4*
Ni-TPDC-MOF **(4)**	Ni-O Ni-C Ni-Ni Ni-O	6.7 ± 0.6 6.2 ± 5.7 5.3 ± 2.1 11.6 ± 5.4	2.05 ± 0.007 3.05 ± 0.080 3.50 ± 0.012 4.39 ± 0.051	8.1 ± 0.8 30.4* 13.4 ± 3.1 19.5*
* This parameter was fixed				

Table A3.2. Lattice space of metal ion-layer-linker-metal ions layers (M-L-M) calculated from XRD pattern or FFT diffraction patterns from the TEM of Ni-BDC-MOF (**1**), Ni-NDC-MOF(**2**), Ni-BPDC-MOF(**3**) and Ni-TPDC-MOF(**4**).

Ni-MOFs	2θ (°)	D (M-L-M, Å) from XRD	D (M-L-M, Å) from FFT
Ni-BDC-MOF (**1**)	8.85	10.03802	10.08
Ni-NDC-MOF (**2**)	7.29	12.21743	11.56
Ni-BPDC-MOF (**3**)	6.24	14.17132	14.77
Ni-TPDC-MOF (**4**)	4.89	18.22506	17.39

3.5 Reference

1) Tahir, M.; Pan, L.; Idrees, F.; Zhang, X.; Wang, L.; Zou, J.-J.; Wang, Z. L. Electrocatalytic oxygen evolution reaction for energy conversion and storage: A comprehensive review. *Nano Energy* **2017**, *37*, 136-157.

2) Hong, W. T.; Risch, M.; Stoerzinger, K. A.; Grimaud, A.; Suntivich, J.; Shao-Horn, Y. Toward the rational design of non-precious transition metal oxides for oxygen electrocatalysis. *Energy & Environmental Science* **2015**, *8*, 1404-1427.

3) Umemura, A.; Diring, S.; Furukawa, S.; Uehara, H.; Tsuruoka, T.; Kitagawa, S. Morphology Design of Porous Coordination Polymer Crystals by Coordination Modulation. *Journal of the American Chemical Society* **2011**, *133*, 15506-15513.

4) Morozan, A.; Jaouen, F. Metal organic frameworks for electrochemical applications. *Energy & Environmental Science* **2012**, *5*, 9269.

5) Xia, W.; Mahmood, A.; Zou, R.; Xu, Q. Metal–organic frameworks and their derived nanostructures for electrochemical energy storage and conversion. *Energy & Environmental Science* **2015**, *8*, 1837-1866..

6) Furukawa, H.; Ko, N.; Go, Y. B.; Aratani, N.; Choi, S. B.; Choi, E.; Yazaydin, A. O.; Snurr, R. Q.; O'Keeffe, M.; Kim, J.; et al. Ultrahigh Porosity in Metal-Organic Frameworks. *Science* **2010**, *329*, 424-428.

7) Gkaniatsou, E.; Sicard, C.; Ricoux, R.; Mahy, J.-P.; Steunou, N.; Serre, C. Metal–organic frameworks: a novel host platform for enzymatic catalysis and detection. *Materials Horizons* **2017**, *4*, 55-63.

8) Hou, C.-C.; Wang, H.-F.; Li, C.; Xu, Q. From metal–organic frameworks to single/dual-atom and cluster metal catalysts for energy applications. *Energy & Environmental Science* **2020**, *13*, 1658-1693.

9) Liu, B.; Shioyama, H.; Akita, T.; Xu, Q. Metal-organic framework as a template for porous carbon synthesis. *Journal of the American Chemical Society* **2008**, *130*, 5390-5391.

10) Kaneti, Y. V.; Tang, J.; Salunkhe, R. R.; Jiang, X.; Yu, A.; Wu, K. C. W.; Yamauchi, Y. Nanoarchitectured Design of Porous Materials and Nanocomposites from Metal-Organic Frameworks.*Advanced Materials* **2017**, *29*, 1604898.

11) Li, S.; Gao, Y.; Li, N.; Ge, L.; Bu, X.; Feng, P. Transition metal-based bimetallic MOFs and MOF-derived catalysts for electrochemical oxygen evolution reaction. *Energy & Environmental Science* **2021**, *14*, 1897-1927.

12) Shi, Q.; Fu, S.; Zhu, C.; Song, J.; Du, D.; Lin, Y. Metal–organic frameworks-based catalysts for electrochemical oxygen evolution. *Materials Horizons* **2019**, *6*, 684-702.

13) Yang, D.; Chen, Y.; Su, Z.; Zhang, X.; Zhang, W.; Srinivas, K. Organic carboxylate-based MOFs and derivatives for electrocatalytic water oxidation. *Coordination Chemistry Reviews* **2021**, *428*, 213619.

14) Thangavel, P.; Ha, M.; Kumaraguru, S.; Meena, A.; Singh, A. N.; Harzandi, A. M.; Kim, K. S. Graphene-nanoplatelets-supported NiFe-MOF: high-efficiency and ultra-stable oxygen electrodes for sustained alkaline anion exchange membrane water electrolysis. *Energy & Environmental Science* **2020**, *13*, 3447-3458.

15) Zheng, W.; Liu, M.; Lee, L. Y. S. Electrochemical Instability of Metal–Organic Frameworks: In Situ Spectroelectrochemical Investigation of the Real Active Sites. *ACS Catalysis* **2019**, *10*, 81-92.

16) Zhao, S.; Tan, C.; He, C.-T.; An, P.; Xie, F.; Jiang, S.; Zhu, Y.; Wu, K.-H.; Zhang, B.; Li, H.; et al. Structural transformation of highly active metal–organic framework electrocatalysts during the oxygen evolution reaction. *Nature Energy* **2020**, *5*, 881-890.

17) Chen, G.; Zhang, J.; Wang, F.; Wang, L.; Liao, Z.; Zschech, E.; Müllen, K.; Feng, X. Cobalt-Based Metal–Organic Framework Nanoarrays as Bifunctional Oxygen Electrocatalysts for Rechargeable Zn-Air Batteries. *Chemistry: A European Journal* **2018**, *24*, 18413-18418.

18) Ji, Q.; Kong, Y.; Wang, C.; Tan, H.; Duan, H.; Hu, W.; Li, G.; Lu, Y.; Li, N.; Wang, Y.; et al. Lattice Strain Induced by Linker Scission in Metal–Organic Framework Nanosheets for Oxygen Evolution Reaction. *ACS Catalysis* **2020**, *10*, 5691-5697.

19) Zhao, S.; Wang, Y.; Dong, J.; He, C.-T.; Yin, H.; An, P.; Zhao, K.; Zhang, X.; Gao, C.; Zhang, L.; et al. Ultrathin metal–organic framework nanosheets for electrocatalytic oxygen evolution. *Nature Energy* **2016**, *1*, 16184.

20) Yuan, S.; Peng, J.; Cai, B.; Huang, Z.; Garcia-Esparza, A. T.; Sokaras, D.; Zhang, Y.; Giordano, L.; Akkiraju, K.; Zhu, Y. G.; et al. Tunable metal hydroxide–organic frameworks for catalysing oxygen evolution. *Nature Materials* **2022**, *21*, 673-680.

21) Corrigan, D. A. The Catalysis of the Oxygen Evolution Reaction by Iron Impurities in Thin Film Nickel Oxide Electrodes. *Journal of the Electrochemical Society* **1987**, *134*, 377-384.

22) Fidelsky, V.; Toroker, M. C. The secret behind the success of doping nickel oxyhydroxide with iron. *Physical Chemistry Chemical Physics* **2017**, *19*, 7491-7497.

23) Friebel, D.; Louie, M. W.; Bajdich, M.; Sanwald, K. E.; Cai, Y.; Wise, A. M.; Cheng, M.-J.; Sokaras, D.; Weng, T.-C.; Alonso-Mori, R.; Davis, R. C.; Bargar, J. R.; Nørskov, J. K.; Nilsson, A.; Bell, A. T. Identification of Highly Active Fe Sites in (Ni,Fe)OOH for Electrocatalytic Water Splitting. *Journal of the American Chemical Society* **2015**, *137*, 1305-1313.

24) Ferreira de Araújo, J.; Dionigi, F.; Merzdorf, T.; Oh, H. S.; Strasser, P. Evidence of Mars-Van-Krevelen Mechanism in the Electrochemical Oxygen Evolution on

Ni-Based Catalysts. *Angewandte Chemie International Edition* **2021**, *60*, 14981-14988.

25) Trotochaud, L.; Young, S. L.; Ranney, J. K.; Boettcher, S. W. Nickel–Iron Oxyhydroxide Oxygen-Evolution Electrocatalysts: The Role of Intentional and Incidental Iron Incorporation. *Journal of the American Chemical Society* **2014**, *136*, 6744-6753.

26) Hou, S.; Li, W.; Watzele, S.; Kluge, R. M.; Xue, S.; Yin, S.; Jiang, X.; Döblinger, M.; Welle, A.; Garlyyev, B.; Koch, M.; Müller-Buschbaum, P.; Wöll,C.; Bandarenka, A. S.; Fischer, R. A. Metamorphosis of Heterostructured Surface-Mounted Metal–Organic Frameworks Yielding Record Oxygen Evolution Mass Activities. *Advanced Materials* **2021**, *33*, 2103218.

27) H. Bode, K. D. a. J. W. Zur Kenntnis der Nickelhydroxidelektrode—I. über das Nickel (II)-Hydro- xidhydrat. *Electrochima. Acta* **1966**, *11*, 1079-1087.

28) Böhm, D.; Beetz, M.; Kutz, C.; Zhang, S.; Scheu, C.; Bein, T.; Fattakhova-Rohlfing, D. V(III)-Doped Nickel Oxide-Based Nanocatalysts for Electrochemical Water Splitting: Influence of Phase, Composition, and Doping on the Electrocatalytic Activity. *Chemistry of Materials* **2020**, *32*, 10394-10406.

29) Klaus, S.; Cai, Y.; Louie, M. W.; Trotochaud, L.; Bell, A. T. Effects of Fe Electrolyte Impurities on Ni(OH)2/NiOOH Structure and Oxygen Evolution Activity. *The Journal of Physical Chemistry C* **2015**, *119*, 7243-7254.

30) Kizil, R.; Irudayaraj, J.; Seetharaman, K. Characterization of irradiated starches by using FT-Raman and FTIR spectroscopy. *Journal of Agricultural and Food Chemistry* **2002**, *50*, 3912-3918.

31) Leikin, S.; Parsegian, V. A.; Yang, W. H.; Walrafen, G. E. Raman spectral evidence for hydration forces between collagen triple helices. *Proceedings of the*

National Academy of Sciences of the United States of America **1997**, *94*, 11312-11317.

32) Kim, S.-H.; Lee, H. H.; Kim, J.-M.; Hong, S. Y.; Lee, S.-Y. Heteromat-framed metal-organic coordination polymer anodes for high-performance lithium-ion batteries. *Energy Storage Materials* **2019**, *19*, 130-136.

33) Cheng, W.; Zhao, X.; Su, H.; Tang, F.; Che, W.; Zhang, H.; Liu, Q. Lattice-strained metal–organic-framework arrays for bifunctional oxygen electrocatalysis. *Nature Energy* **2019**, *4*, 115-122.

34) Hadjiivanov, K. I.; Panayotov, D. A.; Mihaylov, M. Y.; Ivanova, E. Z.; Chakarova, K. K.; Andonova, S. M.; Drenchev, N. L. Power of Infrared and Raman Spectroscopies to Characterize Metal-Organic Frameworks and Investigate Their Interaction with Guest Molecules. *Chemical Reviews* **2020**, *121*, 1286-1424.

35) Butova, V. V.; Budnyk, A. P.; Charykov, K. M.; Vetlitsyna-Novikova, K. S.; Bugaev, A. L.; Guda, A. A.; Damin, A.; Chavan, S. M.; Øien-Ødegaard, S.; Lillerud, K. P.; et al. Partial and Complete Substitution of the 1,4-Benzenedicarboxylate Linker in UiO-66 with 1,4-Naphthalenedicarboxylate: Synthesis, Characterization, and H2-Adsorption Properties. Inorganic Chemistry **2019**, *58*, 1607-1620.

36) Atzori, C.; Shearer, G. C.; Maschio, L.; Civalleri, B.; Bonino, F.; Lamberti, C.; Svelle, S.; Lillerud, K. P.; Bordiga, S. Effect of Benzoic Acid as a Modulator in the Structure of UiO-66: An Experimental and Computational Study. *The Journal of Physical Chemistry C* **2017**, *121*, 9312-9324.

37) Hall, D. S.; Lockwood, D. J.; Poirier, S.; Bock, C.; MacDougall, B. R. Raman and Infrared Spectroscopy of α and β Phases of Thin Nickel Hydroxide Films Electrochemically Formed on Nickel. *The Journal of Physical Chemistry A* **2012**, *116*, 6771-6784.

38) Hall, D. S.; Lockwood, D. J.; Poirier, S.; Bock, C.; MacDougall, B. R. Applications of in Situ Raman Spectroscopy for Identifying Nickel Hydroxide Materials and Surface Layers during Chemical Aging. ACS Applied Materials & Interfaces **2014**, *6*, 3141-3149.

39) Lee, S.; Banjac, K.; Lingenfelder, M.; Hu, X. Oxygen Isotope Labeling Experiments Reveal Different Reaction Sites for the Oxygen Evolution Reaction on Nickel and Nickel Iron Oxides. *Angewandte Chemie International Edition* **2019**, *58*, 10295-10299.

40) Diaz-Morales, O.; Ferrus-Suspedra, D.; Koper, M. T. M. The importance of nickel oxyhydroxide deprotonation on its activity towards electrochemical water oxidation. *Chemical Science* **2016**, *7*, 2639-2645.

41) Ding, M.; Cai, X.; Jiang, H. Improving MOF stability: approaches and applications. *Chemical Science* **2019**,*10*, 10209-10230.

42) Li, C.-F.; Zhao, J.-W.; Xie, L.-J.; Wu, J.-Q.; Ren, Q.; Wang, Y.; Li, G.-R., Surface-Adsorbed Carboxylate Ligands on Layered Double Hydroxides/Metal–Organic Frameworks Promote the Electrocatalytic Oxygen Evolution Reaction. *Angewandte Chemie International Edition* **2021**, *60*, 18129-18137.

43) Li, C.-F.; Xie, L.-J.; Zhao, J.-W.; Gu, L.-F.; Tang, H.-B.; Zheng, L.; Li, G.-R., Interfacial Fe−O−Ni−O−Fe Bonding Regulates the Active Ni Sites of Ni-MOFs via Iron Doping and Decorating with FeOOH for Super-Efficient Oxygen Evolution. *Angewandte Chemie International Edition* **2022,** *61*, e202116934.

44) Bernhard S.; Infrared and Raman Spectroscopy: Methods and Applications. VCH, **1995**, ISBN 3-527-26446-9.

45) Shieh, S. R.; Duffy, T. S. Raman Spectroscopy of Co(OH)2 at High Pressures: Implications for Amorphization and Hydrogen Repulsion. *Physical Review B 2002*, 66 134301

46) Brindley, G. W ; Kao, Chih-Chun. Structural and IR Relations AmongBrucite-Like Divalent Metal Hydroxides. *Physics and Chemistry of Minerals* **1984**, *10*, 187-191.

Chapter 4

4. Tuning the Reconstruction of Metal-Organic Frameworks during the Oxygen Evolution Reaction

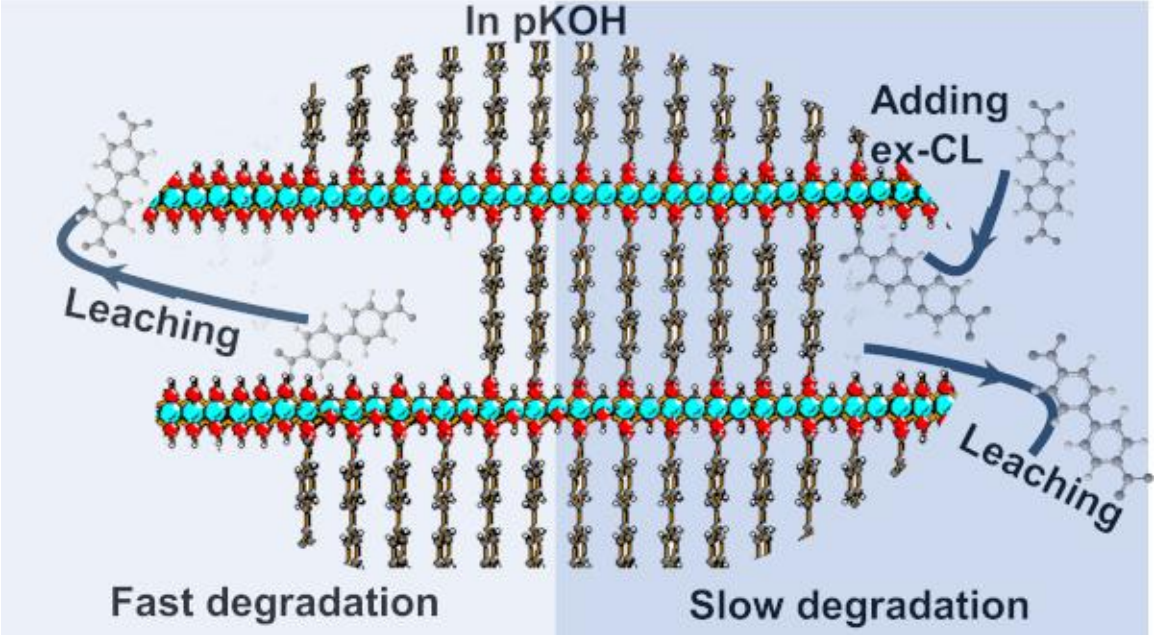

This is chapter is based on a manuscript of the same title from X. Ma, L. Schröck, G. Gao, Q. Ai, M, Zarrabeitia, C. Liang, M. Z. Hussain, R. Khare, K. Song, D. J. Zheng, M. Koch, I. E.L. Stephens, S. Hou, Y. Shao-Horn, J. Warnan, A. S. Bandarenka, R. A. Fischer, with the title 'Tuning the Reconstruction of Metal-Organic Frameworks during the Oxygen Evolution Reaction' *ACS Catalysis* 2024, **14**(21), 15916–15926, reprinted with permission under Copyright © 2024 The Authors. (Published by American Chemical Society with license CC-BY 4.0).

The project was designed by X. Ma, and R.A. Fischer. The progress was regularly discussed with R. A. Fischer. J. Warnan, and A.S. Bandarenka. The synthesis experiments and most of the characterizations and electrochemical test were performed by X. Ma. The ICP-OES was performed by M. Koch, The HRETM was performed by G. Gao, Q. Ai, The XAFS was performed R. Khare. The EC-MS was tested by C. Liang and Ifan E.L.Stephens . The XPS was tested by M. Zarrabeitia The final manuscript was written by X. Ma and discussed and edited by all co-authors.

Abstract

Recently, there has been a growing interest in conversion of metal-organic frameworks (MOFs) into metal-hydroxide catalysts for alkaline oxygen evolution reactions (OER). While studies have shown that the initial OER performance of MOF-derived intermediates surpasses that of traditional metal-hydroxide catalysts, ongoing debates persist regarding these catalysts' durability and electrochemical stability. Moreover, the inevitable reorganization (aging) of MOF-derived catalysts from disordered to ordered phases, particularly those primarily composed of nickel oxyhydroxides, remains a topic of discussion. To address these issues, we propose a straightforward approach to mitigating MOF reconstruction and modulating aging in harsh alkaline environments by introducing additional organic carboxylate linkers into the electrolytes. Specifically, we focus on two examples: Ni-BPDC-MOFs and NiFe-BPDC-MOFs, of formula [M2(OH)2BPDC] (M: Ni and Fe; BPDC = 4,4'-biphenyldicarboxylate). Experimental results indicate that alkaline electrolytes containing additional BPDC linkers exhibit enhanced OER activity and prolonged electrochemical lifespan. Complemented by in-situ Raman spectroscopy, our findings suggest that manipulating the coordination equilibrium of the organic linker involved in Ni-MOF formation (linker assembly) and reconstruction (linker leaching) leads to the formation of more disordered nickel oxyhydroxide phases as the active catalyst material, that show enhanced OER performance.

4.1 Introduction

Selecting suitable electrocatalysts is crucial for advancing the oxygen evolution reaction (OER), a key step in hydrogen production.[1,2] Given the depletion of fossil fuels, finding alternatives is vital for the evolving energy landscape.[3,4] Since their inception, metal-organic frameworks (MOFs) have captured considerable attention as potential OER catalysts.[5-11] This recognition stems from their structural versatility,[12-16] the diverse array of metal nodes, and, notably, their demonstrated efficacy in reported OER applications. [17-21]

Following an in-depth discourse on the role of MOFs in alkaline OER, it has become apparent that many MOFs primarily function as precursors, i.e. as pre-catalysts to the active phase. When directly employed in OER applications, they undergo reconstruction, forming metal hydroxide or oxyhydroxide.[22,23] Substantial research has indicated that catalysts derived from MOFs in this way can exhibit superior activity compared to the closely related but conventional reference systems, particularly those featuring non-noble metals like Ni, Co, Fe, and Mn.[24-26] Moreover, when compared to noble metals, the non-noble electrocatalysts, especially prevalent Ni-based electrocatalysts, offer general advantages in terms of high abundance and low cost albeit often grappled with stability issues.[27,28] For instance, pristine $Ni(OH)_2$ struggles with the aging process in alkaline environments, transitioning from the disordered α-$Ni(OH)_2$ to the more ordered β-$Ni(OH)_2$ phase, resulting in a decline in OER activity.[29,30]

In a previous study, we explored an isoreticular series of $[Ni_2(OH)_2L]$ featuring carboxylate-linkers of varying lengths that modulate the over-all stability of the MOF in the electrolyte and during OER (L = Linker = 1,4-benzendedicarboxylate, BDC; 2,6-napthalenedicarboxylate, NDC; 4,4'-biphenyldicarboxylate BPDC; and 4,4''*p*-terphenyldicarboxylate TPDC).[31] In this and related systems it has been shown that the MOF will tranfer to metal hydryoxide first then to oxyhydroxide during OER process, but interestingly the choice of the linker exerted control over the

transformation of Ni-MOF, guiding it into distinct nickel hydroxide phases with a ratio depending on the type of linker chosen. The linker plays a pivotal role in affecting the MOF activation and decelerating the degradation and reconstruction processes, *i.e*. in modulating the reconstruction kinetics, resulting in tuning the OER activity. When considering the MOF reconstruction to the metal hydroxides as a chemical equilibrium, the process can take the form by:

$$[Ni_2(OH)_2L](s) + 2\ OH^-(aq) \rightarrow 2\ Ni(OH)_2(s) + L^{2-}(aq);\ pK_R(L)\ (L: Linker)$$

This assumption prompted a consideration: what if additional free linkers were to be introduced to the alkaline electrolyte? Would the equilibrium be shifted and the reconstruction reaction decelerate as the concentration of available linker increases? How would that influence the OER performance of the system?

Motivated by this, we investigated the impact of introducing additional free linkers to a strong alkaline electrolyte during electrocatalysis, hypothesizing its potential to decelerate the reconstruction reaction, as shown in **Figure 4.1a**. We selected $[Ni_2(OH)_2BPDC]$ for a detailed evaluation, and found that this system to have prolonged stability, reduced reconstruction, and enhanced electrochemical lifetime with the introduction of the extra carboxylate linker (ex-CL = BPDC) in the electrolyte. Expanding this hypothesis to NiFe-MOFs as another case study, revealed similar behavior, although NiFe-MOFs displayed higher intrinsic instability and a tendency to transition into a more disordered phase with Fe assistance, compared to pure Ni-MOF systems.

4.2 Results and Discussion

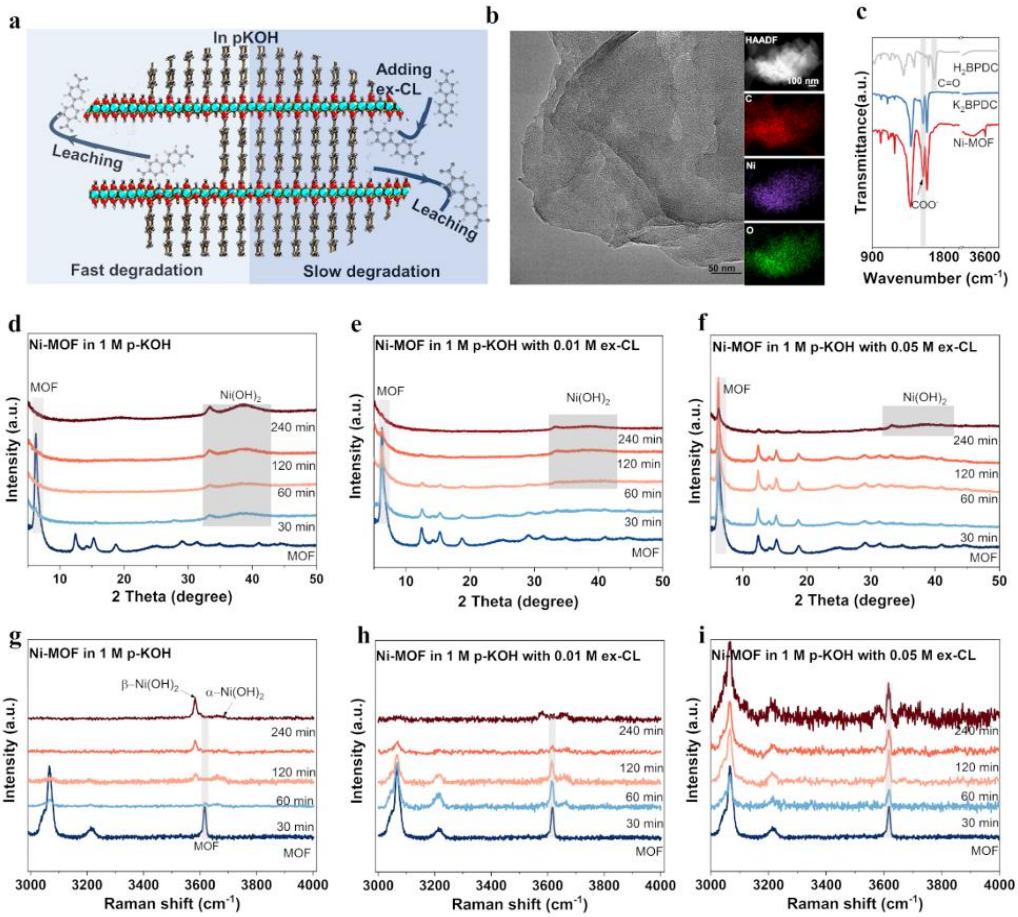

Figure 4.1 a) Schematic illustration of the degradation process of Ni-MOF ([$Ni_2(OH)_2BPDC$]) in alkaline electrolytes with/without extra carboxylate linker. b) TEM and HAADF images of Ni-MOF along with the corresponding EDS elemental maps with Ni, O, and C. c) FTIR of H_2BPDC, of the potassium linker salt K_2BPDC, and of the Ni-MOF. The XRD pattern of time dependence for Ni-MOFs in 1 M purified KOH (p-KOH; Fe trace free, similar to [31]) with the presence of various concentrations of K_2BPDC (extra-linker, ex-CL): d) 0.00 M ex-CL (linker-free), e) 0.01 M ex-CL, and f) 0.05 M ex-CL. Time-dependent Raman spectra of Ni-MOFs in 1 M p-KOH with the presence of various concentrations of ex-CL: g) 0.00 M ex-CL (linker-free), h) 0.01 M ex-CL, and i) 0.05 M ex-CL.

The Ni-MOF, with the formula [$Ni_2(OH)_2BPDC$], was synthesized following our previous method,[31] revealing distinctive 2D morphologies with C, O, and Ni elements

in **Figure 4.1b**. Atomic force microscopy (AFM) characterization confirmed this nanosheet structure with a thickness of under 10 nm (**Figure A4.1)**. XANES analysis (**Figure A4.2)** verified the presence of Ni^{2+}, and showcased a characteristic and sharp μ^3-OH band at ~3611 cm^{-1} in the FTIR spectra (**Figure 4.1c)**.

Following structural characterization, we further investigated the MOF's behavior under various electrolytes without applied potentials. Given the known sensitivity of OER activity to pH changes, and considering our previous findings on the impact of pH on MOF reconstruction, we used the potassium salt K_2BPDC (ex-CL) instead of H_2BPDC to avoid any significant changes of the pH upon addition of ex-CL to the electrolyte, as indicated in **Table A4.1**. As shown in **Figure 4.1c**, the ν(C=O) of the COOH species at 1679 cm^{-1} in H_2BPDC shifted to 1586 cm^{-1} and 1543 cm^{-1} in the deprotonated COO^- species of K_2BPDC and Ni-BPDC-MOF, respectively.[32]

The powder X-ray diffraction (PXRD) patterns of Ni-MOF in **Figure 4.1d** revealed distinct characteristic reflections at 6.2°, signifying the metal-ligand-metal lattice spacing of around 14.2 nm.[31] These reflections began to degrade upon immersion in 1 M purified KOH (p-KOH) and vanished after 60 minutes. Concurrently, α/β-$Ni(OH)_2$ phases emerged at around 19°, 33°, and 38°, with their intensity increasing with prolonged exposure time.[33] In contrast, the introduction of the extra carboxylate linker (K_2BPDC, ex-CL) significantly enhanced the stability of the MOF as its reflection at at 6.2° were still observed after 120 minutes of immersion in 1 M p-KOH with 0.01 M ex-CL (**Figure 4.1e**). Higher ex-CL concentrations improved the MOF's stability, with clear MOF reflections observed even after 240 minutes of treatment in 1 M p-KOH with 0.02 M and 0.05 M ex-CL (**Figures A4.3 and 1f**). Interestingly, the $Ni(OH)_2$ reflections resulting from the MOF conversion exhibited significantly broader peaks in the presence of ex-CL, suggesting more disordered phases being formed under these conditions.

Raman spectra in **Figures 4.1g-i** and **A4.4-6** provided detailed insights into the transformation process, quantifying derived $Ni(OH)_2$ phases during exposure in 1 M

p-KOH with and without the addition of 0.01-0.05 M ex-CL. The characteristic bands of phenyl rings and carboxylate groups from Ni-MOF decreased with the increasing exposure time in 1 M p-KOH, with new broad peaks centered at 311 (E_g) and 450 cm^{-1} (A_{1g}) for the $Ni(OH)_2$ phase appeared in **Figure A4.4**.[29,33] Simultaneously, the μ^3-OH bridge signal for pristine Ni-MOF at 3617 cm^{-1} decreased, transforming into two new bands, assigned to β-$Ni(OH)_2$ at ~3582 cm^{-1} and α-$Ni(OH)_2$ at around ~3673 cm^{-1} (**Figure 4.1g**).[34] After 240 minutes of exposure in 1 M p-KOH, the β-$Ni(OH)_2$ band was 6.15 times stronger than that of α-$Ni(OH)_2$. In contrast, the addition of ex-CL slowed down the aging process from the disordered α-$Ni(OH)_2$ to the ordered β-$Ni(OH)_2$ (**Figures A4.5-6** and **4.1h-i**),while the phenyl ring bands at 1603 cm^{-1}, which are characteristic of the MOF, remained prominent.[35] Specifically, for the Ni-MOF in 0.01 M ex-CL in p-KOH after 60 minutes, the Raman band at 3673 cm^{-1} assigned to α-$Ni(OH)_2$ was now stronger than β-$Ni(OH)_2$. After 240 minutes, the ratio β-$Ni(OH)_2$: α-$Ni(OH)_2$ was 1.2 for Ni-MOF in 0.01 M ex-CL in p-KOH, and 0.94 and 0.88 for Ni-MOF in 0.02 M and 0.05 M ex-CL in p-KOH, respectively.

In summary, the presence of additional linker resulted in a significant decrease in the β:α phase of $Ni(OH)_2$. By combining the above-discussed time-dependent XRD and Raman findings, we affirm the validity of our hypothesis, demonstrating a discernible influence of the extra carboxylate linker on the reconstruction of Ni-MOF, the improved stability of the Ni-MOF in the alkaline environment, and the inhibition of the aging process in the derived $Ni(OH)_2$.

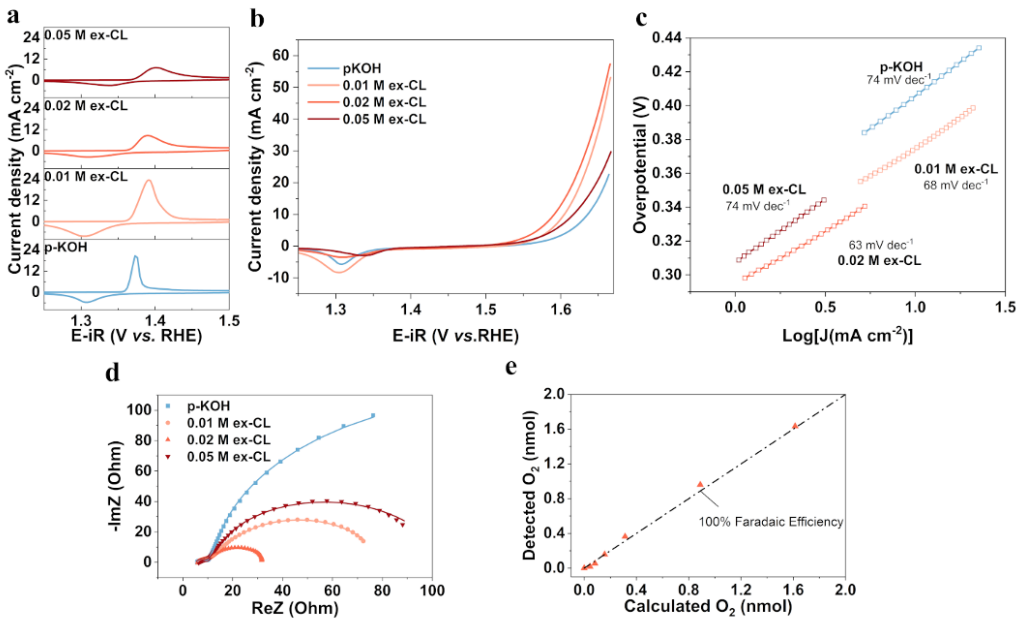

Figure 4.2. Electrochemical characterization of Ni-MOF in 1M p-KOH with the addition of 0.00 0.05 M of ex-CL. The Ni-MOFs were cycled (activation process) from 1.13 to 1.67 V *vs*. the RHE with IR correction at10 mV/s (Hg/HgO was used as the experimental reference electrode and potentials were corrected for RHE, glassy carbon as RDE working elerctrode, **Figure A4.7**). The reported electrochemical data were taken when the intensity of anodic peaks of of Ni^{3+}/Ni^{2+} did not no longer increase: a) Redox peaks of $Ni^{2+/3+}$. b) OER activity; c) Tafel slope. d) Electrochemical Impedance Spectroscopy (EIS) with fitting line at 1.546 V *vs*.RHE. e) Faradaic efficiency of with 0.02 M ex-CL. All results given here were measured after the CV activation process (details see SI).

Shifting our focus to extra-linkers' influence on electrochemistry, Ni-MOF (48 µg) deposition on glass carbon (GC) was carried out using a standard drop-casting method (ink preparation and method details are available in SI). Throughout this work, unless specified otherwise, glassy carbon (GC) serves as the working electrode. Cyclic voltammograms (CV) were executed in alkaline electrolytes (1 M p-KOH with [ex-CL] = 0.00-0.05 M) from 1.13 to 1.67 V *vs*.RHE with IR correction (glassy carbon as RDE working elerctrode, and Hg/HgO as the experimental reference electrode, with potentials corrected for RHE, **Figure A4.7**) and a scan speed of 10 mV/s, as

visualized in **Figures A4.8-9**. The redox peaks of Ni^{3+}/Ni^{2+} in Ni-MOF display an ascending pattern starting from the first cycle in 1 M p-KOH (**Figure A4.8a**), indicating the degradation and subsequent reconstruction of the Ni-MOF into $Ni(OH)_2$/NiOOH.

Furthermore, the OER activity was assessed after the intensity of the anodic peaks did not increase, as depicted in **Figures 4.2a and b**. The oxidation peaks of Ni^{3+}/Ni^{2+} exhibited a slight positive (anodic) shift with the introduction of the ex-CL, transitioning from 1.37 (in p-KOH) to 1.39 (with 0.01 M and 0.02 M ex-CL), and to 1.40 V *vs*. RHE (with 0.05 M ex-CL). The overpotential at 10 mA cm^{-2}, indicative of OER activity, decreased from 404±11 mV in 1 M p-KOH to 375±4 mV and 355±7 mV with 0.01 and 0.02 M ex-CL, respectively. However, it increased to 363 ± 6, 371 ± 3 mV and 380±13 mV for 0.03, 0.04, and 0.05 M ex-CL respectively. (**Figures 4.2b and A4.10**). Correspondingly, the Tafel slope (**Figure 4.2c**) was calculated to 74, 68, 63, and 74 mV dec^{-1} with 0.00, 0.01, 0.02 and 0.05 M ex-CL, respectively, highlighting the enhanced OER kinetics for Ni-MOFs in an alkaline environment in the presence of extra carboxylate linkers. Moreover, the turnover frequencies (TOF) were calculated using two methods: inductively coupled plasma atomic emission spectroscopy (ICP-OES) measurements of Ni in the MOF-coated electrodes and the integration of the oxidation peak in the OER in **Figure A4.11**. These methods determined the number of moles of Ni deposited on the GC electrode and the molar amount of exlectrochemically accessible Ni reacted during the CV activation process, respectively. The ex-CL addition yielded higher TOF values compared to the linker-free electrolyte, with the highest values observed at 0.02 M ex-CL with 0.11 s^{-1} and 0.40 s^{-1} for Ni, based on ICP-OES and the $Ni^{2+/3+}$ oxidation peak integration as the lower and the upper limit, respectively, for TOF.

Figure A4.12 displays the electrochemical impedance spectroscopy (EIS) results within a potential range from 1.466 to 1.586 V *vs.* RHE. The adsorption resistances (**R_a**) of Ni-MOF with various electrolytes were compared to the values obtained under

1.546 V *vs.* RHE using an equivalent electric circuit (EEC) model, as depicted in **Figures 4.2d and A4.13**. Compared with the negligible difference of the resistance of the electrolyte ($\mathbf{R_s}$) in different electrolytes in **Figure A4.14**, the $\mathbf{R_a}$ drops as the ex-CL increases to 0.01-0.02 M, indicating easier formation of the active intermediates γ-NiOOH from α-$Ni(OH)_2$, potentially contributing to their higher activity.[36]

To delve deeper into the electrochemical implications of the extra-linker in the electrolytes, we used a reference β-$Ni(OH)_2$ bulk sample, which avoids the original phase influence based on the Bode scheme and the self-linkers' interference from MOFs. This reference catalyst was compared with the Ni-MOFs' OER behavior in alkaline conditions selecting extra linker-free conditions and 0.01 M ex-CL addition in p-KOH (**Figure A4.15)**. The very similar activities of this reference systems indicates that the effect of the ex-CL on a $Ni(OH)_2$/NiOOH catalyst's surface, e.g. adsorption and modulating the active sites, can be considered negligible also in our case of the Ni-MOF derived catalyst materials.[37] Rather, it implies that the observed effect of ex-CL on OER in our case relates to the intrinsic kinetics of the Ni-MOF reconstruction and the phase ratio of the derived NiOOH.

Moreover, the electrochemical stability of ex-CL under the conditions of our experiments was carefully verified to avoid misinterpretations. Specially, activated β-$Ni(OH)_2$ reference catalysts on GC were exposed to constant potentials of 1.6 to 2.3 V *vs*. RHE (1.6, 1.8 and 2.3 V) for 20 minutes (for each potential) in a neutral solution containing 0.05 M ex-CL (the choice of the neutral solution is to avoid the interference of the alkali for HPLC, details as shown in SI). After the electrochemical measurements, each electrolyte solution underwent HPLC analysis, revealing no traces of degradation products of the carboxylate linkers, such as biphenyl **(Table A4.2**).[38] Additionally, the pristine glassy carbon electrode was tested in the linker-free 1 M p-KOH and with 0.02 M ex-CL and no remarkable changes were found (**Figure A4.16**). Finally, the Faradaic efficiency were measured to be 103±2.4 % for our Ni-MOF derived OER catalyst tested in 0.02 M ex-CL (**Figure 4.2e)**. Combining these

results with the unchanged NMR results of the electrolytes before and after CV (**Figure A4.17**), it is suggested that the oxidation of the carboxylate linker here, for example, involving possible decarboxylation and biphenyl formation, could be ignored.[39]

As is common, the presence of Fe in alkaline electrolytes significantly enhances the performance of Ni-based catalysts in OER applications.[39] To investigate potential contamination, elemental mappings using electron diffraction spectroscopy (EDS) in transmission electron microscopy (TEM) mode were conducted on Ni-MOF samples after 30 cycles of CV (1.13 to 1.67 V *vs*. the RHE, 10mV/s) in both 1 M p-KOH (Fe-free) and with the addition of 0.02 M ex-CL. No Fe was detected in **Figures 4.3a-b**. Furthermore, ICP-OES (**Figure A4.18**) results indicated that the as-prepared K_2BPDC salt contained a low trace concentration of Fe (0.025 ppm), suggesting that trace level Fe contamination is not responsible for the observed enhancement in OER activity with alkaline electrolytes containing extra carboxylate linkers.[29]

Additionally, Ni-MOF derived electrodes operated in different electrolytes were investigated post-OER experiments. In **Figure A4.19**, ex-situ high-resolution transmission electron microscopy (HRTEM) analysis revealed clear lattice fringes with spacings of approximately 0.20 and 0.24 nm, corresponding to the (101) planes of NiO phase and (002) planes of NiOOH, respectively.[41] These findings confirm the reconstruction process during OER for both Ni-MOF samples in linker-free alkaline electrolytes and those with 0.02 M ex-CL. Furthermore, ex-situ X-ray photoelectron spectroscopy (XPS) analysis was performed to investigate changes in the surface chemical states of the cycled electrodes. In **Figure 4.3c**, the O 1s spectrum of pristine Ni-MOF exhibited four components at approximately 533.9, 532.6, 532.3 and 531.3 eV, corresponding to O=C-O* (oxygen bonded to a single bond to a carbonyl group), C-O (ether group), *O=C-O (the oxygen bonded to a double bond to the carbonate), and Ni-OH bonds, respectively.[42] The intensities of the carbonaceous species (C-O and O=C-O) notably decreased after electrochemical activation, suggesting the

leaching of the carbonylate linker.

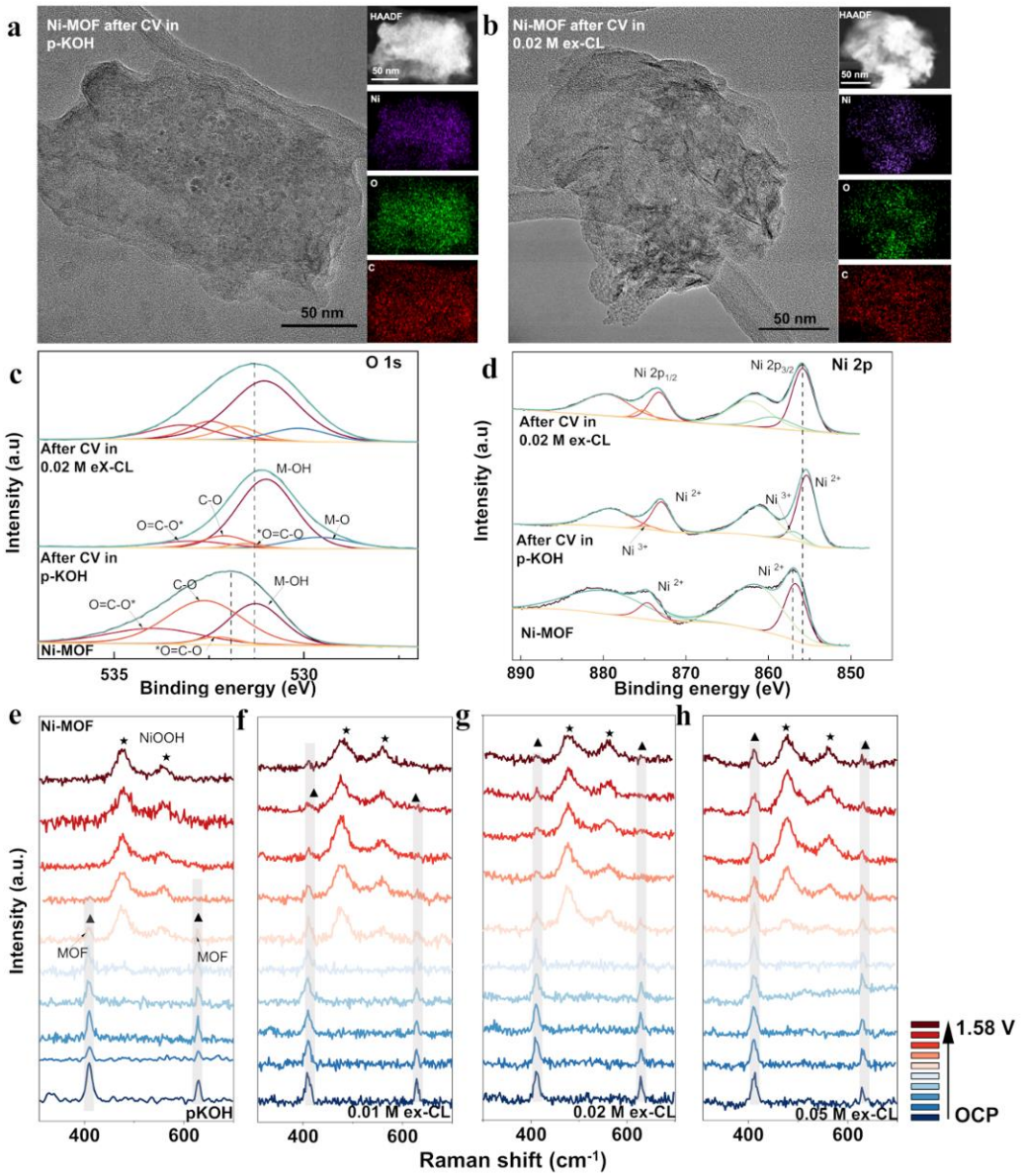

Figure 4.3. TEM and HAADF images along with the corresponding EDS elemental mapping of Ni-MOF measured ex-situ after 30 cycles of CV (1.13 to 1.67 V *vs*. the RHE, 10mV s^{-1}) in a) 1M p-KOH, and b) 1 M p-KOH with 0.02 M ex-CL. Corresponding XPS spectras of c) O 1s and d) Ni 2p photoelectrons. *In-situ* Raman spectra of Ni-MOF around 300 to 700 cm^{-1}, a range diagnostic for distinguishing Ni-MOF from NiOOH species, were recorded in a home-made electrochemical cell in 1 M p-KOH with : e) 0.00 M ex-CL (linker-free), f) 0.01M ex-CL, g) 0.02 M ex-CL, and h) 0.05 M ex-CL, ranging from open circuit potential (OCP) to 1.58 V *vs.* RHE

with (OCP, 1.03, 1.13, 1.23, 1.33, 1.38, 1.43, 1.48, 1.53, 1.58 V *vs*. RHE). A quartz substrate coated with Au of 0.785 cm^{-2} was used as the working electrode for *In-situ* Raman test, Hg/HgO as the reference electrode, and Pt wire as the counter. All potentials have been corrected to RHE. In the Figure 4.3e-h, the symbol of ▲ represents MOF peak, the symbol of ★ represents NiOOH.

For the cycled Ni-MOF derived electrodes, an additional peak at lower binding energies (529.6 eV) was observed in both electrolytes, likely attributable to Ni-oxide (Ni-O) species. It should be noted that the Ni-MOFs showed insulating character during the XPS experiment, which was mitigated by an electron gun. However, small charging effects were still observed. The Ni 2p spectrum of pristine MOFs shows multiplet splitting and satellite peaks that were centered at binding energies of about 856.9 (Ni $2p_{3/2}$) and 874.8 eV (Ni $2p_{1/2}$) in **Figure 4.3d**, which is assigned to oxidation state Ni^{2+}, in line with the results from XANES (**Figure A4.2**). Meanwhile, the Ni $2p_{3/2}$ spectra of cycled electrodes revealed two distinct peaks: $Ni(OH)_2$/NiO and Ni^{3+}, due to the NiOOH formation. A negative shift of the Ni 2p peaks to lower binding energies after cycling in both electrolytes suggests an altered local electronic structure of the Ni atom on the surface due to the gradual leaching of the carboxylate linkers, particularly due to the formation of NiO-like moieties, confirmed by HRTEM patterns, which typically exhibits lower binding energy than $Ni(OH)_2$ and Ni-MOF.[43]

In-situ Raman spectroscopy was also employed to systematically explore the impact of structural reconstruction during OER with the addition of ex-CL, as illustrated in **Figures 4.3e-h and A4.20–22**. When the Ni-MOF was tested in ex-CL free p-KOH (**Figure 3e**), two distinct bands at 407 and 629 cm^{-1} emerged at open circuit potential (OCP), originating from the framework incorporated linker of the Ni-MOF (**Figure A4.23**). Specifically, the 407 cm^{-1} band corresponds to out-of-plane skeletal vibrations, while the 629 cm^{-1} band corresponds to ring deformation of the linker.[44] These characteristic MOF bands remained unchanged until the potential was raised to 1.38 V

vs. RHE. Subsequently, two new Raman bands emerged around 479 cm^{-1} (Eg bending) and 560 cm^{-1} (A1g stretching), attributed to Ni-O vibrations of the surface intermediate NiOOH, concomitant with a decrease in MOF band intensity.[45] Upon applying higher potentials in 1 M p-KOH, the MOF bands degraded and disappeared at 1.48 V. Notably, the MOF bands persisted longer with the additional ex-CL, seen in **Figures 4.3f-h**; and particularly, a prominent band at 407 cm^{-1} of MOF can still be observed even at 1.58 V *ys*. RHE in p-KOH with 0.05 M ex-CL. Interestingly, the presence of the coordinated COO^- species at 1429 cm^{-1} in the Ni-MOF decreased as the potential increased in **Figures A4.20-22**. However, the presence of the free (uncoordinated) COO^- at 1390 cm^{-1}, which resulted from the addition of ex-CL, remained clearly visible. The intensity ratio of the two Ni-O Raman bands (I_{560}/I_{479}) serves as a metric for evaluating the structural disorder/defect of derived NiOOH. Specifically, a higher I_{560}/I_{479} ratio indicates a more disordered phase.[46] In 1 M p-KOH, the ratio of I_{560}/I_{479} reached 0.41 at 1.58 V vs. RHE, significantly lower than the ratios observed in presence of ex-CL *i.e.,* 0.77, 0.79, and 0.64 in 0.01 M, 0.02 M, and 0.05 M ex-CL, respectively. These results indicate that the additional ex-CL in the electrolye induces a more disordered intermediate than in the normal (pure) alkaline solution. Given that the O-H group between 3000-4000 cm^{-1} was masked by a significant water band during *in-situ* Raman testing, our study combines *in-situ* findings with time-dependent Raman results that track O-H changes and MOF degradation observed in XRD results. This supports the hypothesis that the use of an additional carboxylate linker can effectively modulate the dynamic equilibrium between the degradation and reconstruction of Ni-MOF precursors, leading to highly OER-active intermediate $Ni(OH)_2$/NiOOH species. Interestingly, this allows for the more disordered and, thus, more OER active phase to be more abundant.

Furthermore, the mixed metal (solid solution) NiFe-MOF ($[(NiFe)_2(OH)_2BPDC]$) was used as another example (unless otherwise mentioned, the Ni:Fe ratio in this work is

around 3:1, **Figure A4.24**) to further investigate the validity and scope of our hypothesis. Despite similarities in morphology and structure between the two isostructural MOFs (**Figures A4.25-28**), NiFe-MOF exhibited rapid degradation in alkaline electrolytes. Specifically, the characteristic MOF peak at 6.2° (001) vanished completely within 30 minutes in 1 M p-KOH, with new peaks attributed to $NiFe(OH)_2$ emerging at 11°, 23°, 34°, and 38° in **Figures A4.29-30**.[47] Furthermore, Raman data of NiFe-MOF submerged in p-KOH for 30 minutes unveiled additional bands at ~453 and ~526 cm^{-1}, indicative of the emergence of Ni–-OH symmetric stretching mode vibrations and structural defects originating from $NiFe(OH)_2$ (**Figures A4.31-32**).[48] Adding extra linkers in the solution barely reduced the degradation of the MOF structure, as no discernible MOF peaks were detected after 30 minutes. However, analysis of the transformation process revealed that the resulting $NiFe(OH)_2$ compound exhibited increased disorder in solutions containing the extra-linker, as illustrated in **Figure A4.33**.

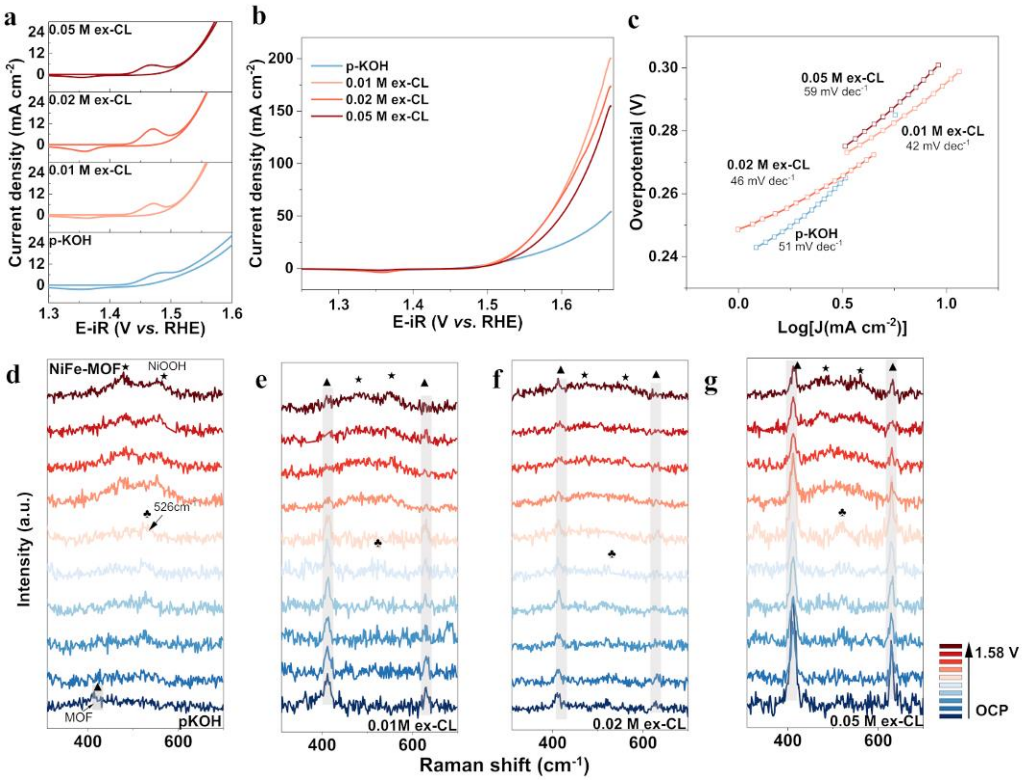

Figure 4.4. Electrochemical characterization of NiFe-MOF in 1M p-KOH with the

addition of 0.00 - 0.05 M of ex-CL. The NiFe-MOFs were cycled (activation process) from 1.13 to 1.67 V *vs*. the RHE with IR correction with 10 mV/s (Hg/HgO was used as the experimental reference electrode and potentials were corrected for RHE, glassy carbon as RDE working elerctrode). The reported electrochemical date were taken when the intensity of anodic peaks of of Ni^{3+}/Ni^{2+} did not no longer increase: a) Redox Peaks of NiFe-MOF ([$(NiFe)_2(OH)_2$BPDC]) in 1 M p-KOH with a 0.00-0.05 M ex-CL. b) OER activity; c) Tafel slope in 1 M P-KOH with a 0.00-0.05 M ex-CL. *In-situ* Raman spectra in 1 M p-KOH with d) 0.00 M ex-CL (linker-free) , e) 0.01 M ex-CL, f) 0.02 M ex-CL, and g) 0.05 M ex-CL, ranging from open circuit potential to 1.58 V *vs*. RHE with (OCP, 1.03,1.13,1.23,1.33,1.38, 1.43,1.48,1.53, 1.58 V *vs*. RHE). In the Figure 4.4d-g, the symbol of ▲ represents MOF peak, the symbol of ★ represents NiOOH, the symbol of ♣ represents $NiFe(OH)_2$.

Electrochemical measurement of NiFe-MOF, following the same activation procedure as the Ni-MOF, yielded interesting insights (**Figures 4.4a–c and A4.34–35**). While the anodic peak remained relatively consistent across different conditions, the introduction of extra linkers resulted in improved OER activities. The overpotentials for 0.01, 0.02, and 0.05 M ex-CL were 295±8, 291±4, and 296±9 mV, respectively, compared to the 313±4 mV overpotential of 1 M p-KOH at 10 mA cm^{-2} in **Figures 4.4b and A4.36**. Tafel slope analysis further supported this trend, with values of 51, 42, 46, and 59 mV dec^{-1} for concentrations increasing from 0.00 to 0.05 M ex-CL.

Furthermore, HRTEM images of cycles NiFe-MOFs in both ex-CL free p-KOH and with an additional linker concentration of 0.02 M revealed distinct lattice fringes corresponding to the (002) planes from NiOOH (or NiFeOOH) (**Figures A4.37-38**).[49] Additionally, EDS mapping confirmed the even distribution of Ni, Fe, O, and residual C (**Figures A4.37-38**). Analysis indicated a transition process during OER, supported by supplementary XPS data showing a decrease in carbonaceous species, such as C-O and O═C-O (O═C-O* and *O═C-O), and an increase of M-O (Ni/Fe) oxides (**Figure A4.39a**). Notably, the Ni 2p spectrum of the pristine NiFe-MOFs resembled those of

Ni^{2+} in the original Ni-MOF, with binding energies around 856.9 and 874.8 eV (**Figure A4.39b**). Post-cycling electrodes exhibited the formation of Ni^{3+} species that were discernible from XPS deconvolution. Meanwhile, the Fe 2p region in the XPS indicates that the Fe oxidation state (Fe^{3+}) remains constant during cycling, which is in agreement with XANES analyses (**Figures A4.39c and A4.40**).

In-situ Raman spectroscopy provided additional insights into electrochemical changes (**Figures 4.4d–g**). In a 1 M p-KOH solution, NiFe-MOF underwent a rapid transformation with MOFs' bands at 407 and 629 cm^{-1} to $NiFe(OH)_2$ at 526 cm^{-1} at OCP, and the MOF bands completely disappeared at 1.03 V *vs*. RHE. Subsequently, the NiOOH peak appeared after 1.43 V *vs*. RHE. Interestingly, the synergy with Fe during reconstruction may induce a transition to a more disordered phase as compared to the process observed with Ni-MOF in p-KOH (1M). Beyond 1.58 V *vs*. RHE, the relative ratio of I_{560} /I_{479} increased to 0.59, significantly higher than that of Ni-MOF. Remarkably, the addition of ex-CL decelerated degradation, allowing MOF peaks to persist longer, as evidenced by peaks retained at 1.43 V *vs*. RHE for 0.01 M ex-CL, and 1.58 V *vs*. RHE for 0.02 M ex-CL and 0.05 M ex-CL. The corresponding I_{560} /I_{479} ratios increased to 1.05, 1.12, and 1.02 for 0.01 M, 0.02 M, and 0.05 M ex-CL, respectively. In conclusion, while the presence of Fe renders NiFe-MOF significantly less stable in 1 M p-KOH solution, the resulting $NiFe(OH)_2$ primarily adopts a disordered α-$Ni(OH)_2$ phase. Despite rapid NiFe-MOF transformations, the addition of ex-CL to the electrolyte may induce a transition to a more amorphous, disordered phase, ultimately enhancing OER efficiency.

Additionally, another type of MOF, such as Ni-BDC-MOF (BDC: terephthalic acid), was explored in 1 M p-KOH with extra linkers (e.g., ex-CL-BDC, K_2BDC) to assess the general applicability of this approach to other MOF systems, as shown in **Figure A4.41**. Ni-BDC-MOF powders were first immersed in 1 M p-KOH, with and without additional carboxylate linkers (K_2BDC, ex-CL-BDC), for 15 minutes to investigate the degradation and reconstruction processes (**Figure A4.41a**). Compared to BPDC-

MOFs, Ni-BDC-MOFs exhibited greater instability, with their characteristic MOF peaks disappearing completely and being replaced by the $Ni(OH)_2$ phase in all samples, even with the addition of ex-CL-BDC (0.00–0.10 M). The XRD patterns of Ni-BDC-MOF in 0.01 M ex-CL closely resembled those in pure KOH, indicating similar reconstruction behavior. However, increasing ex-CL-BDC concentrations (e.g., 0.05 M and 0.10 M) resulted in broader $Ni(OH)_2$ peaks, suggesting a more disordered structure at higher concentrations.

The OER activities of Ni-BDC-MOF in alkaline electrolytes with varying ex-CL-BDC concentrations (0.00–0.10 M) were further examined, as shown in **Figure A4.41b**. Significant improvements in OER performance were observed at 0.10 M and 0.05 M ex-CL-BDC, with overpotentials of 392 mV and 423 mV, respectively, which were substantially lower than the 468 mV measured in pure KOH. Thus, beyond BPDC-MOFs, this strategy of adding extra carboxylate linkers also proves effective in modifying the surface reconstruction process in BDC-type MOFs (Ni), despite their inherent instability in alkaline electrolytes.

Prior to conducting chronopotentiometry experiments, the influence of pH on MOF degradation and reconstruction was explored (**Figures A4.42-43**). Ni-MOF in this work exhibited high stability at pH levels of 11 and 13, with only a small amount of α-$Ni(OH)_2$ formation observed after immersion in a 0.1 M p-KOH solution with a pH of 13.2 for 240 minutes. NiFe-MOF degradation was somewhat inhibited, with distinct MOF bands still visible after immersion in solutions with pH levels of 11 for 240 minutes and 13.2 for 30 minutes. Nevertheless, the pH level impacts the reconstruction process. This is supported by data showing a correlation between lower pH levels and more disorder in the resultant $NiFe(OH)_2$. Additionally, the amount of β-$Ni(OH)_2$ phase, estimated from the ν(OH) Raman peak at ~3580 cm^{-1}, is reduced when the pH is lower. For example, the amount of β-$Ni(OH)_2$ after 240 minutes at a pH of 13.2 was lower compared to that at pH 14.

Upon MOF activation in various pH electrolytes until reaching a stable state, the OER

performance was evaluated (**Figures 4.5a–b** and **A4.44**). Surprisingly, the impact of pH on the current density of Ni-MOFs does not follow a linear trend but exhibits a volcano-like pattern, with maximum current density observed at pH 13.5 (0.5 M p-KOH) at 1.55 V *vs*. RHE. NiFe-MOF exhibits more linear behavior across all pH levels; however, the slope between pH 14 and 13.5 is less steep than between pH 13.5 and 12. These results suggest that OER activity is reliant on pH level, as the precursor MOF to the active phases is significantly influenced by the pH. Consequently, chronopotentiometry analysis of Ni/NiFe MOF was conducted not only in pure solution or an extra-linker solution (0.02 M ex-CL) but also at varying pH levels, specifically pH 13.5 and 14.

Figure 4.5c illustrates the electrochemical durability of Ni-MOF deposited on a GC electrode at a current density of 10 mA cm^{-2}. The data indicate that a decrease in pH positively influences electrochemical stability. For instance, Ni-MOF tested in a 0.5 M p-KOH solution with a pH of 13.5 can maintain activity for about two hours under a current density of 10 mA cm^{-2}, whereas under comparable conditions but with a pH of 14, deactivation takes place in less than one hour. The introduction of the additional linker to the electrolytes extends the duration under a current density of 10 mA cm^{-2}, approximately to 2.24 hours in a 1 M p-KOH solution with pH 14 using a concentration of 0.02 M of ex-CL. In a 0.5 M p-KOH solution (pH 13.5), the duration extends to about 5.2 hours for Ni-MOF with the same concentration of ex-CL. Importantly, the presence of Fe enhances electrochemical stability at a current density of 10 mA cm^{-2}. NiFe-MOF remains active even in highly alkaline solutions of 1 M p-KOH for a duration of 5.5 hours, with degradation rates of 3.2% and 2.6% observed for 0.5 M p-KOH in **Figure 4.5d**. Upon the addition of 0.02M ex-CL, the system exhibits increased stability, with the potential almost constant and experiencing a mere 0.9% and 0.7% increase at pH 14 and pH 13.5, respectively. Considering the limitations on the GC substrate, NiFe-MOF was also applied to carbon paper to assess chronopotentiometry at a current density of 10 mA cm^{-2} in a 1 M p-KOH solution

with 0.02 M ex-CL in **Figure 4.5e**. Even after 100 hours, electrochemical stability remained satisfactory. These findings from electrochemical stability tests and pH impact demonstrate that modulating the reconstruction process of MOFs toward the more disordered active metal hydroxide phases can enhance activities related to OER and can improve long-term electrochemical performance.

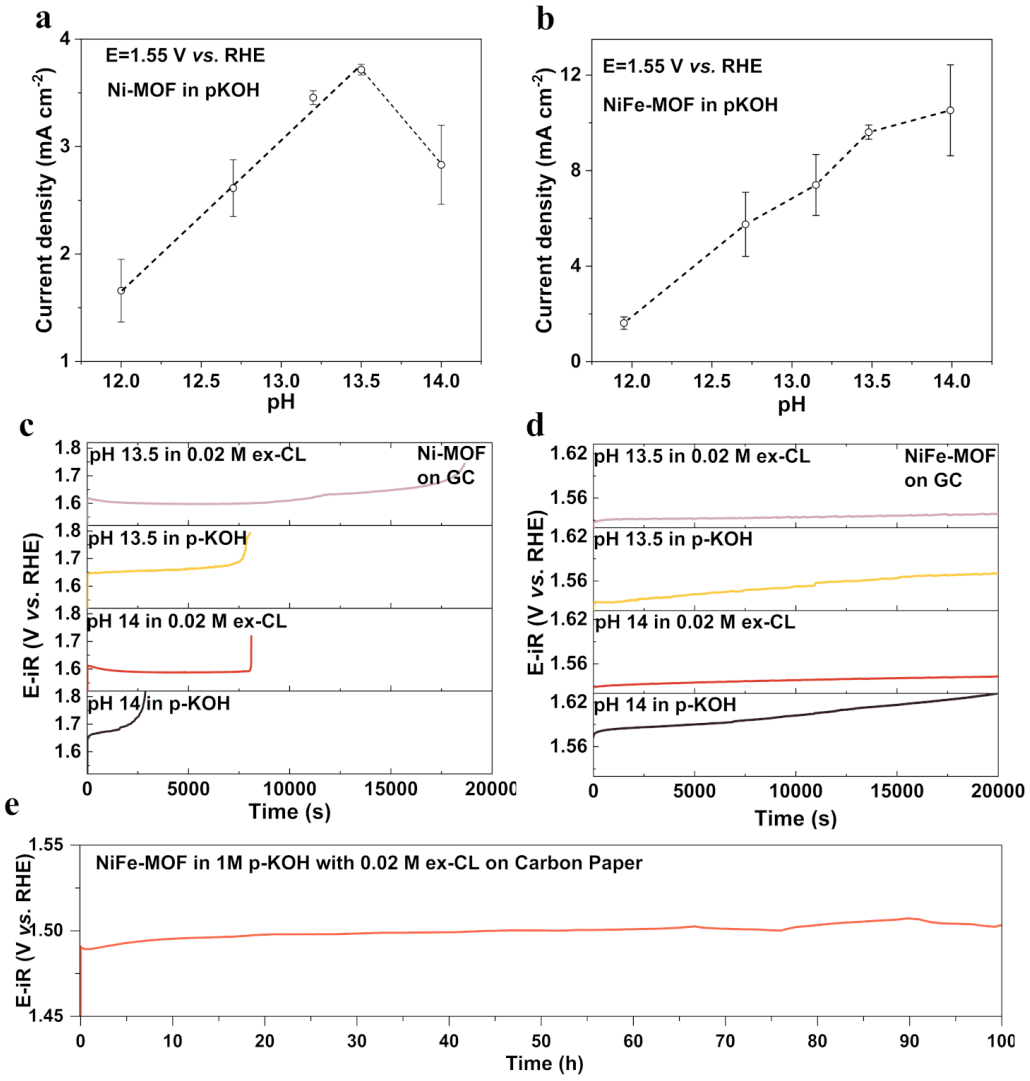

Figure 4.5. pH effect of a) Ni-MOF, and b) NiFe-MOF in Fe-free pKOH with pH 12.0-14.0. Chronopotentiometric response of c) Ni-MOF and d) NiFe-MOF on the glass carbon (RDE) in p-KOH with pH 14.0 and pH 13.5, with and without ex-CL under current density at 10 mA cm^{-2}. e) Chronopotentiometry response of NiFe-MOF in 1M p-KOH (pH:14) with 0.02 M ex-CL using carbon paper as collector under current density at 10 mA cm^{-2}.

4.3 Conclusion

During the OER process, (Fe)Ni-MOFs undergo reconstruction in the alkaline environment, transitioning from MOF precursors to metal hydroxides and eventually oxyhydroxides, which serve as active species. In this study, we manipulated the underlying MOF reconstruction process by employing a coordination modulation strategy. This strategy involved introducing additional carboxylate ligands to shift the coordination equilibrium at the metal sites, thereby competing with hydroxide ions, water, and other ligands. Time-resolved analyses using PXRD and Raman spectroscopy revealed that the presence of extra carboxylate linkers slows down the reconstruction of the MOFs without applied potentials. Moreover, increasing the concentration of linkers in alkaline solutions prolongs the preservation of the MOF bulk structure after alkali treatment. This influences the reconstruction process, also delaying the transition from a disordered to an ordered metal hydroxide phase. *In-situ* Raman spectroscopy during OER demonstrates that this reconstruction process is the primary factor contributing to the observed increase in OER activity. The Introduction of extra linkers extends the electrochemical lifetime in harsh alkaline environments by modifying the phase composition towards the more disordered and more active metaloxhydroxide phase, which becomes more abundant. These results provide new insights into improving the electrochemical performance of derived materials as OER catalysts in alkaline electrolytes, offering a deeper understanding of their electrocatalytic mechanisms.

4.4 Appendix

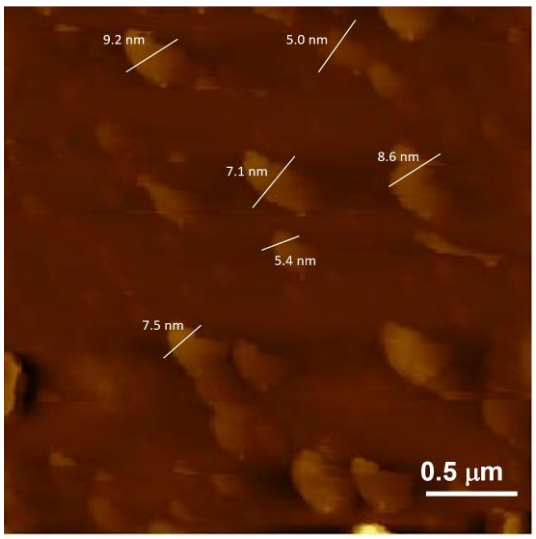

Figure A4.1. AFM image of Ni-BPDC-MOF(Ni-MOF, $[Ni_2(OH)_2BPDC]$).

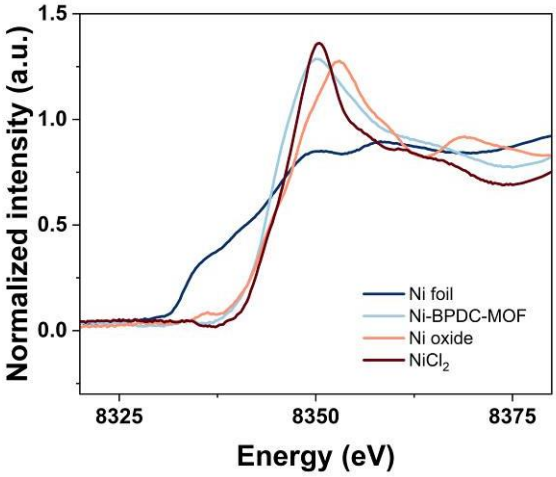

Figure A4.2. Ni K-edge XANES data of Ni-BPDC-MOF and reference samples.

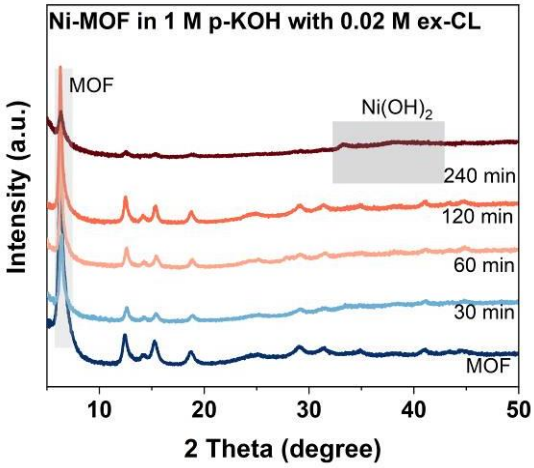

Figure A4.3. The XRD of time dependence effects of Ni-MOF in 1 M purified KOH (p-KOH, PH:14) with 0.02 M extra carboxylate linker (ex-CL).

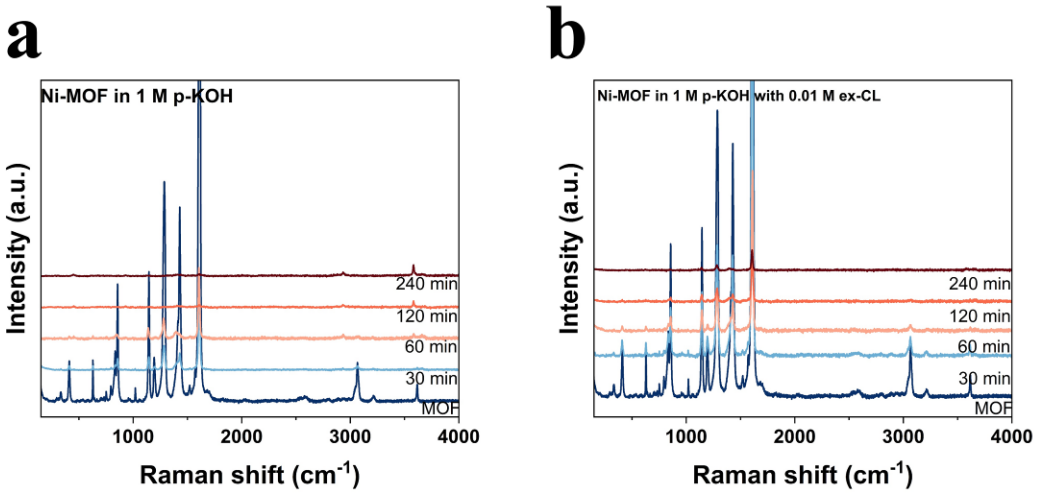

Figure A4.4. The Raman spectra of time dependence effects of Ni-MOF in 1 M p-KOH and with 0.01 M ex-CL.

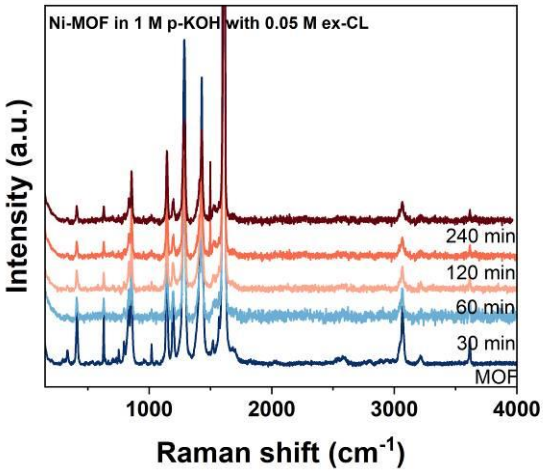

Figure A4.5. The Raman spectra of time dependence effects of Ni-MOF in 1 M p-KOH with 0.05 M ex-CL.

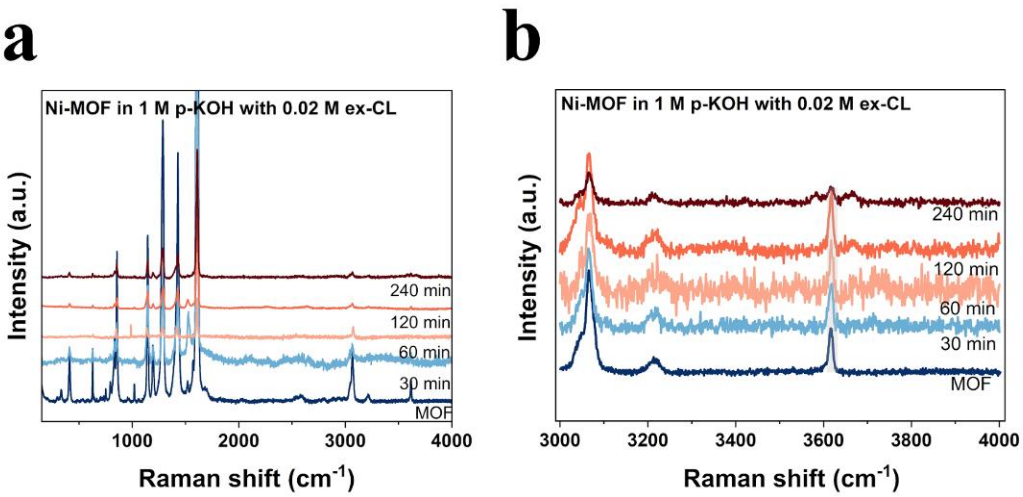

Figure A4.6. The Raman spectra of time dependence effects of Ni-MOF in 1 M p-KOH with 0.02 M ex-CL. a) Full spectra b) the spectra between 3000-4000 cm^{-1}.

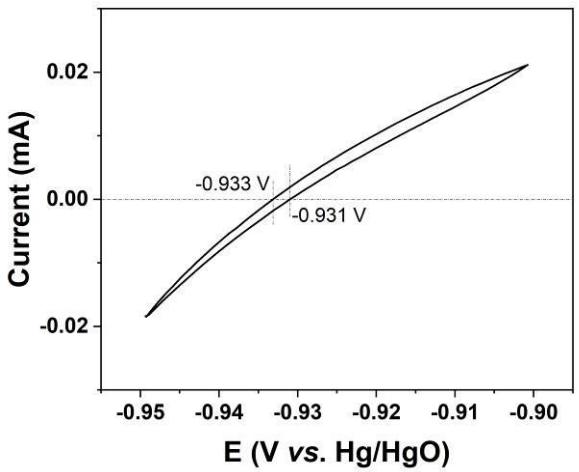

Figure A4.7. Potential calibration of the Hg/HgO reference electrode using a 1M NaOH solution as the filling liquid. The calibration experiment used a high-purity H_2 1 M p-KOH (pH = 14) electrolyte. The working electrode and counter electrode were made of two Pt wires, respectively. The CV test was conducted with a scanning rate of 5mV s^{-1}. The corresponding average potential (-0.932 V) represents the thermodynamic potential of the hydrogen evolution reaction. It shows that the E_{RHE} $=E_{Hg/HgO}$ +0.059pH+ 0.106.

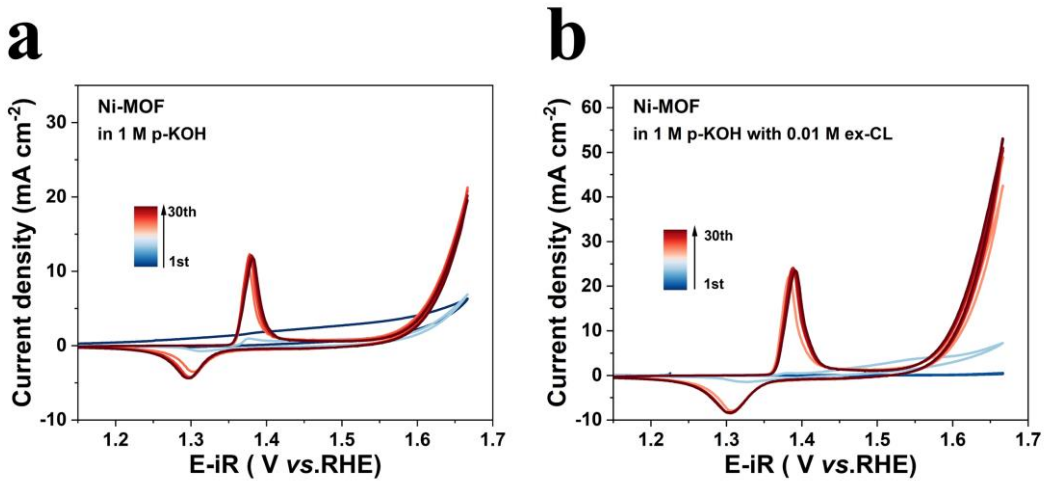

Figure A4.8. Continuous cyclic voltammogram study (activation process) of Ni-BPDC-MOF in a) 1M p-KOH and b) 1M p-KOH with 0.01 M ex-CL, from 1.13 to 1.67 V *vs*. the RHE at a scan rate of 10 mV s^{-1}. Every 5 CV cycles are plotted here.

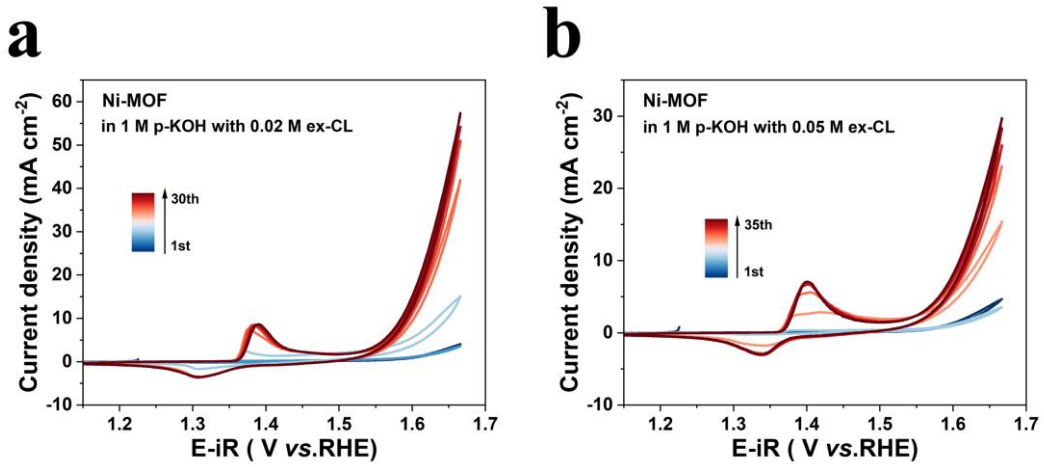

Figure A4.9. Continuous cyclic voltammogram (activation process) study of Ni-BPDC-MOF in a) 1M p-KOH with 0.02 M ex-CL and b) 1M p-KOH with 0.05 M ex-CL, from 1.13 to 1.67 V *vs*. the RHE at a scan rate of 10 mV s^{-1} . Every 5 CV cycles are plotted here.

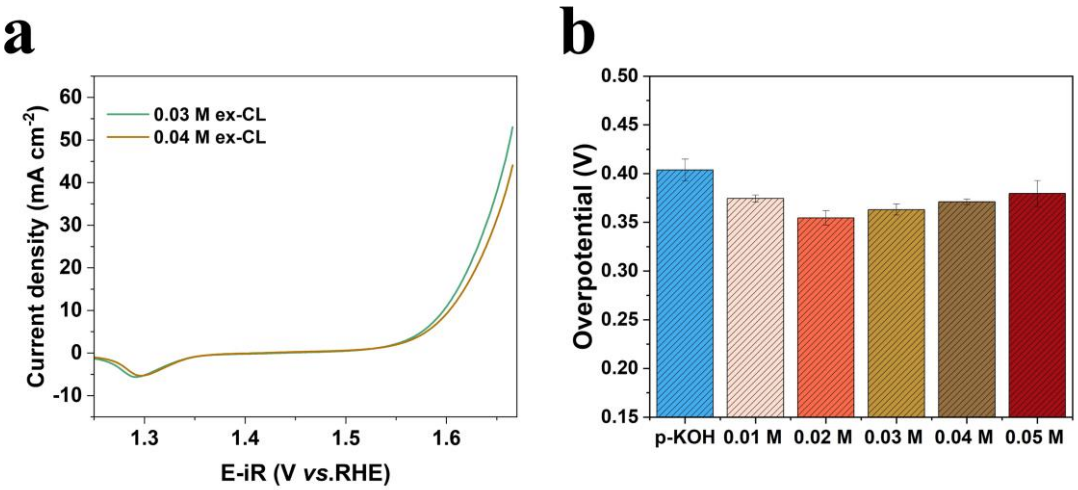

Figure A4.10. a) OER activities of Ni-BPDC-MOF in 1M p-KOH with 0.03 and 0.04 M ex-CL, in which the Ni-MOFs were cycled in 1M p-KOH with 0.03 and 0.04 M ex-CL from 1.13 to 1.67 V vs. the RHE with IR correction at 10 mV/s (Hg/HgO was used as the experimental reference electrode and potentials were corrected for RHE, glassy carbon as the RDE working electrode. The LSV data were taken when the intensity of anodic peaks of Ni^{3+}/Ni^{2+} no longer increased. b) Overpotentials of the

Ni-MOFs in 0-0.05M ex-CL at current density at 10 mA cm^{-2}.

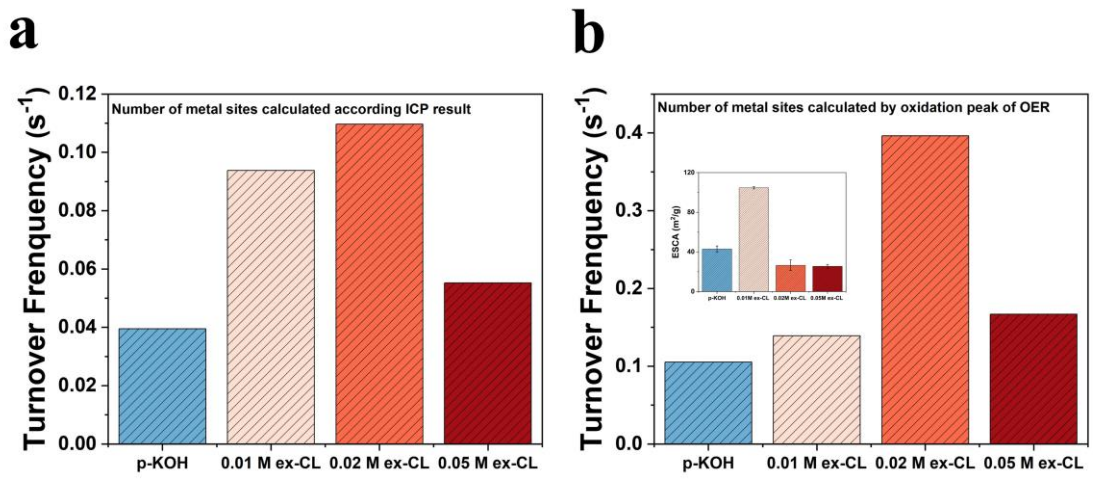

Figure A4.11. TOFs of Ni-MOFs in the pKOH electrolytes with 0.00-0.05 M ex-CL. The TOF values are based on the results of Figures 2a and b. a) TOFs calculated using the Ni site numbers according to the ICP-OES results with 24% Ni element of pristine Ni-MOFs. b) TOFs calculated the Ni site numbers according to OER's oxidation peak area analysis. The interior illustration of Figure A4.11b is the ECSA results of the Ni-MOFs in the 1 M KOH with 0.00-0.05 M ex-CL, which are calculated by integrated redox peak (Ni^{3+}/Ni^{2+}).[50-53] The formula ECSA=Q/(mq_0), Q is the charge required for the anodic oxidation (Ni^{3+}/Ni^{2+}) in LSV, m is the catalyst loading on the GCE surface (~0.245 mg cm^{-2}) and q_0 is the specific charge related to the formation of α-$Ni(OH)_2$ monolayer and it is 257 μC cm^{-2}. [50, 54-55] Moreover, the TOFs were determined using the formula:

TOF = (j × A)/(4F × n), where j × A(surface area of GC electrode, 0.196 cm^{-2})

denotes the current at an overpotential of 420 mV (1.65V *vs.* RHE), and n represents the number of moles of Ni deposited at the GC electrode, and the number of the moles calculated by oxidation peak, which is lined with the surface exposed Ni-sites

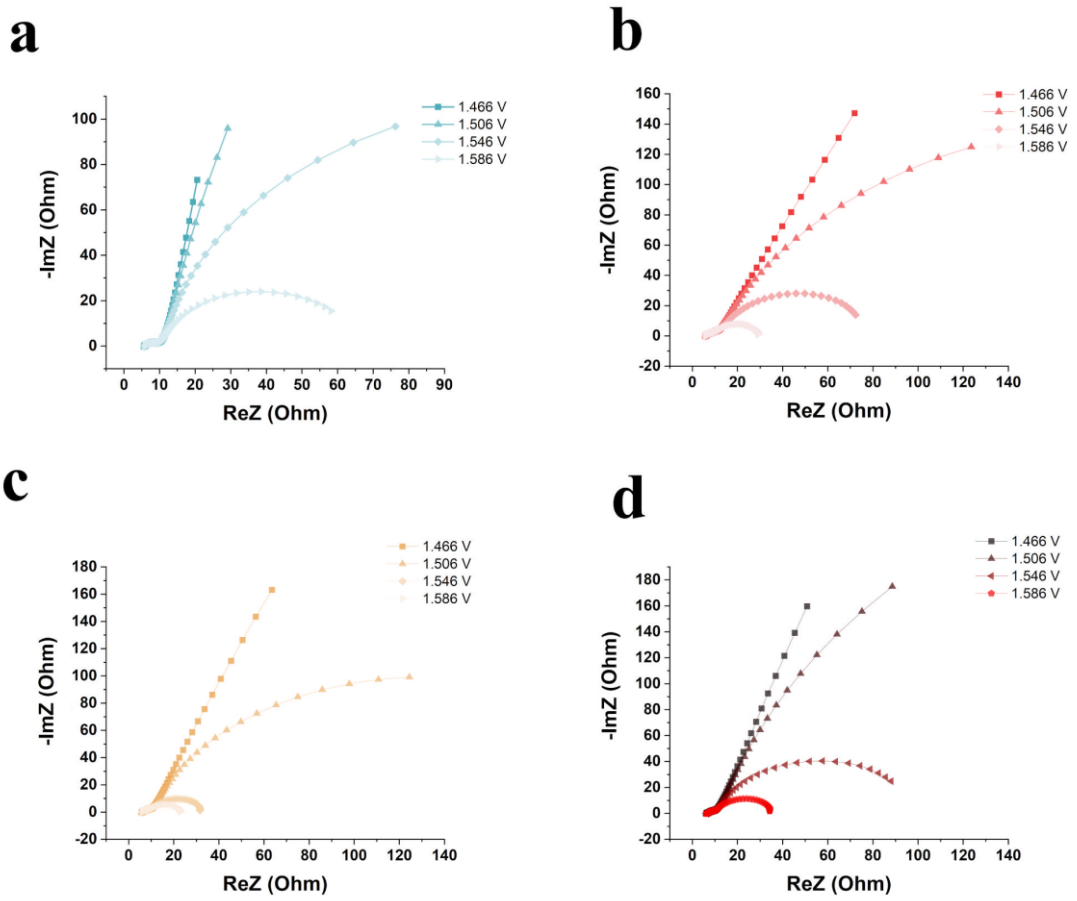

Figure A4.12. Electrochemical impedance spectroscopy (EIS) measurements of Ni -MOF in 1M p-KOH with a) Free-linker, b) 0.01 M ex-CL, c) 0.02 M ex-CL, d) 0.05 M ex-CL.

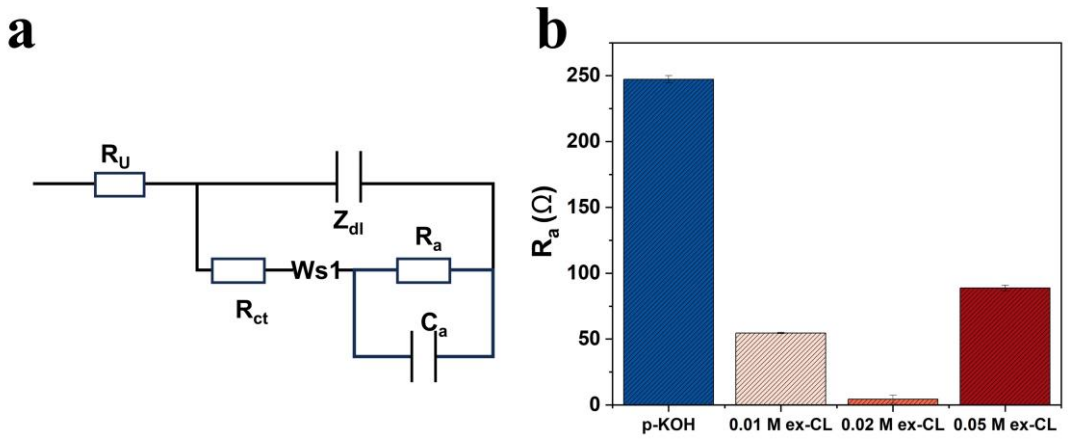

Figure A4.13. a) Fitting model for the EIS results with electrolyte resistance (Ru), a double layer impedance (Zdl), a charge transfer resistance (Rct), Warburg short element (W_{S1}), adsorption resistance (Ra), and the adsorption capacitance (Ca). b) Comparison of the adsorption resistance of Ni-MOF under different electrolytes at 1.546V *vs.* RHE.

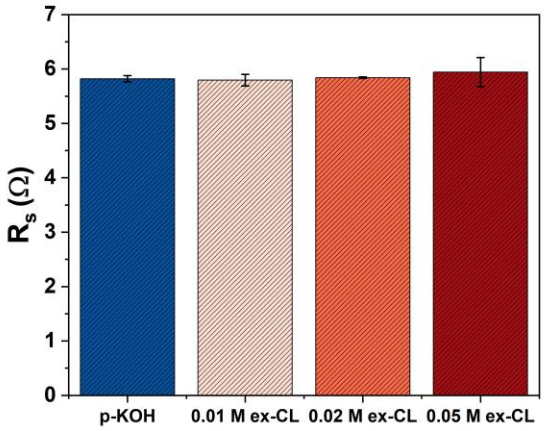

Figure A4.14. Resistance of the electrolyte (Rs) in different electrolytes. Notably, the volume of electrolytes used was about 100 ml, and a 97% iR correction was utilized during the electrochemical testing. The resistance changes of the electrolytes with the ex-CL (K_2BPDC) salt here can be ignored.

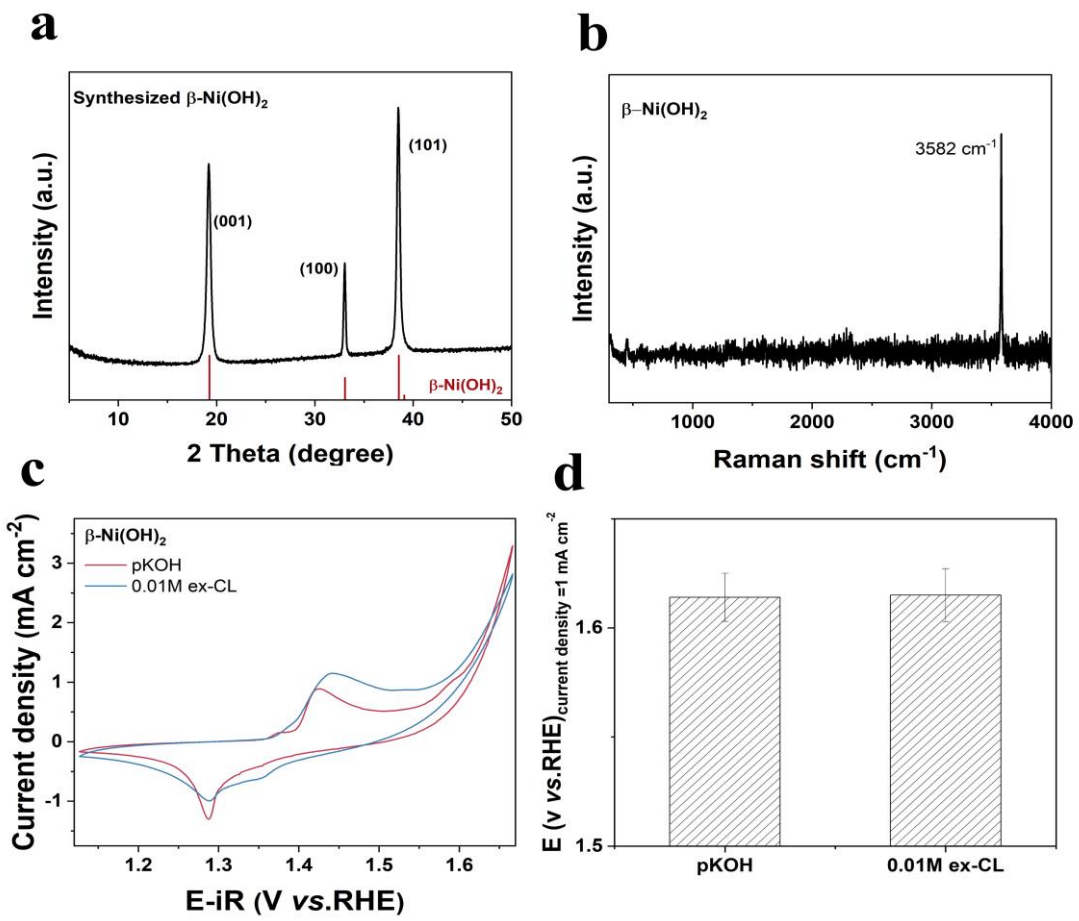

Figure A4.15. a) the XRD and b) Raman of the β-$Ni(OH)_2$ as the reference sample. c) OER activities of β-$Ni(OH)_2$ in 1M p-KOH with 0.00 and 0.01 M ex-CL and d) the comparing of the potential at current density = 1mA cm^{-2} of β-$Ni(OH)_2$ in 1M p-KOH with 0.00 and 0.01 M ex-CL. A similar performance identified the effect of the extra-linker on the electrode surface is neglectable, which allows us to focus on the influence of the ex-CL on the MOFs' reconstruction.

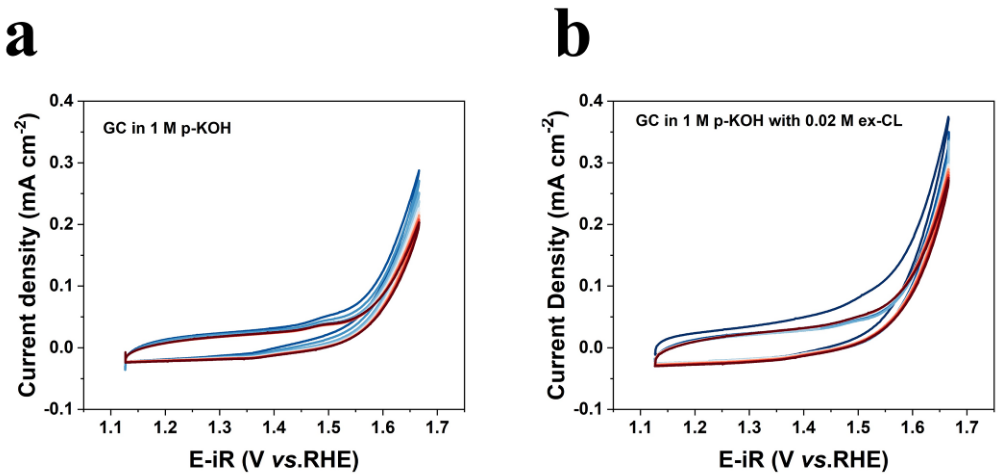

Figure A4.16. CV of black glass carbon (GC) in a) 1M linker-free p-KOH and b) 1M p-KOH with 0.02 M ex-CL from 1.13 to 1.67 V *vs*. the RHE with 97% IR correction with 10 mV s^{-1}.

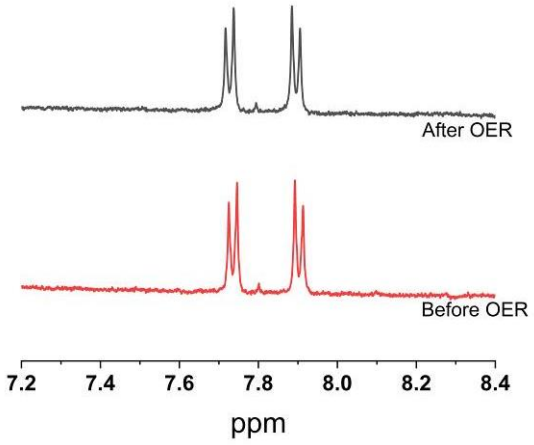

Figure A4.17. ^{1}H NMR spectra of 1M KOH electrolytes in D_2O (NMR solvent) with 0.02 M ex-CL before and after CV.

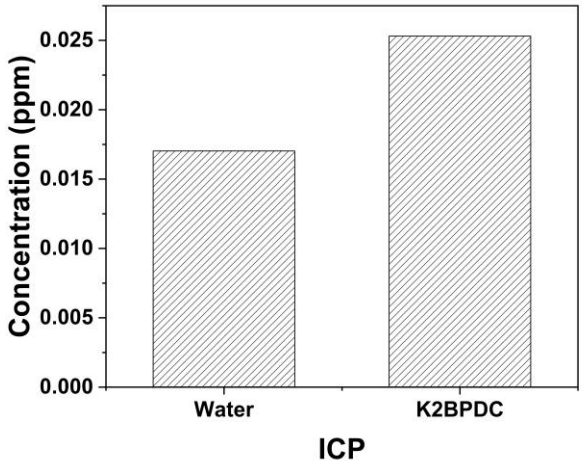

Figure A4.18. ICP-OES of 0.02 M ex-CL (K_2BPDC dissolved in DI water)

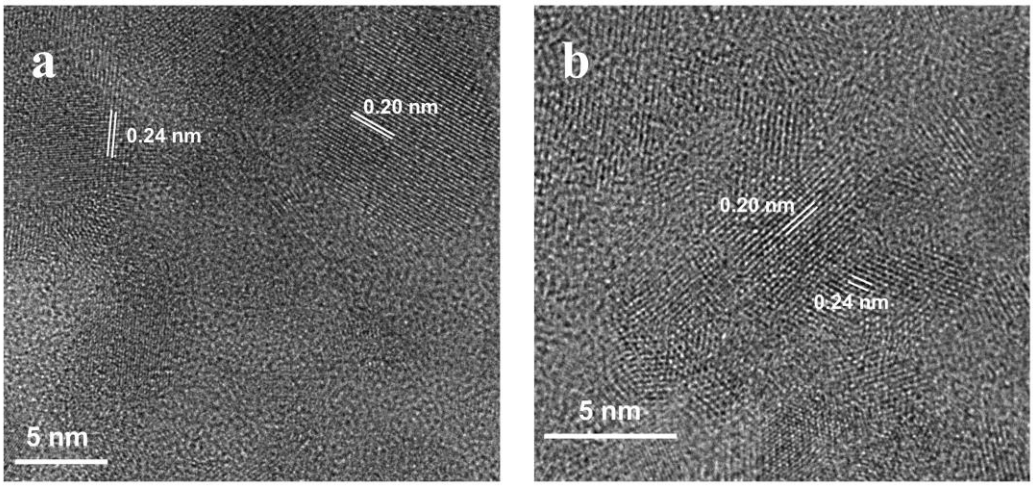

Figure A4.19. HRTEM of Ni-MOF after 30 CV cycles in a) 1 M p-KOH and b) 1 M p-KOH with 0.02 M ex-CL,lattice fringes with spacings of approximately 0.20 and 0.24 nm, corresponding to the (101) planes of NiO phase and (002) planes of NiOOH, respectively.

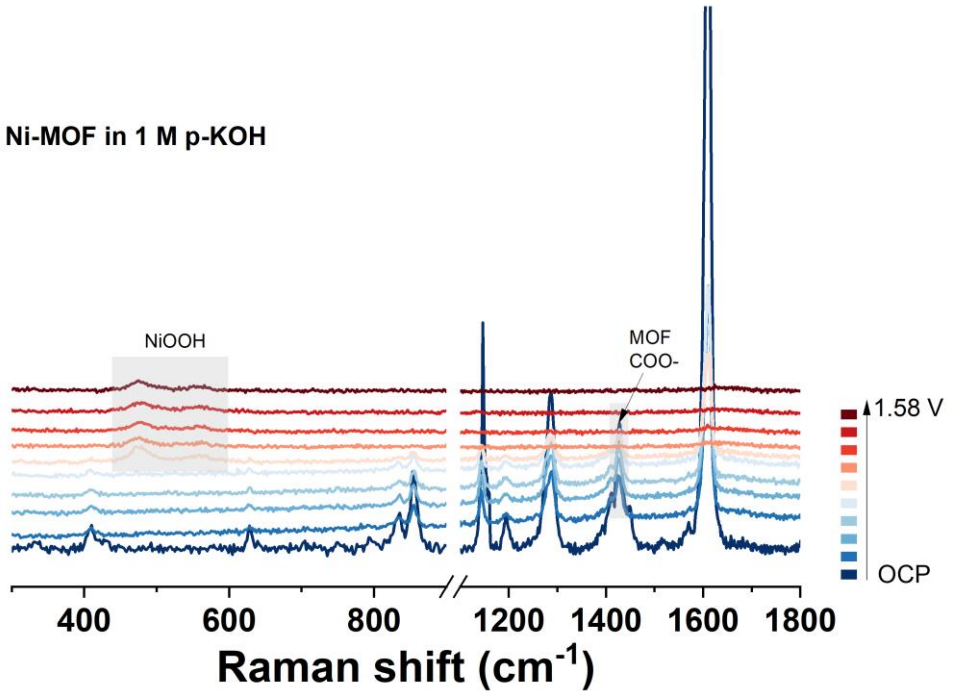

Figure A4.20. In-situ Raman spectra of Ni MOF in 1 M p-KOH from OCP to 1.58 V *vs*. RHE (OCP, 1.03, 1.13, 1.23, 1.33, 1.38, 1.43, 1.48, 1.53, 1.58 V *vs*.RHE).

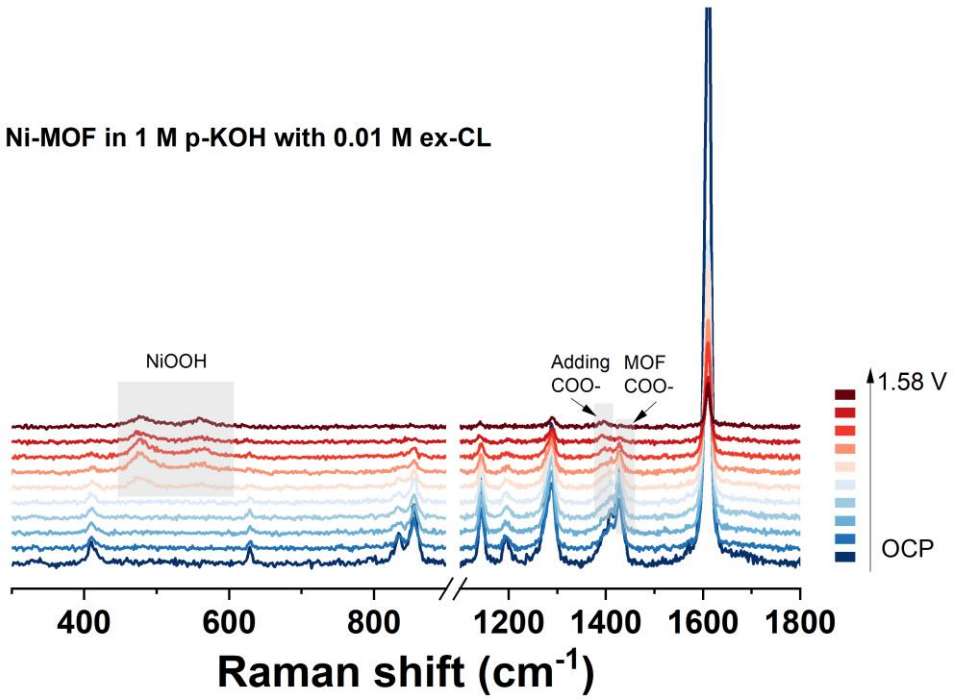

Figure A4.21. In-situ Raman spectra of Ni MOF in 1 M p-KOH with 0.01 M ex-CL from OCP to 1.58 V *vs*. RHE (OCP, 1.03, 1.13, 1.23, 1.33,1.38, 1.43, 1.48, 1.53, 1.58

V *vs.*RHE).

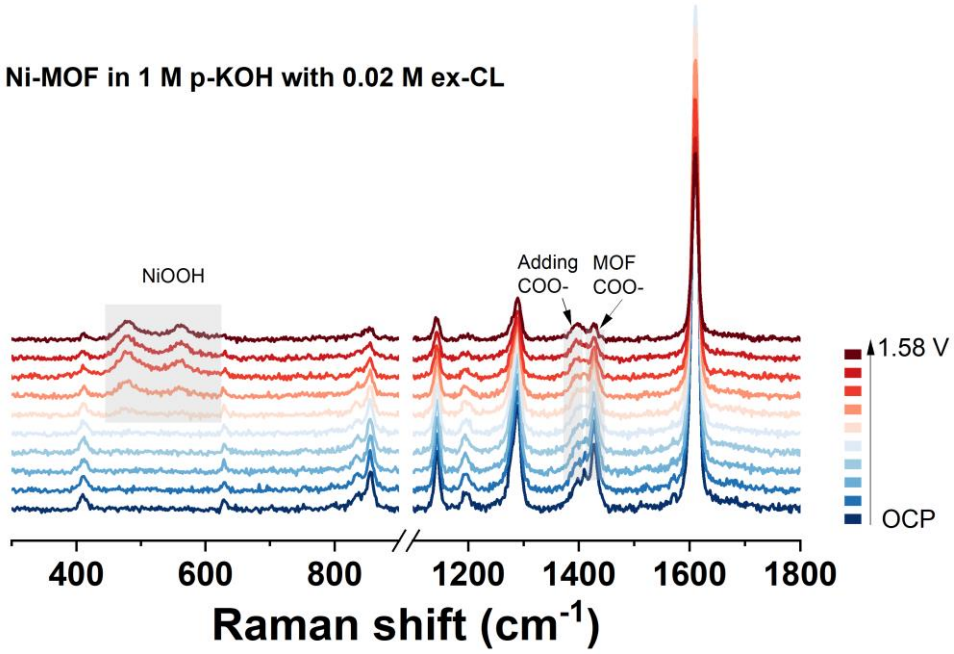

Figure A4.22. In-situ Raman spectra of Ni-MOF in 1M p-KOH with 0.02 M ex-CL from OCP to 1.58 V *vs*. RHE (OCP, 1.03, 1.13, 1.23, 1.33, 1.38, 1.43, 1.48, 1.53, 1.58 V *vs.*RHE).

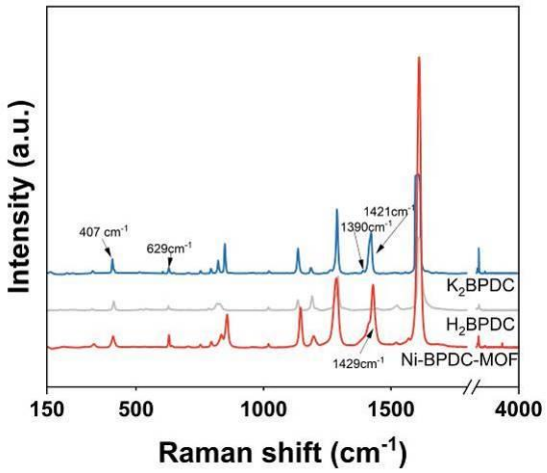

Figure A4.23. Raman spectroscope results of Ni-MOF (Ni-BPDC-MOF), H_2BPDC and K_2BPDC.

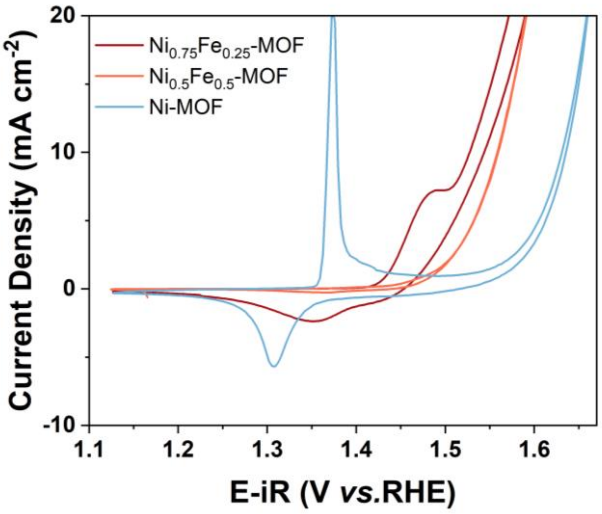

Figure A4.24. The OER activities of NiFe-BPDC-MOF with different Ni and Fe ratios were evaluated with 97% IR correction at a scan speed of 10 mV s^{-1} after the CV activation process. As shown in Figure A4.24, the OER activities of $Ni_{0.75}Fe_{0.25}$-MOF are superior to those of $Ni_{0.5}Fe_{0.5}$-MOF. Additionally, the oxidation peak is less visible in $Ni_{0.5}Fe_{0.5}$-MOF due to the high Fe concentration. It is well-known that a Ni: Fe ratio of approximately 3:1 in $NiFe(OH)_2$ yields good OER activities.[56] Therefore, in our work, unless otherwise specified, we used $Ni_{0.75}Fe_{0.25}$-MOF with a Ni: Fe ratio of around 3:1 as another example to further study the influence of ex-CL.

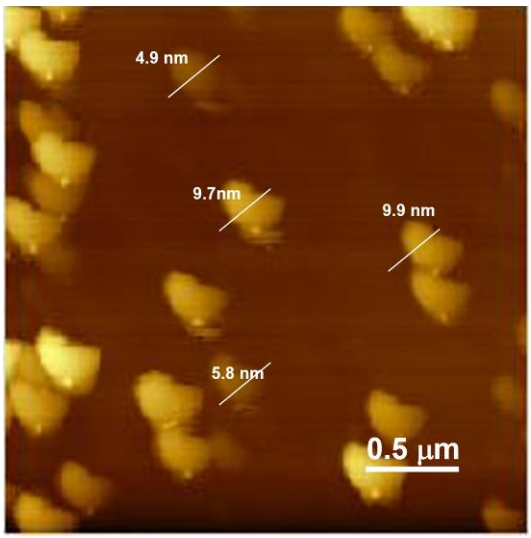

Figure A4.25. AFM image of NiFe- BPDC-MOF.

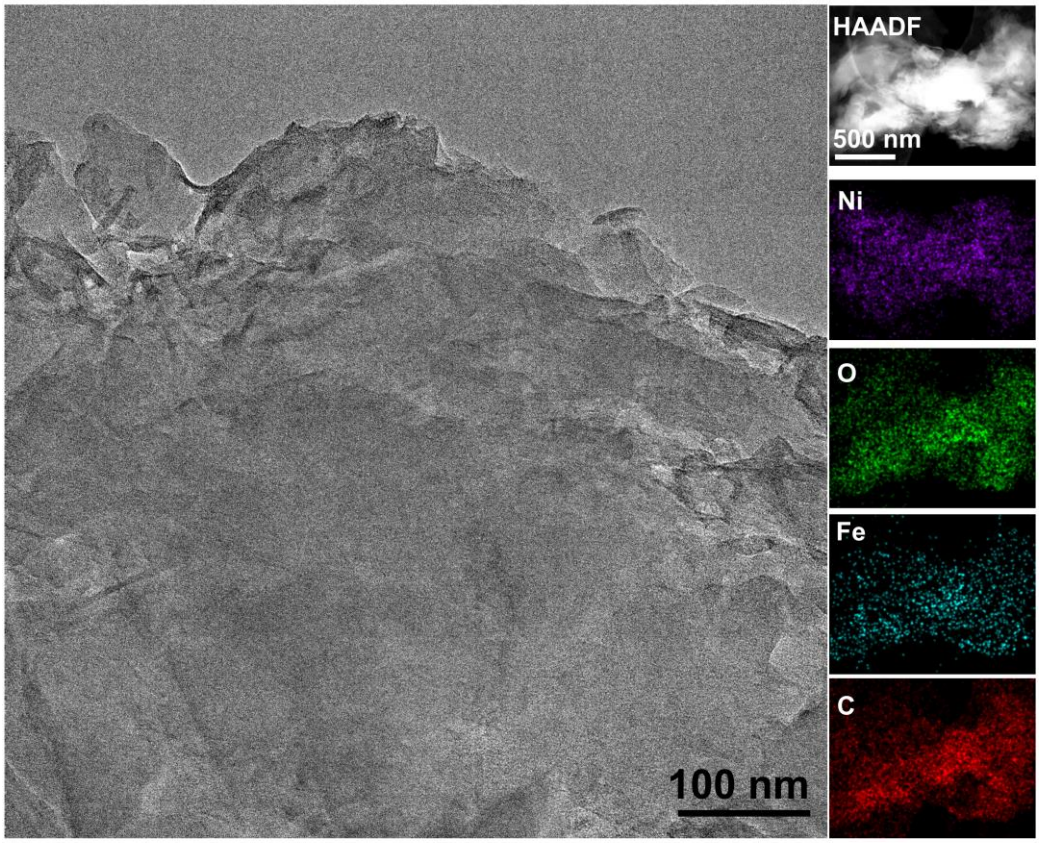

Figure A4.26. TEM and HAADF images of NiFe-MOF along with the corresponding EDS elemental maps with Ni, O, C, and Fe.

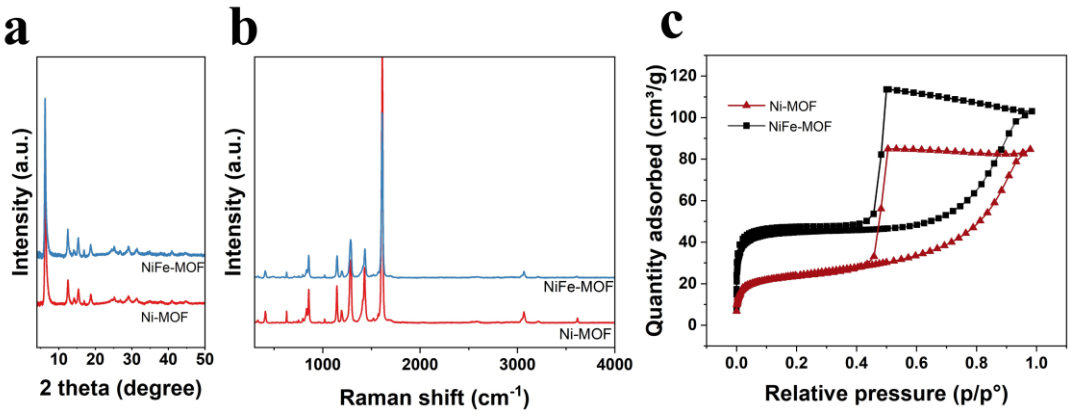

Figure A4.27. The comparison between NiFe-MOF with the Ni-MOF in a) XRD, b) Raman, and c) Brunauer-Emmett-Teller (BET) isotherm plots. The BET data were obtained under standard N_2 sorption measurements at 77 K, with both MOF powders

activated by degassing at 120°C for 40 hours. The results show that NiFe-MOF exhibits a higher BET surface area (177.72 ± 0.11 m²/g) compared to Ni-MOF (88.37 ± 0.13 m²/g), likely due to the incorporation of Fe into the structure.[57]

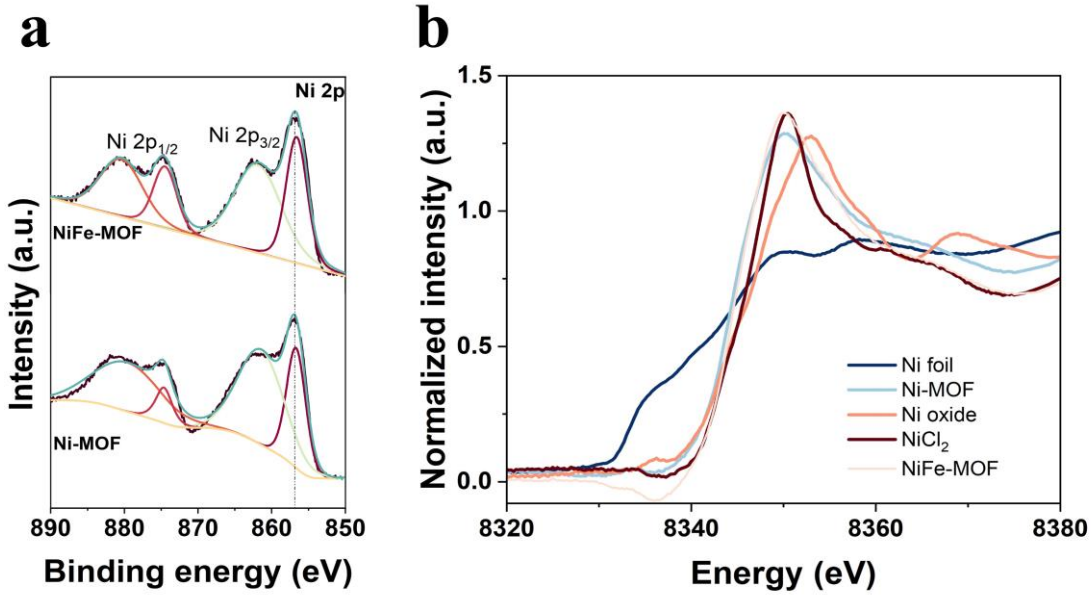

Figure A4.28. The comparison between NiFe-MOF with the Ni-MOF in a) XPS and b) XANES. It shows that the Ni state of 2+ in NiFe-MOF is similar to that in Ni-MOFs.

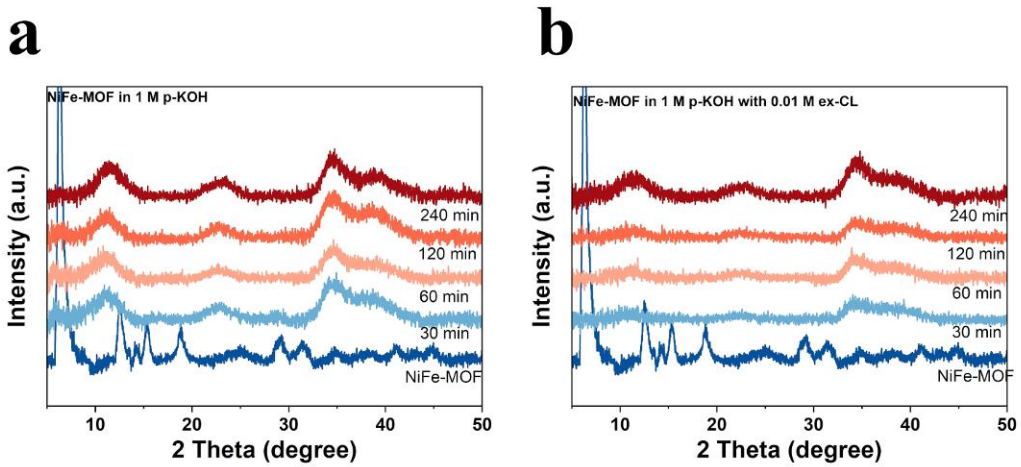

Figure A4.29. Monitoring structural transformation via time-dependent PXRD patterns during NiFe-MOF derivation in different alkaline electrolyte solution

without potential. a) in 1M linker free p-KOH, and b)1M p-KOH with 0.01 M ex-CL

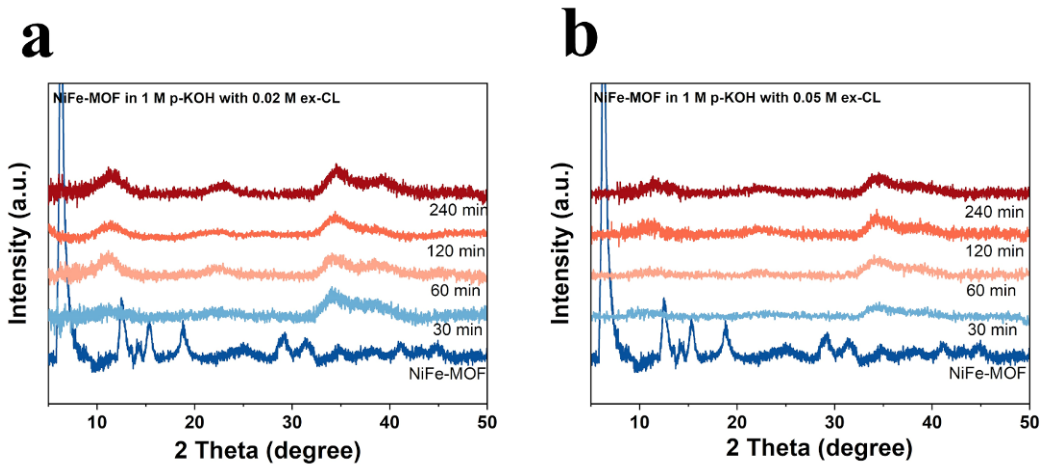

Figure A4.30. Monitoring structural transformation during NiFe-MOF derivation in different alkaline electrolyte solution without potential. a) in 1 M p-KOH with 0.02 M ex-CL, and b)1 M p-KOH with 0.05 M ex-CL.

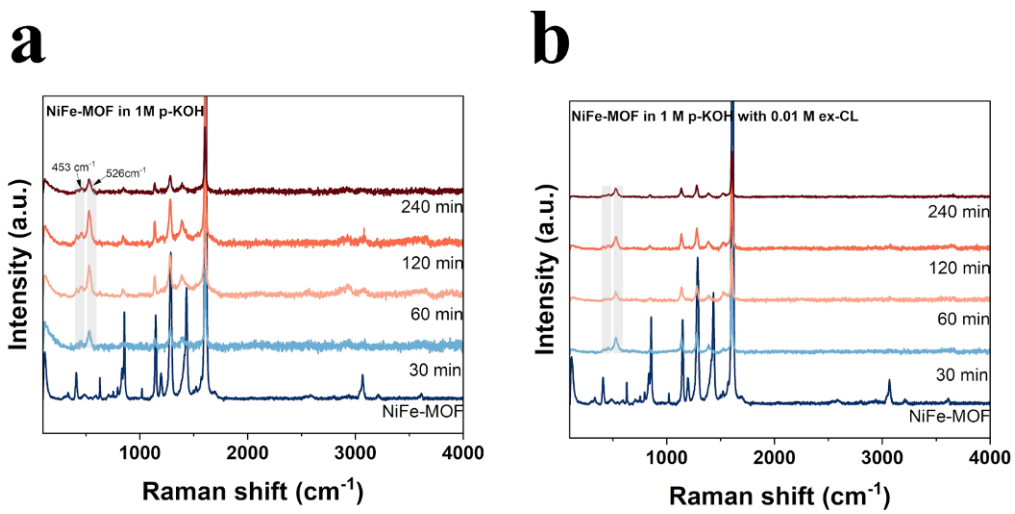

Figure A4.31. The Raman spectra of time dependence effects of NiFe-MOF in a) 1 M p-KOH and 1 M p-KOH with 0.01 M ex-CL for 0-240 min.

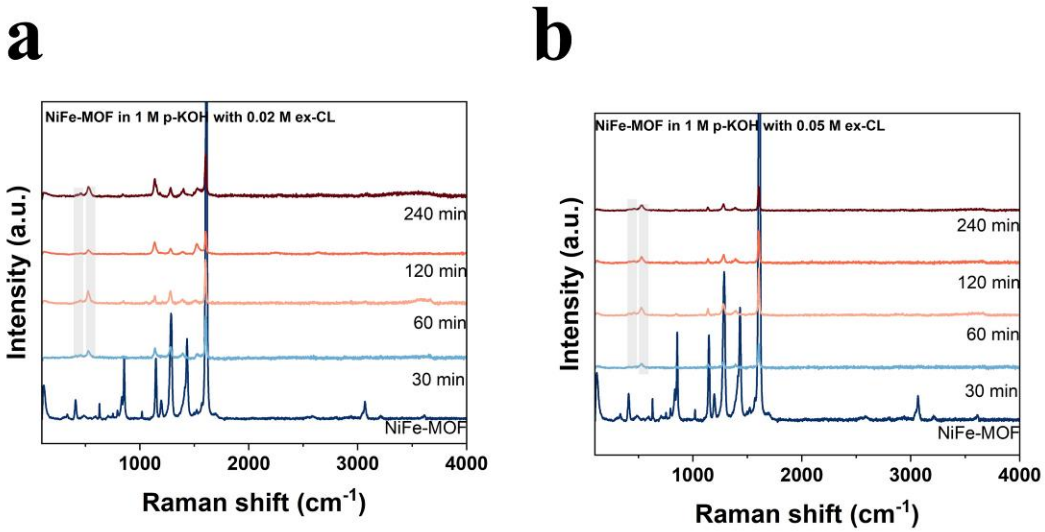

Figure A4.32. The Raman spectra of time dependence effects of NiFe-MOF in a) 1 M p-KOH with 0.02 M ex-CL and b)1 M p-KOH with 0.05 M ex-CL for 0-240 min.

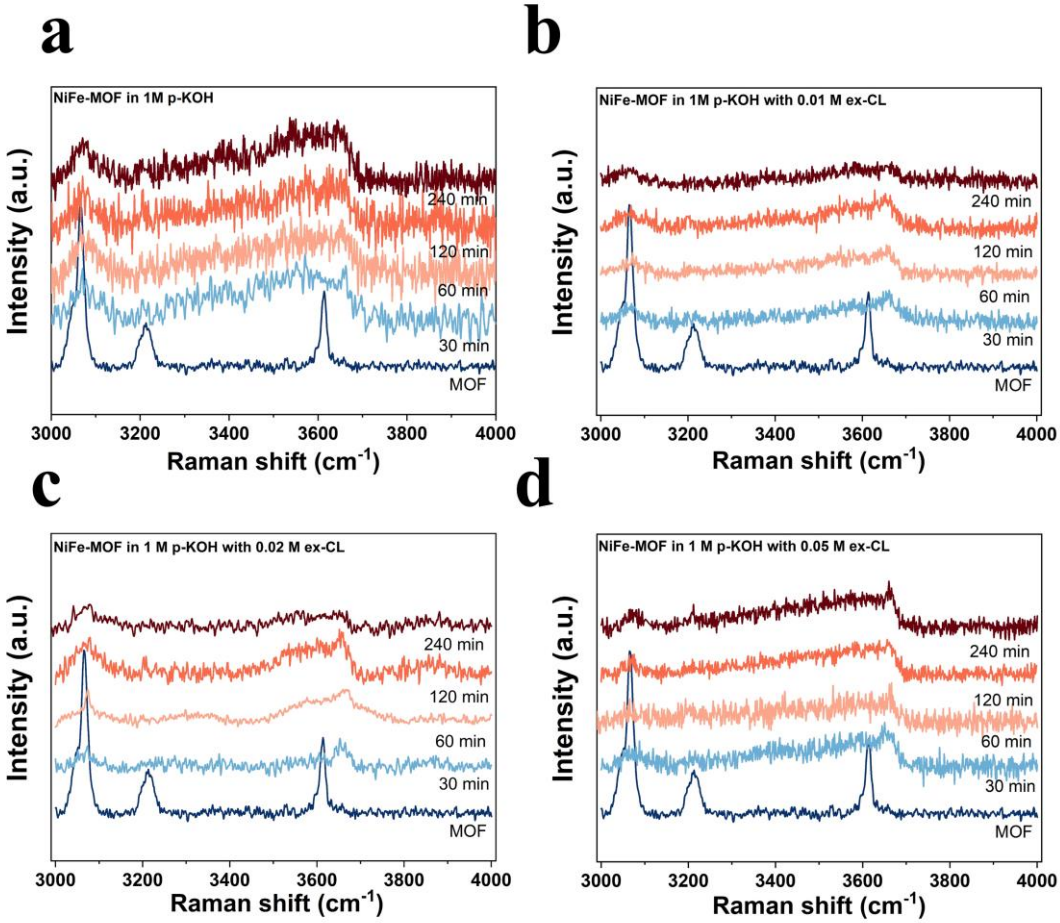

Figure A4.33. The Raman spectra of time-dependent effects of NiFe-MOF in a) 1M p-KOH b) with 0.01 M ex-CL, c) with 0.02 M ex-CL, d) and 1 M p-KOH with 0.05

M ex-CL for 0-240 min.

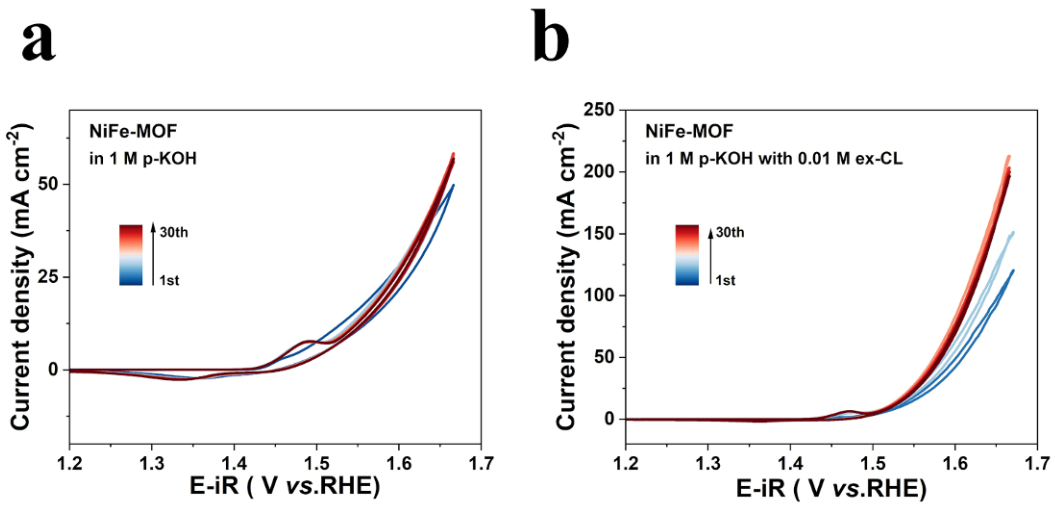

Figure A4.34. Continuous cyclic voltammograms study of NiFe-MOF for in a) 1M p-KOH and b) 1 M p-KOH with 0.01 M ex-CL, from 1.13 to 1.67 V *vs*. the RHE at a scan rate of 10 mV s^{-1}. Every 5 cycles were plotted here.

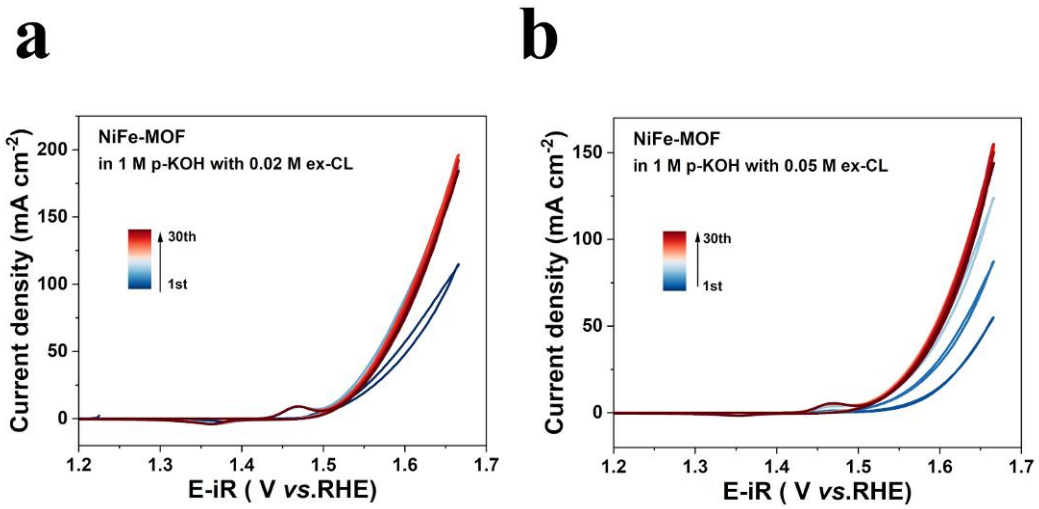

Figure A4.35. Continuous cyclic voltammograms study of NiFe-MOF 30 cycles in a) 1 M p-KOH with 0.02 M ex-CL and b) 1M p-KOH with 0.05 M ex-CL, from 1.13 to 1.67 V *vs*. the RHE at a scan rate of 10 mV s^{-1}. Every 5 cycles were plotted here.

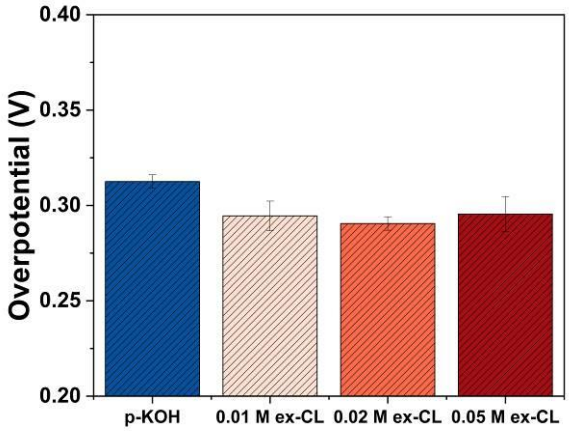

Figure A4.36. OER activities of NiFe-BPDC-MOF in 1 M p-KOH with 0.00-0.05 M ex-CL at current density at 10 mA cm^{-2}.

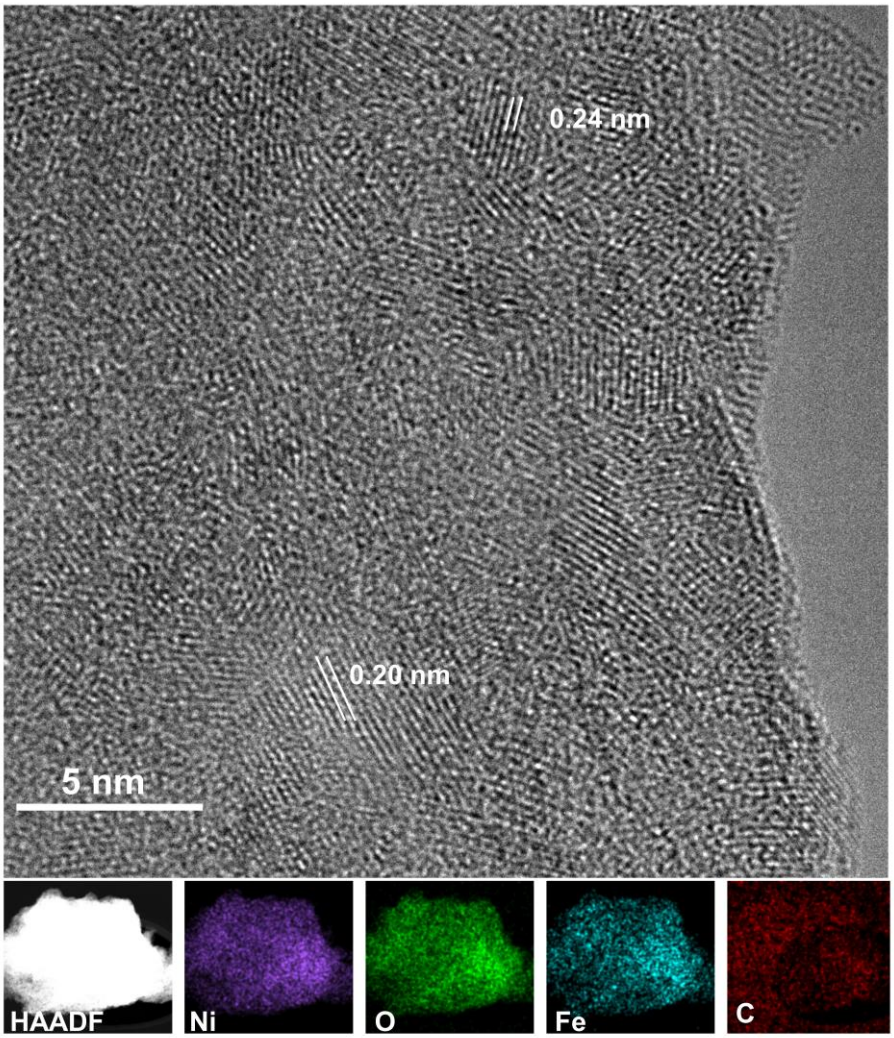

Figure A4.37. HRTEM and HAADF images of NiFe-MOF after 30 CV cycles in 1 M

p-KOH along with the corresponding EDS elemental maps with Ni, O, C, and Fe, the lattice fringes with spacings of approximately 0.20 and 0.24 nm, corresponding to the (101) planes of NiO phase and (002) planes of NiOOH, respectively.

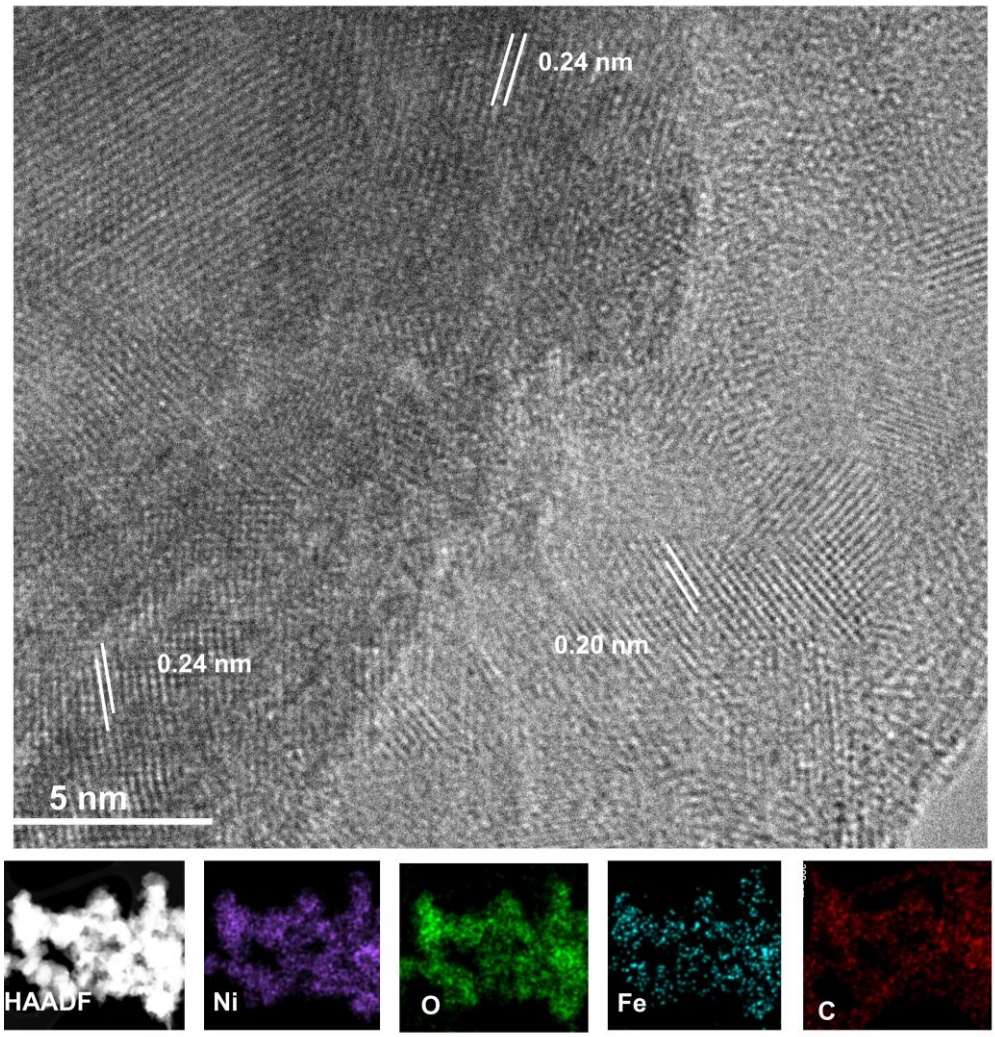

Figure A4.38. HRTEM and HAADF images of NiFe-MOF after 30 CV cycles in 1 M p-KOH with 0.02 M ex-CL along with the corresponding EDS elemental maps with Ni, O, C, and Fe, the lattice fringes with spacings of approximately 0.20 and 0.24 nm, corresponding to the (101) planes of NiO phase and (002) planes of NiOOH, respectively.

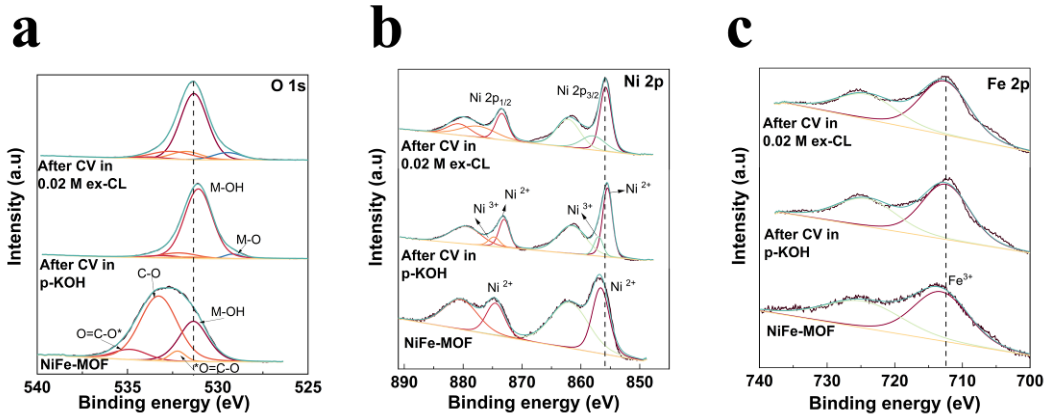

Figure A4.39. Ex-situ XPS spectra of the NiFe MOF a) O 1s, b) Ni 2p and c) Fe 2p photoelectrons.

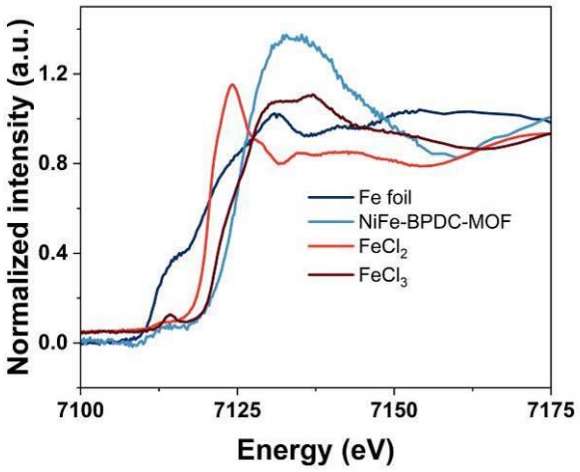

Figure A4.40. Fe K-edge XANES data of NiFe-BPDC-MOF and reference samples.

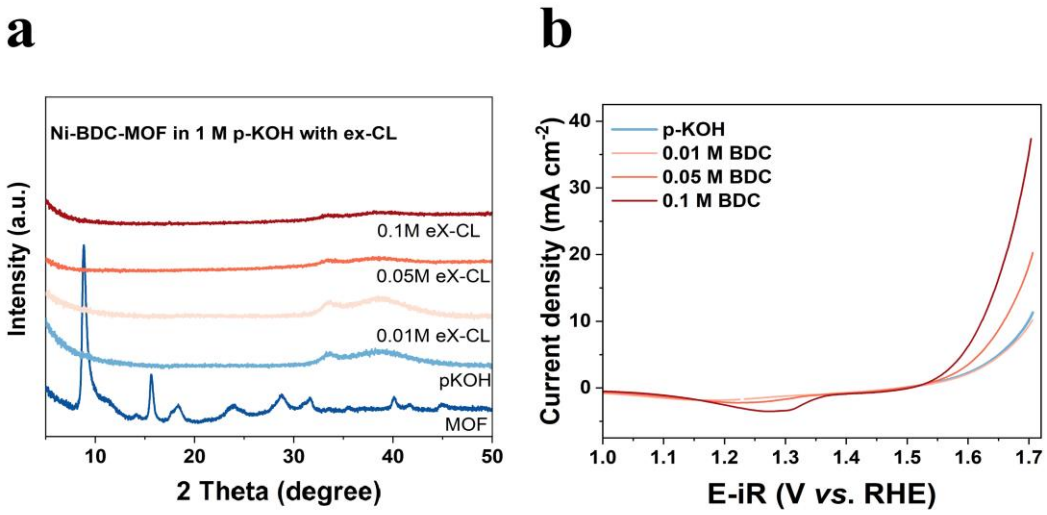

Figure A4.41.a) The PXRD of time dependence effects of Ni-BDC-MOF in 1 M purified KOH (p-KOH, PH:14) with 0.00- 0.10 M extra carboxylate linker (K_2BDC, ex-CL-BDC). b) The OER activity of Ni-BDC-MOF with 0.00-0.10 M ex-CL-BDC with a scan speed 10 mV s^{-1} and GC (RDE) as the working electrode. OER results were performed after stable CV curve (CV scan rate: 10 mV s^{-1}) with no increase in redox peaks in each electrolyte.

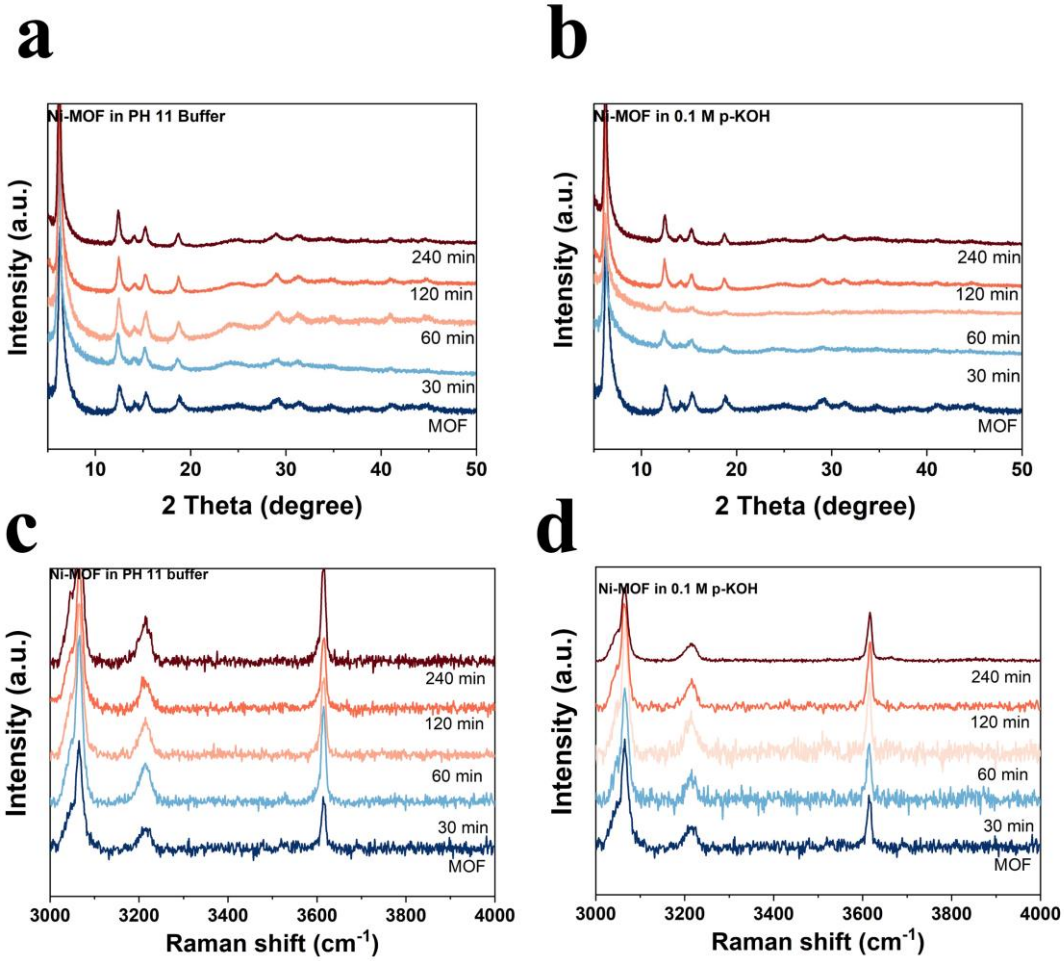

Figure A4.42. The PXRD patterns of time-dependent pH effects of Ni-MOF in a) pH 11 buffer b) 0.1 M p-KOH with pH 13.2. The Raman spectra of pH effects of Ni-MOF in c) pH 11 buffer d) 0.1 M p-KOH with pH 13.2.

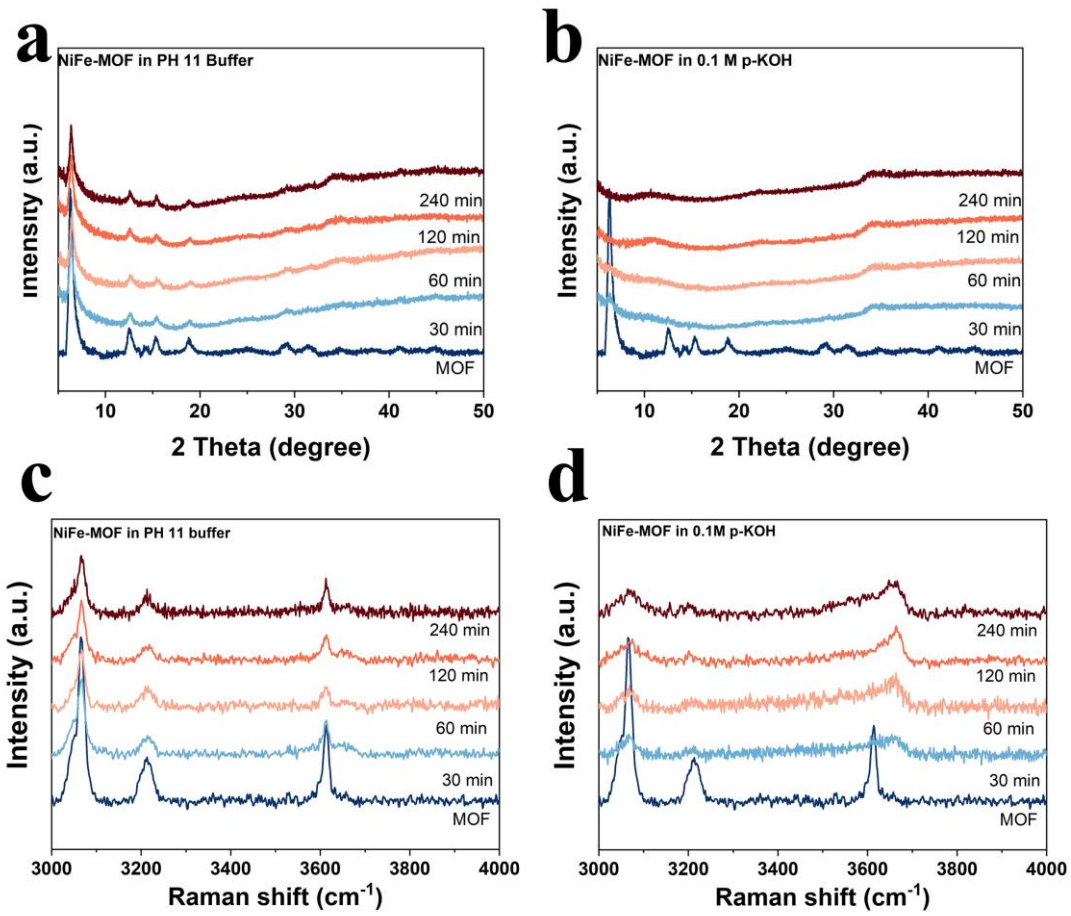

Figure A4.42. The PXRD patterns of time-dependent of pH effects of NiFe-MOF in a) pH 11 buffer b) 0.1 M p-KOH with pH 13.2. The Raman spectra of pH effects of NiFe-MOF in c) pH 11 buffer d) 0.1 M p-KOH with pH 13.2.

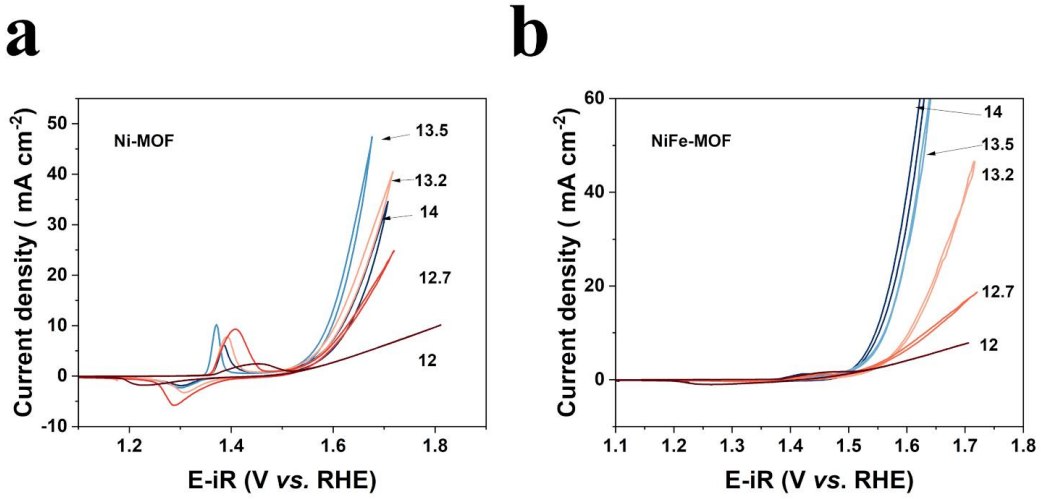

Figure A4.43. The OER activity of a) Ni-MOF and b) NiFe-MOF in various pH (12–14) with a scan speed $5mV^{-1}$ and GC (RDE) as the working electrode. OER results

were performed after a stable CV curve (CV scan rate: 20 mV^{-1}) with no increase in redox peaks in each electrolytes.

Table A4.1 pH values of 1M p-KOH electrolytes with 0.00-0.05 M ex-CL (K_2BPDC).

K2BPDC	pH value
1 M p-KOH	14.0
1M p-KOH with 0.01M ex-CL	14.0
1M p-KOH with 0.02 M ex-CL	14.0
1M p-KOH with 0.05 M ex-CL	14.0

Table A4.2 High-performance liquid chromatography results of the β-$Ni(OH)_2$ tested in 1 M Na_2SO_4 with 0.05 M ex-CL at a constant voltage of 1.6–2.3 V *vs.* RHE, were kept for 20 minutes. The retention time of the K_2BPDC as a reference appears at 12.02 and 21,55, while 25.16 for biphenyl. After testing, no biphenyl and other compounds can be detected, indicating there is no oxidation of the linker or decarboxylation reaction

	Reference Compounds	**Retention time**	
Reference	K_2BPDC	12.02 21.55	
	Biphenyl		25.16
	Constant Voltage(20min)	**Retention time**	
$Ni(OH)_2$	1.6V (*vs.* RHE)	11.93 23.68	NO

	1.8 V (*vs.* RHE)	11.79 23.66	NO
	2.3 V (*vs.* RHE)	12.00 23.66	NO

4.5 Reference

1) Hu, C.; Zhang, L.; Gong, J., Recent progress made in the mechanism comprehension and design of electrocatalysts for alkaline water splitting. *Energy & Environmental Science* **2019**, *12*, 2620-2645.

2) Ding, J.; Guo, D.; Wang, N.; Wang, H.-F.; Yang, X.; Shen, K.; Chen, L.; Li, Y. Defect Engineered Metal–Organic Framework with Accelerated Structural Transformation for Efficient Oxygen Evolution Reaction. *Angewandte Chemie International Edition* **2023**, *62* e202311909.

3) Chu, S.; Majumdar, A., Opportunities and challenges for a sustainable energy future. *Nature* **2012**, *488* , 294-303.

4) Turner, J. A., Sustainable Hydrogen Production. *Science* **2004**, *305*, 972-974.

5) Zhao, S.; Tan, C.; He, C.-T.; An, P.; Xie, F.; Jiang, S.; Zhu, Y.; Wu, K.-H.; Zhang, B.; Li, H.; Zhang, J.; Chen, Y.; Liu, S.; Dong, J.; Tang, Z., Structural transformation of highly active metal–organic framework electrocatalysts during the oxygen evolution reaction. *Nature Energy* **2020**, *5*, 881-890.

6) Cheng, W.; Zhao, X.; Su, H.; Tang, F.; Che, W.; Zhang, H.; Liu, Q., Lattice-strained metal–organic-framework arrays for bifunctional oxygen electrocatalysis. *Nature Energy* **2019**, 4, *115*-122.

7) Yuan, S.; Peng, J.; Cai, B.; Huang, Z.; Garcia-Esparza, A. T.; Sokaras, D.; Zhang, Y.; Giordano, L.; Akkiraju, K.; Zhu, Y. G.; Hübner, R.; Zou, X.; Román-

Leshkov, Y.; Shao-Horn, Y., Tunable metal hydroxide–organic frameworks for catalysing oxygen evolution. *Nature Materials* **2022**, *21*, 673-680.

8) Xue, Z.; Liu, K.; Liu, Q.; Li, Y.; Li, M.; Su, C.-Y.; Ogiwara, N.; Kobayashi, H.; Kitagawa, H.; Liu, M.; Li, G., Missing-linker metal-organic frameworks for oxygen evolution reaction. *Nature Communications* **2019**, *10*, 5048.

9) Yang, J.; Shen, Y.; Sun, Y.; Xian, J.; Long, Y.; Li, G. Ir Nanoparticles Anchored on Metal-Organic Frameworks for Efficient Overall Water Splitting under pH-Universal Conditions. *Angewandte Chemie International Edition* **2023**, *62*, e202302220.

10) Wang, X.; Zhou, W.; Zhai, S.; Chen, X.; Peng, Z.; Liu, Z.; Deng, W.-Q.; Wu, H. Metal-Organic Frameworks: Direct Synthesis by Organic Acid-Etching and Reconstruction Disclosure as Oxygen Evolution Electrocatalysts. *Angewandte Chemie International Edition* **2024**, *63*, e202400323.

11) Thangasamy, P.; Shanmuganathan, S.; Subramanian, V. A NiCo-MOF nanosheet array based electrocatalyst for the oxygen evolution reaction. *Nanoscale Advances* **2020**, *2*, 2073-2079.

12) Yin, C.; Xu, L.; Pan, Y.; Pan, C. Metal–Organic Framework as Anode Materials for Lithium-Ion Batteries with High Capacity and Rate Performance. *ACS Applied Energy Materials* **2020**, *3*, 10776-10786.

13) Chowdhury, S.; Torad, N. L.; Godara, M.; El-Amir, A. A. M.; Gumilar, G.; Ashok, A.; Rezaul Karim, M.; Abdullah Alnaser, I.; Chaikittisilp, W.; Ray, N.; et al. Hierarchical bimetallic metal-organic frameworks with controllable assembling sub-units and interior architectures for enhanced ammonia detection. *Chemical Engineering Journal* **2024**, *480*, 147990.

14) Fan, Z.-S.; Valentino Kaneti, Y.; Chowdhury, S.; Wang, X.; Karim, M. R.; Alnaser, I. A.; Zhang, F.-B. Weak base-modulated synthesis of bundle-like carbon

superstructures from metal-organic framework for high-performance supercapacitors. *Chemical Engineering Journal* **2023**, *462*, 142094.

15) Cheng, P.; Wang, X.; Markus, J.; Abdul Wahab, M.; Chowdhury, S.; Xin, R.; Alshehri, S. M.; Bando, Y.; Yamauchi, Y.; Kaneti, Y. V. Carbon nanotube-decorated hierarchical porous nickel/carbon hybrid derived from nickel-based metal-organic framework for enhanced methyl blue adsorption. *Journal of Colloid and Interface Science* **2023**, *638*, 220-230.

16) Yan, L.; Gopal, A.; Kashif, S.; Hazelton, P.; Lan, M.; Zhang, W.; Chen, X. Metal organic frameworks for antibacterial applications. *Chemical Engineering Journal* **2022**, *435*, 134975.

17) Bennett, T. D.; Coudert, F. X.; James, S. L.; Cooper, A. I., The changing state of porous materials. *Nature Materials* **2021**, *20*, 1179-1187.

18) Ehrling, S.; Reynolds, E. M.; Bon, V.; Senkovska, I.; Gorelik, T. E.; Evans, J. D.; Rauche, M.; Mendt, M.; Weiss, M. S.; Poppl, A.; Brunner, E.; Kaiser, U.; Goodwin, A. L.; Kaskel, S., Adaptive response of a metal-organic framework through reversible disorder-disorder transitions. *Nature Chemistry* **2021**, *13*, 568-574.

19) Wu, Y.-P.; Zhou, W.; Zhao, J.; Dong, W.-W.; Lan, Y.-Q.; Li, D.-S.; Sun, C.; Bu, X., Surfactant-Assisted Phase-Selective Synthesis of New Cobalt MOFs and Their Efficient Electrocatalytic Hydrogen Evolution Reaction. *Angewandte Chemie International Edition* **2017**, *56*, 13001-13005.

20) Chen, Y.; Liao, P.; Jin, K.; Zheng, Y.; Shao, H.; Li, G. Current progress in metal–organic frameworks and their derivatives for electrocatalytic water splitting. *Inorganic Chemistry Frontiers* **2023**, *10*, 6489-6505.

21) Jia, Y.; Zhang, F.; Liu, Q.; Yang, J.; Xian, J.; Sun, Y.; Li, Y.; Li, G. Single-atomic Fe anchored on hierarchically porous carbon frame for efficient oxygen reduction performance. *Chinese Chemical Letters* **2022**, *33*, 1070-1073.

22) Zheng, W.; Liu, M.; Lee, L. Y. S., Electrochemical Instability of Metal–Organic Frameworks: In Situ Spectroelectrochemical Investigation of the Real Active Sites. *ACS Catalysis* **2019**, *10*, 81-92.

23) Zheng, W.; Lee, L. Y. S., Metal–Organic Frameworks for Electrocatalysis: Catalyst or Precatalyst? *ACS Energy Letters* **2021**, *6*, 2838-2843.

24) Li, F.-L.; Shao, Q.; Huang, X.; Lang, J.-P., Nanoscale Trimetallic Metal-Organic Frameworks Enable Efficient Oxygen Evolution Electrocatalysis. *Angewandte Chemie International Edition* **2018**, *57*, 1888-1892.

25) Duan, J.; Chen, S.; Zhao, C., Ultrathin metal-organic framework array for efficient electrocatalytic water splitting. *Nature Communications* **2017**, *8*, 15341.

26) Wang, C.-P.; Feng, Y.; Sun, H.; Wang, Y.; Yin, J.; Yao, Z.; Bu, X.-H.; Zhu, J., Self-Optimized Metal–Organic Framework Electrocatalysts with Structural Stability and High Current Tolerance for Water Oxidation. *ACS Catalysis* **2021**, *11*, 7132-7143.

27) Li, A.; Kong, S.; Guo, C.; Ooka, H.; Adachi, K.; Hashizume, D.; Jiang, Q.; Han, H.; Xiao, J.; Nakamura, R., Enhancing the stability of cobalt spinel oxide towards sustainable oxygen evolution in acid. *Nature Catalysis* **2022**, *5*, 109-118.

28) Lin, C.; Li, J.-L.; Li, X.; Yang, S.; Luo, W.; Zhang, Y.; Kim, S.-H.; Kim, D.-H.; Shinde, S. S.; Li, Y.-F.; Liu, Z.-P.; Jiang, Z.; Lee, J.-H., In-situ reconstructed Ru atom array on α-MnO2 with enhanced performance for acidic water oxidation. *Nature Catalysis* **2021**, *4*, 1012-1023.

29) Klaus, S.; Cai, Y.; Louie, M. W.; Trotochaud, L.; Bell, A. T., Effects of Fe Electrolyte Impurities on Ni(OH)2/NiOOH Structure and Oxygen Evolution Activity. *The Journal of Physical Chemistry C* **2015**, *119*, 7243-7254.

30) Lee, S.-Y.; Kim, I.-S.; Cho, H.-S.; Kim, C.-H.; Lee, Y.-K., Resolving Potential-Dependent Degradation of Electrodeposited Ni(OH)2 Catalysts in Alkaline Oxygen

Evolution Reaction (OER): In Situ XANES Studies. *Applied Catalysis B: Environmental* **2021**, *284*, 119729.

31) Ma, X.; Zheng, D. J.; Hou, S.; Mukherjee, S.; Khare, R.; Gao, G.; Ai, Q.; Garlyyev, B.; Li, W.; Koch, M.; Mink, J.; Shao-Horn, Y.; Warnan, J.; Bandarenka, A. S.; Fischer, R. A., Structure–Activity Relationships in Ni- Carboxylate-Type Metal–Organic Frameworks' Metamorphosis for the Oxygen Evolution Reaction. *ACS Catalysis* **2023**, *13*, 7587-7596.

32) Choi, A.; Kim, Y. K.; Kim, T. K.; Kwon, M.-S.; Lee, K. T.; Moon, H. R., 4,4′-Biphenyldicarboxylate sodium coordination compounds as anodes for Na-ion batteries. *J. Mater. Chem. A* **2014**, *2*, 14986-14993.

33) Böhm, D.; Beetz, M.; Kutz, C.; Zhang, S.; Scheu, C.; Bein, T.; Fattakhova-Rohlfing, D., V(III)-Doped Nickel Oxide-Based Nanocatalysts for Electrochemical Water Splitting: Influence of Phase, Composition, and Doping on the Electrocatalytic Activity. *Chemistry of Materials* **2020**, *32*, 10394-10406.

34) Hall, D. S.; Lockwood, D. J.; Poirier, S.; Bock, C.; MacDougall, B. R., Raman and Infrared Spectroscopy of α and β Phases of Thin Nickel Hydroxide Films Electrochemically Formed on Nickel. *The Journal of Physical Chemistry A* **2012**, *116* , 6771-6784.

35) Butova, V. V.; Budnyk, A. P.; Charykov, K. M.; Vetlitsyna-Novikova, K. S.; Bugaev, A. L.; Guda, A. A.; Damin, A.; Chavan, S. M.; Øien-Ødegaard, S.; Lillerud, K. P.; Soldatov, A. V.; Lamberti, C., Partial and Complete Substitution of the 1,4-Benzenedicarboxylate Linker in UiO-66 with 1,4-Naphthalenedicarboxylate: Synthesis, Characterization, and H2-Adsorption Properties. *Inorganic Chemistry* **2019**, *58*, 1607-1620.

36) Aufa, M. H.; Watzele, S. A.; Hou, S.; Haid, R. W.; Kluge, R. M.; Bandarenka, A. S.; Garlyyev, B., Fast and accurate determination of the electroactive surface area of MnOx. *Electrochimica Acta* **2021**, *389*, 138692.

37) Hou, S.; Xu, L.; Mukherjee, S.; Zhou, J.; Song, K.-T.; Zhou, Z.; Zhang, S.; Ma, X.; Warnan, J.; Bandarenka, A. S.; Fischer, R. A., Impact of Organic Anions on Metal Hydroxide Oxygen Evolution Catalysts. *ACS Catalysis* **2024**, *14*, 12074-12081.

38) Qiu, Y.; Lopez-Ruiz, J. A.; Sanyal, U.; Andrews, E.; Gutiérrez, O. Y.; Holladay, J. D., Anodic electrocatalytic conversion of carboxylic acids on thin films of RuO2, IrO2, and Pt. *Applied Catalysis B: Environmental* **2020**, *277*, 119277.

39) Qiu, Y.; Lopez-Ruiz, J. A.; Zhu, G.; Engelhard, M. H.; Gutiérrez, O. Y.; Holladay, J. D., Electrocatalytic decarboxylation of carboxylic acids over RuO2 and Pt nanoparticles. *Applied Catalysis B: Environmental* **2022**, *305*, 121060.

40) Farhat, R.; Dhainy, J.; Halaoui, L. I., OER Catalysis at Activated and Codeposited NiFe-Oxo/Hydroxide Thin Films Is Due to Postdeposition Surface-Fe and Is Not Sustainable without Fe in Solution. *ACS Catalysis* **2019**, *10*, 20-35.

41) Qian, Q.; Li, Y.; Liu, Y.; Yu, L.; Zhang, G., Ambient Fast Synthesis and Active Sites Deciphering of Hierarchical Foam-Like Trimetal–Organic Framework Nanostructures as a Platform for Highly Efficient Oxygen Evolution Electrocatalysis. *Advanced Materials* **2019**, *31*, 1901139.

42) Hou, S.; Li, W.; Watzele, S.; Kluge, R. M.; Xue, S.; Yin, S.; Jiang, X.; Döblinger, M.; Welle, A.; Garlyyev, B.; Koch, M.; Müller-Buschbaum, P.; Wöll, C.; Bandarenka, A. S.; Fischer, R. A., Metamorphosis of Heterostructured Surface-Mounted Metal–Organic Frameworks Yielding Record Oxygen Evolution Mass Activities. *Advanced Materials* **2021**, *33*, 2103218.

43) Zheng, D. J.; Görlin, M.; McCormack, K.; Kim, J.; Peng, J.; Xu, H.; Ma, X.; LeBeau, J. M.; Fischer, R. A.; Román-Leshkov, Y.; Shao-Horn, Y., Linker-

Dependent Stability of Metal-Hydroxide Organic Frameworks for Oxygen Evolution. *Chemistry of Materials* **2023**, *35*, 5017-5031.

44) Eom, S. Y.; Lee, Y. R.; Kwon, C. H.; Kim, H. L., Surface enhanced Raman scattering of 2,2′-biphenyl dicarboxylic acid on silver surfaces: Structure and orientation upon adsorption. *Journal of Molecular Structure* **2016**, *1115*, 70-74.

45) Lee, S.; Banjac, K.; Lingenfelder, M.; Hu, X., Oxygen Isotope Labeling Experiments Reveal Different Reaction Sites for the Oxygen Evolution Reaction on Nickel and Nickel Iron Oxides. *Angewandte Chemie International Edition* **2019**, *58*, 10295-10299.

46) McLarnon, R. K. F., Electrochemical and In Situ Raman Spectroscopic Characterization of Nickel Hydroxide Electrodes. *J. Electrochem. Soc* **1997**, *144*, 485-493.

47) Yinfeng Han, Z.-H. L., Zupei Yang, Zenling Wang, Xiuhua Tang, Tao Wang, Lihong Fan, and Kenta Ooi, Preparation of Ni2+-Fe3+ Layered Double Hydroxide Material with High Crystallinity and Well-Defined Hexagonal Shapes. *Chemistry of Materials.* **2008**, *20*, 360-363.

48) Qiu, Z.; Tai, C.-W.; Niklasson, G. A.; Edvinsson, T., Direct observation of active catalyst surface phases and the effect of dynamic self-optimization in NiFe-layered double hydroxides for alkaline water splitting. Energy & Environmental Science **2019**, *12*, 572-581.

49) Rui, K.; Zhao, G.; Chen, Y.; Lin, Y.; Zhou, Q.; Chen, J.; Zhu, J.; Sun, W.; Huang, W.; Dou, S. X., Hybrid 2D Dual-Metal-Organic Frameworks for Enhanced Water Oxidation Catalysis. *Advanced Functional Materials* **2018**, *28*, 1801554.

50) Martínez-Hincapié, R.; Wegner, J.; Anwar, M. U.; Raza-Khan, A.; Franzka, S.; Kleszczynski, S.; Čolić, V., The determination of the electrochemically active surface

area and its effects on the electrocatalytic properties of structured nickel electrodes produced by additive manufacturing. *Electrochimica Acta* **2024**, 476.

51) Jaramillo, e. G. a. T. F., A Bifunctional Nonprecious Metal Catalyst for Oxygen Reduction and Water Oxidation. *Journal of the American Chemical Society* **2010**, *132*, 13612–13614.

52) Anantharaj, S.; Kundu, S., Do the Evaluation Parameters Reflect Intrinsic Activity of Electrocatalysts in Electrochemical Water Splitting? *ACS Energy Letters* **2019**, *4*, 1260-1264.

53) Wei, C.; Sun, S.; Mandler, D.; Wang, X.; Qiao, S. Z.; Xu, Z. J., Approaches for measuring the surface areas of metal oxide electrocatalysts for determining their intrinsic electrocatalytic activity. *Chem Soc Rev* **2019**, *48*, 2518-2534.

54) Singh, R. K.; Schechter, A., Electrochemical investigation of urea oxidation reaction on β Ni(OH)2 and Ni/Ni(OH)2. *Electrochimica Acta* **2018**, *278*, 405-411.

55) Huang, S.-Y.; Ganesan, P.; Popov, B. N., Titania supported platinum catalyst with high electrocatalytic activity and stability for polymer electrolyte membrane fuel cell. *Applied Catalysis B: Environmental* **2011**, *102* , 71-77.

56) Trotochaud, L.; Young, S. L.; Ranney, J. K.; Boettcher, S. W., Nickel–Iron Oxyhydroxide Oxygen-Evolution Electrocatalysts: The Role of Intentional and Incidental Iron Incorporation. *Journal of the American Chemical Society* **2014**, *136*, 6744-6753.

57) Garai, B.; Bon, V.; Krause, S.; Schwotzer, F.; Gerlach, M.; Senkovska, I.; Kaskel, S., Tunable Flexibility and Porosity of the Metal-Organic Framework DUT-49 through Postsynthetic Metal Exchange. *Chemistry of Materials* **2020**, *32*, 889-896.

5. Experimental Part

To elucidate the complex relationships between the structures of MOFs and their activities in the OER, a range of ex situ and in situ characterization techniques is utilized. These techniques are pivotal for thoroughly investigating the structural configurations, electronic properties, and morphologies of these catalysts.

This chapter offers a comprehensive overview of the experimental techniques and strategies employed to explore the conversion mechanisms of MOFs during OER applications. It also includes detailed discussions on the synthesis of MOFs and the methods used for electrochemical testing. Together, these sections aim to provide detailed tools to investigate the MOFs as effective electrocatalysts in OER application

5.1 Characterization Techniques

5.1.1 Powder X-ray Diffraction

Powder X-ray Diffraction (PXRD) is a powerful tool to determine the MOFs' topologies and the structure according to the compare the results with the CCDC database. Here, PXRD patterns were obtained using a Rigaku MiniFlex 600-C diffractometer with a Rigaku D/teX Ultra2 detector at 298 K, the measurement underwent voltage and intensity were 45 kV and 40 mA with a Cu Kα irradiation source (λ = 1.54056 Å). The measurement range was from 3.0° to 50.0° (2θ) at a speed of 10°/min. The MOF powder samples were placed on a zero-background silicon wafer.

5.1.2 Raman Spectroscopy

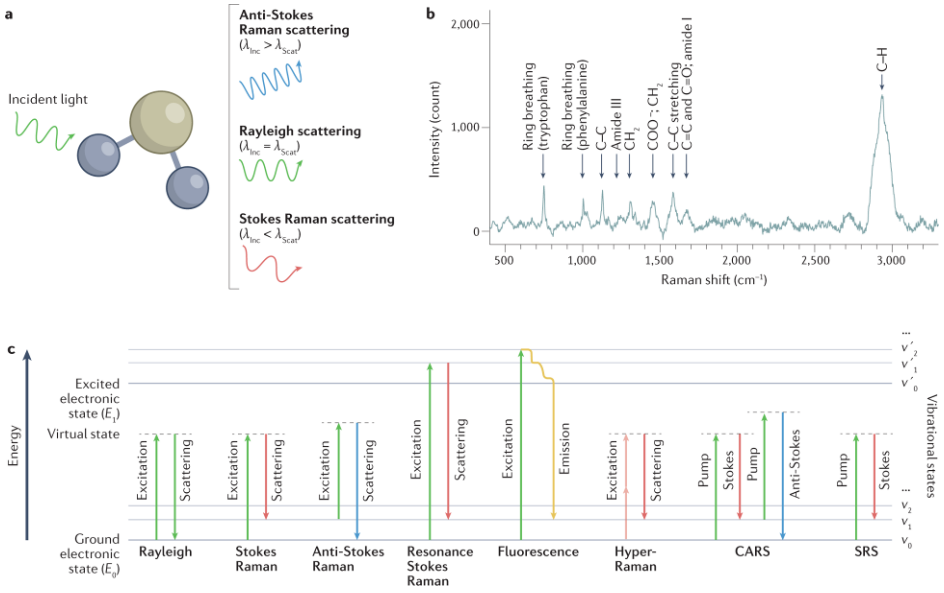

Figure 5.1. Schematic of Raman spectroscopy. a) Three types of scattering signal that are generated as a result of interactions between light and a molecule. b) A processed Raman spectrum of a single bacterium (*Vibrio alginolyticus*). c) Energy level diagrams representing the generation of emission signals. Colours of the arrows represent the wavelength. Reprinted under the permission from ref[1].

Raman spectroscopy is an analytical method based on a light scattering technique, where a molecule scatters incident light from a high-intensity laser. While most of this light, known as Rayleigh scatter, is scattered at the same wavelength as the laser and does not yield useful information, a minuscule fraction (approximately 0.0000001%) is scattered at different wavelengths or colors.[1-4] This phenomenon, known as Raman scatter, varies depending on the chemical structure of the analyte and is the basis for Raman spectroscopy in the **Figure 5.1**. Raman spectroscopy offers distinct chemical fingerprints for a specific molecule or substance, providing comprehensive insights into a sample's chemical structure, phase, morphology, crystallinity, and molecular interactions.

In this thesis, Raman spectroscopy measurements were used on the Renishaw inVia ReflexRaman microscope with a 633 nm laser source (Chapter 3). with a 532 nm laser source (Chapter 4). In Chapter 3, for sample preparation, the ink was prepared

with 5 mg MOF powders mixed with 500 ul ethanol and 500 Water. 100 µl ink was coated on the Pt quartz crystal wafer electrodes (Stanford Research Systems, USA) with a surface area of 1.37 cm^{-2}. Wire software was used for data acquisition. Before the H/D Isotope labeling Raman studying, the ink (same proportion) of BDC-OH and BDC-OD MOF deposited on the 0.5cm*0.5cm Au substrates under 1.16 to 1.64 V vs. RHE in a 10ml volume cell with the scan rate is 20 mV/s during cycling.

In addition, the OER process was monitored in real-time using in-situ Raman spectroscopy to observe changes in the electrode-electrolyte interface. In Chapter 4, a homemade in-situ Raman cell with polytetrafluoroethylene materials as shown in the **Figure 5.2**, with an Au quartz substrate serving as the working electrode, a Hg/HgO electrode as the reference, and a Pt wire as the counter electrode. All Raman measurements were carried out using the Autolab (PGSTAT302N) instrument.

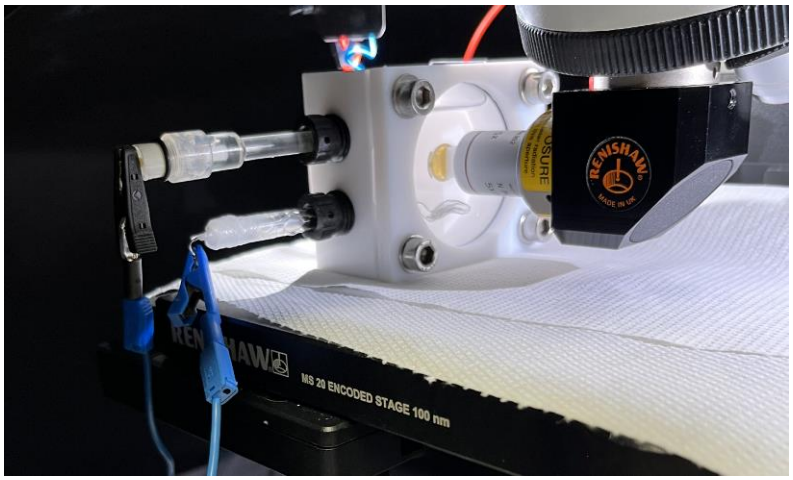

Figure 5.2 Home-made setup of in-situ Raman.

5.1.3 Fourier Transform Infrared Spectroscopy

Fourier Transform Infrared Spectroscopy, also known as FTIR Spectroscopy, is an analytical technique used to identify organic, polymeric, and, in some cases, inorganic materials. The FTIR analysis method uses infrared light to scan test samples, providing information about molecular vibrations and the identification of chemical compounds' functional groups.

5.1.4 Atomic Force Microscopy

Atomic force microscopy (AFM) is a very effective method that allows for the visualization of nearly any surface while also providing the ability to quantify and pinpoint various forces, such as adhesion strength, magnetic forces, and the thickness of thin materials. The AFM here was employed to investigate sample morphology using the Nanosurf FlexAFM instrument from Switzerland.

5.1.5 Morphologies Characterization

The field emission scanning electron microscope (SEM) and transmission electron microscope (TEM) are the critical steps in monitoring the basic features of bulk materials' morphologies and powder sizes. Meanwhile, the high-resolution transmission electron microscope (HRTEM) can provide in-depth information about the material’s crystallinity, lattice space, etc. Furthermore, combining energy-dispersive X-ray spectroscopy with high-angle annular dark-field scanning TEM (HAADF-STEM) images can determine the chemical composition and spatial distribution. Here, we used the SEM instrument from the Zeiss Gemini NVision 40 operated at 5 kV with a working distance of 3.5 mm. The TEM, HRTEM, HAADF-STEM, and relative EDS were performed with double correctors Titan cubed Themis G2 operated at 300kV from the Electron Microscopy Center (EMC) of Shared Equipment Authority (SEA) at Rice University. The microscope is equipped with a Ceta camera, Gatan Quantum 966 energy filter, and an electron monochromator.

5.1.6 X-ray Photoelectron Spectroscopy

X-ray Photoelectron Spectroscopy (XPS) is an advanced analytical technique derived from the principles of the photoelectric effect, initially discovered by Heinrich Hertz in 1887. Hertz observed that the exposure of materials to light resulted in the emission of electrons. Albert Einstein expanded upon this fundamental observation, providing a formal description of the photoelectric effect in 1905, leading to his Nobel Prize in Physics award in 1921. The specific phenomenon of photoemission following X-ray irradiation was initially noted by Robinson and Rawlinson in 1914.

It wasn't until 1951 that Steinhardt and Serfass first utilized photoemission as an analytical method.[5] However, the significant development of what we now recognize as X-ray Photoelectron Spectroscopy primarily occurred in the mid-20th century. Spearheaded by Kai Siegbahn during the 1950s -1960s, the technique was initially termed Electron Spectroscopy for Chemical Analysis (ESCA).[6] Siegbahn's pioneering work laid the groundwork for XPS to evolve into a critical tool for the investigation of surface chemistry, for which he was awarded the Nobel Prize in Physics in 1981. X-ray photoelectron spectroscopy (XPS) is sensitive to surface properties, as it can only probe a few nanometers deep. It is commonly used to analyze elements' composition and valence states by measuring their binding energies.

In this thesis, A survey of XPS was performed using a Kratos Axis Supra spectrometer for Chapter 3 in a vacuum of 110–9 mbar and a monochromatic Mg K X-ray source operating at 150 W. The data were processed with XPS PEAK software, and the C 1s peak at 284.8 eV was utilized to calibrate the spectrometer. For Chapter 4, Phoibos spectrometer and a monochromatic Al Kα X-ray source (1486.6 eV) was used. High-resolution scans were acquired at 350 W, (14 kV), 20 eV pass energy and 0.1 eV energy step at Fixed transition mode. Charging effects were compensated with a flood gun set at 50 μA and 2.0 V. The recorded O 1s, Ni 2p and Fe 2p spectra were fitted by Casaxps software.

5.1.7 X-ray Absorption Spectroscopy

X-ray Absorption Spectroscopy (XAS) includes the extended X-ray Absorption Fine Structure (EXAFS) and X-ray Absorption Near-Edge Structure (XANES) techniques. This method is widely employed to investigate materials' local atomic structures and electronic states.

An important benefit of XAS is its ability to identify elements specifically, allowing for focused analysis of individual components within a material's structure. It is also used to acquire comprehensive information to examine materials' oxidation state and coordination environment.

In chapter 3, ex situ Ni K-edge XAS measurements were performed at the P65 beamline of the German electron synchrotron (DESY) in Hamburg, Germany.[7] The PETRA III storage ring was operated at 6 GeV energy and 100 mA beam current in top-up mode. A water-cooled Si (111) double crystal monochromator (DCM) was used for 7 obtaining monochromatic X-rays. Two Si mirrors were installed in front of the DCM to reject higher harmonics. The DCM was calibrated for Ni K-edge by measuring a Ni-foil and defining the first major inflection point as 8333 eV. Subsequently, a Ni-foil was also placed between the second and third ionization chambers for the energy calibration of each measured spectrum. The energy resolution of the beamline is estimated to be ~1.2 eV at the Ni K-edge. The XAS spectra were measured in both transmission mode using ionization chambers and in fluorescence mode using a passivated implanted planar silicon (PIPS) detector. The spot-size of X-ray beam at the sample was 1.6 mm (horizontal) × 300 μm (vertical). Spectra for both XANES analyses and EXAFS analyses were measured in continuous scanning mode. The data were monitored for any signs of X-ray beam damage and several successive scans were averaged to reduce signal-to-noise ratio and improve the data quality. For XANES analyses, the spectra were normalized and flattened. For EXAFS fitting, spectra were background subtracted, normalized, k2 -weighted, and Fourier-transformed in the k range of 2.7–11 $Å^{-1}$. EXAFS fitting was performed in k-space between 2.7 and 11 $Å^{-1}$ simultaneously on the k1-, k2-, and k3-weighted data. During the fitting, E_0 was set such that energy-shift (ΔE_0) obtained during the fit was less than 2 eV. A metal-foil was first fitted to obtain the amplitude reduction factor, S02 = 0.85, which was then used in the subsequent fits. XANES and EXAFS data analyses were performed using ATHENA and ARTEMIS software packages.[8]

In chapter 4, XAS were recorded on a lab-scale benchtop easyXAFS300+ equipped with a spherically bent Bragg crystal analyzer Si (531) (for Fe K-edge) and Si (551) (for Ni-K edge) as monochromators. The X-ray tube was operated at 40 kV and 30 mA. A calculated amount of MOF samples was diluted with cellulose and pressed

into a pellet to obtain a homogeneous sample. The reason for chosen amount of MOF sample was to obtain the absorption of 1.5 at the Fe K-edge and Ni K-edge. The pellets were sealed in Kapton tape and measured at room temperature. The XANES region of the MOF samples and the references were recorded at the Ni K-edge and Fe K-edge independently by adding 10 scans of 36 minutes each. The Ni K-edge (8333 eV) of a Ni-foil and Fe K-edge (7112 eV) was used to calibrate the energies respectively.

5.1.8 Nuclear Magnetic Resonance

Nuclear Magnetic Resonance (NMR) spectra were acquired using a Bruker Ultrashield DRX400 spectrometer, operating at frequencies of 400.13 MHz for ^{1}H at an ambient temperature of 298 K. The spectral data were referenced to the residual solvent signals of deuterium oxide, with a chemical shift of 4.79 ppm. The spectra were analyzed using MestReNova software, which facilitated detailed spectral interpretation and quantification.

5.2 Electrochemical Measurements

All electrochemical experiments, such as cyclic voltammetry (CV) activation, OER testing, electrochemical impedance spectroscopy (EIS), performance measurements for stability assessment and estimation of apparent activation were performed using a three-electrode setup under O_2-saturated purified KOH solution as shown in **Figure 5.3**. For electrochemical investigations, a VSP-300 potentiostat (Bio-Logic, France) were employed. A rotating disk electrode (Glassy carbon) served as the working electrode, with a Pt wire and Hg/HgO (1 M NaOH) electrode serving as the counter and reference electrodes, respectively.

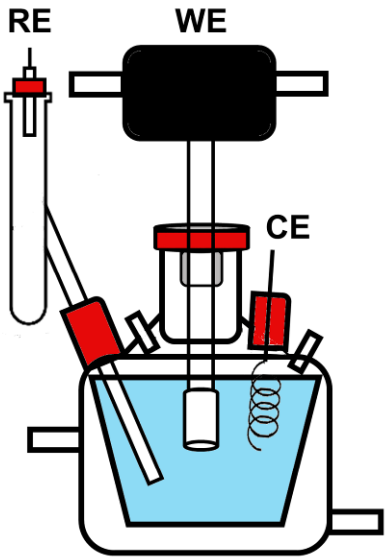

Figure 5.3 Schematics of the electrochemical cells.

5.3 Experiment Part of Chapter 3

5.3.1. Materials Preparation

Synthesis of Ni-MOFs [$Ni_2(OH)_2L$] The Ni-MOFs **1-4** were synthesized through a reported strategy in a 200 ml glass bottle.[9] To get layered Ni-MOFs with different length of ligands, firstly, 64 ml N,N-Dimethylformamide (DMF,99.99%, Fisher Chemical) were mixed with 4 ml pure ethanol (99.9%, Th. Geyer GmbH & Co. KG, Germany), and 4 ml DI-water(18.2 MΩ). Then, the 1.5 mmol ligand such as terephthalic acid (H_2BDC, 98%, Sigma-Aldrich), naphthalene-2,6-dicarboxylic acid (H_2NDC, 99%, Sigma-Aldrich), biphenyl-4,4'-dicarboxylic acid (H_2BPDC, 98%, Sigma-Aldrich), p-terphenyl-4,4''-dicarboxylic acid (H_2TPDC,95%, AmBeed) were dissolved in above solvent, respectively. After sonicated for 10 min, 1.5 mmol $NiCl_2 \cdot 6H_2O$ (99.3%, Alfa Aesar), were added into above solution. 1600 ul trimethylamine (Et3N, Acros) was quickly dropped in the above uniform solution after other 10 min for sonicating. Then, the solution was continuously sonicated for 8 h under a power of 40 kHz. After fabrication, the Ni-MOFs obtained via centrifugation, and the powders was wash by DMF once and ethanol washing with 2 times. At last, obtained products was drying in oven at 80 ℃ for overnight.

Synthesis of [Ni(NDC)(H_2O)$_4$] In order to better understand the coordination of Ni-MOFs in our work, we synthesized [Ni(NDC)(H_2O)$_4$] as a reference structure based on previous work.[10] To begin, deprotonate naphthalene-2,6-dicarboxylic acid (H_2NDC; 46.3 mmol) in potassium hydroxide solution (0.97 M, 200 ml). After 3 hours of stirring, the solution was rotary evaporated until a creamy white precipitate was obtained. To obtain Na_2NDC, the solid was washed five times with ethanol. The 10.6 mmol $Ni(NO_3)_2 \cdot 6H_2O$ (97 percent, Sigma-Aldrich) in deionized water (20 ml) was then combined with another water solution (20 ml) containing Na_2NDC (2.5 g). To obtain light green powders, the mixture was agitated for 24 hours. After centrifugation, the [Ni(NDC)(H_2O)$_4$] powders were dried overnight at 80 °C.

Synthesis of [$Ni_2(OD)_2$BDC] To begin, 8 ml of N,N-Dimethylformamide (anhydrous, 99.8%, Sigma-Aldrich) was placed in a 20 ml glass bottle with a white top and 0.19 mmol terephthalic acid (H_2BDC, 98%, Sigma-Aldrich) was added. After sonicating for 10 minutes and dissolving the linker, 0.19 mmol of $NiCl_2 \cdot 6H_2O$ (99.3%, Alfa Aesar) were mixed with to the aforementioned solution. After sonicated for another 10 min, 2ml of deuterium oxide (D_2O,99.9%, Sigma-Aldrich) were added drop by drop. The solution was then ultrasonicated for 5 minutes and heated at 120 °C for 8 hours. The [$Ni_2(OD)_2BDC_2$] (BDC-OD) powders were dried at 80°C overnight after centrifugation and two washes with D_2O.

Synthesis of Ni(OD)$_2$ The powders of Ni(OD)$_2$ were used as a reference material for Ni-MOFs. 1.8mmol $NiCl_2 \cdot 6H_2O$ (99.3%, Alfa Aesar) were added in the 5ml heavy water (D_2O,99.9%, Sigma-Aldrich). After stirred for 10min, the liquid was transferred to a 25 ml glass vial containing 15 ml of 1M potassium deuteroxide solution (KOD,98 atom % D). After centrifugation and two washing with D_2O, the green Ni(OD)$_2$ powders could be collected after constantly stirring for 12 hours at 140 °C in an oil bath.

KOH Electrolyte The 1 M KOH electrolyte was purified according to earlier work to avoid the influence of Fe.[11] In a 50 ml centrifuge tube, 2 g of $NiSO_4 \cdot 6H_2O$ (99 %

Sigma-Aldrich) were dissolved in 4 ml of 18.2 MΩ water. After that, 20 ml of 1 M KOH were added to precipitate $Ni(OH)_2$ which would occlude traces of Fe. After shaking and centrifuging, the $Ni(OH)_2$ particles were collected and washed three times in a tube with 20 ml of DI water and 2 ml of 1 M KOH. The high purity $Ni(OH)_2$ precipitates were obtained after centrifugation and solvent removal. The tube was then filled with 45 ml of 1 M potassium hydroxide (KOH, 85%, Carl Roth GmbH & Co. KG) for purification over the prepared $Ni(OH)_2$ solid. The suspension was shaken and sonicated for at least 10 minutes before sedimentation and being kept motionless for 24 hours. The purified 1M KOH(aq) supernatant was separated from the soild by centrifugation.

5.3.2 Electrochemical measurements

For electrode preparation, the powders of Ni-MOFs (5 mg) were dispersed in a mixed solution with 480 µl water, 480 µl ethanol, and 40 µl 5 wt % Nafion solution. First, the mixture was ultrasonicated for 10 minutes using a vigorous sonicator (Fisher Scientific, FB120, 120 W) at 35% amplitude, and 30 minutes using bath sonicator. Then, 10 µL of the mixture was dropped onto a glassy carbon electrode with a diameter of 0.5 cm, which served as the working electrode. For electrochemical investigations, a three-electrode setup and a VSP-300 potentiostat (Bio-Logic, France) were employed. Glassy carbon served as the working electrode, with a Pt wire and Hg/HgO electrode (1 M NaOH, potential *vs.* NHE of 0.140 V) serving as the counter and reference electrodes, respectively.

Choosing an appropriate counter electrode material raises discussion due to the possible Pt "contamination." It reported the low potential condition, for instance, under 0.62 V *vs.* RHE at the counter electrode (corresponding to 0.05 V *vs.* RHE at the working electrode) could strongly mitigate the Pt dissolution.[12] OER here was tested from 1.16 to 1.64 V vs. RHE at the working electrode, while HER occurs at the relative counter electrode (Pt). Furthermore, any possible dissolution and redeposition of Pt traces at the actual OER catalyst would not affect the data (and the

conclusions) as potential species (e.g., PtOx) are much less catalytically active than the NiOx are.[13] Hence, Pt is still suggested as the counter material in OER cases, whereas hydrogen evolution and oxygen reduction (cathodic potentials) require more attention.[14-15]

Electrochemical cyclic voltammetry (CV) tests were performed in an O_2-saturated 1 M purified KOH solution between 0.194 and 0.674 vs. Hg/HgO (1.16 or 1.64 V vs. RHE) at a scan rate of 20 mV s^{-1} for 30 cycles for the pre-catalytic CV working electrode conditioning process unless otherwise mentioned. Then, using a scan rate of 5 mV s^{-1}, OER curves were collected by CV in the potential range of 0.194 to 0.774 V *vs.* Hg/HgO (1.16 or 1.74 V vs. RHE). All polarization curves were gathered with an automatically adjusted 95 % iR–compensation. The measured potentials were converted *vs.* RHE, overpotential at 10 mV cm^{-2} = E_{RHE} – 1.23 V =$E_{Hg/HgO}$ + 0.140 + 0.059 × pH(14) – 1.23 V. TOF = (j × A)/(4F × n), where j × A(surface area of GC electrode) denotes the current at an overpotential of 400 mV and n represents the number of moles of Ni deposited at the GC electrode.

5.4 Experiment part of Chapter 4

5.4.1 Materials Preparation

The Ni-BPDC-MOF synthesis procedure followed our previously reported method,[16] which involved combining 64 ml of N, N-Dimethylformamide (DMF, 99.9%, Sigma-Aldrich), 4 ml of absolute ethanol (EMPARTA), and 4 ml of DI-water (18.2 MΩ). Subsequently, 1.5 mmol of biphenyl-4,4'-dicarboxylic acid (H_2BPDC, 98%, abcr) was dissolved in the aforementioned solvent. After sonicating for 10 minutes, 1.5 mmol of $NiCl_2$·6H2O (Fischer Scientific) was introduced to the solution. Following an additional 10 minutes of sonication, 1600 ul of trimethylamine (Et3N, 99.5% Sigma-Aldrich) was swiftly added to the uniform solution. The mixture was then continuously sonicated for 8 hours at 40 kHz. Upon completion, the Ni-MOFs were obtained via centrifugation, and the resulting powders were washed once with DMF and twice with ethanol. The compounds were subsequently soaked in 99.8%

methanol (Sigma-Aldrich) for three days. Finally, the resulting products were dried in an oven at 80℃ overnight.

The synthesis of NiFe-BPDC-MOF followed a similar procedure to that described above, with the exception that 1.125 mmol of $NiCl_2 \cdot 6H_2O$ was combined with 0.375 mmol of $FeCl_2 \cdot 4H_2O$ (99.98%, Sigma-Aldrich) for $Ni_{0.75}Fe_{0.25}$-BPDC-MOF (unless otherwise specified, the NiFe-BPDC-MOF in the main text is $Ni_{0.75}Fe_{0.25}$-MOF) and 0.75 mmol of $NiCl_2 \cdot 6H_2O$ and of $FeCl_2 \cdot 4H_2O$ for $Ni_{0.5}Fe_{0.5}$- BPDC-MOF and dissolved in the same solvent mixture.

The K_2BPDC salt was synthesized from biphenyl-4,4'-dicarboxylic acid (H_2BPDC, 98%, abcr) in a 500 ml round-bottomed flask containing 1 M purified KOH. After stirring in an 80℃ oil bath overnight, the resulting transparent light yellow solution was filtered to remove any possible impurities. Acetone (Sigma-Aldrich, ≥99.5%) was then added to the solution until white powders formed. The white powder was collected by filtration, washed with acetone and ethanol several times, and dried overnight at 80℃.

β-$Ni(OH)_2$ was synthesized in a 45 ml autoclave using 0.429 g of $NiCl_2 \cdot 6H_2O$, 5 ml of deionized water, and 15 ml of 1M pKOH solution. After stirring for 30 minutes, the mixture was heated to 140℃ for 12 hours. The resultant green powder was collected via centrifugation, washed with water, and then dried overnight at 80°C.

5.4.2 Electrochemical measurements

Throughout this investigation, all potassium hydroxide (KOH) solutions underwent purification as outlined in previously published methodologies.[11] For electrode preparation, 5 mg of MOF powder was mixed with 300 µl of water, 700 µl of ethanol, and 40 µl of 5 wt% Nafion solution. This mixture underwent ultrasonication for 10 minutes using a Fisher Scientific FB120 sonicator set to 35% amplitude, followed by an additional 30 minutes in a bath sonicator. The ink was then applied onto a 0.5 cm diameter glassy carbon RDE electrode, with 10 µl of the mixture deposited. Electrochemical experiments were conducted using a three-electrode setup and a

VSP-300 potentiostat from Bio-Logic. The working electrode was glassy carbon, while a Pt wire and a Hg/HgO (1 M NaOH) electrode served as the counter and reference electrodes, respectively. The reference electrode was calibrated under a highly pure H_2 atmosphere. Electrochemical cyclic voltammetry (CV) measurements were performed in an O_2-saturated electrolytes within a voltage range of 1.13 to 1.67 V *vs*. RHE, utilizing 97% IR correction and a scan rate of 10 mV s^{-1}. Stability testing involved chronopotentiometry at a current density of 10 mA cm^{-2} following a pre-CV-cycling process with RDE 1600 rpm. Same volume of MOFs (10 µl of ink as above preparation) were dropped on the glass carbon. When the carbon paper (1*1 cm, **Figure 5e**) as the substrate for the stability testing, 40 µl of the above ink was deposited on it. Furthermore, considering to better compared the pH results, the conversion from $E_{Hg/HgO}$ to E_{RHE} is following the calibration results as shown in **Figure A4.7 (**$E_{RHE} = E_{Hg/HgO} + 0.059pH + 0.106$. details seeing in Figure A4.7**) .** The Electrochemical impedance spectroscopy (EIS) measurements was carried out in a potential range of 1.466-1.586 V vs. RHE with a 40 mV step with 1600 rotating speed. A frequency range from 100 kHz to 0.2 Hz and a 10 mV probing amplitude were used in this measurement.

For the exploration of oxidation issue for extra linker in neutral electrolytes, 5 mg of b-$Ni(OH)_2$ or powder (Sigma-Aldrich) was mixed with 300 µl of water, 700 µl of ethanol, and 40 µl of a 5 wt% Nafion solution. 10 µl of the ink was deposited on the glass carbon. Before testing constant voltage treatment for HPLC in 1 M Na_2SO_4(The choice of the Na_2SO_4 is to avoid the interference of the alkali for HPLC) with or without 0.05 M ex-CL as the electrolytes, the b-$Ni(OH)_2$ on GC was activated in the purified 1M KOH for 30 CV cycles within a voltage range of 1.13 to 1.62 V vs. RHE with a 20 mV s^{-1} scan rate.

The oxygen release during OER was quantified using chip-based electrochemical mass spectrometry from SpectroInlets. Samples were deposited on a 5 mm diameter glassy carbon disk and measured in 0.1 M KOH with addition of 0.02 M ex-CL. A

$Hg/HgSO_4$ electrode and a Pt mesh were used as reference and counter electrodes, respectively. The catalysts were operated under constant potential at 1.41, 1.43, 1.45, 1.47, 1.49 and 1.51 V *vs.* RHE, with each step holding for 120 s to allow O_2 produced by the reaction to diffuse into the carrier gas and pass though the mass spectrometer. Helium was used as a carrier gas during EC-MS experiments. The resulting M/Z=32 signal was recorded and integrated to determine the oxygen amount. Prior to the measurement, the M/Z=32 signal was calibrated to oxygen concentration using OER on a clean Pt disk electrode in 0.1 M $HClO_4$ as reference.

5.5 Reference

1) Lee, K. S.; Landry, Z.; Pereira, F. C.; Wagner, M.; Berry, D.; Huang, W. E.; Taylor, G. T.; Kneipp, J.; Popp, J.; Zhang, M.; Cheng, J.-X.; Stocker, R., Raman microspectroscopy for microbiology. *Nature Reviews Methods Primers* **2021,** *1*, 80.

2) Mosca, S.; Conti, C.; Stone, N.; Matousek, P., Spatially offset Raman spectroscopy. *Nature Reviews Methods Primers* **2021,** *1*,21.

3) C. V. RAMAN , K. S. K., A New Type of Secondary Radiation. *Nature* **1928,** *121*, 501–502

4) Stevie, F. A.; Donley, C. L., Introduction to x-ray photoelectron spectroscopy. *Journal of Vacuum Science & Technology A: Vacuum, Surfaces, and Films* **2020,** *38*.

5) Steinhardt, R.; Serfass, E., X-Ray Photoelectron Spectrometer for Chemical Analysis. *Analytical Chemistry* **1951,** *23*, 1585–1590.

6) Carl Nordling, E. S., and Kai Siegbahn, Precision Method for Obtaining Absolute Values of Atomic Binding Energies. *Physical Review* **1957**, *105*, 1676.

7) Welter, E.; Chernikov, R.; Herrmann, M.; Nemausat, R. A beamline for bulk sample x-ray absorption spectroscopy at the high brilliance storage ring PETRA III. *AIP Conference Proceedings* **2019**, *2054*, 040002.

8) Ravel, B.; Newville, M. ATHENA, ARTEMIS, HEPHAESTUS: data analysis for X-ray absorption spectroscopy using IFEFFIT. *Journal of Synchrotron Radiation* **2005**, *12*, 537-541.

9) Zhao, S.; Wang, Y.; Dong, J.; He, C.-T.; Yin, H.; An, P.; Zhao, K.; Zhang, X.; Gao, C.; Zhang, L.; Lv, J.; Wang, J.; Zhang, J.; Khattak, A. M.; Khan, N. A.; Wei, Z.; Zhang, J.; Liu, S.; Zhao, H.; Tang, Z. Ultrathin metal–organic framework nanosheets for electrocatalytic oxygen evolution. *Nature Energy* **2016**, *1*, 16184.

10) Kim, S.-H.; Lee, H. H.; Kim, J.-M.; Hong, S. Y.; Lee, S.-Y. Heteromat-Framed Metal-Organic Coordination Polymer Anodes for High-Performance Lithium-Ion Batteries. *Energy Storage Materials* **2019**, *19*, 130-136.

11) Trotochaud, L.; Young, S. L.; Ranney, J. K.; Boettcher, S. W. Nickel – Iron Oxyhydroxide Oxygen-Evolution Electrocatalysts: The Role of Intentional and Incidental Iron Incorporation. *Journal of the American Chemical Society* **2014**, *136* , 6744-6753.

12) Tian, M.; Cousins, C.; Beauchemin, D.; Furuya, Y.; Ohma, A.; Jerkiewicz, G. Influence of the Working and Counter Electrode Surface Area Ratios on the Dissolution of Platinum under Electrochemical Conditions. *ACS Catalysis* **2016**, *6*, 5108−5116.

13) Reier, T.; Oezaslan, M.; Strasser, P. Electrocatalytic oxygen evolution reaction (OER) on Ru, Ir, and Pt catalysts: a comparative study of nanoparticles and bulk materials. *ACS Catalysis* **2012**, *2*, 1765– 1772.

14) Cui, Z.; Sheng, W. Thoughts about Choosing a Proper Counter Electrode. *ACS Catalysis* **2023**, *13*, 2534–2541.

15) Jerkiewicz, G. Applicability of Platinum as a Counter-Electrode Material in Electrocatalysis Research. *ACS Catalysis* **2022**, *12*, 2661– 2670,

16) Ma, X.; Zheng, D. J.; Hou, S.; Mukherjee, S.; Khare, R.; Gao, G.; Ai, Q.; Garlyyev, B.; Li, W.; Koch, M.; Mink, J.; Shao-Horn, Y.; Warnan, J.; Bandarenka, A. S.; Fischer, R. A., Structure–Activity Relationships in Ni- Carboxylate-Type Metal–Organic Frameworks' Metamorphosis for the Oxygen Evolution Reaction. *ACS Catalysis* **2023**, *13*, 7587-7596.

6. Conclusion and perspective

In this dissertation, a series of Ni(Fe) MOFs based on carboxylate linkers were investigated to determine the active sites of the MOFs and the relationship between MOFs, derived intermediates, and OER activities. We further examined the electrochemical characteristics and changes in crystal structures during the degradation and reconstruction processes.

Chapter 3 focused on whether pristine MOFs act as catalysts or precursors first. Using the ultrasonication method, we synthesized thin 2D MOFs and found that these MOFs were quite unstable in 1 M alkaline electrolytes, indicating that pristine MOFs serve as precursors rather than catalysts in the alkaline OER process. We then explored whether the pristine MOF structure influences OER activity by comparing a series of Ni-MOFs (formula [Ni2(OH)2L]) with various carboxylate linker lengths (L = 1,4-azodicarboxylate, 2,6-naphthalene dicarboxylate, biphenyl-4,4'-dicarboxylate, and p-terphenyl-4,4"-dicarboxylate).The different Ni-MOF results demonstrated that the pristine MOF's structure indeed affects the electrocatalytic behavior after excluding other interfering factors like morphology, Fe impurities, and substrates. Using ex-situ methods to simulate the alkaline OER process, we systematically investigated the degradation and reconstruction of MOFs in alkaline electrolytes via time-dependent PXRD and Raman spectroscopy. The choice of linker was found to influence the transformation of Ni-MOF into distinct nickel hydroxide phases and the conversion from disordered α-$Ni(OH)_2$ to ordered β-$Ni(OH)_2$. Additionally, the stability of the MOFs, influenced by linker selection, impacts the MOF reconstruction process under OER conditions, explaining the varying OER activities of different Ni-MOFs.

In **Chapter 4**, we further investigated the influence of MOF structure stability on OER activities using more in-situ and ex-situ characterization techniques. Inspired by

the coordination equilibrium equation, we introduced an extra linker in the electrolyte to enhance the alkali stability of MOFs and control the reconstruction process. Ni(Fe)-BPDC-MOF was selected for this study due to its superior OER performance based on the Chapter 3. The presence of the extra linker improved the stability of the MOF in harsh alkaline environments, delaying the transition from disordered to ordered metal hydroxide phases as observed in ex-situ measurements. In-situ Raman spectroscopy during OER revealed that the addition of the linker resulted in more disordered metal oxyhydroxides, which exhibited enhanced OER performance.

Despite the complexity of MOFs, which makes it challenging to study their mechanism in OER applications compared to other materials, their diversity and unique coordination structures offer abundant opportunities in the field of electrocatalysis. This work aimed to elucidate the behavior of MOFs and their transformation mechanisms in alkaline solutions. Looking forward, this research is expected to guide the design of MOF catalysts with exceptional activity. It is with more expectation that the unique structures of MOFs will deepen our understanding and open new avenues in the mechanisms toward more microscale of OER, electrocatalysis, and catalysis filed.

7. Appendix

List of publications

This thesis is based on the following published (in preparation) manuscripts and conference contributions:

1.**Ma, X.**; Zheng, D. J.; Hou, S.; Mukherjee, S.; Khare, R.; Gao, G.; Ai, Q.; Garlyyev, B.; Li, W.; Koch, M.; Mink, J.; Shao-Horn, Y.; Warnan, J.; Bandarenka, A. S.; Fischer, R. A., Structure–Activity Relationships in Ni- Carboxylate-Type Metal–Organic Frameworks' Metamorphosis for the Oxygen Evolution Reaction. *ACS Catalysis* **2023**, *13* (11), 7587-7596.

2. **Ma,, X.** Schröck, L., Gao, G., Ai, Q. Zarrabeitia, M. Liang, C., Hussain, M., Khare,R., Song,K., Zheng, D., Koch,M., Stephens, E. I. , Hou, S. Shao-Horn,Y., Warnan, J., Bandarenka, S. A, & Fischer, R. A. Tuning the Reconstruction of Metal-Organic Frameworks during the Oxygen Evolution Reaction. *ACS Catalysis* **2024**, *14*, (21), 15916–15926

Other publications:

3.Liu, K. S.; **Ma, X.**; Rizzato, R.; Semrau, A. L.; Henning, A.; Sharp, I. D.; Fischer, R. A.; Bucher, D. B., Using Metal–Organic Frameworks to Confine Liquid Samples for Nanoscale NV-NMR. *Nano Letters* **2022**, *22* (24), 9876-9882.(Co-first-author)

4.Zheng, D. J.; Görlin, M.; McCormack, K.; Kim, J.; Peng, J.; Xu, H.; Ma, X.; LeBeau, J. M.; Fischer, R. A.; Román-Leshkov, Y.; Shao-Horn, Y., Linker-Dependent Stability of Metal-Hydroxide Organic Frameworks for Oxygen Evolution. *Chemistry of Materials* **2023,** *35* (13), 5017-5031.

5. Hou, S., Xu, L., Mukherjee, S. Zhou, J., Song, K.-T., Zhou, Z., Zhang, S., **Ma, X.** Warnan, J., Bandarenka, S. A, & Fischer, R. A. Impact of organic anions on metal hydroxide oxygen evolution catalysts *ACS Catalysis* **2024**, *14* (16), 12074–12081

List of conference

1. The SUNCAT Summer Institute: Catalysis for a Sustainable Future, virtual meeting, 16 - 19 August 2021. (Attendance)

2. Virtual Conference on Metal-Organic Frameworks and Open Framework Compounds (MOF2020web), Dresen, virtual conference, 21-24. September 2020 (attendance)

3. **Xiaoxin Ma**, Julien Warnan, Roland Fischer, Understanding the Conversion of Alkali-treated Metal Organic Frameworks for Electrocatalytic Oxygen Evolution Reaction, 8th International Conference on Metal-Organic Frameworks and Open Framework Compounds, Dresden, Germany, 4 - 7 September 2022 (Oral presentation)

Reprint Permissions

ELSEVIER LICENSE
TERMS AND CONDITIONS

Nov 09, 2024

This Agreement between Technical University of Munich---Xiaoxin Ma ("You") and Elsevier ("Elsevier") consists of your license details and the terms and conditions provided by Elsevier and Copyright Clearance Center.

License Number	5904861454390
License date	Nov 09, 2024
Licensed Content Publisher	Elsevier
Licensed Content Publication	Trends in Chemistry
Licensed Content Title	Electronic-Structure Tuning of Water-Splitting Nanocatalysts
Licensed Content Author	Wenxiu Yang,Zichen Wang,Weiyu Zhang,Shaojun Guo
Licensed Content Date	May 1, 2019
Licensed Content Volume	93
Licensed Content Issue	1
Licensed Content Pages	13
Start Page	259
End Page	271
Type of Use	reuse in a thesis/dissertation

1. The publisher for this copyrighted material is Elsevier. By clicking "accept" in connection with completing this licensing transaction, you agree that the following terms and conditions apply to this transaction (along with the Billing and Payment terms and conditions established by Copyright Clearance Center, Inc. ("CCC"), at the time that you opened your RightsLink account and that are available at any time at https://myaccount.copyright.com).

GENERAL TERMS

2. Elsevier hereby grants you permission to reproduce the aforementioned material subject to the terms and conditions indicated.

3. Acknowledgement: If any part of the material to be used (for example, figures) has appeared in our publication with credit or acknowledgement to another source, permission must also be sought from that source. If such permission is not obtained then that material may not be included in your publication/copies. Suitable acknowledgement to the source must be made, either as a footnote or in a reference list at the end of your publication, as follows:

"Reprinted from Publication title, Vol /edition number, Author(s), Title of article / title of chapter, Pages No., Copyright (Year), with permission from Elsevier [OR APPLICABLE SOCIETY COPYRIGHT OWNER]." Also Lancet special credit - "Reprinted from The Lancet, Vol. number, Author(s), Title of article, Pages No., Copyright (Year), with permission from Elsevier."

4. Reproduction of this material is confined to the purpose and/or media for which permission is hereby given. The material may not be reproduced or used in any other way, including use in combination with an artificial intelligence tool (including to train an algorithm, test, process, analyse, generate output and/or develop any form of artificial intelligence tool), or to create any derivative work and/or service (including resulting from the use of artificial intelligence tools).

5. Altering/Modifying Material: Not Permitted. However figures and illustrations may be altered/adapted minimally to serve your work. Any other abbreviations, additions, deletions and/or any other alterations shall be made only with prior written authorization of Elsevier Ltd. (Please contact Elsevier's permissions helpdesk here). No modifications can be made to any Lancet figures/tables and they must be reproduced in full.

6. If the permission fee for the requested use of our material is waived in this instance, please be advised that your future requests for Elsevier materials may attract a fee.

7. Reservation of Rights: Publisher reserves all rights not specifically granted in the combination of (i) the license details provided by you and accepted in the course of this licensing transaction, (ii) these terms and conditions and (iii) CCC's Billing and Payment terms and conditions.

8. License Contingent Upon Payment: While you may exercise the rights licensed immediately upon issuance of the license at the end of the licensing process for the transaction, provided that you have disclosed complete and accurate details of your proposed use, no license is finally effective unless and until full payment is received from you (either by publisher or by CCC) as provided in CCC's Billing and Payment terms and conditions. If full payment is not received on a timely basis, then any license preliminarily granted shall be deemed automatically revoked and shall be void as if never granted. Further, in the event that you breach any of these terms and conditions or any of CCC's Billing and Payment terms and conditions, the license is automatically revoked and shall be void as if never granted. Use of materials as described in a revoked license, as well as any use of the materials beyond the scope of an unrevoked license, may constitute copyright infringement and publisher reserves the right to take any and all action to protect its copyright in the materials.

9. Warranties: Publisher makes no representations or warranties with respect to the licensed material.

10. Indemnity: You hereby indemnify and agree to hold harmless publisher and CCC, and their respective officers, directors, employees and agents, from and against any and all claims arising out of your use of the licensed material other than as specifically authorized pursuant to this license.

11. No Transfer of License: This license is personal to you and may not be sublicensed, assigned, or transferred by you to any other person without publisher's written permission.

12. No Amendment Except in Writing: This license may not be amended except in a writing signed by both parties (or, in the case of publisher, by CCC on publisher's behalf).

13. Objection to Contrary Terms: Publisher hereby objects to any terms contained in any purchase order, acknowledgment, check endorsement or other writing prepared by you, which terms are inconsistent with these terms and conditions or CCC's Billing and Payment terms and conditions. These terms and conditions, together with CCC's Billing and Payment terms and conditions (which are incorporated herein), comprise the entire agreement between you and publisher (and CCC) concerning this licensing transaction. In the event of any conflict between your obligations established by these terms and conditions and those established by CCC's Billing and Payment terms and conditions, these terms and conditions shall control.

14. Revocation: Elsevier or Copyright Clearance Center may deny the permissions described in this License at their sole discretion, for any reason or no reason, with a full refund payable to you. Notice of such denial will be made using the contact information provided by you. Failure to receive such notice will not alter or invalidate the denial. In no event will Elsevier or Copyright Clearance Center be responsible or liable for any costs, expenses or damage incurred by you as a result of a denial of your permission request, other than a refund of the amount(s) paid by you to Elsevier and/or Copyright Clearance Center for denied permissions.

LIMITED LICENSE

The following terms and conditions apply only to specific license types:

15. **Translation**: This permission is granted for non-exclusive world **English** rights only unless your license was granted for translation rights. If you licensed translation rights you may only translate this content into the languages you requested. A professional translator must perform all translations and reproduce the content word for word preserving the integrity of the article.

16. **Posting licensed content on any Website**: The following terms and conditions apply as follows: Licensing material from an Elsevier journal: All content posted to the web site must maintain the copyright information line on the bottom of each image; A hyper-text must be included to the Homepage of the journal from which you are licensing at http://www.sciencedirect.com/science/journal/xxxxx or the Elsevier homepage for books at http://www.elsevier.com; Central Storage: This license does not include permission for a scanned version of the material to be stored in a central repository such as that provided by Heron/XanEdu.

Licensing material from an Elsevier book: A hyper-text link must be included to the Elsevier homepage at http://www.elsevier.com . All content posted to the web site must maintain the copyright information line on the bottom of each image.

Posting licensed content on Electronic reserve: In addition to the above the following clauses are applicable: The web site must be password-protected and made available only

to bona fide students registered on a relevant course. This permission is granted for 1 year only. You may obtain a new license for future website posting.

17. **For journal authors:** the following clauses are applicable in addition to the above:

Preprints:

A preprint is an author's own write-up of research results and analysis, it has not been peer-reviewed, nor has it had any other value added to it by a publisher (such as formatting, copyright, technical enhancement etc.).

Authors can share their preprints anywhere at any time. Preprints should not be added to or enhanced in any way in order to appear more like, or to substitute for, the final versions of articles however authors can update their preprints on arXiv or RePEc with their Accepted Author Manuscript (see below).

If accepted for publication, we encourage authors to link from the preprint to their formal publication via its DOI. Millions of researchers have access to the formal publications on ScienceDirect, and so links will help users to find, access, cite and use the best available version. Please note that Cell Press, The Lancet and some society-owned have different preprint policies. Information on these policies is available on the journal homepage.

Accepted Author Manuscripts: An accepted author manuscript is the manuscript of an article that has been accepted for publication and which typically includes author-incorporated changes suggested during submission, peer review and editor-author communications.

Authors can share their accepted author manuscript:

- immediately
  - via their non-commercial person homepage or blog
  - by updating a preprint in arXiv or RePEc with the accepted manuscript
  - via their research institute or institutional repository for internal institutional uses or as part of an invitation-only research collaboration work-group
  - directly by providing copies to their students or to research collaborators for their personal use
  - for private scholarly sharing as part of an invitation-only work group on commercial sites with which Elsevier has an agreement
- After the embargo period
  - via non-commercial hosting platforms such as their institutional repository
  - via commercial sites with which Elsevier has an agreement

In all cases accepted manuscripts should:

- link to the formal publication via its DOI
- bear a CC-BY-NC-ND license - this is easy to do
- if aggregated with other manuscripts, for example in a repository or other site, be shared in alignment with our hosting policy not be added to or enhanced in any way to appear more like, or to substitute for, the published journal article.

Published journal article (JPA): A published journal article (PJA) is the definitive final record of published research that appears or will appear in the journal and embodies all value-adding publishing activities including peer review co-ordination, copy-editing, formatting, (if relevant) pagination and online enrichment.

Policies for sharing publishing journal articles differ for subscription and gold open access articles:

Subscription Articles: If you are an author, please share a link to your article rather than the full-text. Millions of researchers have access to the formal publications on ScienceDirect, and so links will help your users to find, access, cite, and use the best available version.

Theses and dissertations which contain embedded PJAs as part of the formal submission can be posted publicly by the awarding institution with DOI links back to the formal publications on ScienceDirect.

If you are affiliated with a library that subscribes to ScienceDirect you have additional private sharing rights for others' research accessed under that agreement. This includes use for classroom teaching and internal training at the institution (including use in course packs and courseware programs), and inclusion of the article for grant funding purposes.

Gold Open Access Articles: May be shared according to the author-selected end-user license and should contain a CrossMark logo, the end user license, and a DOI link to the formal publication on ScienceDirect.

Please refer to Elsevier's posting policy for further information.

18. **For book authors** the following clauses are applicable in addition to the above: Authors are permitted to place a brief summary of their work online only. You are not allowed to download and post the published electronic version of your chapter, nor may you scan the printed edition to create an electronic version. **Posting to a repository:** Authors are permitted to post a summary of their chapter only in their institution's repository.

19. **Thesis/Dissertation**: If your license is for use in a thesis/dissertation your thesis may be submitted to your institution in either print or electronic form. Should your thesis be published commercially, please reapply for permission. These requirements include permission for the Library and Archives of Canada to supply single copies, on demand, of the complete thesis and include permission for Proquest/UMI to supply single copies, on demand, of the complete thesis. Should your thesis be published commercially, please reapply for permission. Theses and dissertations which contain embedded PJAs as part of the formal submission can be posted publicly by the awarding institution with DOI links back to the formal publications on ScienceDirect.

Elsevier Open Access Terms and Conditions

You can publish open access with Elsevier in hundreds of open access journals or in nearly 2000 established subscription journals that support open access publishing. Permitted third party re-use of these open access articles is defined by the author's choice of Creative Commons user license. See our open access license policy for more information.

Terms & Conditions applicable to all Open Access articles published with Elsevier:

Any reuse of the article must not represent the author as endorsing the adaptation of the article nor should the article be modified in such a way as to damage the author's honour or reputation. If any changes have been made, such changes must be clearly indicated.

The author(s) must be appropriately credited and we ask that you include the end user license and a DOI link to the formal publication on ScienceDirect.

If any part of the material to be used (for example, figures) has appeared in our publication with credit or acknowledgement to another source it is the responsibility of the

user to ensure their reuse complies with the terms and conditions determined by the rights holder.

Additional Terms & Conditions applicable to each Creative Commons user license:

CC BY: The CC-BY license allows users to copy, to create extracts, abstracts and new works from the Article, to alter and revise the Article and to make commercial use of the Article (including reuse and/or resale of the Article by commercial entities), provided the user gives appropriate credit (with a link to the formal publication through the relevant DOI), provides a link to the license, indicates if changes were made and the licensor is not represented as endorsing the use made of the work. The full details of the license are available at http://creativecommons.org/licenses/by/4.0.

CC BY NC SA: The CC BY-NC-SA license allows users to copy, to create extracts, abstracts and new works from the Article, to alter and revise the Article, provided this is not done for commercial purposes, and that the user gives appropriate credit (with a link to the formal publication through the relevant DOI), provides a link to the license, indicates if changes were made and the licensor is not represented as endorsing the use made of the work. Further, any new works must be made available on the same conditions. The full details of the license are available at http://creativecommons.org/licenses/by-nc-sa/4.0.

CC BY NC ND: The CC BY-NC-ND license allows users to copy and distribute the Article, provided this is not done for commercial purposes and further does not permit distribution of the Article if it is changed or edited in any way, and provided the user gives appropriate credit (with a link to the formal publication through the relevant DOI), provides a link to the license, and that the licensor is not represented as endorsing the use made of the work. The full details of the license are available at http://creativecommons.org/licenses/by-nc-nd/4.0. Any commercial reuse of Open Access articles published with a CC BY NC SA or CC BY NC ND license requires permission from Elsevier and will be subject to a fee.

Commercial reuse includes:

- Associating advertising with the full text of the Article
- Charging fees for document delivery or access
- Article aggregation
- Systematic distribution via e-mail lists or share buttons

Posting or linking by commercial companies for use by customers of those companies.

20. **Other Conditions**:

v1.10

Questions? customercare@copyright.com.

JOHN WILEY AND SONS LICENSE
TERMS AND CONDITIONS

Nov 09, 2024

This Agreement between Technical of University of Munich--Xiaoxin Ma ("You") and John Wiley and Sons ("John Wiley and Sons") consists of your license details and the terms and conditions provided by John Wiley and Sons and Copyright Clearance Center.

License Number	5904890309030
License date	Nov 09, 2024
Licensed Content Publisher	John Wiley and Sons
Licensed Content Publication	Angewandte Chemie International Edition
Licensed Content Title	Advancing the Electrochemistry of the Hydrogen-Evolution Reaction through Combining Experiment and Theory
Licensed Content Author	Shi Zhang Qiao, Mietek Jaroniec, Yan Jiao, et al
Licensed Content Date	Nov 10, 2014
Licensed Content Volume	54
Licensed Content Issue	1
Licensed Content Pages	14
Type of use	Dissertation/Thesis
Requestor type	University/Academic
Format	Print and electronic

Portion	Figure/table
Number of figures/tables	2
Will you be translating?	No
Title of new work	Deciphering the Active Role of Carboxylate-type MOFs in Alkaline OER: From Pristine Structures to Functional Intermediates
Institution name	Technical University of Munich
Expected presentation date	Nov 2024
Portions	Figure 8.a, Figure 8.c
The Requesting Person / Organization to Appear on the License	Technical of University of Munich--Xiaoxin Ma
Requestor Location	xiaoxin ma Technical University of Munich,Garching Munich, Not US or Canada 85748 Germany
Publisher Tax ID	EU826007151
Total	0.00 EUR
Terms and Conditions	

TERMS AND CONDITIONS

This copyrighted material is owned by or exclusively licensed to John Wiley & Sons, Inc. or one of its group companies (each a"Wiley Company") or handled on behalf of a society with which a Wiley Company has exclusive publishing rights in relation to a particular work (collectively "WILEY"). By clicking "accept" in connection with completing this licensing transaction, you agree that the following terms and conditions apply to this transaction (along with the billing and payment terms and conditions established by the Copyright Clearance Center Inc., ("CCC's Billing and Payment terms and conditions"), at the time that you opened your RightsLink account (these are available at any time at http://myaccount.copyright.com).

Terms and Conditions

- The materials you have requested permission to reproduce or reuse (the "Wiley Materials") are protected by copyright.

- You are hereby granted a personal, non-exclusive, non-sub licensable (on a stand-alone basis), non-transferable, worldwide, limited license to reproduce the Wiley Materials for the purpose specified in the licensing process. This license, **and any CONTENT (PDF or image file) purchased as part of your order,** is for a one-time use only and limited to any maximum distribution number specified in the license. The first instance of republication or reuse granted by this license must be completed within two years of the date of the grant of this license (although copies prepared before the end date may be distributed thereafter). The Wiley Materials shall not be used in any other manner or for any other purpose, beyond what is granted in the license. Permission is granted subject to an appropriate acknowledgement given to the author, title of the material/book/journal and the publisher. You shall also duplicate the copyright notice that appears in the Wiley publication in your use of the Wiley Material. Permission is also granted on the understanding that nowhere in the text is a previously published source acknowledged for all or part of this Wiley Material. Any third party content is expressly excluded from this permission.

- With respect to the Wiley Materials, all rights are reserved. Except as expressly granted by the terms of the license, no part of the Wiley Materials may be copied, modified, adapted (except for minor reformatting required by the new Publication), translated, reproduced, transferred or distributed, in any form or by any means, and no derivative works may be made based on the Wiley Materials without the prior permission of the respective copyright owner.**For STM Signatory Publishers clearing permission under the terms of the STM Permissions Guidelines only, the terms of the license are extended to include subsequent editions and for editions in other languages, provided such editions are for the work as a whole in situ and does not involve the separate exploitation of the permitted figures or extracts,** You may not alter, remove or suppress in any manner any copyright, trademark or other notices displayed by the Wiley Materials. You may not license, rent, sell, loan, lease, pledge, offer as security, transfer or assign the Wiley Materials on a stand-alone basis, or any of the rights granted to you hereunder to any other person.

- The Wiley Materials and all of the intellectual property rights therein shall at all times remain the exclusive property of John Wiley & Sons Inc, the Wiley Companies, or their respective licensors, and your interest therein is only that of having possession of and the right to reproduce the Wiley Materials pursuant to Section 2 herein during the continuance of this Agreement. You agree that you own no right, title or interest in or to the Wiley Materials or any of the intellectual property rights therein. You shall have no rights hereunder other than the license as provided for above in Section 2. No right, license or interest to any trademark, trade name, service mark or other branding ("Marks") of WILEY or its licensors is granted hereunder, and you agree that you shall not assert any such right, license or interest with respect thereto

- NEITHER WILEY NOR ITS LICENSORS MAKES ANY WARRANTY OR REPRESENTATION OF ANY KIND TO YOU OR ANY THIRD PARTY, EXPRESS, IMPLIED OR STATUTORY, WITH RESPECT TO THE MATERIALS OR THE ACCURACY OF ANY INFORMATION CONTAINED IN THE MATERIALS, INCLUDING, WITHOUT LIMITATION, ANY IMPLIED WARRANTY OF MERCHANTABILITY, ACCURACY, SATISFACTORY QUALITY, FITNESS FOR A PARTICULAR PURPOSE, USABILITY,

INTEGRATION OR NON-INFRINGEMENT AND ALL SUCH WARRANTIES ARE HEREBY EXCLUDED BY WILEY AND ITS LICENSORS AND WAIVED BY YOU.

- WILEY shall have the right to terminate this Agreement immediately upon breach of this Agreement by you.
- You shall indemnify, defend and hold harmless WILEY, its Licensors and their respective directors, officers, agents and employees, from and against any actual or threatened claims, demands, causes of action or proceedings arising from any breach of this Agreement by you.
- IN NO EVENT SHALL WILEY OR ITS LICENSORS BE LIABLE TO YOU OR ANY OTHER PARTY OR ANY OTHER PERSON OR ENTITY FOR ANY SPECIAL, CONSEQUENTIAL, INCIDENTAL, INDIRECT, EXEMPLARY OR PUNITIVE DAMAGES, HOWEVER CAUSED, ARISING OUT OF OR IN CONNECTION WITH THE DOWNLOADING, PROVISIONING, VIEWING OR USE OF THE MATERIALS REGARDLESS OF THE FORM OF ACTION, WHETHER FOR BREACH OF CONTRACT, BREACH OF WARRANTY, TORT, NEGLIGENCE, INFRINGEMENT OR OTHERWISE (INCLUDING, WITHOUT LIMITATION, DAMAGES BASED ON LOSS OF PROFITS, DATA, FILES, USE, BUSINESS OPPORTUNITY OR CLAIMS OF THIRD PARTIES), AND WHETHER OR NOT THE PARTY HAS BEEN ADVISED OF THE POSSIBILITY OF SUCH DAMAGES. THIS LIMITATION SHALL APPLY NOTWITHSTANDING ANY FAILURE OF ESSENTIAL PURPOSE OF ANY LIMITED REMEDY PROVIDED HEREIN.
- Should any provision of this Agreement be held by a court of competent jurisdiction to be illegal, invalid, or unenforceable, that provision shall be deemed amended to achieve as nearly as possible the same economic effect as the original provision, and the legality, validity and enforceability of the remaining provisions of this Agreement shall not be affected or impaired thereby.
- The failure of either party to enforce any term or condition of this Agreement shall not constitute a waiver of either party's right to enforce each and every term and condition of this Agreement. No breach under this agreement shall be deemed waived or excused by either party unless such waiver or consent is in writing signed by the party granting such waiver or consent. The waiver by or consent of a party to a breach of any provision of this Agreement shall not operate or be construed as a waiver of or consent to any other or subsequent breach by such other party.
- This Agreement may not be assigned (including by operation of law or otherwise) by you without WILEY's prior written consent.
- Any fee required for this permission shall be non-refundable after thirty (30) days from receipt by the CCC.
- These terms and conditions together with CCC's Billing and Payment terms and conditions (which are incorporated herein) form the entire agreement between you and WILEY concerning this licensing transaction and (in the absence of fraud) supersedes all prior agreements and representations of the parties, oral or written. This Agreement may not be amended except in writing signed by both parties. This Agreement shall be binding upon and inure to the benefit of the parties' successors, legal representatives, and authorized assigns.
- In the event of any conflict between your obligations established by these terms and conditions and those established by CCC's Billing and Payment terms and

conditions, these terms and conditions shall prevail.

- WILEY expressly reserves all rights not specifically granted in the combination of (i) the license details provided by you and accepted in the course of this licensing transaction, (ii) these terms and conditions and (iii) CCC's Billing and Payment terms and conditions.
- This Agreement will be void if the Type of Use, Format, Circulation, or Requestor Type was misrepresented during the licensing process.
- This Agreement shall be governed by and construed in accordance with the laws of the State of New York, USA, without regards to such state's conflict of law rules. Any legal action, suit or proceeding arising out of or relating to these Terms and Conditions or the breach thereof shall be instituted in a court of competent jurisdiction in New York County in the State of New York in the United States of America and each party hereby consents and submits to the personal jurisdiction of such court, waives any objection to venue in such court and consents to service of process by registered or certified mail, return receipt requested, at the last known address of such party.

WILEY OPEN ACCESS TERMS AND CONDITIONS

Wiley Publishes Open Access Articles in fully Open Access Journals and in Subscription journals offering Online Open. Although most of the fully Open Access journals publish open access articles under the terms of the Creative Commons Attribution (CC BY) License only, the subscription journals and a few of the Open Access Journals offer a choice of Creative Commons Licenses. The license type is clearly identified on the article.

The Creative Commons Attribution License

The Creative Commons Attribution License (CC-BY) allows users to copy, distribute and transmit an article, adapt the article and make commercial use of the article. The CC-BY license permits commercial and non-

Creative Commons Attribution Non-Commercial License

The Creative Commons Attribution Non-Commercial (CC-BY-NC)License permits use, distribution and reproduction in any medium, provided the original work is properly cited and is not used for commercial purposes.(see below)

Creative Commons Attribution-Non-Commercial-NoDerivs License

The Creative Commons Attribution Non-Commercial-NoDerivs License (CC-BY-NC-ND) permits use, distribution and reproduction in any medium, provided the original work is properly cited, is not used for commercial purposes and no modifications or adaptations are made. (see below)

Use by commercial "for-profit" organizations

Use of Wiley Open Access articles for commercial, promotional, or marketing purposes requires further explicit permission from Wiley and will be subject to a fee.

Further details can be found on Wiley Online Library
http://olabout.wiley.com/WileyCDA/Section/id-410895.html

Other Terms and Conditions:

v1.10 Last updated September 2015

Questions? customercare@copyright.com.

Marketplace

This is a License Agreement between Technical of University of Munich---Xiaoxin Ma ("User") and Copyright Clearance Center, Inc. ("CCC") on behalf of the Rightsholder identified in the order details below. The license consists of the order details, the Marketplace Permissions General Terms and Conditions below, and any Rightsholder Terms and Conditions which are included below.

All payments must be made in full to CCC in accordance with the Marketplace Permissions General Terms and Conditions below.

Order Date	09-Nov-2024	**Type of Use**	Republish in a thesis/dissertation
Order License ID	1544375-1	**Publisher**	ROYAL SOCIETY OF CHEMISTRY, ETC.]
ISSN	0306-0012	**Portion**	Image/photo/illustration

LICENSED CONTENT

Publication Title	Chemical Society reviews	**Rightsholder**	Royal Society of Chemistry
Article Title	A review on fundamentals for designing oxygen evolution electrocatalysts.	**Publication Type**	Journal
		Start Page	2196
Author / Editor	CHEMICAL SOCIETY (GREAT BRITAIN)	**End Page**	2214
		Issue	7
Date	01/01/1972	**Volume**	49
Language	English		
Country	United Kingdom of Great Britain and Northern Ireland		

REQUEST DETAILS

Portion Type	Image/photo/illustration	**Distribution**	Worldwide
Number of Images / Photos / Illustrations	10	**Translation**	Original language of publication
Format (select all that apply)	Print, Electronic	**Copies for the Disabled?**	No
		Minor Editing Privileges?	No
Who Will Republish the Content?	Academic institution	**Incidental Promotional Use?**	No
Duration of Use	Life of current edition	**Currency**	EUR
Lifetime Unit Quantity	Up to 499		
Rights Requested	Main product		

NEW WORK DETAILS

Title	Deciphering the Active Role of Carboxylate-type MOFs in Alkaline OER: From Pristine Structures to Functional Intermediates	**Institution Name**	Technical of university of Munich
		Expected Presentation Date	2024-11-30
Instructor Name	Roland Fischer		

ADDITIONAL DETAILS

Order Reference Number	N/A	**The Requesting Person / Organization to Appear on the License**	Technical of University of Munich---Xiaoxin Ma

REQUESTED CONTENT DETAILS

Title, Description or Numeric Reference of the Portion(s)	Figure10	**Title of the Article / Chapter the Portion Is From**	A review on fundamentals for designing oxygen evolution electrocatalysts.
Editor of Portion(s)	Song, Jiajia; Wei, Chao; Huang, Zhen-Feng; Liu, Chuntai; Zeng, Lin; Wang, Xin; Xu, Zhichuan J.	**Author of Portion(s)**	Song, Jiajia; Wei, Chao; Huang, Zhen-Feng; Liu, Chuntai; Zeng, Lin; Wang, Xin; Xu, Zhichuan J.
Volume / Edition	49	**Issue, if Republishing an Article From a Serial**	7
Page or Page Range of Portion	2196-2214	**Publication Date of Portion**	2020-04-07

Marketplace Permissions General Terms and Conditions

The following terms and conditions ("General Terms"), together with any applicable Publisher Terms and Conditions, govern User's use of Works pursuant to the Licenses granted by Copyright Clearance Center, Inc. ("CCC") on behalf of the applicable Rightsholders of such Works through CCC's applicable Marketplace transactional licensing services (each, a "Service").

1) **Definitions.** For purposes of these General Terms, the following definitions apply:

"License" is the licensed use the User obtains via the Marketplace platform in a particular licensing transaction, as set forth in the Order Confirmation.

"Order Confirmation" is the confirmation CCC provides to the User at the conclusion of each Marketplace transaction. "Order Confirmation Terms" are additional terms set forth on specific Order Confirmations not set forth in the General Terms that can include terms applicable to a particular CCC transactional licensing service and/or any Rightsholder-specific terms.

"Rightsholder(s)" are the holders of copyright rights in the Works for which a User obtains licenses via the Marketplace platform, which are displayed on specific Order Confirmations.

"Terms" means the terms and conditions set forth in these General Terms and any additional Order Confirmation Terms collectively.

"User" or "you" is the person or entity making the use granted under the relevant License. Where the person accepting the Terms on behalf of a User is a freelancer or other third party who the User authorized to accept the General Terms on the User's behalf, such person shall be deemed jointly a User for purposes of such Terms.

"Work(s)" are the copyright protected works described in relevant Order Confirmations.

2) **Description of Service.** CCC's Marketplace enables Users to obtain Licenses to use one or more Works in accordance with all relevant Terms. CCC grants Licenses as an agent on behalf of the copyright rightsholder identified in the relevant Order Confirmation.

3) **Applicability of Terms.** The Terms govern User's use of Works in connection with the relevant License. In the event of any conflict between General Terms and Order Confirmation Terms, the latter shall govern. User acknowledges that Rightsholders have complete discretion whether to grant any permission, and whether to place any limitations on any grant, and that CCC has no right to supersede or to modify any such discretionary act by a Rightsholder.

4) **Representations; Acceptance.** By using the Service, User represents and warrants that User has been duly authorized by the User to accept, and hereby does accept, all Terms.

5) **Scope of License; Limitations and Obligations.** All Works and all rights therein, including copyright rights, remain the sole and exclusive property of the Rightsholder. The License provides only those rights expressly set forth in the terms and conveys no other rights in any Works

6) **General Payment Terms.** User may pay at time of checkout by credit card or choose to be invoiced. If the User chooses to be invoiced, the User shall: (i) remit payments in the manner identified on specific invoices, (ii) unless otherwise specifically stated in an Order Confirmation or separate written agreement, Users shall remit payments upon receipt of the relevant invoice from CCC, either by delivery or notification of availability of the invoice via the Marketplace platform, and (iii) if the User does not pay the invoice within 30 days of receipt, the User may incur a service charge of 1.5% per month or the maximum rate allowed by applicable law, whichever is less. While User may exercise the rights in the License immediately upon receiving the Order Confirmation, the License is automatically revoked and is null and void, as if it had never been issued, if CCC does not receive complete payment on a timely basis.

7) **General Limits on Use.** Unless otherwise provided in the Order Confirmation, any grant of rights to User (i) involves only the rights set forth in the Terms and does not include subsequent or additional uses, (ii) is non-exclusive and non-transferable, and (iii) is subject to any and all limitations and restrictions (such as, but not limited to, limitations on duration of use or circulation) included in the Terms. Upon completion of the licensed use as set forth in the Order Confirmation, User shall either secure a new permission for further use of the Work(s) or immediately cease any new use of the Work(s) and shall render inaccessible (such as by deleting or by removing or severing links or other locators) any further copies of the Work. User may only make alterations to the Work if and as expressly set forth in the Order Confirmation. No Work may be used in any way that is unlawful, including without limitation if such use would violate applicable sanctions laws or regulations, would be defamatory, violate the rights of third parties (including such third parties' rights of copyright, privacy, publicity, or other tangible or intangible property), or is otherwise illegal, sexually explicit, or obscene. In addition, User may not conjoin a Work with any other material that may result in damage to the reputation of the Rightsholder. Any unlawful use will render any licenses hereunder null and void. User agrees to inform CCC if it becomes aware of any infringement of any rights in a Work and to cooperate with any reasonable request of CCC or the Rightsholder in connection therewith.

8) **Third Party Materials.** In the event that the material for which a License is sought includes third party materials (such as photographs, illustrations, graphs, inserts and similar materials) that are identified in such material as having been used by permission (or a similar indicator), User is responsible for identifying, and seeking separate licenses (under this Service, if available, or otherwise) for any of such third party materials; without a separate license, User may not use such third party materials via the License.

9) **Copyright Notice.** Use of proper copyright notice for a Work is required as a condition of any License granted under the Service. Unless otherwise provided in the Order Confirmation, a proper copyright notice will read substantially as follows: "Used with permission of [Rightsholder's name], from [Work's title, author, volume, edition number and year of copyright]; permission conveyed through Copyright Clearance Center, Inc." Such notice must be provided in a reasonably legible font size and must be placed either on a cover page or in another location that any person, upon gaining access to the material which is the subject of a permission, shall see, or in the case of republication Licenses, immediately adjacent to the Work as used (for example, as part of a by-line or footnote) or in the place where substantially all other credits or notices for the new work containing the republished Work are located. Failure to include the required notice results in loss to the Rightsholder and CCC, and the User shall be liable to pay liquidated damages for each such failure equal to twice the use fee specified in the Order Confirmation, in addition to the use fee itself and any other fees and charges specified.

10) **Indemnity.** User hereby indemnifies and agrees to defend the Rightsholder and CCC, and their respective employees and directors, against all claims, liability, damages, costs, and expenses, including legal fees and expenses, arising out of any use of a Work beyond the scope of the rights granted herein and in the Order Confirmation, or any use of a Work which has been altered in any unauthorized way by User, including claims of defamation or infringement of rights of copyright, publicity, privacy, or other tangible or intangible property.

11) **Limitation of Liability.** UNDER NO CIRCUMSTANCES WILL CCC OR THE RIGHTSHOLDER BE LIABLE FOR ANY DIRECT, INDIRECT, CONSEQUENTIAL, OR INCIDENTAL DAMAGES (INCLUDING WITHOUT LIMITATION DAMAGES FOR LOSS OF BUSINESS PROFITS OR INFORMATION, OR FOR BUSINESS INTERRUPTION) ARISING OUT OF THE USE OR INABILITY TO USE A WORK, EVEN IF ONE OR BOTH OF THEM HAS BEEN ADVISED OF THE POSSIBILITY OF SUCH DAMAGES. In any event, the total liability of the Rightsholder and CCC (including their respective employees and directors) shall not exceed the total amount actually paid by User for the relevant License. User assumes full liability for the actions and omissions of its principals, employees, agents, affiliates, successors, and assigns.

12) **Limited Warranties.** THE WORK(S) AND RIGHT(S) ARE PROVIDED "AS IS." CCC HAS THE RIGHT TO GRANT TO USER THE RIGHTS GRANTED IN THE ORDER CONFIRMATION DOCUMENT. CCC AND THE RIGHTSHOLDER DISCLAIM ALL OTHER WARRANTIES RELATING TO THE WORK(S) AND RIGHT(S), EITHER EXPRESS OR IMPLIED, INCLUDING WITHOUT LIMITATION IMPLIED WARRANTIES OF MERCHANTABILITY OR FITNESS FOR A PARTICULAR PURPOSE. ADDITIONAL RIGHTS MAY BE REQUIRED TO USE ILLUSTRATIONS, GRAPHS, PHOTOGRAPHS, ABSTRACTS, INSERTS, OR OTHER PORTIONS OF THE WORK (AS OPPOSED TO THE ENTIRE WORK) IN A MANNER CONTEMPLATED BY USER; USER UNDERSTANDS AND AGREES THAT NEITHER CCC NOR THE RIGHTSHOLDER MAY HAVE SUCH ADDITIONAL RIGHTS TO GRANT.

13) **Effect of Breach.** Any failure by User to pay any amount when due, or any use by User of a Work beyond the scope of the License set forth in the Order Confirmation and/or the Terms, shall be a material breach of such License. Any breach

not cured within 10 days of written notice thereof shall result in immediate termination of such License without further notice. Any unauthorized (but licensable) use of a Work that is terminated immediately upon notice thereof may be liquidated by payment of the Rightsholder's ordinary license price therefor; any unauthorized (and unlicensable) use that is not terminated immediately for any reason (including, for example, because materials containing the Work cannot reasonably be recalled) will be subject to all remedies available at law or in equity, but in no event to a payment of less than three times the Rightsholder's ordinary license price for the most closely analogous licensable use plus Rightsholder's and/or CCC's costs and expenses incurred in collecting such payment.

14) **Additional Terms for Specific Products and Services.** If a User is making one of the uses described in this Section 14, the additional terms and conditions apply:

a) ***Print Uses of Academic Course Content and Materials (photocopies for academic coursepacks or classroom handouts).*** For photocopies for academic coursepacks or classroom handouts the following additional terms apply:

i) The copies and anthologies created under this License may be made and assembled by faculty members individually or at their request by on-campus bookstores or copy centers, or by off-campus copy shops and other similar entities.

ii) No License granted shall in any way: (i) include any right by User to create a substantively non-identical copy of the Work or to edit or in any other way modify the Work (except by means of deleting material immediately preceding or following the entire portion of the Work copied) (ii) permit "publishing ventures" where any particular anthology would be systematically marketed at multiple institutions.

iii) Subject to any Publisher Terms (and notwithstanding any apparent contradiction in the Order Confirmation arising from data provided by User), any use authorized under the academic pay-per-use service is limited as follows:

A) any License granted shall apply to only one class (bearing a unique identifier as assigned by the institution, and thereby including all sections or other subparts of the class) at one institution;

B) use is limited to not more than 25% of the text of a book or of the items in a published collection of essays, poems or articles;

C) use is limited to no more than the greater of (a) 25% of the text of an issue of a journal or other periodical or (b) two articles from such an issue;

D) no User may sell or distribute any particular anthology, whether photocopied or electronic, at more than one institution of learning;

E) in the case of a photocopy permission, no materials may be entered into electronic memory by User except in order to produce an identical copy of a Work before or during the academic term (or analogous period) as to which any particular permission is granted. In the event that User shall choose to retain materials that are the subject of a photocopy permission in electronic memory for purposes of producing identical copies more than one day after such retention (but still within the scope of any permission granted), User must notify CCC of such fact in the applicable permission request and such retention shall constitute one copy actually sold for purposes of calculating permission fees due; and

F) any permission granted shall expire at the end of the class. No permission granted shall in any way include any right by User to create a substantively non-identical copy of the Work or to edit or in any other way modify the Work (except by means of deleting material immediately preceding or following the entire portion of the Work copied).

iv) Books and Records; Right to Audit. As to each permission granted under the academic pay-per-use Service, User shall maintain for at least four full calendar years books and records sufficient for CCC to determine the numbers of copies made by User under such permission. CCC and any representatives it may designate shall have the right to audit such books and records at any time during User's ordinary business hours, upon two days' prior notice. If any such audit shall determine that User shall have underpaid for, or underreported, any photocopies sold or by three percent (3%) or more, then User shall bear all the costs of any such audit; otherwise, CCC shall bear the costs of any such audit. Any amount determined by such audit to have been underpaid by User shall immediately be paid to CCC by User, together with interest thereon at the rate of 10% per annum from the date such amount was originally due. The provisions of this paragraph shall survive the termination of this License for any reason.

b) ***Digital Pay-Per-Uses of Academic Course Content and Materials (e-coursepacks, electronic reserves, learning management systems, academic institution intranets).*** For uses in e-coursepacks, posts in electronic reserves, posts in learning management systems, or posts on academic institution intranets, the following additional terms apply:

i) The pay-per-uses subject to this Section 14(b) include:

A) **Posting e-reserves, course management systems, e-coursepacks for text-based content,** which grants authorizations to import requested material in electronic format, and allows electronic access to this material to members of a designated college or university class, under the direction of an instructor designated by the college or university, accessible only under appropriate electronic controls (e.g., password);

B) **Posting e-reserves, course management systems, e-coursepacks for material consisting of photographs or other still images not embedded in text,** which grants not only the authorizations described in Section 14(b)(i)(A) above, but also the following authorization: to include the requested material in course materials for use consistent with Section 14(b)(i)(A) above, including any necessary resizing, reformatting or modification of the resolution of such requested material (provided that such modification does not alter the underlying editorial content or meaning of the requested material, and provided that the resulting modified content is used solely within the scope of, and in a manner consistent with, the particular authorization described in the Order Confirmation and the Terms), but not including any other form of manipulation, alteration or editing of the requested material;

C) **Posting e-reserves, course management systems, e-coursepacks or other academic distribution for audiovisual content,** which grants not only the authorizations described in Section 14(b)(i)(A) above, but also the following authorizations: (i) to include the requested material in course materials for use consistent with Section 14(b)(i)(A) above; (ii) to display and perform the requested material to such members of such class in the physical classroom or remotely by means of streaming media or other video formats; and (iii) to "clip" or reformat the requested material for purposes of time or content management or ease of delivery, provided that such "clipping" or reformatting does not alter the underlying editorial content or meaning of the requested material and that the resulting material is used solely within the scope of, and in a manner consistent with, the particular authorization described in the Order Confirmation and the Terms. Unless expressly set forth in the relevant Order Conformation, the License does not authorize any other form of manipulation, alteration or editing of the requested material.

ii) Unless expressly set forth in the relevant Order Confirmation, no License granted shall in any way: (i) include any right by User to create a substantively non-identical copy of the Work or to edit or in any other way modify the Work (except by means of deleting material immediately preceding or following the entire portion of the Work copied or, in the case of Works subject to Sections 14(b)(1)(B) or (C) above, as described in such Sections) (ii) permit "publishing ventures" where any particular course materials would be systematically marketed at multiple institutions.

iii) Subject to any further limitations determined in the Rightsholder Terms (and notwithstanding any apparent contradiction in the Order Confirmation arising from data provided by User), any use authorized under the electronic course content pay-per-use service is limited as follows:

A) any License granted shall apply to only one class (bearing a unique identifier as assigned by the institution, and thereby including all sections or other subparts of the class) at one institution;

B) use is limited to not more than 25% of the text of a book or of the items in a published collection of essays, poems or articles;

C) use is limited to not more than the greater of (a) 25% of the text of an issue of a journal or other periodical or (b) two articles from such an issue;

D) no User may sell or distribute any particular materials, whether photocopied or electronic, at more than one institution of learning;

E) electronic access to material which is the subject of an electronic-use permission must be limited by means of electronic password, student identification or other control permitting access solely to students and instructors in the class;

F) User must ensure (through use of an electronic cover page or other appropriate means) that any person, upon gaining electronic access to the material, which is the subject of a permission, shall see:

- a proper copyright notice, identifying the Rightsholder in whose name CCC has granted permission,
- a statement to the effect that such copy was made pursuant to permission,
- a statement identifying the class to which the material applies and notifying the reader that the material has been made available electronically solely for use in the class, and

- a statement to the effect that the material may not be further distributed to any person outside the class, whether by copying or by transmission and whether electronically or in paper form, and User must also ensure that such cover page or other means will print out in the event that the person accessing the material chooses to print out the material or any part thereof.

G) any permission granted shall expire at the end of the class and, absent some other form of authorization, User is thereupon required to delete the applicable material from any electronic storage or to block electronic access to the applicable material.

iv) Uses of separate portions of a Work, even if they are to be included in the same course material or the same university or college class, require separate permissions under the electronic course content pay-per-use Service. Unless otherwise provided in the Order Confirmation, any grant of rights to User is limited to use completed no later than the end of the academic term (or analogous period) as to which any particular permission is granted.

v) Books and Records; Right to Audit. As to each permission granted under the electronic course content Service, User shall maintain for at least four full calendar years books and records sufficient for CCC to determine the numbers of copies made by User under such permission. CCC and any representatives it may designate shall have the right to audit such books and records at any time during User's ordinary business hours, upon two days' prior notice. If any such audit shall determine that User shall have underpaid for, or underreported, any electronic copies used by three percent (3%) or more, then User shall bear all the costs of any such audit; otherwise, CCC shall bear the costs of any such audit. Any amount determined by such audit to have been underpaid by User shall immediately be paid to CCC by User, together with interest thereon at the rate of 10% per annum from the date such amount was originally due. The provisions of this paragraph shall survive the termination of this license for any reason.

c) ***Pay-Per-Use Permissions for Certain Reproductions (Academic photocopies for library reserves and interlibrary loan reporting) (Non-academic internal/external business uses and commercial document delivery).*** The License expressly excludes the uses listed in Section (c)(i)-(v) below (which must be subject to separate license from the applicable Rightsholder) for: academic photocopies for library reserves and interlibrary loan reporting; and non-academic internal/external business uses and commercial document delivery.

i) electronic storage of any reproduction (whether in plain-text, PDF, or any other format) other than on a transitory basis;

ii) the input of Works or reproductions thereof into any computerized database;

iii) reproduction of an entire Work (cover-to-cover copying) except where the Work is a single article;

iv) reproduction for resale to anyone other than a specific customer of User;

v) republication in any different form. Please obtain authorizations for these uses through other CCC services or directly from the rightsholder.

Any license granted is further limited as set forth in any restrictions included in the Order Confirmation and/or in these Terms.

d) ***Electronic Reproductions in Online Environments (Non-Academic-email, intranet, internet and extranet).*** For "electronic reproductions", which generally includes e-mail use (including instant messaging or other electronic transmission to a defined group of recipients) or posting on an intranet, extranet or Intranet site (including any display or performance incidental thereto), the following additional terms apply:

i) Unless otherwise set forth in the Order Confirmation, the License is limited to use completed within 30 days for any use on the Internet, 60 days for any use on an intranet or extranet and one year for any other use, all as measured from the "republication date" as identified in the Order Confirmation, if any, and otherwise from the date of the Order Confirmation.

ii) User may not make or permit any alterations to the Work, unless expressly set forth in the Order Confirmation (after request by User and approval by Rightsholder); provided, however, that a Work consisting of photographs or other still images not embedded in text may, if necessary, be resized, reformatted or have its resolution modified without additional express permission, and a Work consisting of audiovisual content may, if necessary, be "clipped" or reformatted for purposes of time or content management or ease of delivery (provided that any such resizing, reformatting, resolution modification or "clipping" does not alter the underlying editorial content or meaning of the Work used, and that the resulting material is used solely within the scope of, and in a manner consistent with, the particular License described in the Order Confirmation and the Terms.

15) **Miscellaneous.**

a) User acknowledges that CCC may, from time to time, make changes or additions to the Service or to the Terms, and that Rightsholder may make changes or additions to the Rightsholder Terms. Such updated Terms will replace the prior terms and conditions in the order workflow and shall be effective as to any subsequent Licenses but shall not apply to Licenses already granted and paid for under a prior set of terms.

b) Use of User-related information collected through the Service is governed by CCC's privacy policy, available online at www.copyright.com/about/privacy-policy/.

c) The License is personal to User. Therefore, User may not assign or transfer to any other person (whether a natural person or an organization of any kind) the License or any rights granted thereunder; provided, however, that, where applicable, User may assign such License in its entirety on written notice to CCC in the event of a transfer of all or substantially all of User's rights in any new material which includes the Work(s) licensed under this Service.

d) No amendment or waiver of any Terms is binding unless set forth in writing and signed by the appropriate parties, including, where applicable, the Rightsholder. The Rightsholder and CCC hereby object to any terms contained in any writing prepared by or on behalf of the User or its principals, employees, agents or affiliates and purporting to govern or otherwise relate to the License described in the Order Confirmation, which terms are in any way inconsistent with any Terms set forth in the Order Confirmation, and/or in CCC's standard operating procedures, whether such writing is prepared prior to, simultaneously with or subsequent to the Order Confirmation, and whether such writing appears on a copy of the Order Confirmation or in a separate instrument.

e) The License described in the Order Confirmation shall be governed by and construed under the law of the State of New York, USA, without regard to the principles thereof of conflicts of law. Any case, controversy, suit, action, or proceeding arising out of, in connection with, or related to such License shall be brought, at CCC's sole discretion, in any federal or state court located in the County of New York, State of New York, USA, or in any federal or state court whose geographical jurisdiction covers the location of the Rightsholder set forth in the Order Confirmation. The parties expressly submit to the personal jurisdiction and venue of each such federal or state court.

Last updated October 2022

JOHN WILEY AND SONS LICENSE
TERMS AND CONDITIONS

Nov 09, 2024

This Agreement between Technical of University of Munich--Xiaoxin Ma ("You") and John Wiley and Sons ("John Wiley and Sons") consists of your license details and the terms and conditions provided by John Wiley and Sons and Copyright Clearance Center.

License Number	5904891194127
License date	Nov 09, 2024
Licensed Content Publisher	John Wiley and Sons
Licensed Content Publication	ChemCatChem
Licensed Content Title	The Mechanism of Water Oxidation: From Electrolysis via Homogeneous to Biological Catalysis
Licensed Content Author	Peter Strasser, Stefan Roggan, Marcel Risch, et al
Licensed Content Date	Jul 7, 2010
Licensed Content Volume	2
Licensed Content Issue	7
Licensed Content Pages	38
Type of use	Dissertation/Thesis
Requestor type	University/Academic
Format	Print and electronic
Portion	Figure/table

Number of figures/tables	1
Will you be translating?	No
Title of new work	Deciphering the Active Role of Carboxylate-type MOFs in Alkaline OER: From Pristine Structures to Functional Intermediates
Institution name	Technical University of Munich
Expected presentation date	Nov 2024
Portions	Figure 4, in the dissertation as Figure 9a
The Requesting Person / Organization to Appear on the License	Technical of University of Munich--Xiaoxin Ma
Requestor Location	xiaoxin ma Technical University of Munich,Garching Munich, Not US or Canada 85748 Germany
Publisher Tax ID	EU826007151
Total	0.00 EUR
Terms and Conditions	

TERMS AND CONDITIONS

This copyrighted material is owned by or exclusively licensed to John Wiley & Sons, Inc. or one of its group companies (each a"Wiley Company") or handled on behalf of a society with which a Wiley Company has exclusive publishing rights in relation to a particular work (collectively "WILEY"). By clicking "accept" in connection with completing this licensing transaction, you agree that the following terms and conditions apply to this transaction (along with the billing and payment terms and conditions established by the Copyright Clearance Center Inc., ("CCC's Billing and Payment terms and conditions"), at the time that you opened your RightsLink account (these are available at any time at http://myaccount.copyright.com).

Terms and Conditions

- The materials you have requested permission to reproduce or reuse (the "Wiley Materials") are protected by copyright.

- You are hereby granted a personal, non-exclusive, non-sub licensable (on a stand-alone basis), non-transferable, worldwide, limited license to reproduce the Wiley Materials for the purpose specified in the licensing process. This license, **and any CONTENT (PDF or image file) purchased as part of your order,** is for a one-time use only and limited to any maximum distribution number specified in the license. The first instance of republication or reuse granted by this license must be completed within two years of the date of the grant of this license (although copies prepared before the end date may be distributed thereafter). The Wiley Materials shall not be used in any other manner or for any other purpose, beyond what is granted in the license. Permission is granted subject to an appropriate acknowledgement given to the author, title of the material/book/journal and the publisher. You shall also duplicate the copyright notice that appears in the Wiley publication in your use of the Wiley Material. Permission is also granted on the understanding that nowhere in the text is a previously published source acknowledged for all or part of this Wiley Material. Any third party content is expressly excluded from this permission.

- With respect to the Wiley Materials, all rights are reserved. Except as expressly granted by the terms of the license, no part of the Wiley Materials may be copied, modified, adapted (except for minor reformatting required by the new Publication), translated, reproduced, transferred or distributed, in any form or by any means, and no derivative works may be made based on the Wiley Materials without the prior permission of the respective copyright owner.**For STM Signatory Publishers clearing permission under the terms of the STM Permissions Guidelines only, the terms of the license are extended to include subsequent editions and for editions in other languages, provided such editions are for the work as a whole in situ and does not involve the separate exploitation of the permitted figures or extracts,** You may not alter, remove or suppress in any manner any copyright, trademark or other notices displayed by the Wiley Materials. You may not license, rent, sell, loan, lease, pledge, offer as security, transfer or assign the Wiley Materials on a stand-alone basis, or any of the rights granted to you hereunder to any other person.

- The Wiley Materials and all of the intellectual property rights therein shall at all times remain the exclusive property of John Wiley & Sons Inc, the Wiley Companies, or their respective licensors, and your interest therein is only that of having possession of and the right to reproduce the Wiley Materials pursuant to Section 2 herein during the continuance of this Agreement. You agree that you own no right, title or interest in or to the Wiley Materials or any of the intellectual property rights therein. You shall have no rights hereunder other than the license as provided for above in Section 2. No right, license or interest to any trademark, trade name, service mark or other branding ("Marks") of WILEY or its licensors is granted hereunder, and you agree that you shall not assert any such right, license or interest with respect thereto

- NEITHER WILEY NOR ITS LICENSORS MAKES ANY WARRANTY OR REPRESENTATION OF ANY KIND TO YOU OR ANY THIRD PARTY, EXPRESS, IMPLIED OR STATUTORY, WITH RESPECT TO THE MATERIALS OR THE ACCURACY OF ANY INFORMATION CONTAINED IN THE MATERIALS, INCLUDING, WITHOUT LIMITATION, ANY IMPLIED WARRANTY OF MERCHANTABILITY, ACCURACY, SATISFACTORY QUALITY, FITNESS FOR A PARTICULAR PURPOSE, USABILITY, INTEGRATION OR NON-INFRINGEMENT AND ALL SUCH WARRANTIES ARE HEREBY EXCLUDED BY WILEY AND ITS LICENSORS AND WAIVED

BY YOU.

- WILEY shall have the right to terminate this Agreement immediately upon breach of this Agreement by you.
- You shall indemnify, defend and hold harmless WILEY, its Licensors and their respective directors, officers, agents and employees, from and against any actual or threatened claims, demands, causes of action or proceedings arising from any breach of this Agreement by you.
- IN NO EVENT SHALL WILEY OR ITS LICENSORS BE LIABLE TO YOU OR ANY OTHER PARTY OR ANY OTHER PERSON OR ENTITY FOR ANY SPECIAL, CONSEQUENTIAL, INCIDENTAL, INDIRECT, EXEMPLARY OR PUNITIVE DAMAGES, HOWEVER CAUSED, ARISING OUT OF OR IN CONNECTION WITH THE DOWNLOADING, PROVISIONING, VIEWING OR USE OF THE MATERIALS REGARDLESS OF THE FORM OF ACTION, WHETHER FOR BREACH OF CONTRACT, BREACH OF WARRANTY, TORT, NEGLIGENCE, INFRINGEMENT OR OTHERWISE (INCLUDING, WITHOUT LIMITATION, DAMAGES BASED ON LOSS OF PROFITS, DATA, FILES, USE, BUSINESS OPPORTUNITY OR CLAIMS OF THIRD PARTIES), AND WHETHER OR NOT THE PARTY HAS BEEN ADVISED OF THE POSSIBILITY OF SUCH DAMAGES. THIS LIMITATION SHALL APPLY NOTWITHSTANDING ANY FAILURE OF ESSENTIAL PURPOSE OF ANY LIMITED REMEDY PROVIDED HEREIN.
- Should any provision of this Agreement be held by a court of competent jurisdiction to be illegal, invalid, or unenforceable, that provision shall be deemed amended to achieve as nearly as possible the same economic effect as the original provision, and the legality, validity and enforceability of the remaining provisions of this Agreement shall not be affected or impaired thereby.
- The failure of either party to enforce any term or condition of this Agreement shall not constitute a waiver of either party's right to enforce each and every term and condition of this Agreement. No breach under this agreement shall be deemed waived or excused by either party unless such waiver or consent is in writing signed by the party granting such waiver or consent. The waiver by or consent of a party to a breach of any provision of this Agreement shall not operate or be construed as a waiver of or consent to any other or subsequent breach by such other party.
- This Agreement may not be assigned (including by operation of law or otherwise) by you without WILEY's prior written consent.
- Any fee required for this permission shall be non-refundable after thirty (30) days from receipt by the CCC.
- These terms and conditions together with CCC's Billing and Payment terms and conditions (which are incorporated herein) form the entire agreement between you and WILEY concerning this licensing transaction and (in the absence of fraud) supersedes all prior agreements and representations of the parties, oral or written. This Agreement may not be amended except in writing signed by both parties. This Agreement shall be binding upon and inure to the benefit of the parties' successors, legal representatives, and authorized assigns.
- In the event of any conflict between your obligations established by these terms and conditions and those established by CCC's Billing and Payment terms and conditions, these terms and conditions shall prevail.

- WILEY expressly reserves all rights not specifically granted in the combination of (i) the license details provided by you and accepted in the course of this licensing transaction, (ii) these terms and conditions and (iii) CCC's Billing and Payment terms and conditions.

- This Agreement will be void if the Type of Use, Format, Circulation, or Requestor Type was misrepresented during the licensing process.

- This Agreement shall be governed by and construed in accordance with the laws of the State of New York, USA, without regards to such state's conflict of law rules. Any legal action, suit or proceeding arising out of or relating to these Terms and Conditions or the breach thereof shall be instituted in a court of competent jurisdiction in New York County in the State of New York in the United States of America and each party hereby consents and submits to the personal jurisdiction of such court, waives any objection to venue in such court and consents to service of process by registered or certified mail, return receipt requested, at the last known address of such party.

WILEY OPEN ACCESS TERMS AND CONDITIONS

Wiley Publishes Open Access Articles in fully Open Access Journals and in Subscription journals offering Online Open. Although most of the fully Open Access journals publish open access articles under the terms of the Creative Commons Attribution (CC BY) License only, the subscription journals and a few of the Open Access Journals offer a choice of Creative Commons Licenses. The license type is clearly identified on the article.

The Creative Commons Attribution License

The Creative Commons Attribution License (CC-BY) allows users to copy, distribute and transmit an article, adapt the article and make commercial use of the article. The CC-BY license permits commercial and non-

Creative Commons Attribution Non-Commercial License

The Creative Commons Attribution Non-Commercial (CC-BY-NC)License permits use, distribution and reproduction in any medium, provided the original work is properly cited and is not used for commercial purposes.(see below)

Creative Commons Attribution-Non-Commercial-NoDerivs License

The Creative Commons Attribution Non-Commercial-NoDerivs License (CC-BY-NC-ND) permits use, distribution and reproduction in any medium, provided the original work is properly cited, is not used for commercial purposes and no modifications or adaptations are made. (see below)

Use by commercial "for-profit" organizations

Use of Wiley Open Access articles for commercial, promotional, or marketing purposes requires further explicit permission from Wiley and will be subject to a fee.

Further details can be found on Wiley Online Library
http://olabout.wiley.com/WileyCDA/Section/id-410895.html

Other Terms and Conditions:

v1.10 Last updated September 2015

Questions? customercare@copyright.com.

JOHN WILEY AND SONS LICENSE
TERMS AND CONDITIONS

Nov 09, 2024

This Agreement between Technical of University of Munich--Xiaoxin Ma ("You") and John Wiley and Sons ("John Wiley and Sons") consists of your license details and the terms and conditions provided by John Wiley and Sons and Copyright Clearance Center.

License Number	5904891069159
License date	Nov 09, 2024
Licensed Content Publisher	John Wiley and Sons
Licensed Content Publication	ChemCatChem
Licensed Content Title	Universality in Oxygen Evolution Electrocatalysis on Oxide Surfaces
Licensed Content Author	Jan Rossmeisl, Jens K. Nørskov, Thomas F. Jaramillo, et al
Licensed Content Date	Mar 16, 2011
Licensed Content Volume	3
Licensed Content Issue	7
Licensed Content Pages	7
Type of use	Dissertation/Thesis
Requestor type	University/Academic
Format	Print and electronic

Portion	Figure/table
Number of figures/tables	1
Will you be translating?	No
Title of new work	Deciphering the Active Role of Carboxylate-type MOFs in Alkaline OER: From Pristine Structures to Functional Intermediates
Institution name	Technical University of Munich
Expected presentation date	Nov 2024
Portions	Figure 4 a, in the dissertation as Figure 9
The Requesting Person / Organization to Appear on the License	Technical of University of Munich--Xiaoxin Ma
Requestor Location	xiaoxin ma Technical University of Munich,Garching Munich, Not US or Canada 85748 Germany
Publisher Tax ID	EU826007151
Total	0.00 EUR

Terms and Conditions

TERMS AND CONDITIONS

This copyrighted material is owned by or exclusively licensed to John Wiley & Sons, Inc. or one of its group companies (each a"Wiley Company") or handled on behalf of a society with which a Wiley Company has exclusive publishing rights in relation to a particular work (collectively "WILEY"). By clicking "accept" in connection with completing this licensing transaction, you agree that the following terms and conditions apply to this transaction (along with the billing and payment terms and conditions established by the Copyright Clearance Center Inc., ("CCC's Billing and Payment terms and conditions"), at the time that you opened your RightsLink account (these are available at any time at http://myaccount.copyright.com).

Terms and Conditions

- The materials you have requested permission to reproduce or reuse (the "Wiley Materials") are protected by copyright.

- You are hereby granted a personal, non-exclusive, non-sub licensable (on a stand-alone basis), non-transferable, worldwide, limited license to reproduce the Wiley Materials for the purpose specified in the licensing process. This license, **and any CONTENT (PDF or image file) purchased as part of your order,** is for a one-time use only and limited to any maximum distribution number specified in the license. The first instance of republication or reuse granted by this license must be completed within two years of the date of the grant of this license (although copies prepared before the end date may be distributed thereafter). The Wiley Materials shall not be used in any other manner or for any other purpose, beyond what is granted in the license. Permission is granted subject to an appropriate acknowledgement given to the author, title of the material/book/journal and the publisher. You shall also duplicate the copyright notice that appears in the Wiley publication in your use of the Wiley Material. Permission is also granted on the understanding that nowhere in the text is a previously published source acknowledged for all or part of this Wiley Material. Any third party content is expressly excluded from this permission.

- With respect to the Wiley Materials, all rights are reserved. Except as expressly granted by the terms of the license, no part of the Wiley Materials may be copied, modified, adapted (except for minor reformatting required by the new Publication), translated, reproduced, transferred or distributed, in any form or by any means, and no derivative works may be made based on the Wiley Materials without the prior permission of the respective copyright owner.**For STM Signatory Publishers clearing permission under the terms of the STM Permissions Guidelines only, the terms of the license are extended to include subsequent editions and for editions in other languages, provided such editions are for the work as a whole in situ and does not involve the separate exploitation of the permitted figures or extracts,** You may not alter, remove or suppress in any manner any copyright, trademark or other notices displayed by the Wiley Materials. You may not license, rent, sell, loan, lease, pledge, offer as security, transfer or assign the Wiley Materials on a stand-alone basis, or any of the rights granted to you hereunder to any other person.

- The Wiley Materials and all of the intellectual property rights therein shall at all times remain the exclusive property of John Wiley & Sons Inc, the Wiley Companies, or their respective licensors, and your interest therein is only that of having possession of and the right to reproduce the Wiley Materials pursuant to Section 2 herein during the continuance of this Agreement. You agree that you own no right, title or interest in or to the Wiley Materials or any of the intellectual property rights therein. You shall have no rights hereunder other than the license as provided for above in Section 2. No right, license or interest to any trademark, trade name, service mark or other branding ("Marks") of WILEY or its licensors is granted hereunder, and you agree that you shall not assert any such right, license or interest with respect thereto

- NEITHER WILEY NOR ITS LICENSORS MAKES ANY WARRANTY OR REPRESENTATION OF ANY KIND TO YOU OR ANY THIRD PARTY, EXPRESS, IMPLIED OR STATUTORY, WITH RESPECT TO THE MATERIALS OR THE ACCURACY OF ANY INFORMATION CONTAINED IN THE MATERIALS, INCLUDING, WITHOUT LIMITATION, ANY IMPLIED WARRANTY OF MERCHANTABILITY, ACCURACY, SATISFACTORY QUALITY, FITNESS FOR A PARTICULAR PURPOSE, USABILITY,

INTEGRATION OR NON-INFRINGEMENT AND ALL SUCH WARRANTIES ARE HEREBY EXCLUDED BY WILEY AND ITS LICENSORS AND WAIVED BY YOU.

- WILEY shall have the right to terminate this Agreement immediately upon breach of this Agreement by you.
- You shall indemnify, defend and hold harmless WILEY, its Licensors and their respective directors, officers, agents and employees, from and against any actual or threatened claims, demands, causes of action or proceedings arising from any breach of this Agreement by you.
- IN NO EVENT SHALL WILEY OR ITS LICENSORS BE LIABLE TO YOU OR ANY OTHER PARTY OR ANY OTHER PERSON OR ENTITY FOR ANY SPECIAL, CONSEQUENTIAL, INCIDENTAL, INDIRECT, EXEMPLARY OR PUNITIVE DAMAGES, HOWEVER CAUSED, ARISING OUT OF OR IN CONNECTION WITH THE DOWNLOADING, PROVISIONING, VIEWING OR USE OF THE MATERIALS REGARDLESS OF THE FORM OF ACTION, WHETHER FOR BREACH OF CONTRACT, BREACH OF WARRANTY, TORT, NEGLIGENCE, INFRINGEMENT OR OTHERWISE (INCLUDING, WITHOUT LIMITATION, DAMAGES BASED ON LOSS OF PROFITS, DATA, FILES, USE, BUSINESS OPPORTUNITY OR CLAIMS OF THIRD PARTIES), AND WHETHER OR NOT THE PARTY HAS BEEN ADVISED OF THE POSSIBILITY OF SUCH DAMAGES. THIS LIMITATION SHALL APPLY NOTWITHSTANDING ANY FAILURE OF ESSENTIAL PURPOSE OF ANY LIMITED REMEDY PROVIDED HEREIN.
- Should any provision of this Agreement be held by a court of competent jurisdiction to be illegal, invalid, or unenforceable, that provision shall be deemed amended to achieve as nearly as possible the same economic effect as the original provision, and the legality, validity and enforceability of the remaining provisions of this Agreement shall not be affected or impaired thereby.
- The failure of either party to enforce any term or condition of this Agreement shall not constitute a waiver of either party's right to enforce each and every term and condition of this Agreement. No breach under this agreement shall be deemed waived or excused by either party unless such waiver or consent is in writing signed by the party granting such waiver or consent. The waiver by or consent of a party to a breach of any provision of this Agreement shall not operate or be construed as a waiver of or consent to any other or subsequent breach by such other party.
- This Agreement may not be assigned (including by operation of law or otherwise) by you without WILEY's prior written consent.
- Any fee required for this permission shall be non-refundable after thirty (30) days from receipt by the CCC.
- These terms and conditions together with CCC's Billing and Payment terms and conditions (which are incorporated herein) form the entire agreement between you and WILEY concerning this licensing transaction and (in the absence of fraud) supersedes all prior agreements and representations of the parties, oral or written. This Agreement may not be amended except in writing signed by both parties. This Agreement shall be binding upon and inure to the benefit of the parties' successors, legal representatives, and authorized assigns.
- In the event of any conflict between your obligations established by these terms and conditions and those established by CCC's Billing and Payment terms and

conditions, these terms and conditions shall prevail.

- WILEY expressly reserves all rights not specifically granted in the combination of (i) the license details provided by you and accepted in the course of this licensing transaction, (ii) these terms and conditions and (iii) CCC's Billing and Payment terms and conditions.
- This Agreement will be void if the Type of Use, Format, Circulation, or Requestor Type was misrepresented during the licensing process.
- This Agreement shall be governed by and construed in accordance with the laws of the State of New York, USA, without regards to such state's conflict of law rules. Any legal action, suit or proceeding arising out of or relating to these Terms and Conditions or the breach thereof shall be instituted in a court of competent jurisdiction in New York County in the State of New York in the United States of America and each party hereby consents and submits to the personal jurisdiction of such court, waives any objection to venue in such court and consents to service of process by registered or certified mail, return receipt requested, at the last known address of such party.

WILEY OPEN ACCESS TERMS AND CONDITIONS

Wiley Publishes Open Access Articles in fully Open Access Journals and in Subscription journals offering Online Open. Although most of the fully Open Access journals publish open access articles under the terms of the Creative Commons Attribution (CC BY) License only, the subscription journals and a few of the Open Access Journals offer a choice of Creative Commons Licenses. The license type is clearly identified on the article.

The Creative Commons Attribution License

The Creative Commons Attribution License (CC-BY) allows users to copy, distribute and transmit an article, adapt the article and make commercial use of the article. The CC-BY license permits commercial and non-

Creative Commons Attribution Non-Commercial License

The Creative Commons Attribution Non-Commercial (CC-BY-NC)License permits use, distribution and reproduction in any medium, provided the original work is properly cited and is not used for commercial purposes.(see below)

Creative Commons Attribution-Non-Commercial-NoDerivs License

The Creative Commons Attribution Non-Commercial-NoDerivs License (CC-BY-NC-ND) permits use, distribution and reproduction in any medium, provided the original work is properly cited, is not used for commercial purposes and no modifications or adaptations are made. (see below)

Use by commercial "for-profit" organizations

Use of Wiley Open Access articles for commercial, promotional, or marketing purposes requires further explicit permission from Wiley and will be subject to a fee.

Further details can be found on Wiley Online Library
http://olabout.wiley.com/WileyCDA/Section/id-410895.html

Other Terms and Conditions:

v1.10 Last updated September 2015

Questions? customercare@copyright.com.

Morphology control through the synthesis of metal-organic frameworks

Author:
Justyna Łuczak,Malwina Kroczewska,Mateusz Baluk,Jakub Sowik,Paweł Mazierski,Adriana Zaleska-Medynska

Publication: Advances in Colloid and Interface Science
Publisher: Elsevier
Date: April 2023

Water electrolysis: from textbook knowledge to the latest scientific strategies and industrial developments

M. Chatenet, B. G. Pollet, D. R. Dekel, F. Dionigi, J. Deseure, P. Millet, R. D. Braatz, M. Z. Bazant, M. Eikerling, I. Staffell, P. Balcombe, Y. Shao-Horn and H. Schäfer, *Chem. Soc. Rev.*, 2022, **51**, 4583 **DOI:** 10.1039/D0CS01079K

RightsLink

ACS Publications
Most Trusted. Most Cited. Most Read.

Metal–Organic Frameworks for Electrocatalysis: Catalyst or Precatalyst?

Author: Weiran Zheng, Lawrence Yoon Suk Lee
Publication: ACS Energy Letters
Publisher: American Chemical Society
Date: Aug 1, 2021

PERMISSION/LICENSE IS GRANTED FOR YOUR ORDER AT NO CHARGE

This type of permission/license, instead of the standard Terms and Conditions, is sent to you because no fee is being charged for your order. Please note the following:

- Permission is granted for your request in both print and electronic formats, and translations.
- If figures and/or tables were requested, they may be adapted or used in part.
- Please print this page for your records and send a copy of it to your publisher/graduate school.
- Appropriate credit for the requested material should be given as follows: "Reprinted (adapted) with permission from {COMPLETE REFERENCE CITATION}. Copyright {YEAR} American Chemical Society." Insert appropriate information in place of the capitalized words.
- One-time permission is granted only for the use specified in your RightsLink request. No additional uses are granted (such as derivative works or other editions). For any uses, please submit a new request.

If credit is given to another source for the material you requested from RightsLink, permission must be obtained from that source.

BACK CLOSE WINDOW

Structure–Activity Relationships in Ni- Carboxylate-Type Metal–Organic Frameworks' Metamorphosis for the Oxygen Evolution Reaction

Author: Xiaoxin Ma, Daniel J. Zheng, Shujin Hou, et al
Publication: ACS Catalysis
Publisher: American Chemical Society
Date: Jun 1, 2023